

HIGH PRECISION MASS MEASUREMENT OF ^{37}Ca AND
DEVELOPMENTS FOR LEBIT

By

Tao Sun

A DISSERTATION

Submitted to
Michigan State University
in partial fulfillment of the requirements
for the degree of

DOCTOR OF PHILOSOPHY

Department of Physics and Astronomy

2006

ABSTRACT

HIGH PRECISION MASS MEASUREMENT OF ^{37}Ca AND DEVELOPMENTS FOR LEBIT

By

Tao Sun

The Low-Energy Beam and Ion Trap facility (LEBIT) installed at the NSCL at MSU allows short-lived radioactive isotopes produced by projectile-fragmentation of relativistic heavy ion beams to be slowed down and prepared in such a manner that precision experiments requiring low energy beams are possible. The first kind of experimental equipment installed is a 9.4-Tesla Penning trap mass spectrometer for high precision mass measurements on short-lived nuclei. Plans for laser spectroscopy studies exist. The present work presents the technical developments that were required to let LEBIT become a reality. This work also presents the results of the first mass measurements on rare isotopes. A complex electrostatic beam transport system was designed based on ion optical simulations. The goal of these simulations was a minimum emittance growth and maximum transmission. Both were achieved in the realized system. A further contribution to the realization of LEBIT was the development of a control and data acquisition system based on LabVIEW and C++. In operation for more than a year, the system has demonstrated high reliability, fast response, and flexibility with respect to system changes and growth. An important component of LEBIT is a beam cooler and buncher based on a gas-filled radiofrequency ion trap. The performance and properties of this system have been systematically studied in a series of measurements. The experimental results have been compared to those from Monte-Carlo simulations and very good agreement was found. The first high precision mass measurement on short-lived isotopes with LEBIT were performed on ^{37}Ca and ^{38}Ca . The subject of the present work focuses on the measurements performed on

^{37}Ca , which has a half-life of only $T_{1/2}=181$ ms. A mass uncertainty of $\delta m = 1.4$ keV was reached, improving the previous mass value by an order of magnitude. The result has been applied to the Isobaric Multiplet Mass Equation (IMME) for the $A=37$, $T=3/2$ quartet. With newly calculated IMME coefficients for this quartet, the energy of the isobaric-analog state in ^{37}Ar can now be predicted with improved precision.

*To My Wife Xiaoli Yuan, My Parents ZhongLiang Sun and Shuying Yuan, My
Sister Liping Sun, and All my Collaborators in the LEBIT Project*

ACKNOWLEDGMENTS

First I want to give my thanks to the NSCL, a great laboratory that hosts a world-class coupled-cyclotron facility for rare isotope research. It provides tremendous new opportunities for exploring the nature of nuclei. Its successful operation and high quality radioactive nuclear beams were important for the successful completion of this thesis. And I would like to salute to all the employees working here. It is only due to your fabulous working that this facility can be so productive and reliable.

Also I want to show my appreciation to those great guys who contribute to the design, machinering, set up and installation of components of the LEBIT facility. Honor should go to designer Matt Johnson, Don Lawton, Jim Moskalik and Jack Ottarson, staff engineer Kelly Davidson, John Priller and Dale Smith. I can not forget the smiling face and great patience of Jim Moskalik each time I went to bug him about the drawings and the tedious conversion from English to metric units. Thank you Jim. And I have to say thank you to the whole group of Cyclotron operators. Although I don't know most of you, I remember the hard and efficient work you have made in those nights during our beam time.

Now it comes to our big family, the members of LEBIT group. Of course the first person I would like to show my gratitude is my supervisor, Prof. Georg Bollen, who introduced me to the beautiful world of ion trap physics and who brought the creative idea of LEBIT to NSCL and made it working so successfully. Another special thankfulness goes to Physicist Stefan Schwarz, who guided me through the beam optics simulation, LabVIEW and C++ programming for the LEBIT control system, calculations of LEBIT buncher and the analysis of the ^{37}Ca mass measurement result. You are actually my second supervisor in this manner. I have to thank two other peer graduate students of LEBIT. Peter Schury did an excellent job on the RFQ simulation, its electronic design and tuning, and bringing the ion guide mass filter to excellent

performance. Ryan Ringle was the key player in the simulation, design and systematic study of Penning Trap. Without the work of both of you LEBIT would not operate so well today. Besides that, a lot of credits should be given to Prof. Dave Morrissey, Postdoc fellows Marius Facina, Jussi Huikari, Leo Weissman who is now an assistant professor in University of Connecticut, and graduate students Debbie Davies, Elaine Kwan, Greg Pang, Amanda Prinke, Josh Savory, Chandana Sumithrarachchi and the ex-undergraduate student Tony Doemer, for their contributions to the progress of the LEBIT project, and its successful operation. Without their excellent work I can not imagine the achievement of LEBIT nowadays, no mention the completion of this thesis.

Next I want to show my genuine thank from the bottom of my heart to my family, my dad Zhongliang Sun, my mom Shuying Yuan, without their selfless devoting to my growth I can not be myself today, my elder sister Liping Sun, who always gives me very good advices both on the life and my study. Especially to my wife, Xiaoli Yuan, her unconditional support in the past six years really means something to me. Although I leave this at the end of my thank list, it does not mean it is less important to me. Without all of these I am afraid I could not achieve what I have achieved, not even a tiny step further.

Contents

1	Introduction	1
1.1	Importance of mass measurement of rare isotopes	3
1.2	Different techniques for mass measurement	6
1.3	Outline of this thesis	9
2	LEBIT overview	10
2.1	The gas stopping station	11
2.2	The test beam ion source	15
2.3	The ion buncher system	16
2.4	The Penning trap system	18
3	The electrostatic beam transport system of LEBIT	22
3.1	Ion optics simulation	27
3.1.1	Tools used in ion optics simulation	27
3.1.2	Simulation example	27
3.1.3	Emittance of the beam	28
3.2	Ion optics simulation of the beam transport system	31
3.2.1	From the gas cell to the N4-shielding wall	32
3.2.2	From the N4-shielding wall to the ion buncher	36
3.2.3	From the ion buncher to the Penning trap and other experi- mental areas	39
3.3	Performance of the beam transport system	45
4	LEBIT control and data acquisition system	47
4.1	Requirements	47
4.2	Devices to be controlled	50
4.3	LEBIT computer hardware	52
4.3.1	The server computer/PXI-bus system	54
4.3.2	The PLC system	56
4.3.3	Fast timing	58
4.4	Software of the LEBIT control and data acquisition system	61
4.4.1	PLC Software	62
4.4.2	Server applications	64
4.4.3	Client applications	69
4.5	System performance and future development	76

5	Beam cooling, accumulation and bunching	78
5.1	The principle of the mass filter	79
5.2	Ion cooling with buffer gas	83
5.3	The LEBIT ion buncher system	85
5.3.1	Electrode configuration	86
5.3.2	Vacuum and gas inlet system	88
5.3.3	Electronic system for RF generation	90
5.3.4	Cryogenic cooling system	93
5.4	Modes of operation	93
5.4.1	Continuous mode	93
5.4.2	Pulsed mode	95
5.4.3	Summary	95
5.5	Experimental systematic studies of the ion buncher	98
5.5.1	Buncher operated in continuous mode	99
5.5.2	Buncher operated in pulsed mode	106
5.5.3	Beam profiles and emittance measurements	116
5.5.4	Buncher section operated as a mass filter	128
5.6	Buncher simulations	131
6	First Penning trap mass measurement of rare isotopes	141
6.1	Concept of the Penning trap	141
6.2	High precision mass measurement of ^{37}Ca with Penning trap mass spectrometer	146
6.3	Application of the ^{37}Ca mass measurement result together with the Isobaric Multiplet Mass Equation	153
6.4	Simulations of resonances under low statistics	157
7	Summary	162
A	Details of ion optical simulation of the beam transport	164
A.1	Notation used in the simulation	164
A.2	From the gas cell to the N4-shielding wall	165
A.3	From the N4-shielding wall to the ion buncher	166
A.3.1	Straight line transport from the N4-shielding wall to the ion buncher	166
A.3.2	From the test ion source to the ion buncher	167
A.4	From the ion buncher to the Penning trap and other experimental areas	170
A.4.1	Straight line beam transport from the ion buncher to the Penning trap	170
A.4.2	Optional beam transport through a switchyard	179
	<i>Bibliography</i>	183

List of Tables

3.1	Voltage switching time of the pulsed drift tube and corresponding width of the axial spatial distribution inside the pulsed drift tube. . .	41
4.1	Devices controlled in LEBIT according to the type of control.	51
4.2	Plain-text ASCII instructions used for communication between the LEBIT server and the client applications.	66
4.3	LEBIT control panels for experiment control.	71
4.4	Sections of the vacuum control application.	73
5.1	Reduced ion mobility K_0 for different ion and buffer gas combinations.	85
5.2	Operating parameters for the RF generating circuit.	92
5.3	Voltages applied to the electrodes in the cooler and μ -RFQ sections. .	97
5.4	Voltages applied to the electrodes in the buncher section for different operation modes.	97
5.5	Optimum RF amplitudes for the three ion buncher sections.	97
5.6	First level ionization potentials for some elements.	110
6.1	Input data and error budget for the determination of the mass of ^{37}Ca .	152
6.2	Comparison of the mass excess values for ^{37}Ca from different sources.	153
6.3	Mass excess (ME) values of ground states (GS) and isobaric analog states (IAS) and excitation energies (E_x) in the $A=37$ and $T=3/2$ quartet.	155
6.4	Extended IMME coefficients including a cubic term.	157
6.5	Improved coefficients of IMME for the $A = 37, T = 3/2$ quartet. . . .	158
A.1	Parameters used in the ion optical simulation of the beam transport from the gas cell to the N4-shielding wall.	165
A.2	Optimum parameters of the elements of the beam transport system from the gas cell ion guide to the N4-shielding wall.	166
A.3	Parameters used in the ion optical simulation for the straight line beam transport from the N4-shielding wall to the ion buncher.	167
A.4	Optimum parameters of the elements for the straight line beam transport from the N4-shielding wall to the ion buncher.	167
A.5	Parameters used in the ion optical simulation of the beam transport from the test ion source to the ion buncher.	168
A.6	Optimum parameters of the elements for the beam transport from the test ion source to the ion buncher.	169

A.7	Parameters used in the ion optical simulation of the beam transport from the ion buncher to BOB4.	171
A.8	Optimum parameters of the elements for the beam transport from the ion buncher to BOB4.	171
A.9	Parameters used in the ion optical simulation of the beam transport from BOB4 to the Penning trap.	176
A.10	Optimum parameters used for the elements of the beam transport from BOB4 to the Penning trap.	176
A.11	Parameters used in the ion optical simulation for the beam transport from BOB4 through a switchyard.	179
A.12	Optimum parameters of the elements for the beam transport from BOB4 through a switchyard.	181
A.13	Effect of the energy spread on the increase of the transverse emittance.	182

List of Figures

2.1	Layout of the Coupled Cyclotron Facility.	10
2.2	Layout of the LEBIT experimental setup.	12
2.3	The gas stopping station.	13
2.4	The test ion source.	15
2.5	The ion buncher system.	17
2.6	The Penning trap system.	19
2.7	A cyclotron resonance curve of $^{82}\text{Kr}^+$ ions.	21
3.1	Microchannel plate detector system.	23
3.2	Examples of component of the LEBIT beam transport system.	24
3.3	Block diagram of the electrostatic beam transport system of LEBIT.	26
3.4	Ion beam focusing through an Einzel lens.	28
3.5	Transport of a real beam.	28
3.6	Evolution of phase space diagrams.	30
3.7	A general situation of the phase space diagram.	31
3.8	SIMION simulation of the ion beam transport from the gas cell to the N4-shielding wall.	33
3.9	Examples of electrodes used in the beam transport from the gas cell to the N4-shielding wall.	34
3.10	Beam properties in the transverse plane at the entrance to the acceleration section.	35
3.11	Transverse phase space diagrams at the center of BOB1.	37
3.12	SIMION simulation of the ion beam transport from BOB1 to BOB3.	37
3.13	SIMION simulation of the ion beam transport from the test ion source to BOB3.	38
3.14	SIMION simulation of the ion beam transport from the ion buncher to the switchyard.	40
3.15	Beam transport to the Penning trap.	42
3.16	COSY simulation for a 60° beam line.	43
3.17	COSY simulation for a 90° beam line.	44
3.18	Beam transmission from the gas cell to the ion buncher as a function of the voltages applied to the Einzel lenses EL2 and EL3.	46
4.1	Two power supply modules used in LEBIT.	53
4.2	Structure of the hardware system used in the LEBIT control and DAQ system.	55
4.3	Timing generator and timing interface.	59

4.4	Structure of the software system used in the LEBIT control and DAQ system.	60
4.5	A ladder program segment of LEBIT's vacuum control PLC.	63
4.6	Overview of a measurement cycle for a cyclotron resonance measurement of $^{86}\text{Kr}^+$	68
4.7	Control panel and popup dialog windows for the LEBIT Penning trap.	70
4.8	Control panel for the LEBIT vacuum system.	72
4.9	Main panel of the parameter scan and DAQ program for a cyclotron frequency measurement of $^{39}\text{K}^+$	74
4.10	Configuration panel for a cyclotron frequency measurement of $^{39}\text{K}^+$	75
5.1	Schematic presentation of a gas-filled RFQ trap and the DC potential inside the trap.	78
5.2	Sketch of a mass filter.	79
5.3	Stability diagrams for a mass filter.	82
5.4	Front view of the fully assembled LEBIT ion buncher.	85
5.5	Electrode configuration of the LEBIT ion buncher system.	87
5.6	Vacuum and gas inlet system of the LEBIT ion buncher.	89
5.7	Sketch of the electronic circuit used to supply the RF voltage to the RFQ electrodes for the ion buncher system.	91
5.8	Side view of the cooling baffle installed in the vacuum chamber.	92
5.9	DC potential on the axis of the ion buncher operated in different modes.	94
5.10	DC potential on the axis of the buncher section for the buncher operated in two extraction scenarios.	96
5.11	Transmission efficiency for a continuous beam.	99
5.12	Time-of-flight distributions of ion pulses sent through the He filled ion buncher when operated in continuous mode.	100
5.13	Dependence of the mean time-of-flight on buffer gas type, pressure and temperature.	101
5.14	Effect of the buffer gas pressure on K_0/K	103
5.15	The width of time of flight distribution vs. the modified effective pressure.	104
5.16	Normalized transmission of ion pulses sent through the cooler as a function of modified effective pressure.	105
5.17	Time-of-flight distributions of extracted $^{39}\text{K}^+$ ion pulses recorded under different operating conditions.	107
5.18	Transmission of $^{40}\text{Ar}^+$ ion through the ion buncher.	108
5.19	Effect of the cooling time on the transmission of $^{39}\text{K}^+$ ions when the ion buncher is operated in the fast extraction scenario.	110
5.20	Ion loss in the buncher due to a long cooling time.	111
5.21	Effect of cooling time on the time-of-flight distribution of $^{86}\text{Kr}^+$ ions extracted from the buncher operated in fast extraction scenario.	113
5.22	Energy acceptance of the ion buncher.	115
5.23	A beam profile extracted from a beam image.	116
5.24	Scattering of the values obtained for the width of the beam profile.	117
5.25	Beam images captured with a CCD camera. (a) defocused beam (b) focused beam.	118

5.26	Structure of a defocused beam spot near the location of a focused beam spot.	118
5.27	Results of the beam emittance measurements obtained with the ion buncher operated at T=300 K.	119
5.28	Sketch of the beam focusing manipulation that is implemented in the SIMION simulation to determine the linear transformation matrix.	121
5.29	Results of the beam emittance measurements obtained with the ion buncher operated at T=200 K.	123
5.30	Effect of the number of injected ions on the beam profile at T=200K.	124
5.31	Effect of the cooling time on the beam profile.	125
5.32	Effect of the RF amplitude used in the buncher section on the beam profile.	127
5.33	Transmission of $^{40}\text{Ar}^+$ ions as a function of RF amplitude V_{rf} and offset voltage $V_{\text{Bunfilter}}$	129
5.34	Transmission of $^{40}\text{Ar}^+$ ions as a function of RF amplitude V_{rf} and offset voltage $V_{\text{Bunfilter}}$ with $V_{\text{Bunfilter}}/V_{\text{rf}}=0.13$	129
5.35	Simulated trajectory of an $^{40}\text{Ar}^+$ ion being cooled and captured in the ion buncher.	131
5.36	Simulated time-of-flight spectra of beam pulses for the ion buncher operated in continuous mode at T=300 K.	134
5.37	Simulated time-of-flight spectra of beam pulses for the ion buncher operated in continuous mode at T=181 K.	135
5.38	Simulated time-of-flight spectra of beam pulses for the ion buncher operated in pulsed mode.	136
5.39	Simulated effect of the cooling time on the time-of-flight distribution of $^{40}\text{Ar}^+$ ion pulses.	136
5.40	Simulated number of extracted $^{40}\text{Ar}^+$ ions as a function of the cooling time.	138
5.41	Simulated axial distributions of $^{40}\text{Ar}^+$ ions for 3 different cooling times.	139
5.42	Simulated transverse emittance of $^{40}\text{Ar}^+$ ion pulses.	140
6.1	Basic electrode configuration of a Penning Trap.	142
6.2	The three eigen motions of an ion stored inside a Penning trap.	143
6.3	Electrode configurations to generate RF field for ion motion excitation.	143
6.4	Conversion between two radial eigen motions in the case of quadrupole excitation.	144
6.5	Resonance profiles for two different RF amplitudes in the case of quadrupole excitation.	145
6.6	Cyclotron resonance for $^{37}\text{Ca}^{2+}$ ions obtained with a time-of-flight resonance detection technique.	148
6.7	Measured cyclotron frequency ratios R between $(\text{H}_3\text{O})^+$ and $^{37}\text{Ca}^{2+}$ relative to the average value \bar{R}	150
6.8	Magnetic field drift over an 18 hour time period of the $^{37}\text{Ca}^{2+}$ mass measurement.	151
6.9	Comparison of ^{37}Ca mass values obtained in different experiments and the literature value.	152

6.10	Plot of mass excess values of isobaric analog states in the A=37 and T=3/2 quartet.	155
6.11	Values of the d coefficient of IMME for all the 25 T=3/2 quartets. . .	156
6.12	Examples of cyclotron resonance curves used to simulate the effect of background events in the case of low-statistics measurements.	158
6.13	Analysis of frequency shifts $\Delta\nu/\nu_c$ due to background events.	160
6.14	Cyclotron resonance curve of H_3O^+	160
A.1	Transverse phase space diagrams for the straight line beam transport from the N4-shielding wall to the ion buncher.	168
A.2	Transverse phase space diagrams at the position of the test ion source.	169
A.3	Transverse phase space diagrams at BOB3.	170
A.4	Transverse phase space diagrams for three different masses at the exit of the transfer tube.	172
A.5	Axial spatial distribution of ions inside the pulsed drift tube with the optimum potential switching time.	173
A.6	Transverse phase space diagrams for three different masses transported from the ion buncher to BOB4 with an final energy of about 2 keV. .	174
A.7	Transverse phase space diagrams for three different masses transported from the ion buncher to BOB4 with an final energy of about 60 keV.	175
A.8	Transverse energy distribution for three different masses before entering the magnetic field.	177
A.9	Transverse energy distribution for three different masses before the center of the magnetic field.	178
A.10	Initial transverse phase space diagrams for the beam transport from BOB4 through a switchyard.	180
A.11	Transverse phase space diagrams of the beam after being bent by 60° to the switchyard.	182
Images in this thesis/dissertation are presented in color.		

Chapter 1

Introduction

Accurate masses of rare isotopes are important for a better understanding of nuclear structure, as input for the modelling of element synthesis in nuclear astrophysics, and for fundamental tests of the weak interaction. Today, a number of techniques exist for mass measurements of short-lived isotopes. A very powerful approach is the employment of Penning traps. Penning trap mass spectrometry offers unprecedented accuracy and can be applied to nuclides with half-lives below a tenth of a second and produced only in minute quantities. Most of the Penning trap mass spectrometers for rare isotopes presently operational are installed at facilities that provide beams of very low (tens of keV) or medium high (a few MeV/u) energies. The only facility presently under construction for mass measurements on rare nuclides produced at energies of the order of 100 MeV/u is the Low-Energy Beam and Ion Trap facility LEBIT at the NSCL at MSU.

The two most important production techniques for radioactive nuclides are the Isotope Separator On-Line (ISOL) technique and the ion-flight separation of relativistic beam fragments. In the case of the ISOL method, a high energy beam of light ions bombards a thick target of heavier elements. The targets are kept at high temperature so that the reaction products can diffuse out of the target material and effuse into an ion source. There the radioactive atoms are ionized. The ions are accelerated to an

energy of a few tens of keV and mass separated in a isotope separator. The low-energy of ISOL beams and their good beam quality makes them well suited for capture in ion traps and for other low energy beam experiments, for example laser spectroscopy. The ISOL method is used at facilities like ISOLDE at CERN or ISAC at TRIUMF. An advantage of the ISOL method is its high production rates for a certain range of isotopes. Drawbacks of this method are its limitation to relatively volatile elements, and its limitation to short-lived isotopes because of significant decay-losses in the targets. In contrast to this, the fragmentation of relativistic heavy-ion beams in thin targets followed by in-flight separation has no chemical limitation and is fast. It is a powerful technique in particular for the study of very exotic isotopes. In-flight separation is for example used at GSI, RIKEN and at the NSCL. The high-energy of the rare isotopes beams at such facilities make them well-suited for Coulomb excitation and reaction studies, but their beam properties do not match the requirements needed for ISOL-type experiments like ion trapping or laser spectroscopy. In order to be useful for such experiments the fast fragments have to be converted to high-quality low-energy beams. At the NSCL it has been demonstrated that this can be achieved by using gas stopping and advanced beam manipulation techniques with ion guides and ion traps. The low-energy exotic beams now available offer new possibilities for studying properties of rare isotopes only available from fast-beam fragmentation. They include in-trap decay studies, laser spectroscopy, and high precision mass measurements. The first experiments performed with LEBIT are high precision mass measurements with a high-field Penning trap mass spectrometer. One of the first rare isotopes studied is ^{37}Ca , which will be discussed in this work.

1.1 Importance of mass measurement of rare isotopes

The ground-state mass of a nucleus is one of the most fundamental nuclear properties. The nuclear mass is inherently connected to the binding energy, which accommodates all the essential information of the nuclear force. That leads to the importance of the mass on the following fields: nuclear astrophysics, nuclear mass models, nuclear structure and fundamental symmetries.

Masses are important input data for a better understanding of the synthesis of the elements. Several processes are known to exist. There are still many questions about the astrophysical scenarios in which they occur and which path they take in producing heavier elements. This is in particular true for the rapid neutron-capture process (r-process) [1]. This process, which is thought to occur in type II supernova or neutron star mergers, creates nearly half of all the heavy elements beyond iron. Beta decay properties and nuclear masses are the most important nuclear physics parameters in r-process calculations. The r-process takes place very far from stability and so far little experimental information on masses is available for nuclides located in its path. Masses are also critical for understanding of the rapid-proton capture process [2], which is thought to occur in explosive scenarios called X-ray bursts. At the high temperatures in this process (10^9 K) there is a competition between proton capture and photodisintegration. The proton capture rate depends critically on the proton separation energies, and the masses of the two nuclides involved. If photodisintegration dominates, the process will stall until a beta decay to a nucleus with higher capture rate occurs. If the nuclide has a lifetime large enough to significantly slow down the overall process then it is referred to as a waiting-point nuclide. Masses of these nuclides are of particular importance for the modelling of the r- process. These waiting point nuclei are located along the $N=Z$ line, examples are ^{68}Se , ^{72}Kr and ^{76}Sr .

A number of nuclear mass models and semi-empirical mass formulas have been

developed to predict nuclear masses, as they are for example required to provide input data for nuclear astrophysics. Their parameters are optimized by fitting to experimental data. As a consequence, most models agree very well with each other and experimental masses where those exist. Far from stability, in regions where masses are unknown the predictions differ significantly [3]. Thus accurate experimental mass values are of significance to test the predictive power of these formula and models and to contribute to their improvement.

The systematic investigation of masses provides insight into how nuclear binding evolves as a function of isospin and mass number. Effects like pairing and shell and subshell closures and their strength are directly observable. Systematic mass measurements far from stability have led to the discovery of important new nuclear structure effects.

Shell closures reveal themselves directly as specific discontinuities in the trend of nuclear binding energies as a function of neutron or proton numbers. The observation of particular stable nuclei close to stability have manifested the “magic” numbers. Today we know that nuclear shell structure evolves as we leave the narrow band of stable nuclei, leading to shell quenching and the appearance of new magic numbers. Mass measurements on neutron-rich Na isotopes [4] provided the first observation of such an effect, leading to the discovery of the island of inversion around $N=20$ [5, 6].

Nuclear pairing is another effect directly observable in the nuclear masses. Nuclei with an even number of neutrons and protons are more bound than their neighbors [7–9]. The pairing also plays a role between neutrons and protons. This is the case along the $N=Z$ lines where nuclei are more bound than those around, the extra binding referred as Wigner energy [10].

Measurements on neutron-rich Li [4] provided the first indications of loosely bound systems, later identified as halo nuclei [11]. Halo nuclei are loosely bound nuclear systems with a compact core and one or two valence nucleons with wave functions extending far compared to the core. A number of light nuclei are known to have a halo

ground state, including ^{11}Li , ^6He , ^{11}Be on the neutron rich side and ^{17}F on the proton rich side of the nuclear chart [12–14]. Precise masses are important for determining the one or two-nucleon separation energies of these nuclei, needed for the theoretical modelling of these systems.

Precise mass measurements of rare isotopes also play an important role in the test of the fundamental symmetries. A key subject is the test of conserved vector current (CVC) hypothesis, introduced by Feynman and Gellmann [15]. It postulates that the vector current part of the weak interaction will not be affected by the strong interaction. This means that if CVC holds, the Ft values which represent the rates of the Fermi super-allowed $0^+ \rightarrow 0^+$ decays are all equal once small nuclear structure and radioactive corrections are taken into account. The decay strength Ft depends on the combination of partial half-life, branching ratio and the Q -value of the reaction that is the mass difference between mother and daughter nuclei. The vector coupling constant G_v can be determined from the average corrected Ft value. G_v can be used to calculate the up-down quark matrix element V_{ud} in the Cabibbo-Kobayashi-Maskawa (CKM) matrix. Together with other matrix elements V_{us} and V_{ub} , this allows for a test of the unitarity of the CKM matrix. Today, there are only twelve well-known CVC test candidates [16]. The study of additional candidates is highly desirable. A new candidate, ^{38}Ca , has been investigated with LEBIT and its mass been determined with sufficient precision. This is the subject of the Ph.D thesis of Ryan Ringle.

The study of isobaric analogue state (IAS) has been used to explore the charge independence of the strong interaction. One test is the Isobaric Multiplet Mass Equation (IMME), which describes the masses of isobaric analogue states with isospin T and projection T_z . The quadratic form of this equation, $M = a + b T_z + c T_z^2$ has been tested in a number of multiplets. High precision tests in many quartets and some quintets have been performed, so far not indicating any need for a cubic term, $d T_z^3$, in the equation. IMME has been employed to predict unknown masses of isobaric analog states, in particular the ground state mass of the proton-rich member of the

multiplet. In this work the mass of ^{37}Ca has been remeasured with high accuracy. Together with IMME this allowed the excitation energy of the isobaric analog state in ^{37}Ar to be predicted.

1.2 Different techniques for mass measurement

A variety of mass measurement techniques have been developed and there are two main approaches. The indirect approach is based on the determination of Q-values measured in nuclear reactions or radioactive decays. The direct method uses mass spectrometers for mass measurements of both stable and unstable nuclides.

The use of Q-value measurements for mass determination far from stability was for a long time the only way to determine masses far from stability. Also the mass of ^{37}Ca was originally determined at MSU [17] via a $^{40}\text{Ca}(^3\text{He}, ^6\text{He})^{37}\text{Ca}$ reaction. Indirect mass measurement techniques are today still useful when direct techniques can not be applied, as for example in the case of unbound systems and excited states. Radioactive decay Q-values can be used to derive the unknown mass when the decay is linked to a nuclide with a known mass. Many masses of isotopes far from stability have been determined in this way, but revisits by direct mass measurements have shown that a number of them are not correct.

Techniques for direct mass measurement are based on the measurement of quantities that are a direct function of the mass to charge ratio of the investigated ion. They were originally used to measure masses of stable nuclides and are still used for this purpose. Magnetic spectrographs and spectrometers were the first instruments and continued to be used until recently [18]. They were followed by radio frequency transmission spectrometers based on the principle conceived and later realized by Smith [19, 20]. Today's choice for mass measurements of stable isotopes with highest precision is Penning trap mass spectrometry. With this technique mass measurements with a precision better than 10^{-10} are possible today [21, 22].

The use of direct mass measurements for rare isotopes was pioneered at CERN, where the first mass measurements of ^{11}Li and neutron-rich Na isotopes [4] were performed with a magnetic spectrometer. This was followed with experimental programs using improved magnetic spectrometers at ISOLDE/CERN [23], at the Chalk River TASC facilities [24] and at St.Petersburg [25, 26]. Today, these techniques have been replaced by time-of-flight (TOF) and frequency measurements. Time-of-flight measurement with fast beams are most sensitive and have practically no half-life limitation. It is therefore the method of choice very far from the valley of stability. The frequency measurement gives the highest precision and the techniques have advanced to a state that allows very short-lived isotopes (tens of milliseconds) to be investigated.

In the case of SPEG [27] at GANIL for example, time of flight and magnetic rigidity of projectile fragments are used to determine their masses. SPEG has performed mainly mass measurements in the light neutron-rich mass region reaching mass uncertainties ranging from 100 keV to a few MeV. The resolving power and achievable precision of time-of-flight measurement are limited by the total flight time of ions and the detector resolution. A typical resolving power for SPEG is 10000. Several attempts have been made to improve the resolution by increasing the flight time. One is based on using many turns in a cyclotron. This technique has been used in SARA [28] at Grenoble and CSS2 [29] at GANIL. A highlight was the measurement of ^{100}Sn [30] from CSS2. The other approach is realized in the Experimental Storage Ring (ESR) at GSI by operating it in an isochronous mode [31]. This offers an access to very short-lived fragments and provides improved accuracy. Examples of results achieved with this technique include the measurements of ^{44}V , ^{48}Mn , ^{41}Ti and ^{45}Cr [31].

Frequency measurement can be performed in storage rings, radio frequency spectrometers, or Penning traps. In the case of a storage ring this technique has been successfully developed at the ESR at GSI. The frequency measurement is performed

with a Schottky technique [32] which requires a cooled beam inside the ring. A large number of masses of long-lived isotopes have been measured in a series of experiments [33]. Despite its success this technique is limited to isotopes with half-lives larger than a second because of the time it takes to cool the stored ion beam. Another frequency measurement device is MISTRAL [34] installed at ISOLDE at CERN. It is a radio frequency transmission spectrometer. Two turns of the ions inside a strong magnetic field combined with narrow slits and a velocity modulation inside an RF cavity are employed to determine the mass of the injected ions. This method is well suited for very short-lived light nuclei and has for example provided improved masses for ^{11}Li and ^{11}Be [35].

As already mentioned, a Penning trap has the possibility to achieve very high precision. They rely on the confinement of charged particles in strong magnetic fields, which allows mass measurements to be performed via a cyclotron frequency determination. ISOLTRAP at ISOLDE was the first system to use Penning trap mass spectrometry for short-lived radioactive nuclei. More than 300 masses [36–41] have so far been measured with this technique. The superior performance of ISOLTRAP has triggered similar projects elsewhere. The Canadian Penning trap (CPT) [42] at Argonne National Laboratory stops medium-energy reaction products in a low-pressure gas cell before transferring them to a 6-Tesla Penning trap. SHIPTRAP [43] at GSI aims towards the study of super-heavy nuclei. Also here a gas stopping and ion guide system is used to convert low-energy reaction products into a low-energy ion beam. JYFLTRAP [44] at Jyväskylä obtains its rare isotopes from the Ion Guide Isotope Separator On-Line (IGISOL) technique. The Trapped Ions at TRIUMF for Atomic and Nuclear Physics facility (TITAN) [45] in Vancouver will use highly charged ions to achieve higher resolving power for the mass measurement. All of these projects use rare isotopes produced or delivered at relatively low-energies. As already mentioned, LEBIT at MSU is so far the only facility that allows mass measurements to be carried out on rare isotope produced by fast-beam fragmentation at energies of about

100 MeV/u. Also here a gas stopping technique is employed for the conversion of relativistic fragments into low-energy ion beams. A high-field 9.4 Tesla Penning trap mass spectrometer is used for high precision mass measurements. In addition to ^{37}Ca discussed in this work, masses of the rare isotopes ^{38}Ca , ^{65}Ge , ^{66}As , ^{67}As and ^{68}Se have been determined with LEBIT so far.

1.3 Outline of this thesis

LEBIT is a large project. Its realization and successful commissioning is due to contributions of many collaborators. In my thesis I will first provide an overview of the whole LEBIT facility followed by a detailed presentation and discussion of the specific contributions I made to this project. These contributions include the ion-optical design of the low-energy beam transport system, the development of an advanced control and data acquisition system and the systematic study of the properties of an ion beam cooler and buncher system which is based on a gas-filled radiofrequency ion trap. In the last part of my thesis I will discuss the successful measurement of the mass of ^{37}Ca and its application to the Isobaric Multiplet Mass Equation.

Chapter 2

LEBIT overview

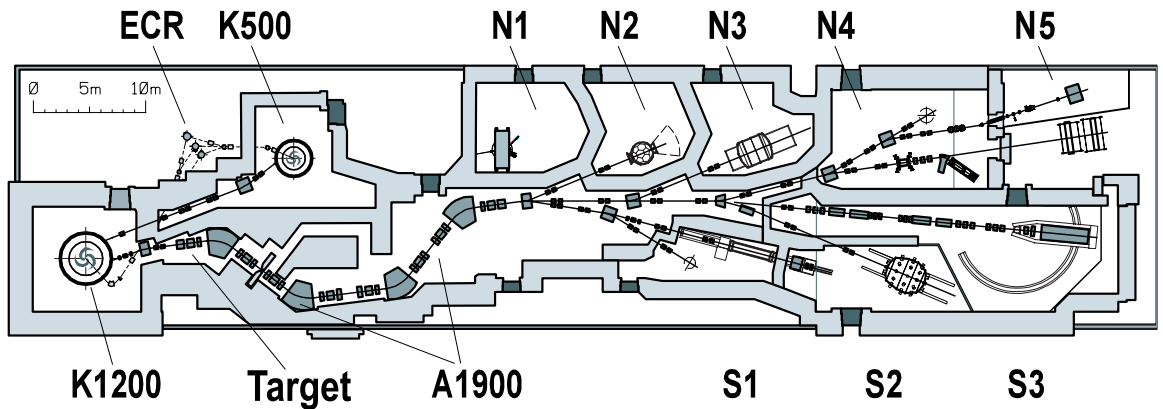


Figure 2.1: Layout of the Coupled Cyclotron Facility.

As shown in Fig. 2.1, the Coupled Cyclotron Facility (CCF) at NSCL consists of an electron cyclotron resonance (ECR) ion source, two coupled cyclotrons of K500 and K1200, a fragmentation separator of A1900 and beam lines located inside experiment vaults. Stable ion beams from the Electron Cyclotron Resonance (ECR) ion source are accelerated in the K500 cyclotron to an energy of typically 14 MeV/A. Then they are ejected into the K1200 where most of their remaining electrons are removed with a stripper foil, and ion energies are increased to around 150 MeV/A. This primary beam is then focused on the production target. The fragment beams are accepted by the A1900 fragment separator, where a small range of nuclides is selected by 2-stage separation with intermediate energy degrading. The gas stopping station of the

low energy beam and ion trap facility (LEBIT) is installed in the N4 vault while the Penning trap of LEBIT is in the N5 vault. This is illustrated in more detail in Fig. 2.2. Along the beam transport direction there are four main components with different functions, which is a gas stopping station for beam thermalization, a test beam ion source for system tuning, calibration and commissioning, a Radio Frequency Quadrupole (RFQ) trap for beam cooling and bunching, and a 9.4 Tesla Penning trap mass spectrometer for high precision mass measurements. An electrostatic beam transport system connects these components.

2.1 The gas stopping station

The gas stopping station stops the high energy beams from the A1900 fragment separator and converts them into low energy beams [46]. As shown in Fig. 2.3(a) of the schematic layout, this system consists of two packages – a gas cell and an ion guide. The leftmost component of the gas cell is a pair of variable glass degraders, which is able to vary the beam energies so that ions can stop inside the gas cell chamber. On its right side there is an aluminum wedge degrader placed at a dispersive image plane, through which the momentum spread of the fragment beams typically ranging from 0.5% to 5% can be significantly reduced [47]. After that is a Beryllium window as the entrance of the gas cell chamber. The gas cell is filled with ultra pure Helium gas at a pressure of typically 1 bar and has a set of drift electrodes (Fig. 2.3(b)) and “flower” focusing electrodes (Fig. 2.3(c)) to guide the ions towards the extraction nozzle. The gas cell is also equipped with an arm that can be moved into its center. A silicon detector and a spark gap are attached to the arm for range measurements or for ion production via discharge.

The supersonic nozzle at the exit of the gas cell serves as the entrance of the ions to the vacuum chamber, which is connected to a large Roots pumping system. Inside the chamber is a segmented RFQ ion guide (Fig. 2.3(d)). The principle of such an

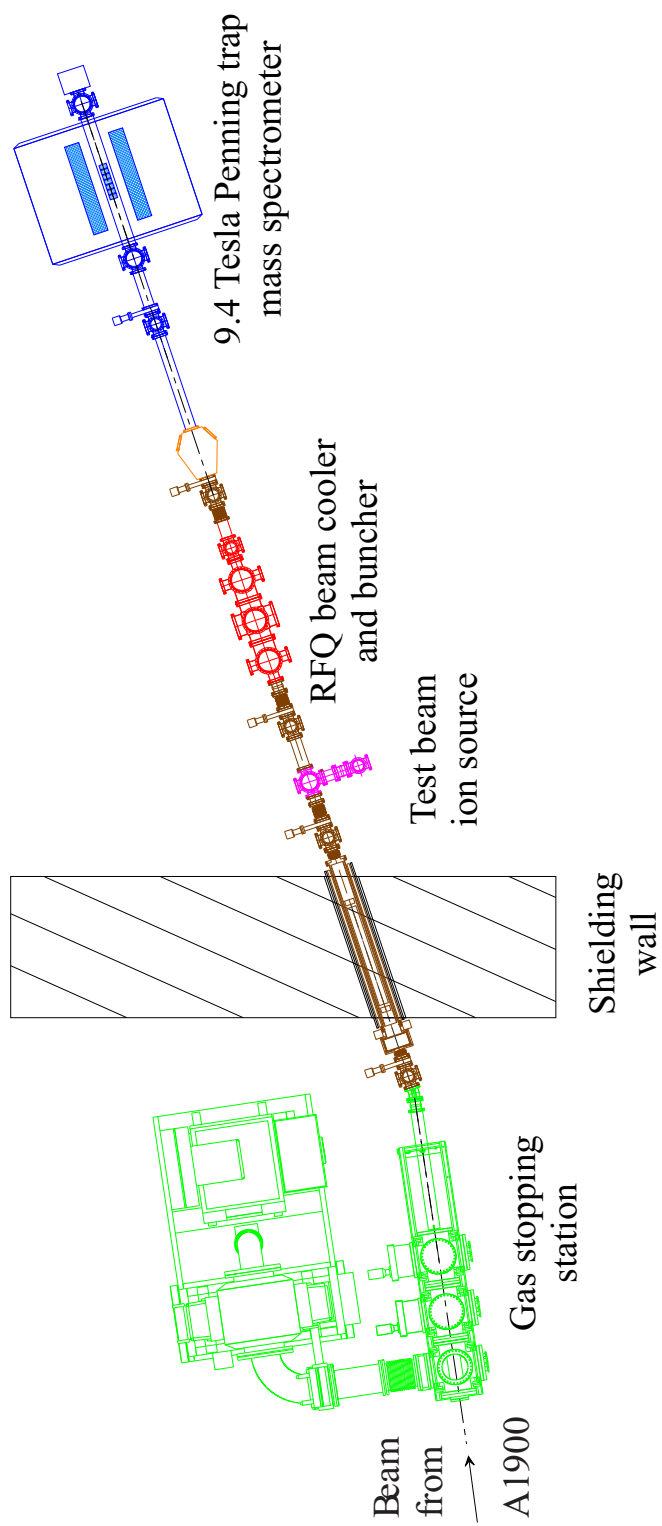


Figure 2.2: Layout of the LEBIT experimental setup.

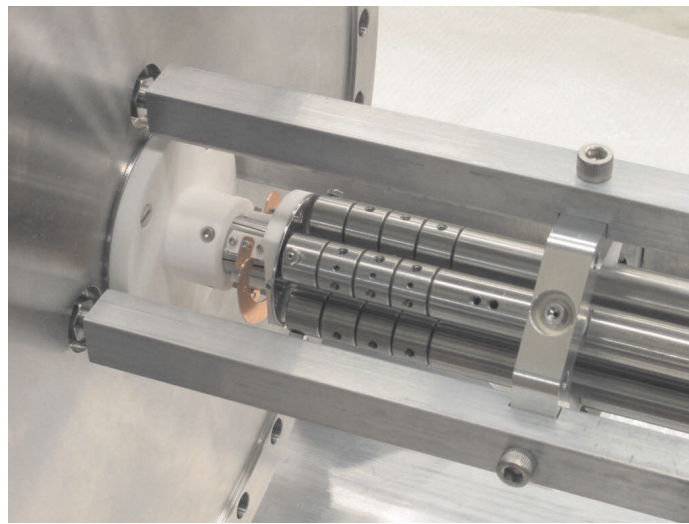
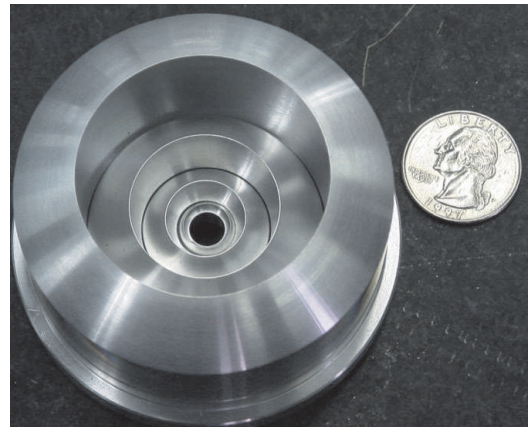
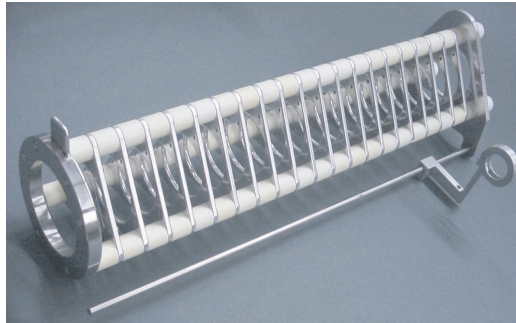
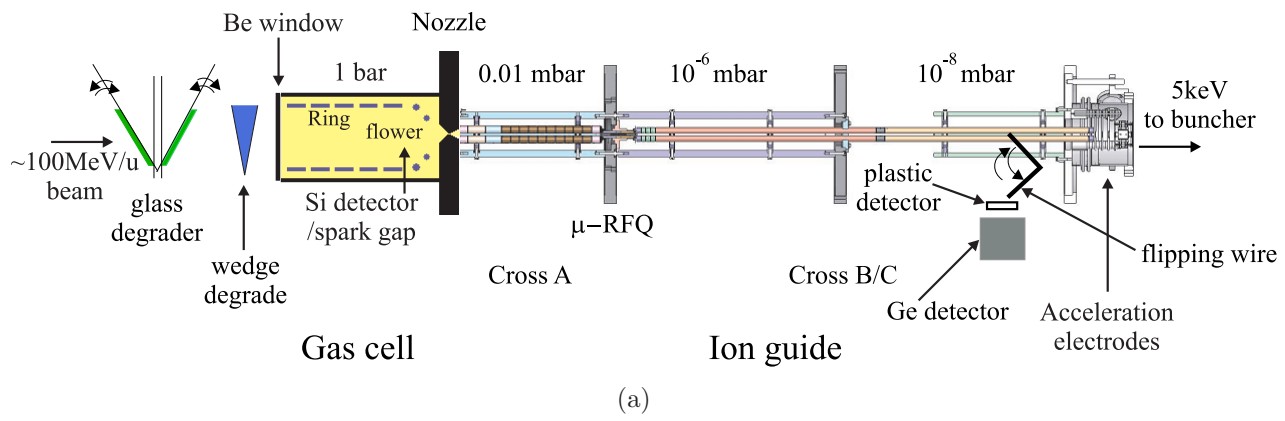


Figure 2.3: The gas stopping station. (a) schematic diagram of experiment layout; (b) gas cell ring electrodes; (c) gas cell “flower” focusing electrodes and nozzle; (d) the second section of RFQ ion guide.

ion guide will be explained in more detail in Chapter 5.1. This ion guide is divided into two sections by an μ -RFQ structure for differential pumping and better beam transmission. Thus the pressure at the left side of the μ -RFQ can be as high as 0.01 mbar, while at its right side the pressure can be kept down to 10^{-6} mbar, achieved with two large turbo pumps. The end part of the last section of the ion guide system is operated as a mass filter, to select the desired ion species and remove contaminants in the beam. A metallic needle is located at the end of the ion guide, which is capable of collecting ions when flipped inside and measuring β and γ activities when flipped close to the plastic scintillator and Germanium detector. This system is used for the measurement of extraction efficiencies and the identification of molecular sidebands from the gas cell and their abundance.

Radioactive beams from the A1900 fragment separator are in high-charge states and have energies of typically 100 MeV/u. Their energies are significantly reduced down to a few MeV after the ions pass through the degraders. Inside the gas cell the ions lose practically all the remaining kinetic energy by collisions with the high pressure buffer gas. During the stopping process the ions also reduce their charge state by charge exchange with He atoms. Depending on their ionization potential, they normally end up as singly or doubly charged ions after the stopping process. The thermalized ions are guided to the nozzle by the DC drifting electric field, produced by the potential on both ring and flower electrodes. The gas flow through the nozzle then provides the force to extract the ions out of the gas cell. The ion guide system transports the ions to the exit of the system. After the ions leave this ion guide system, they pass through a system of acceleration electrodes, where their energy is increased to 5 keV for their further transport to the cooler and buncher system of LEBIT.

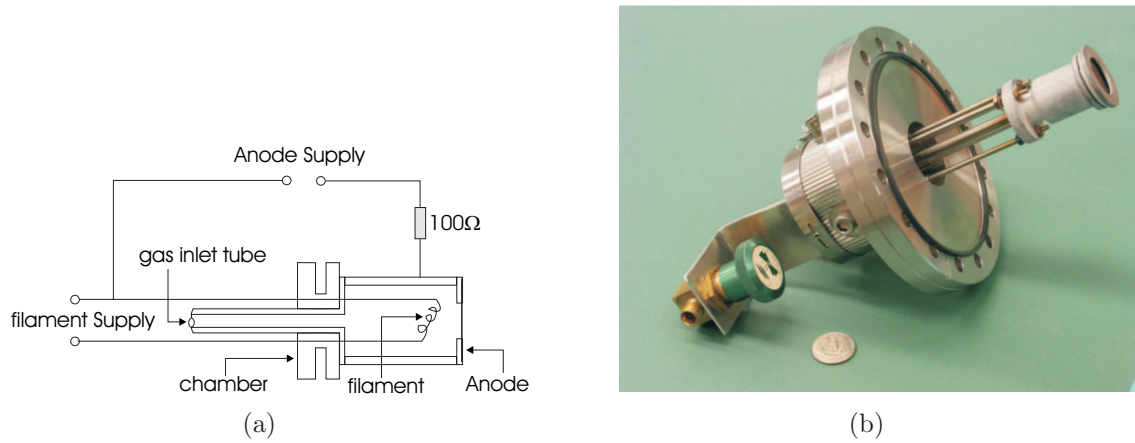


Figure 2.4: The test ion source. (a) schematic layout of the assembly; (b) photograph of the whole package.

2.2 The test beam ion source

The LEBIT facility can be operated either with a radioactive nuclear beam from the fragment separator or with a beam of stable ions from the test ion source. The test beam ion source chamber is installed between the shielding wall and the ion cooler and buncher, 90° from the main beam line. It is used to send a beam either downstream or upstream for system tuning, calibration and commissioning, and for the systematic study of all the major components of LEBIT.

The test beam ion source system is based on a Colutron ion source, whose assembly diagram and photograph are shown in Fig. 2.4. A modification has been made by adding an extraction lens after the anode, which is not shown in the figure. Gas is introduced into the ion source chamber through the gas inlet tube, where noble gases like Ne, Ar or Kr are normally used to operate this source. The Tungsten filament is heated to produce electrons and biased to 100 V to generate a discharge. Depending on the polarity of this voltage, the output can be either noble gas ions or alkali ions, which are from the thermal ionization of the surface materials in the filament or the holder. The electric field created by the anode potential and the extraction lens potential guides the ions through a 1 mm exit hole to the beam transport system. An RFQ ion guide located after the lens is used to transport a selected mass to an

acceleration stage.

2.3 The ion buncher system

Details of ion cooling and bunching in the ion buncher system will be discussed in Chapter 5. A brief description is given in this section. This gas-filled radiofrequency quadrupole ion guide and trap system accepts ions from either the gas stopping station or the test beam ion source. Injected ions are cooled due to collisions with the buffer gas atoms. The ions are trapped until their motions have thermalized and then ejected as bunched pulses. The ion buncher system is a modified version of a linear Paul trap. The transverse confinement of the ion motion is achieved with an RFQ field by applying RF voltages to the four-rods structure. The axial confinement is realized with a DC potential well.

Fig. 2.5(a) shows the electrode configuration of the ion buncher system. The essential components of this system are three RFQ structures, i.e., a cooler section, a μ -RFQ, and a buncher section. The ion cooler (Fig. 2.5(b)) is filled with buffer gas at a pressure of a few 10^{-2} mbar. The injected ions lose their kinetic energies due to collisions with the gas atoms. In the case where collision-induced dissociation is needed to break up molecular ion beams, Ne is used as a buffer gas, otherwise He is used. To realize differential pumping, a μ -RFQ (miniature RFQ structure) is installed between the cooler and the buncher sections, where the latter (Fig. 2.5(c)) is normally operated with He at a pressure of about 10^{-3} mbar. If the buncher section is operated in the pulsed mode (see Chapter 5.4), ions inside can be further cooled and brought to rest after being trapped for enough time and then ejected as a pulse.

The incoming ions are decelerated from 5 keV to a few electronvolts with a set of retardation electrodes located before the entrance of the cooler section. Via buffer gas cooling, their energies are further reduced after they are injected into the cooler section. The slowed ions are guided by the electric drift field inside the cooler section

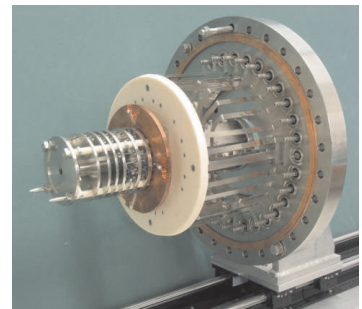
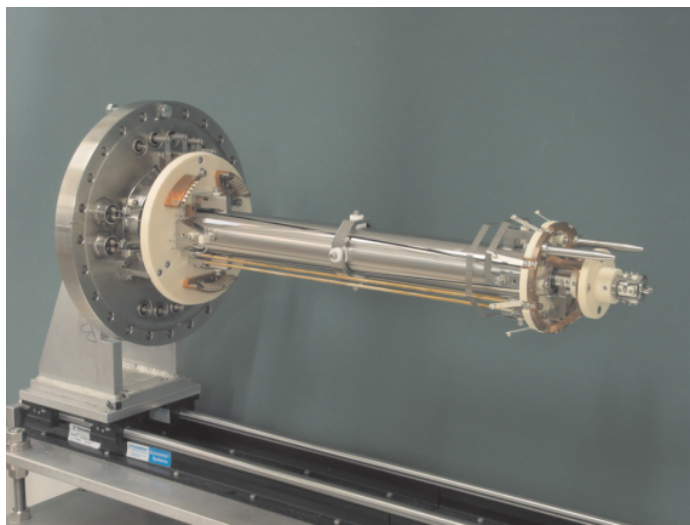
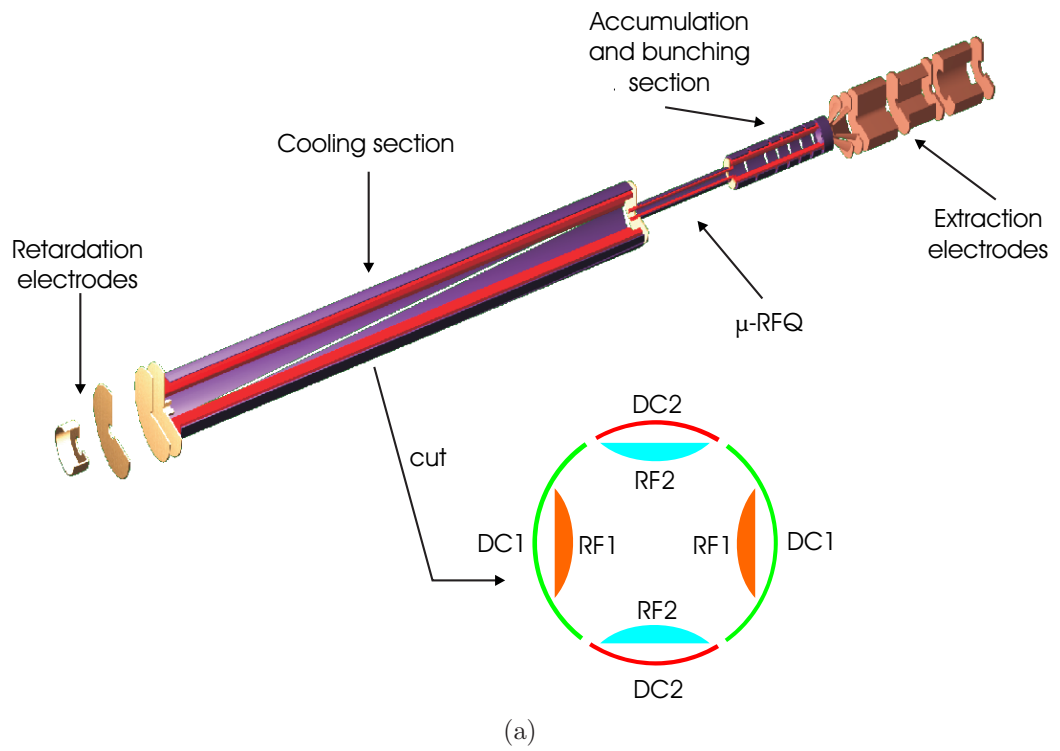


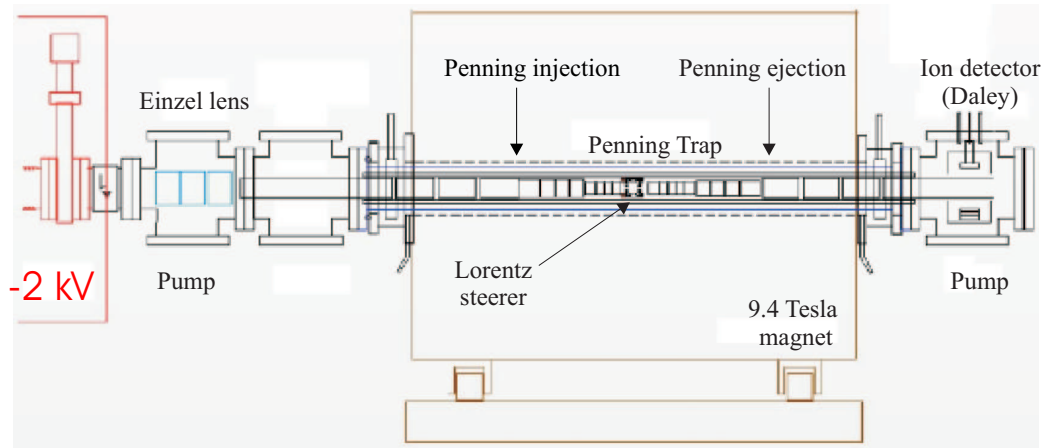
Figure 2.5: The ion buncher system. (a) overview of the electrode configuration; (b) cooler section and μ -RFQ; (c) accumulation and bunching section.

through the μ -RFQ into the buncher section. There, they are confined in the buncher by a potential trap, where they are thermalized and accumulated until they are ejected as pulses. This is achieved by rapidly ($<1 \mu\text{s}$) lowering of the potential at the exit side of the trap. The extracted ion pulses are then reaccelerated to 2 keV by a set of extraction electrodes for further transport to the Penning trap.

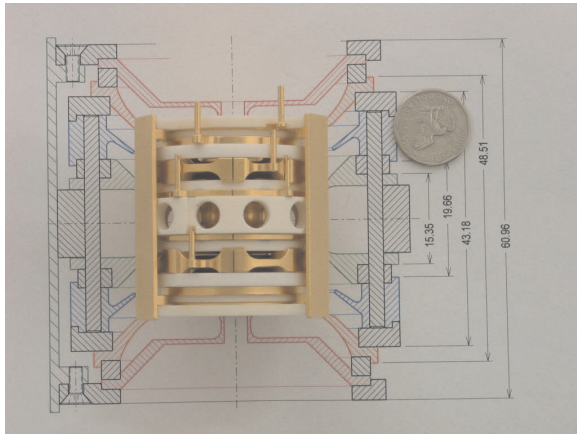
2.4 The Penning trap system

The 9.4 Tesla Penning trap system of LEBIT is used to determine the mass of the rare isotopes via cyclotron frequency measurements. A detailed description of the Penning trap mass spectrometer will be given in Chapter 6.

Fig. 2.6(a) shows the schematic layout of the experimental setup of the LEBIT Penning trap system. Among all the components, the largest is the actively shielded 9.4 Tesla superconducting magnet system (Fig. 2.6(c)). The magnetic field is homogenous over a large region, as required for high-precision mass measurements with a Penning trap. Fig. 2.6(d) shows the full assembly of the Penning trap and the beam injection/ejection sections, which are housed inside a vacuum chamber. The vacuum chamber is mounted inside the room-temperature bore tube of the magnet, and serves as the ion optics bench for the trap electrode system. This bore tube is wrapped with copper wires which allows for either baking or compensation of the natural decay of the main magnetic field during measurements. The tube is pumped with two turbo molecular pumps. In addition, the chamber can be cryogenically cooled, in order to be able to lower the residual gas pressure inside the trap. Two ion-optical packages for beam injection and ejection, respectively, are located at opposite ends of the chamber, with a Penning trap at the center. The Penning trap mass spectrometer consists of a cylindrical ring structure and an end cap at each end with hyperbolic shapes in the cross section (See Fig. 2.6(b)). With a DC voltage applied between the ring and the end cap electrodes, a quadrupole electric field is created. Together with the axial



(a)



(b)



(c)



(d)

Figure 2.6: The Penning trap system. (a) schematic layout of the experiment setup; (b) close-up view of Penning trap chamber; (c) 9.4 Tesla superconducting magnet; (d) full assembly of the Penning trap and beam injection/ejection sections.

magnetic field, a 3-dimensional ion confinement can be achieved.

Pulsed ion beams at an energy of 2 keV out of the ion buncher first pass through an Einzel lens, so that they can be focused for the injection into the magnetic field of the Penning trap. A set of retardation electrodes in front of the Penning trap is used to lower the beam energy to several tens of electronvolts. In the last segment of the injection package, the slow ions experience an electric dipole field, created by a pair of “Lorentz” steerer electrodes. Due to this deflection, the ions are forced to enter the Penning trap off-axis. In order to capture an ion bunch in the trap, the voltages applied to the entrance electrodes are first lowered and then switched back to their nominal voltages, once the ions are inside the trap. The motion of the stored ions inside the Penning trap is then excited with RF voltages. They are ejected and their time-of-flight from the trap exit to the detector is measured as a function of the RF excitation frequency. The result is a cyclotron resonance curve, an example for $^{82}\text{Kr}^+$ ions is shown in Fig. 2.7. The mass can be obtained from the center frequency, which equals the cyclotron frequency ω_c of the ions, via

$$m = \frac{q}{\omega_c} \cdot B \quad (2.1)$$

where q is the charge of an ion with mass m and B is the magnetic field strength.

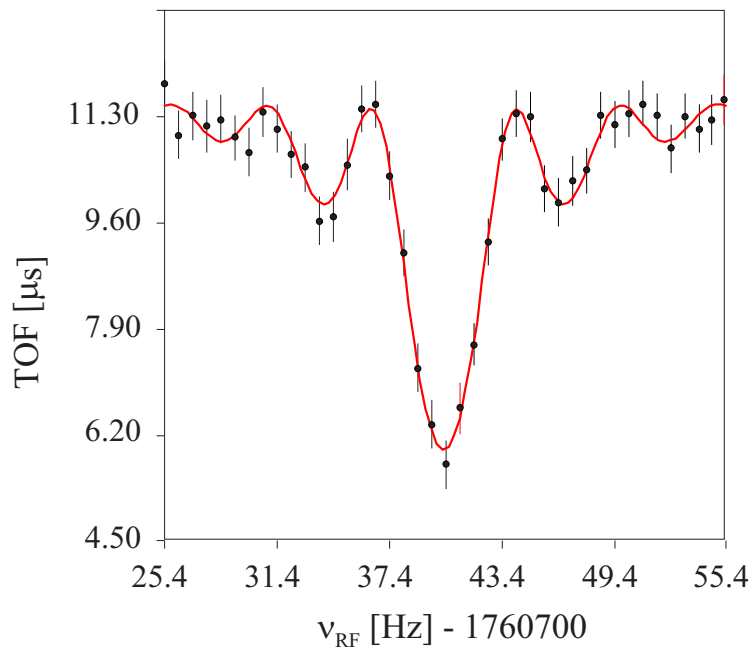


Figure 2.7: A cyclotron resonance curve of $^{82}\text{Kr}^+$ ions. The mean time-of-flight of ions from the trap exit to the detector is plotted as a function of the RF excitation frequency. The solid line is a fit of the theoretical line profile to the data points.

Chapter 3

The electrostatic beam transport system of LEBIT

An electrostatic beam transport system has been built to transport ion beams between the major components of the LEBIT facility. Its design is based on ion optical simulations that will be discussed in this chapter.

The typical energy of the beam in the transport system is a few keV, which allows for the use of an electrostatic ion optical system. Compared to magnetic systems, its advantage is that ion deflection depends on the kinetic energy instead of the mass-to-charge ratio. The possibility for beam observation has been implemented at several places where beam focusing is needed. Beam observation boxes (BOBs) have been designed, which can house several detector systems to measure beam properties. The first type of detector is a Faraday cup, which is normally used to measure DC beam current down to pico-amps. Fig. 3.1(a) shows the schematic of the other type of detector, a microchannel plate (MCP). It is a matrix of thousands of miniature electron multipliers oriented parallel to one another and fabricated on a lead glass. The length to diameter ratio of each channel is typically around 60, and the channel axis is normally biased at a small angle to the MCP input surface. Thus the incident particle can strike out a large number of secondary electrons when a typical voltage

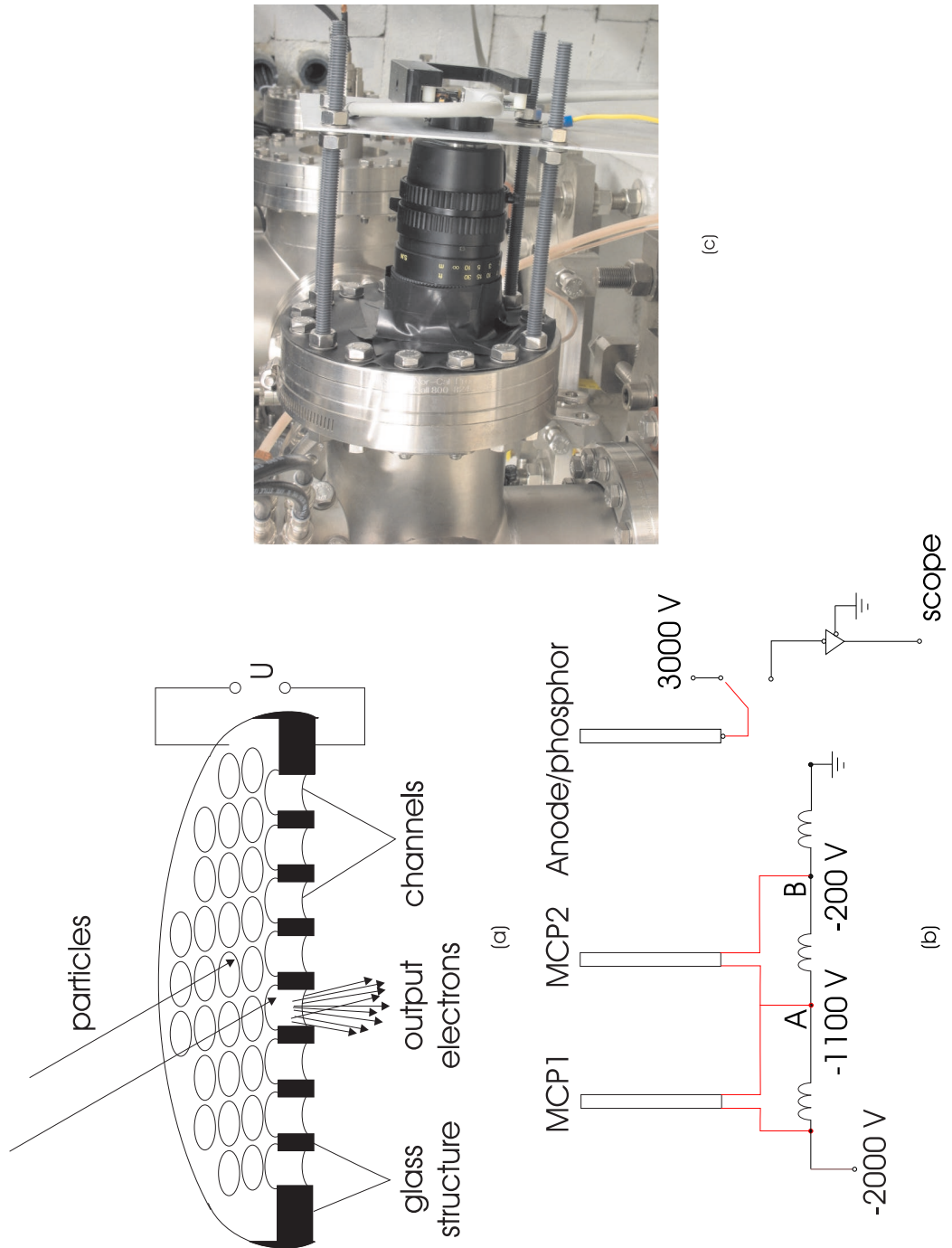


Figure 3.1: Microchannel plate detector system. (a) schematic of a microchannel plate (MCP); (b) a typical voltage configuration for an MCP system in practice; (c) photograph of the experimental setup for the beam image measurement. It includes a CCD camera and the MCP+phosphor screen housed inside the vacuum chamber.

of 1 kV is applied between the two sides of the MCP. With a typical gain of several 10^4 it provides the capability to detect single ions. Since this detector is fast, it is also used for obtaining the time-of-flight information on ions. A tandem assembly of two MCPs is used in practice to enhance the signal multiplication. Fig. 3.1(b) shows a typical detector arrangement. The applied voltage of -2000 V is split with a voltage divider that consists of three resistors. The first two resistors are the same, with a resistance larger than that of the third resistor. In the scenario shown, the voltage at the two nodes A and B are -1100 V and -200 V. That gives a voltage difference of -900 V between two sides of the MCP for both MCP1 and MCP2. The secondary electrons out of these two plates are caught by an aluminized phosphor screen that acts as an anode. When this phosphor screen is connected to a scope through an amplifier, it allows for recording of the timing information of the ions hitting the detector. When the phosphor screen is connected to an power supply of 3000 V, the secondary electrons will be accelerated sufficiently to penetrate the aluminum layer and create fluorescence in the phosphor screen. The resulting beam image can be captured with a CCD camera (Fig. 3.1(d)) (see section 5.5.3 for detail).

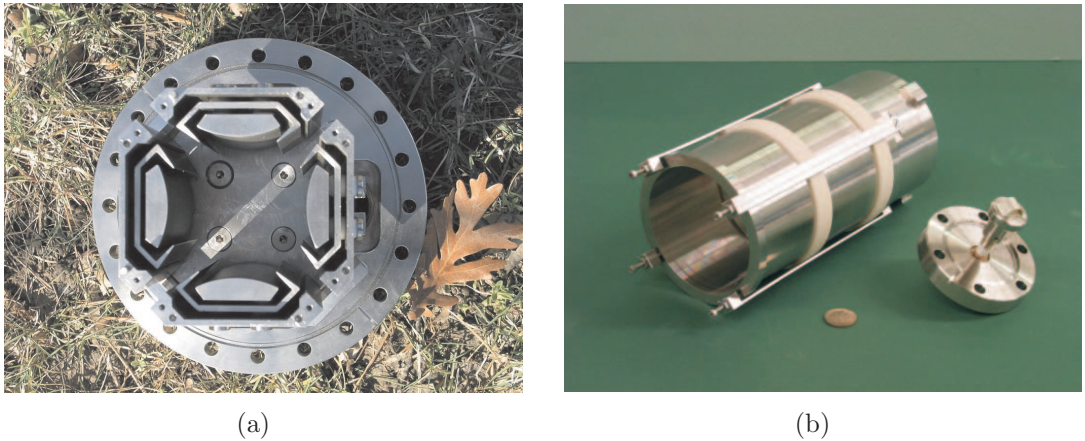


Figure 3.2: Examples of component of the LEBIT beam transport system. (a) 90 degree quadrupole deflector; (b) Einzel lens.

Several other optical devices are also used in this beam transport system. Among them, the first example is a 90 degree quadrupole deflector (Fig. 3.2(a)). This deflects

the incoming ion beam at 90° by means of a two-dimensional electrostatic quadrupole field. The quadrupole field is created by applying appropriate voltages to a combination of cylindrical and shim electrodes. Another example of a beam transport component is an Einzel lens (EL)(Fig. 3.2(b)), which is a three-segment structure for beam focusing. A beam-focusing electric field is created by applying a non-zero voltage on the center electrode and leaving the external electrodes at ground.

Fig. 3.3 shows the schematic diagram of the LEBIT beam transport system. It starts from the gas cell ion guide, followed by a set of acceleration electrodes to accelerate the ions to an energy of 5 keV. After an EL with outer electrodes biased at -5 kV, there is a 10-degree beam deflector to bend the ion beams towards the main beam line direction. Following it is a large ion optical package installed on a high voltage and operated at -5 kV. The first electrode of this package is a beam observation box (BOB1). The second element of this package is a long EL mounted inside the shielding wall, which connects the N4 vault where the gas stopping station is located and the N5 vault which houses the ion buncher and the Penning trap. Two Einzel lenses and the quadrupole deflector are located between BOB2 and BOB3 for beam focusing. The High Voltage (HV) platform is followed by the ion buncher, and a pulsed drift tube with a variable bias. The present function of the drift tube is to fine tune the beam energy. As an option it could be used to accelerate the beam to 60 keV. In this case the beam would reach a switchyard (not yet installed) which could bend the beam sideways or upwards for other experiments like decay studies and laser spectroscopies. The pulsed drift tube is followed by a HV platform operated on -2 kV. It houses two beam observation boxes, BOB4 and BOB5, each having an EL in front of it. Outside the platform there is an EL biased at -2 kV, for focusing the beam into the magnetic field of the Penning trap. The last element after the Penning trap is another beam observation box, BOB6, housing an MCP+phosphor detector system and a silicon-detector.

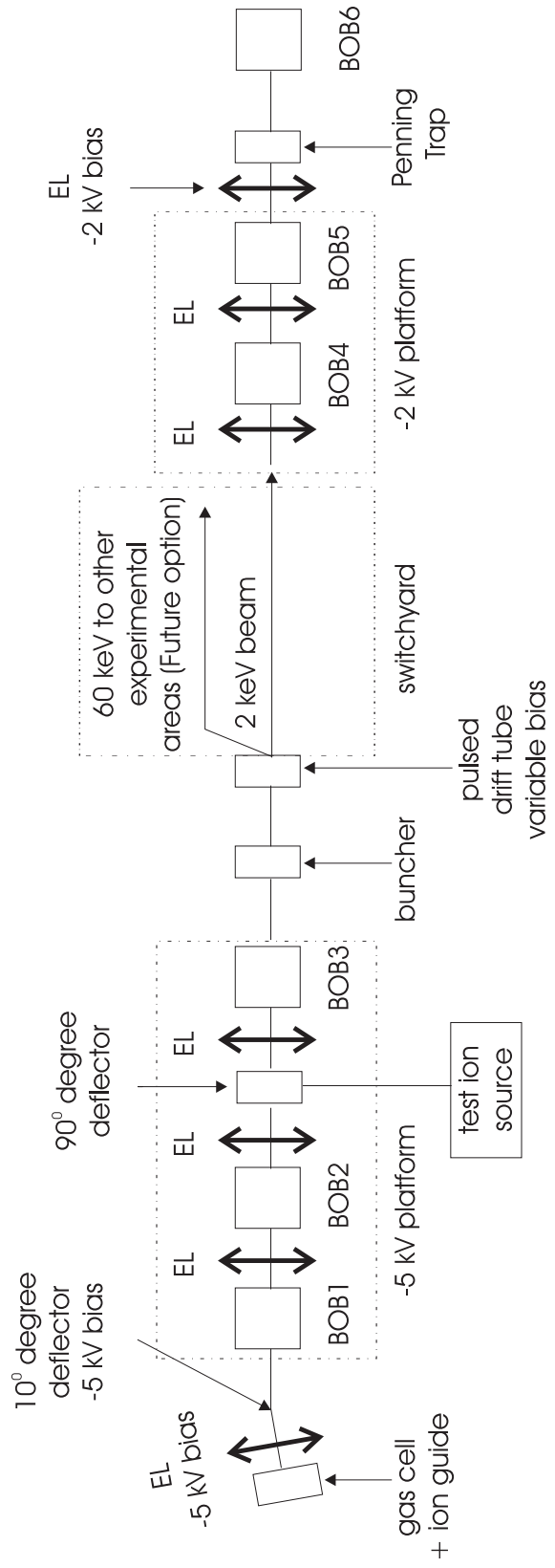


Figure 3.3: Block diagram of the electrostatic beam transport system of LEBIT.

3.1 Ion optics simulation

3.1.1 Tools used in ion optics simulation

Two simulation programs, SIMION and COSY, have been used for the ion optics calculation of the beam transport system of LEBIT.

SIMION

SIMION [48] is a very common software package for modelling of electron and ion optics. It uses a relaxation technique for solving the Laplace equation for a system of electrodes and applied voltages. The equation of motion of ions in the resulting fields is solved via numerical integration. A large amount of ion optical elements can be configured in a geometry file, where potentials of different elements are superimposed. Dynamic adjustment of potentials is possible through a user program, as well as a 2-dimensional or 3-dimensional view of the configurations and beam trajectories. It has been used for the simulation of all the einzel lens and beam acceleration/deceleration systems and for the 10 and 90 degree beam deflectors.

COSY INFINITY

COSY INFINITY [49] is an arbitrary-order beam dynamics simulation and analysis code based on matrix optics. It provides a large set of modules for standard elements like multipoles and electromagnetic cylindrical lenses. It works very fast for the calculation of ion beam transport through large beam optics systems. It is also able to calculate the dependence of the overall system performance on any available parameter, so it can be used for fitting.

3.1.2 Simulation example

A SIMION simulation result of ion beam focusing through an Einzel lens is shown in Fig. 3.4. Several equipotential lines are drawn to represent the electric field inside the

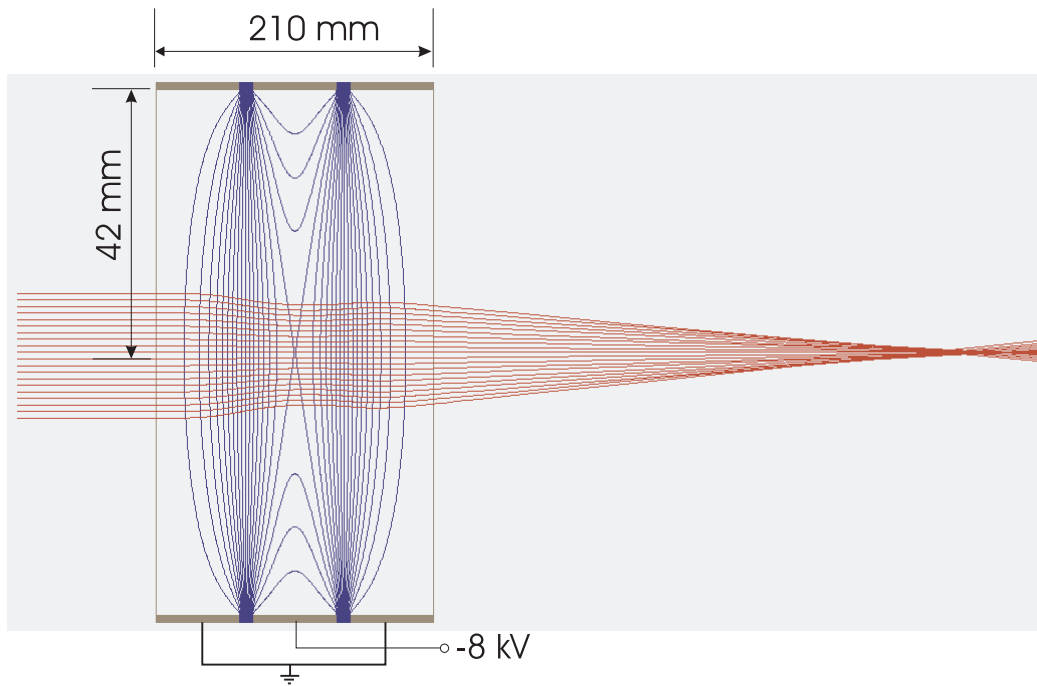


Figure 3.4: Ion beam focusing through an Einzel lens. Different scales are used in axial and transverse directions.

lens, which is created by applying -8 kV on the center electrode and 0 V on the other two. A perfectly parallel beam with an energy of 5 keV and a large diameter of 20 mm is sent into the lens. Depending on the displacement from the axis the deflection angle of each ion is different. The further away from the axis the more bending the ion will experience. All the ions' paths intersect at a position about 500 mm away from the lens center, which corresponds to the beam focus.

3.1.3 Emittance of the beam

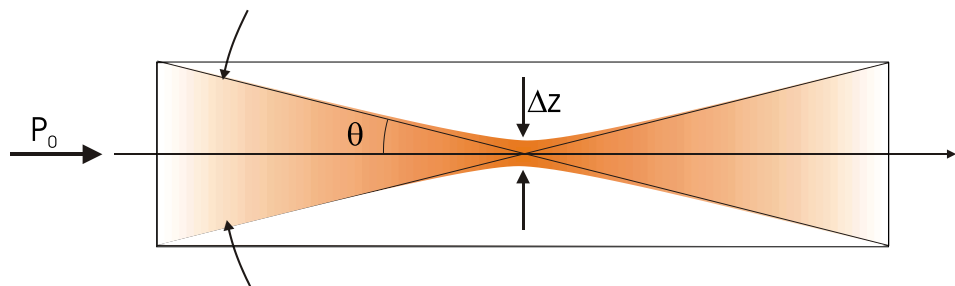


Figure 3.5: Transport of a real beam.

A beam is represented by the size of its cross section and the range of angles with which individual particle trajectories pass through this cross section [50]. A real beam with an initial axial momentum p_0 can not be completely parallel, nor have a zero-area spot at the focus. Instead it is observed to have a convergence/divergence angle θ with respect to the transport axis and a nonzero beam size Δz at focus, as illustrated in Fig. 3.5¹. In a similar fashion this also remains true along the axial direction for the pulsed beam, where energy spread and temporal spread can never be zero. To describe these phenomena, phase space diagrams have to be introduced. They are plots of position and momentum of all the particles of the beam as a function of time, or plots of energy and time as a function of beam position. The area of the phase space diagram then can be defined as emittance, in the transverse and longitudinal directions expressed as

$$\varepsilon_{\text{trans}} = \Delta p \cdot \Delta z \quad (3.1)$$

and

$$\varepsilon_{\text{long}} = \Delta E \cdot \Delta t \quad (3.2)$$

where Δp and Δz are the momentum and spatial spreads, ΔE and Δt are the energy and temporal spreads, respectively. This transverse emittance is commonly used for the continuous beam transport, in the condition where the energy spread is negligible. In contrast to that, the longitudinal emittance is important for pulsed beams. The beam emittance is inversely proportional to the beam energy, which results in an normalized beam emittance

$$\varepsilon_{\text{norm}} = \varepsilon \cdot \sqrt{E_0/E} \quad (3.3)$$

where E and E_0 are beam energy and the reference beam energy for normalization.

¹The coordinate orientation used in this chapter and Appendix A follows the convention used in SIMION, which takes x as the beam transport direction and (y,z) as the transverse directions.

For the discussions in this chapter, a derived version of the transverse emittance

$$\varepsilon_{\text{trans}} = \arctan(\Delta p/p_0) \cdot \Delta z \cdot \sqrt{E_0/E} \quad (3.4)$$

is used, where $\arctan(\Delta p/p_0)$ represents the beam's convergence or divergence angle.

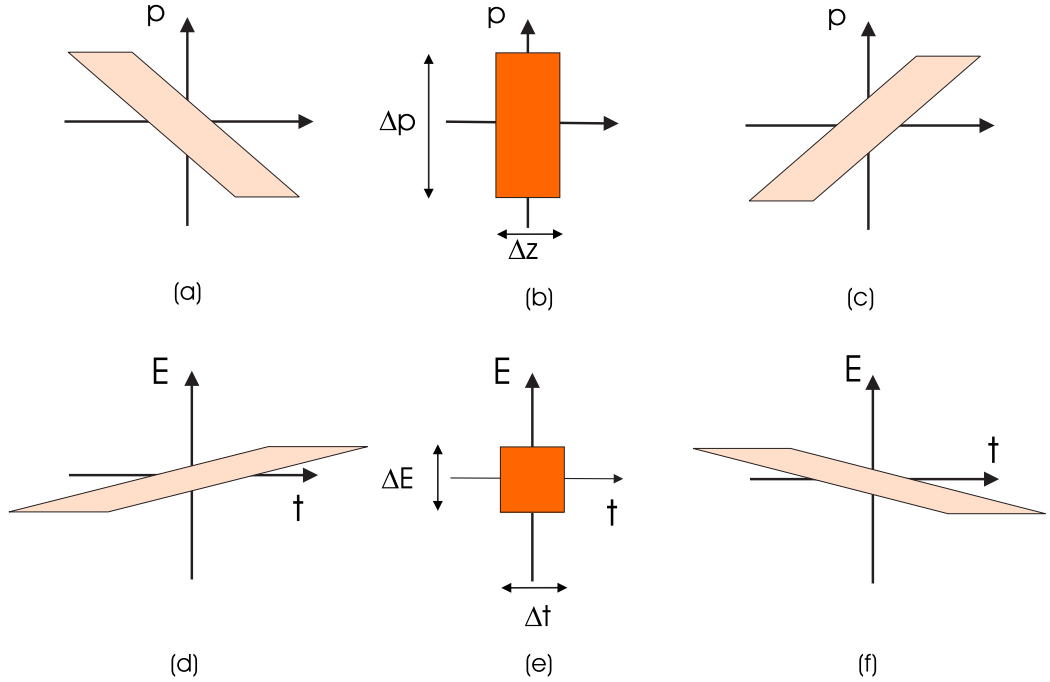


Figure 3.6: Evolution of phase space diagrams. (a)(b)(c) in the transverse phase space; (d)(e)(f) in the longitudinal phase space.

A commonly observable feature of the phase space diagram is its shape variation. Fig. 3.6 illustrates the evolutions of the diagrams in both transverse and longitudinal phase space. In both cases they are observed to have a rectangular shape on the beam focus, and stretch to either side while off focus. The more general situation is a more irregular distribution, for example (used by) aberrations. A practical emittance value can be estimated with the area of an ellipse tightly wrapping the boundaries of the distributino. An example of that is shown in Fig. 3.7, where the deformed region marked in yellow is the actual phase space diagram, and the regular ellipse marked in orange is the effective diagram that will be used to calculate the emittance. Most of the cases discussed in this chapter fall into this category.

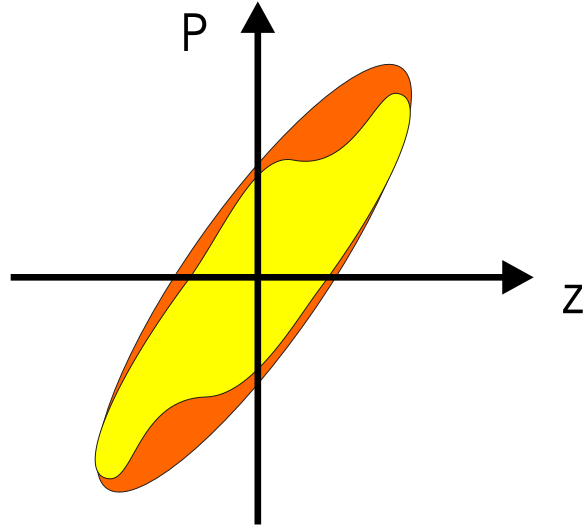


Figure 3.7: A general situation of the phase space diagram. The irregular shape (yellow) inside is the actual diagram and the regular ellipse (orange) outside is the effective one which will be taken for emittance calculation.

The most interesting property of emittance is its conservation in electromagnetic fields. That is governed by Liouville's theorem, which is known for thermodynamics as

For a cloud of particles moving in a conservative force field, the particle density $\rho(x, p_x, y, p_y, z, p_z)$ in phase space is an invariant.

According to this theorem, an ensemble of particles that fills a phase space area at a time t_1 may change its shape at a later time t_2 but not the magnitude of its area, the emittance. This will be largely used in this chapter to gauge the ion optical simulations.

3.2 Ion optics simulation of the beam transport system

The LEBIT beam transport system can be divided into three consecutive sections. That leads to compact subsystems which simplifies the beam simulations. The properties of the ions in the output beam from a preceding section can be used as input

parameters for the succeeding section. Along the beam transport direction the three sections are

1. From the gas cell to the N4-shielding wall
2. From the N4-shielding wall to the ion buncher
3. From the ion buncher to the Penning trap and other experimental areas

In the following discussion of the beam ion optics simulation, I will give an evaluation of the phase space diagram and the optimal voltages as an example only for the first section. For the other sections this detailed information will be presented in Appendix A.

3.2.1 From the gas cell to the N4-shielding wall

The first beam transport section connects the end of the gas stopping station to the first beam observation box (BOB1). This is the only section where details of simulations are given in this chapter. Fig. 3.8 shows the schematic layout of the electrostatic elements and the result of simulation with SIMION. The first ion optical component considered in this section are the last two segments of the RFQ ion guide. This is the start position of the ions for this simulation. Following these segments is a set of acceleration electrodes (Fig. 3.9(a)) to take the beam energy up to 5 keV. After that there is an adjustable Einzel lens (EL0) (Fig. 3.9(b)) to focus the beam at the position of BOB1. A set of voltages can be applied to three of the seven electrodes to move the effective position of the lens. This feature provides some flexibility in the beam transport. The 10-degree deflector in front of BOB1 has spherical deflector plates in order to ensure a symmetric beam spot at BOB1.

This simulation starts with a beam of 1000 ions, their phase space distributions are based on simulation results for the ion guide (See Peter Schury's Ph.D thesis). The ions are starting inside the gas cell ion guide, where the beam emittance is not

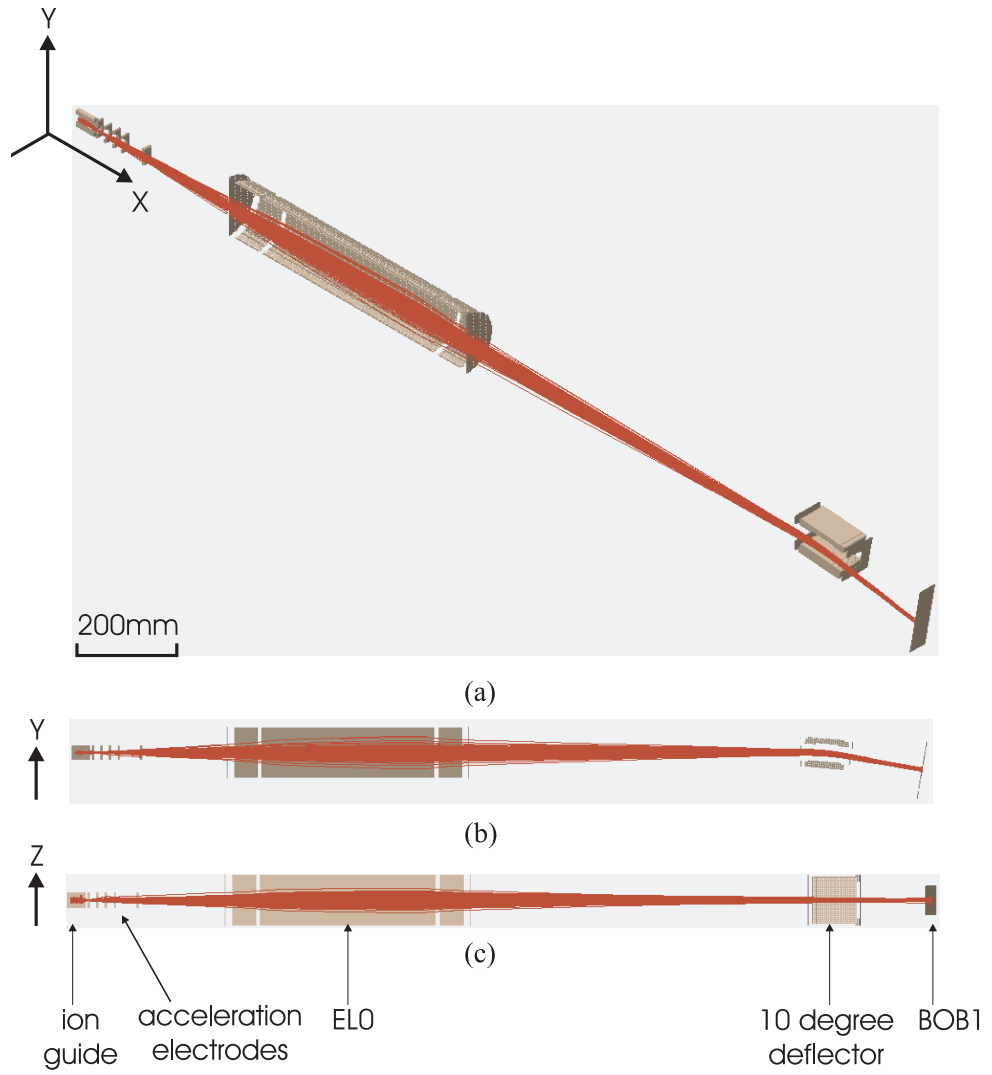
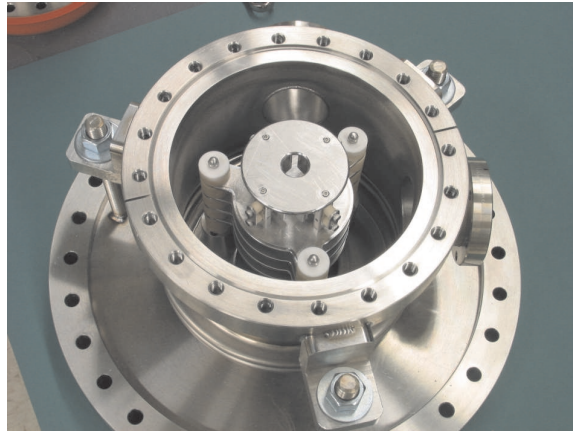


Figure 3.8: SIMION simulation of the ion beam transport from gas cell to N4-shielding wall. (a) 3-dimensional view; (b) 2-dimensional view in the x-y plane; (c) 2-dimensional view in the z-x plane.

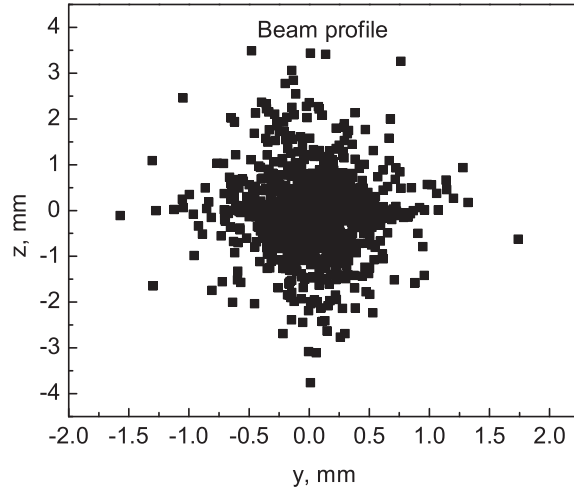


(a)

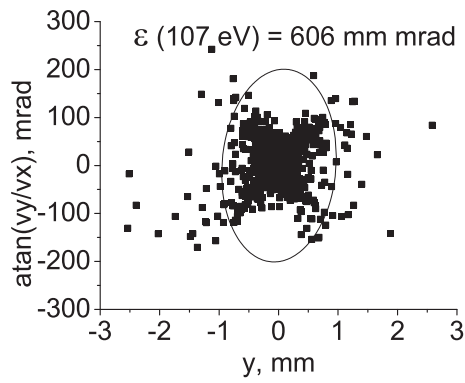


(b)

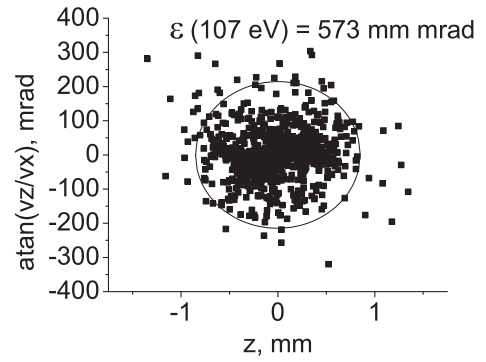
Figure 3.9: Examples of electrodes used in the beam transport from the gas cell to the N4-shielding wall. (a) acceleration electrodes; (b) adjustable Einzel lens (EL0).



(a)



(b)



(c)

Figure 3.10: Beam properties in the transverse plane at the entrance to the acceleration section. (a) beam profile; (b) phase space diagram in the y-direction; (c) phase space diagram in the z-direction.

conserved due to the presence of RF field. For the comparison of emittance the beam is recorded at the entrance of the acceleration electrodes, with spatial and phase space properties shown in Fig. 3.10. The width of the energy distribution is about 0.5 eV, which is less than 0.5% of the averaged beam energy of 107 eV at this point. That spread can be ignored, which means we only have to concentrate on the study of the transverse phase space diagrams. The emittance of each diagram is determined by an area that covers 95% of the ions. This method has been used for all the emittance evaluations in this thesis, unless specifically noted otherwise. The normalized beam emittance for an energy of 5 keV is $\varepsilon_y = 89$ mm·mrad and $\varepsilon_z = 84$ mm·mrad. This is an extreme case where the beam is not symmetric, due to the effect of the mass filter field in the RFQ ion guide simulation. The design of the actual beam transport section is based on the simulation with a symmetric beam. In order to find the best ion optics, layout variations of the system shown in Fig. 3.8 have been considered and the involved potentials have been optimized (see Appendix A.2). The resulting phase space diagrams for the optimal geometry and voltages are shown in Fig. 3.11. The emittance values of the two phase spaces are $\varepsilon_y = 87$ mm·mrad and $\varepsilon_z = 90$ mm·mrad. The uncertainty of the emittance evaluation is estimated to be 3% or about 3 mm·mrad. This means no significant emittance growth of the beam from the start of the section to its end is observed.

3.2.2 From the N4-shielding wall to the ion buncher

This section is used to deliver the 5 keV beam from BOB1 through the N4-shielding wall to the ion buncher. Also included is the beam transport from the test ion source to the ion buncher. The complete schematic layout of the straight beam transport and SIMION simulation result is illustrated in Fig. 3.12. An Einzel lens of 1.2 m length (Wall lens) is located inside the beam tube connecting the beam transport in N4 to downstream. It is used to take the beam from BOB1 and focus it at a position where a beam observation box (BOB2) is located. After that there are two short Einzel lenses

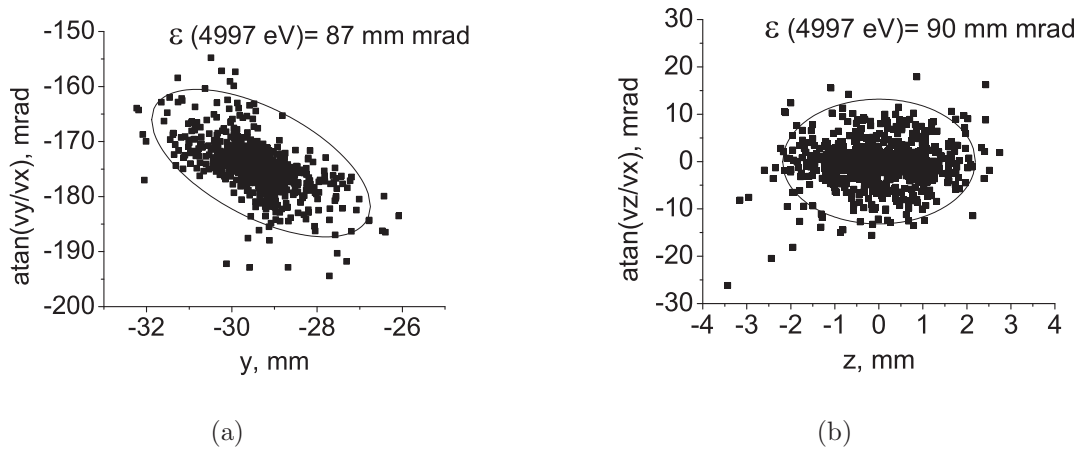


Figure 3.11: Transverse phase space diagrams at the center of BOB1. (a) in the y -direction; (b) in the z -direction.

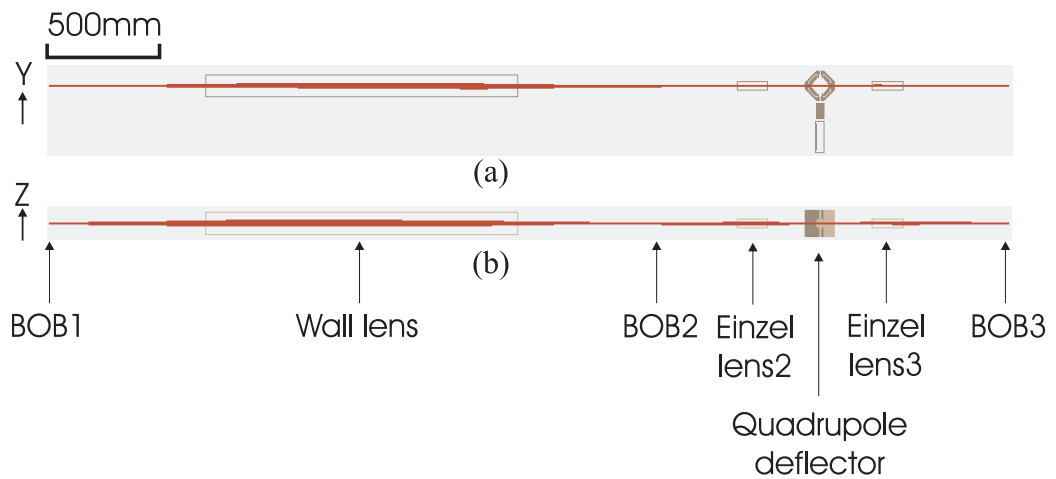


Figure 3.12: SIMION simulation of the ion beam transport from BOB1 to BOB3. (a) 2-dimensional view of the ion optics in the y - x plane; (b) 2-dimensional view of the ion optics in the z - x plane.

(EL2 and EL3), which focus the beam such that it can be efficiently injected into the ion buncher. A beam observation box (BOB3) located after EL3 allows the beam current to be measured and used as a reference for the transport efficiency evaluation. Between EL2 and EL3 there is a 90-degree deflector, which is only operated when the beam from the test ion source is used. With the help of beam simulations the whole system has been optimized with the beam profile calculated at BOB1 as input. Details of this simulation are presented in Appendix A.3.1. The beam is transported without any losses. The beam emittance calculated at BOB3 is $\varepsilon_y = 82 \text{ mm}\cdot\text{mrad}$ and $\varepsilon_z = 88 \text{ mm}\cdot\text{mrad}$, respectively. By comparing these two numbers to the emittance values at BOB1 we can see that the emittance is again conserved.

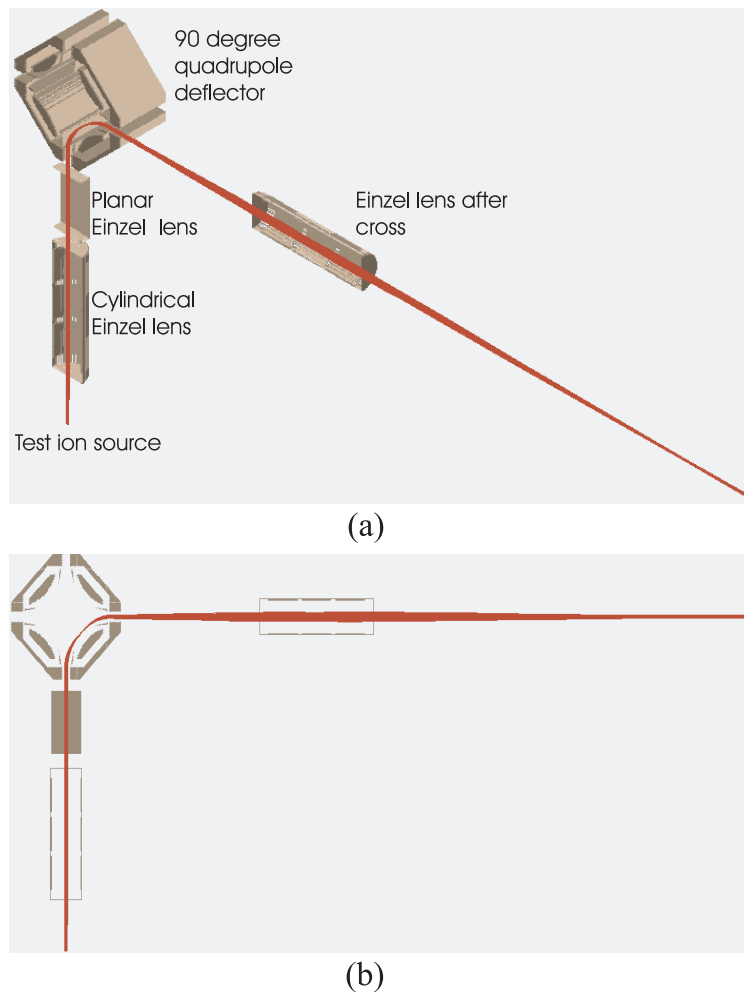


Figure 3.13: SIMION simulation of the ion beam transport from the test ion source to BOB3. (a) 3-dimensional view of the ion optics; (b) 2-dimensional view of the ion optics in the z-x plane.

The layout of the beam transport from the test ion source to the ion buncher as well as the SIMION simulation results are shown in Fig. 3.13. The test ion source is located on a line perpendicular to the downstream beam line. The first element assumed to be present after the ion source is a cylindrical Einzel lens, which is used to focus the beam into the center of the quadrupole deflector. After this lens there is a planar Einzel lens, which provides beam focusing only in the direction perpendicular to the bending plane of the 90-degree deflector. This is needed to compensate the unbalanced focusing of the quadrupole deflector. The 90-degree deflector, an eight segment structure (see Fig. 3.2(a)), consists of four sets of electrodes that allow a beam coming from one of the four slits to be bent by 90 degrees. This system has been optimized with an incoming beam, whose spatial and momentum distributions were created by random number generation algorithm (see Appendix A.3.2). Emittance calculated at BOB3 with the optimal settings gives $\varepsilon_y = 177$ mm·mrad and $\varepsilon_z = 134$ mm·mrad. The emittance growth is less than 10% when comparing with the input, $\varepsilon_y = 161$ mm·mrad and $\varepsilon_z = 128$ mm·mrad.

The assumptions of the input beam profile made in the simulations do not fully agree with those later realized in LEBIT. The ion optics has been found not to match the ion beam properties present after the installation of an additional mass filter between the ion source and the cylindrical lens. A redesign of the optics after the ion source is presently on its way, though it is not critical since the ion source can deliver enough beam.

3.2.3 From the ion buncher to the Penning trap and other experimental areas

This section handles the beam transport from the exit of the ion buncher to the Penning trap. A beam transport energy of 2 keV is chosen. As an optional feature it will be possible to accelerate the ions to energies up to 60 keV and bend the beam

by either 60° or 90° away from the downstream direction to a switchyard. This is for future experiments like decay or laser spectroscopy studies. Unlike previous transport sections, pulsed beams have to be considered in the simulations, which means that both longitudinal and transverse phase space diagrams have to be considered.

Beam transport from the ion buncher to the Penning trap

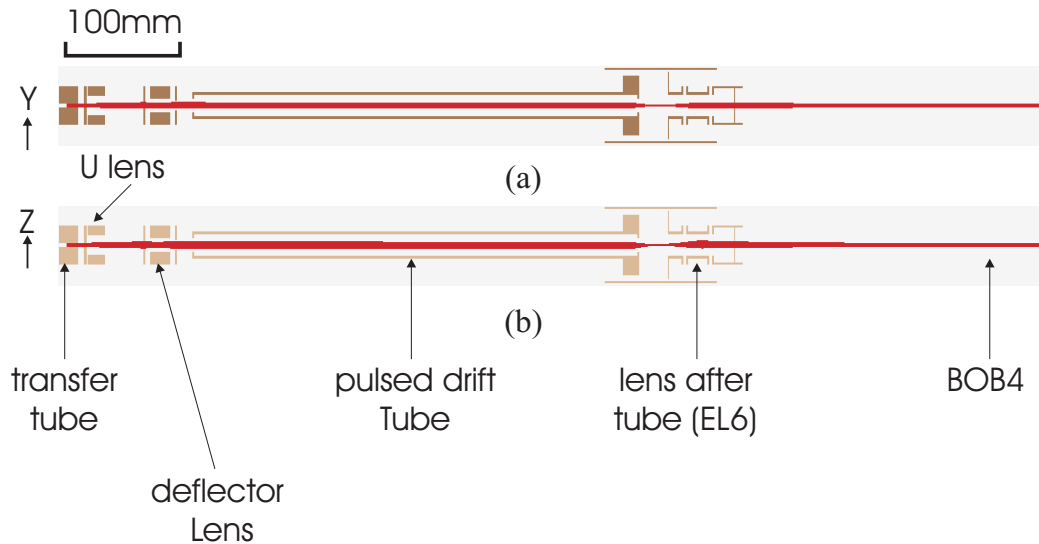


Figure 3.14: SIMION simulation of the ion beam transport from the ion buncher to the switchyard. (a) 2-dimensional view of the ion optics in the y-x plane; (b) 2-dimensional view of the ion optics in the z-x plane.

One task of this beam transport section is to dynamically change the energy of the 2 keV ion pulse delivered by the ion buncher. A pulsed drift tube is used for this purpose. Its voltage can be quickly changed when the ion pulsed passes through it. In total three beam foci are desired after the pulsed drift tube. At the first two foci beam observation boxes (BOB4 and BOB5) are located. The third focus is close to the center of the magnetic field, where the Penning trap is located. To achieve all these foci, three Einzel lens are used. An important goal is to minimize the radial energy pick up of the ion when entering the solenoidal magnetic field of the Penning trap.

For the simulations, the complete system for the beam transport for the ion

Table 3.1: Voltage switching time of the pulsed drift tube after ion ejection for the ion buncher and width of the axial spatial distribution inside the pulsed drift tube.

Ion mass number	23	133	200
Switching time, μs	8.5	19.5	24.5
width, mm	123	111	104

buncher to the Penning trap has been divided into two sections. Fig. 3.14 gives the layout of the beam transport system as well as SIMION simulation results for the first part. Pulsed beams with an energy of 1 keV start from inside of a transfer tube, which is also used for differential pumping between the ion buncher and the nested vacuum section. A set of lenses focus the beam for further transport downstream. The pulsed drift tube has two voltages to switch between, one for the beam injection and the other for the ejection. Thus the ion pulse can have an energy change that is proportional to the voltage difference. In the simulation, different masses have to be considered because of the mass dependence of the time-of-flight of the ions. The optimum tube voltage switching time is mass dependent. At present, the pulse drift tube is not used to make large beam energies. It is used to fine tune the energy for optimum capture in the Penning trap. Directly after the pulsed tube there is an Einzel lens (EL6), which is used to focus the beam at the position of the beam observation box (BOB4).

The simulation starts with three beam profiles for ions with mass numbers 23, 133 and 200, respectively. The initial beam properties were calculated by a Monte-Carlo method using realistic ion-atom potentials. Details can be found in Chapter 5. SIMION has been used to determine the optimum voltage switching times of the pulsed drift tube, as well as the minimum tube length required. They are listed in Table 3.1. Based on this simulation, it was decided to make the pulsed drift tube 600 mm long. Comparison of the transverse beam emittance for all the three masses shows that the normalized emittance growth is small, which ensures the further transport

at BOB4 (see Appendix A.4.1).

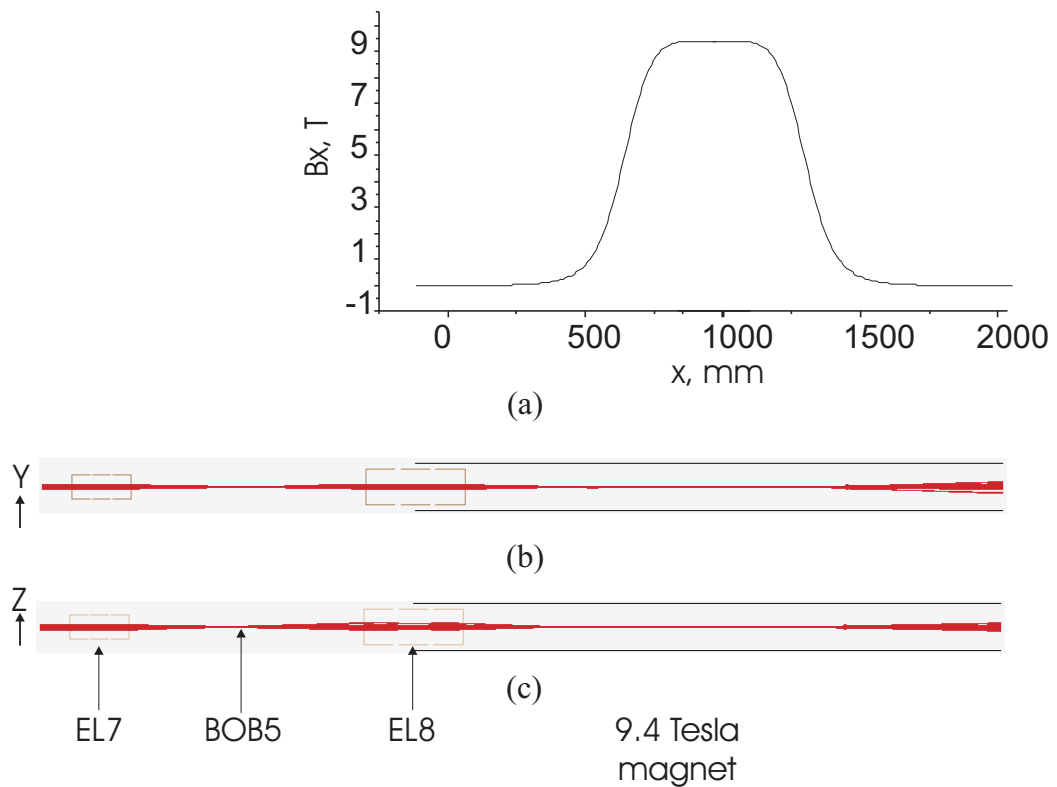


Figure 3.15: Beam transport to the Penning trap. (a) axial magnetic field strength along the field axis; (b) 2-dimensional view of the ion optics in the y - x plane; (c) 2-dimensional view of the ion optics in the z - x plane.

Fig. 3.15 gives the layout of the beam transport from BOB4 into the Penning trap, which is located at the center of a 9.4 Tesla superconducting magnet. It also shows the axial magnetic field strength along the magnet axis. Pulsed beams at an energy of 2 keV from BOB4 first pass an Einzel lens (EL7), which focuses the beam at the position of observation box (BOB5). Another Einzel lens (EL8) focuses the beam before the center of magnetic field. The beam is transported at an energy of 2 keV until it is close to the Penning trap, where the final retardation takes place.

In this simulation we are mostly concerned about the radial energy pick up of the ions when entering the initial magnetic field. Simulations for ions with three mass numbers, 23, 133 and 200 with almost zero radial energy have been performed based on the electrode configurations shown in Fig. 3.15. Optimized results give a maximum radial energy spread below 5 eV (See Appendix A.4.1) for the lightest mass.

Optional beam transport through a switchyard

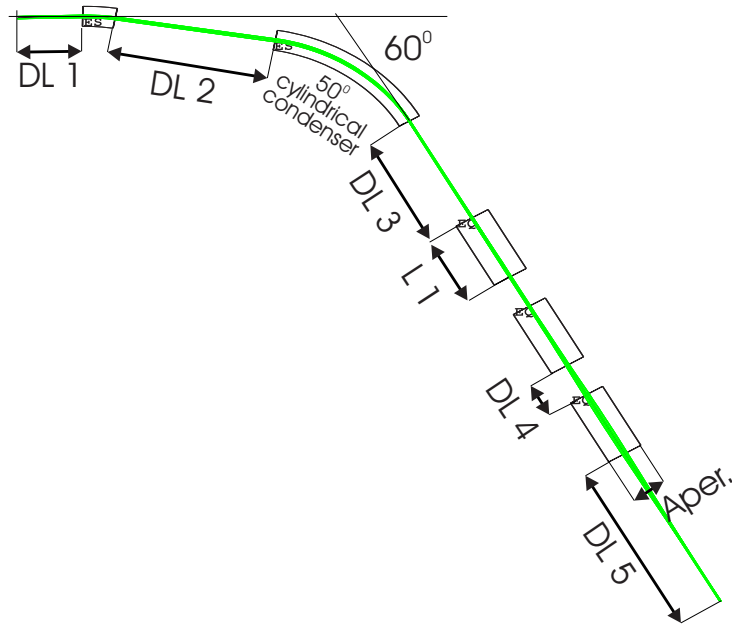


Figure 3.16: COSY simulation for a 60° beam line.

This is an optional section that has not yet been implemented in LEBIT but may be built later in order to expand LEBIT to other experiments. It is assumed that a beam of 30 keV energy (achieved with the pulsed drift tube) needs to be transported. Beam bending by 60° and 90° have been studied. Fig. 3.16 and Fig. 3.17 show schematic layout of these two beam transport scenarios and the COSY simulation results. The first ion optical element in the 60° bending scenario (Fig. 3.16) is a beam kicker. It is a two parallel plate structure, which can be used to pre-bend the beam either upwards or downwards with variable orientations. After the beam kicker there is a 50° cylindrical condenser, which can give the beam a second bending by 50° . In this case the beam is deflected by 60° in total. After the beam kicker and condenser, there is a quadrupole triplet, which is a consecutive structure of three identical quadrupole lenses to focus the beam. The 90° bending beam line is almost same as this one, except the second deflection angle is 80° .

The simulations were performed using COSY up to the third order. The input ions at an energy of 30 keV are assumed to be distributed randomly inside a rectangle of

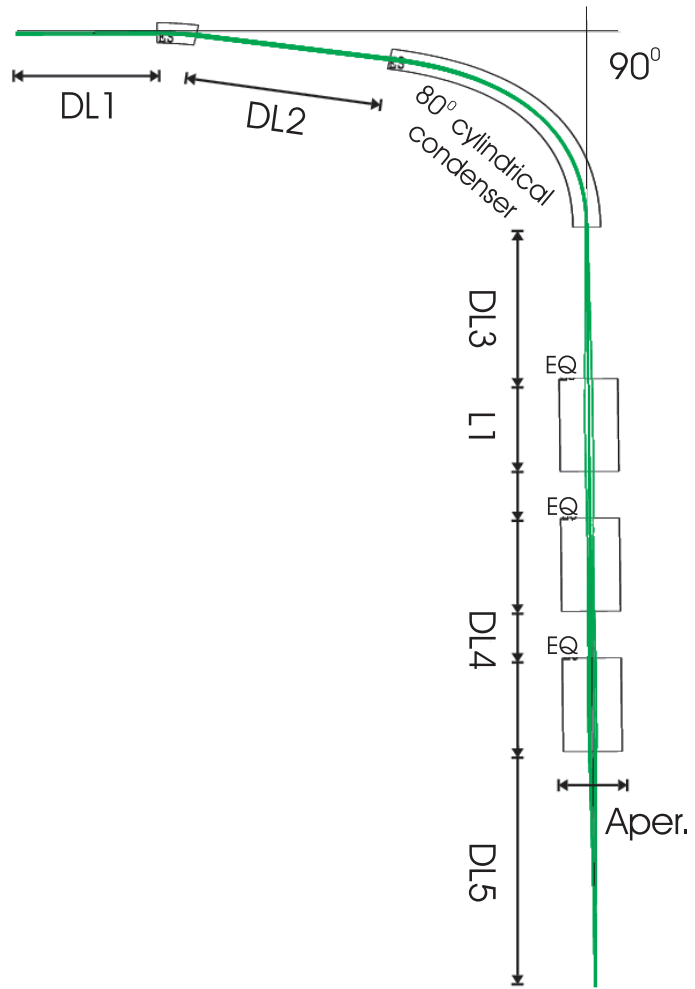


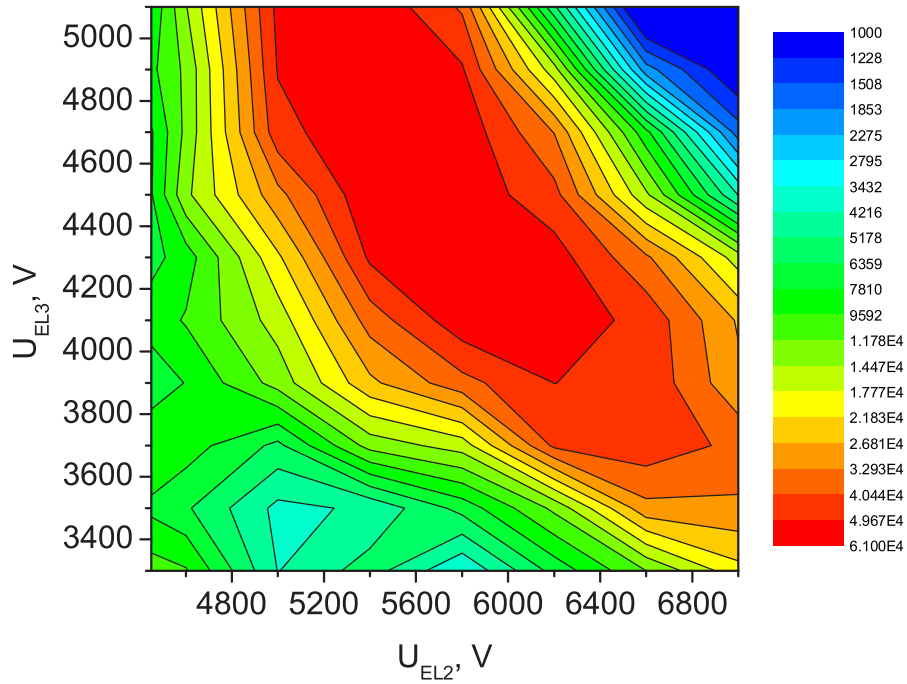
Figure 3.17: COSY simulation for a 90° beam line.

the phase space. The normalized beam emittance to an energy of 60 keV is less than 10% larger than that calculated at BOB4 from the section 3.2.3. That ensures the possibility of the beam transport from the ion buncher. After optimization for both bending scenarios, the final beam emittance growth is less than 6%.

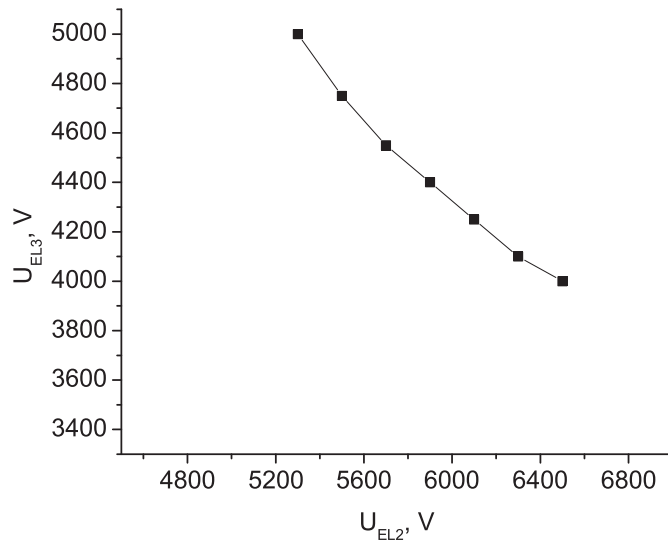
3.3 Performance of the beam transport system

The beam transport system has been designed and built according to the results of the beam simulations discussed above. Now being in operation, the actual voltages used in the beam transport are found to be typically within 10% of the calculated values. There is practically no beam loss observed in the beam transport from the gas cell to ion buncher and from buncher to the Penning trap.

The following measurement is an example of a comparison of the simulation results and measured optical properties of the beam transport system. Fig. 3.18(a) shows the result of a 2-dimensional voltage scan. The beam transmission from the gas cell into the ion buncher has been measured as a function of the voltages applied to the einzel lenses EL2 and EL3 (see Fig. 3.12). The result of a corresponding SIMION simulation is shown in the lower figure. This simulation started with the optimal voltages of both EL2 and EL3 ($U_{\text{EL2}}=5300$ V and $U_{\text{EL3}}=5000$ V) for which the beam focuses at the entrance of the ion buncher. The voltage of EL2 is then increased by 200 V, resulting in a shift of the beam focus. In order to focus the beam back to its original position, the voltage of EL3 has to be adjusted to a different value. This procedure is repeated several times until the voltage of EL2 is $U_{\text{EL2}}=6500$ V. The resulting voltage of EL3 for the same beam focus is plotted as a function of the corresponding EL2 voltage, as shown in Fig. 3.12(b). This curve matches very well the area of maximum beam transmission shown in Fig. 3.12.



(a)



(b)

Figure 3.18: Beam transmission from the gas cell to the ion buncher as a function of the voltages applied to the Einzel lenses EL2 and EL3. (a) result of a 2-dimensional voltage scan of EL2 and EL3; (b) result of a SIMION simulation of the same beam transport scenario.

Chapter 4

LEBIT control and data acquisition system

The LEBIT facility consists of four main functional units, discussed in Chapter 2, and an electrostatic beam transport system, discussed in Chapter 3. The LEBIT control and data acquisition system has been developed to remotely control these units and the beam transport system. It also allows the experimental data to be collected and processed for the on-line and off-line analysis.

4.1 Requirements

LEBIT is a complex system that has a large number and variety of devices that need to be controlled. DC voltages are to be set and monitored for the transport of the ions and for their manipulation in ion guides and ion traps, and for the actual mass measurements. A large number of valves, pumps are to be operated in order to maintain a desired vacuum in each experimental section. Remote actuators are used to move detectors onto the beam axis. Radio-Frequency (RF) voltages need to be generated and controlled for the ion confinement in the gas cell ion guide, and the ion buncher. Radio-frequency voltages are also required for the excitation of the ion

motion in the Penning trap. Timing signals need to be generated for the switching of DC and RF voltages, for example, for ion bunching, ion capture, beam gate operation, and ion motion excitation.

The LEBIT control and DAQ system has to fulfill the following requirements. The first concern is the reliability of the system. The system should be able to run without major failure for a long period. Each of the operating parameters has to stay at its last updated status until a new operation is performed. When a potentially harmful operation is detected, the system should be able to recognize it and alarm the operator before any further operation proceeds. This system should have the ability to automatically take over the operations when a unpredictable system failure occurs and put the system into a safe mode to prevent damage to the facility.

The second requirement is the high precision of the system. An example in the case of the timing signals is the beam injection into the Penning trap, where a timing of ± 100 ns is needed. Voltages applied to some power supplies also need to be very accurate. One example is the ion buncher, where the voltages applied to the trap electrodes need to be as precise as 0.1 V.

The system has to respond quickly to many operations from the user. This is especially essential in the case of voltage scanning for beam tuning and system calibration. The time to set a new voltage to a power supply should be less than a few hundreds of milliseconds. In the case of 2-dimensional voltage scanning, the overall response time of the system for one scan cycle should be around 1 second.

The fourth requirement is the flexibility of the system. The system volume should be changeable without large difficulty. That involves the addition of new components, the replacement of old components, and removing components when system modifications are necessary. Any of these changes should not require a considerable redevelopment of the system.

The fifth requirement is the operational safety of the system. The ultra-high vacuum beam-line system and the other components of LEBIT is achieved with two

turbo pumps. Once a system failure happens and is undiscovered for a large period of time, it will take considerable time and effort to recover the ultra-high vacuum condition. Thus the controls of the vacuum system should be separated from the controls of the experimental part which is less sensitive to the harmful operations and system failure. Another system safety concern is the interruption from outside. Any network failure or uncontrolled access from outside can cause unpredictable problems for the operation of LEBIT. Therefore, the LEBIT control system should be isolated from free access from the outside and have its own network.

An intuitive control by the user is desirable. The control system should provide Graphic User Interfaces (GUI), each presenting a schematic layout of the corresponding section. Each controllable device should be accessible via one of the GUIs and labelled with a meaningful nickname that corresponds to its function. Each GUI should provide a feature for the user to save the present settings and to reload them if desired. Another necessary feature of the control system is data logging, which can record all the selected operational parameters and acquired data for future analysis. The GUIs should be able to operate at multiple places at the same time. GUIs for the same control section but launched at different places should communicate with each other and share the updated information for the involved devices.

Based on these requirements, a dedicated control and DAQ system has been considered as the best option for LEBIT. The system is different from the NSCL lab control system, which for example does not have a combined parameter scanning and data acquisition feature. The computer hardware of the LEBIT control system consists of a Programmable Logic Controller (PLC) system and a server computer which is connected to a PCI Extension for Instrumentation (PXI) bus. The PLC system with its various input and output modules controls most of the power supplies, valves, pumps and actuators. The server computer/PXI-bus system is used to control all the remaining devices via different industrial-standard interface modules plugged into the PXI-bus. The software package consists of both server and client

applications running on the Microsoft Windows platform. Two types of server applications are running on the server computer. Both of them have been developed with LabVIEW. The “LEBIT server”, discussed in this thesis, is mainly responsible for the control of the PLC-controlled devices. The other server is based on the GSI-CS, which is a control system developed at GSI. This server is mainly used for the data acquisition in parameter scanning, which includes also the mass measurements. Two types of client applications corresponding to these two servers are running on the client computers. The LEBIT control panels, which communicate with the “LEBIT server”, are developed with LabVIEW. The parameter scanning and data acquisition program, which communicates with the GSI-CS is, developed in C++.

4.2 Devices to be controlled

The LEBIT control and DAQ system controls different types of devices, e.g., power supplies (PS), RF generators, etc. Table 4.1 lists all these devices according to their type of control. Thermocouples and most of the power supplies are controlled via analog PLC-modules. Valves, turbo pumps and actuators are controlled via digital PLC-modules. Some low voltage bipolar power supplies, RF switches and beam gates are also controlled via TTL signals. RF generators, cryogenic level meters and multi-meters are controlled via GPIB. Vacuum gauge controllers are controlled via RS-485. A timing generator, the digital counter, and digital scope are directly controlled via the PXI-bus.

Among all these devices, two home-made power supplies are very common and important. They are widely used together with the LEBIT backplane, which provides power and control signals to such modules. Most of the analog control signals are in the range of -10 V to +10 V or 0 V to +10 V. The “Bipolar150”, shown in Fig. 4.1(a), is a multi-purpose 2-channel bipolar low-voltage power supply. It is used to provide DC voltages for the ion guides, the ion traps and beam gates. Depending on the chip

Table 4.1: Devices controlled in LEBIT according to the type of control. The number of channels to be controlled is listed in column 2.

Type of control	Number	Device
PLC-analog ^a ADC	200	Low voltage power supply (≤ 400 V)
	200	High voltage power supply (≤ 15 kV)
	8	Thermocouples
PLC-digital ^b	20	Valves for vacuum system
	12	Turbo pumps
	12	Actuators
TTL	15	Low voltage PS (Bipolar) switches
	10	RF-switches
	2	Beam gates
GPIB ^c	8	RF generators
	2	Cryogenic level meters
	1	Multimeter
Directly controlled ^d via PXI-bus	1	Timing generator
	1	Counter
	1	Digital scope
RS485 ^e	20	Vacuum gauge controllers

^aPLC analog to digital converter/digital to analog converter modules

^bPLC digital input/output modules

^cGeneral Purpose Interface Bus modules.

^dDedicated PXI (See section 4.3.1) modules

^eSerial RS485 connection interface

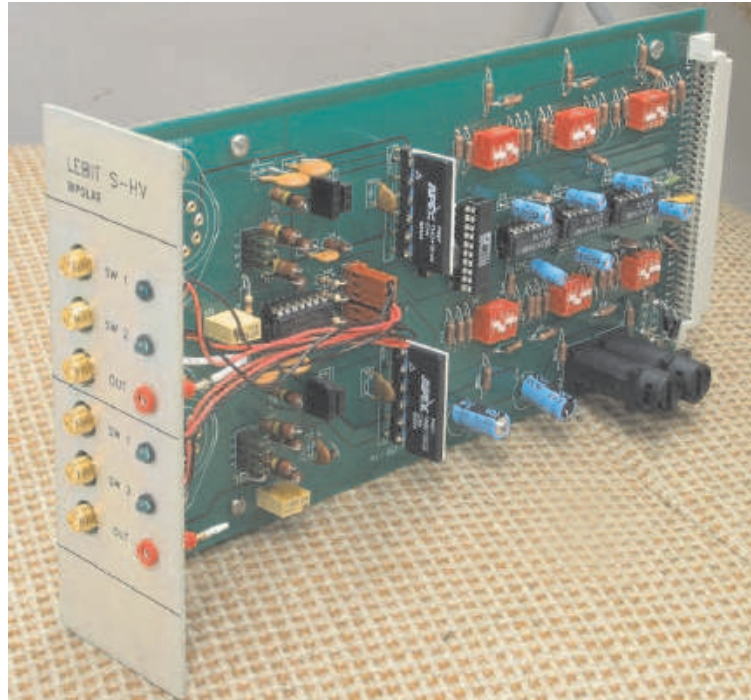
configuration it can output voltages up to ± 400 V. Each channel has three control voltage inputs that are used to program the output voltage. A solid-state switch, actuated by 2 external TTL-levels, allows fast switching between the three selected output levels of each channel. The typical slew rate is about 100 V/ μ s. The “ISEG”¹ is another power-supply module which uses commercial HV-DC/DC converters to provide high voltages up to ± 15 kV. This type of module is mainly used to power electrodes for which high voltage is needed, for example an LEBIT Einzel lens (See Fig. 3.3). Fig. 4.1(b) shows the picture of a module configured to output up to 3 kV.

4.3 LEBIT computer hardware

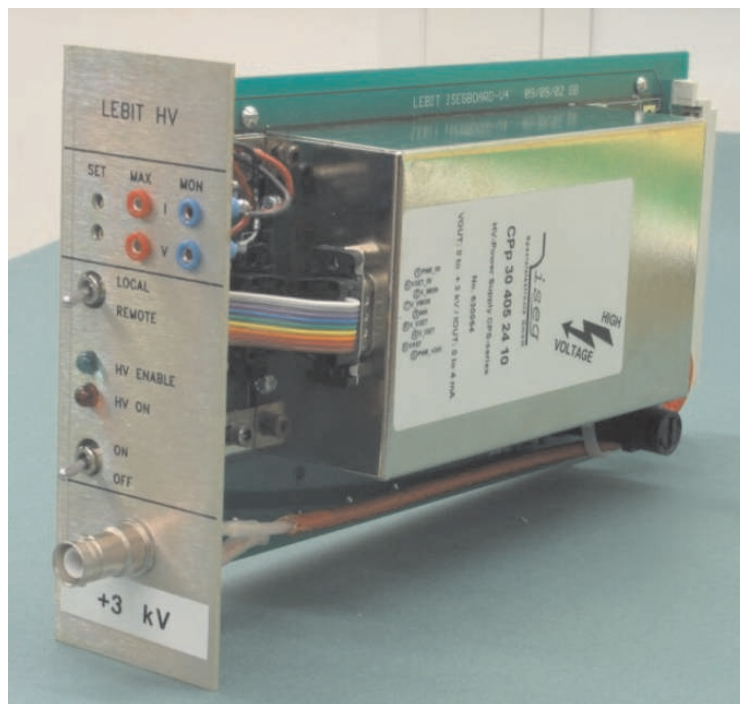
Most of devices in LEBIT are controlled with analog or digital PLC-modules. The PLC system is a remote self-contained and hardware-oriented control system with its own Central Processing Unit (CPU) and hardware modules. A CPU can support hundreds of inputs/outputs (I/O) via modules installed in the CPU base or expansion bases. Analog I/O modules or digital I/O modules with different precision can be mounted in these bases. The DL405 PLC-system from Automation Direct and corresponding hardware modules have been chosen because they are cost effective and easy to program. There are typically 4 to 16 I/O channels on each module depending on the module specification. Each channel can handle a particular operation of the device that connects to it, for instance, setting a voltage on the power supply, opening a gate valve, etc. In LEBIT several PLC systems (with their own CPUs) are used to control different groups of devices.

The remaining devices are controlled by a server computer/PXI-bus system, which provides a high speed connection. Hardware components are either connected to the server computer via industrial standard interfaces, or directly controlled via the PXI-bus. The PXI-bus is actually a component of the server computer. It is located close

¹It is based on the CPS-series HV-power supply from ISEG Spezialelektronik GmbH



(a)



(b)

Figure 4.1: Two power supply modules used in LEBIT. (a) a bipolar power supply for voltage up to ± 400 V; (b) a version of the high voltage module that outputs 0 V to +3 kV.

enough to the server computer to facilitate a high-speed serial connection.

The two computer systems, the server PC/PXI-bus system and the PLC system, are the frame of the hardware part of the LEBIT control and data acquisition system. Fig. 4.2 shows the complete hardware structure of this system. All the components are grouped into five blocks. The first (red) block consists of the server computer which serves as the core of the whole system. Connections between this server computer and hardware components in other blocks are represented by red arrows. The second (blue) block includes the equipment which connects directly to the server computer. This block can be divided into two subcategories. The first category consists of three to five client computers. The second category consists of the available PXI modules (blue boxes with round corners), which connect to the server computer via the PXI-bus. There are two types of PXI modules with respect to their functionalities. The digital scope, the counter and the timing generator are stand-alone modules that are controlled directly by the PXI-bus. All the others are industrial standard interface modules including Ethernet, GPIB and RS485, which are used to connect devices to the server computer. Connections between components in this block and other blocks are represented with blue arrows. The third (pink) block consists of all the PLC units of the PLC system. Connections between components in this block and other blocks are represented with pink arrows. The fourth (yellow) block consists of all the devices that are controlled by the PLC system. The fifth (green) block includes all the devices controlled by the PXI interface interface modules, such as the vacuum gauge controllers (via RS485) and RF generators (via GPIB).

4.3.1 The server computer/PXI-bus system

The LEBIT PXI chassis provides fourteen slots for industrial standard CompactPCI or PXI modules. The PXI-bus expands the PCI bus and offers the benefits of the PCI architecture, including fast speed and good performance. It is compatible with the industrial-standard compact-PCI but and a capability to integrate modules from

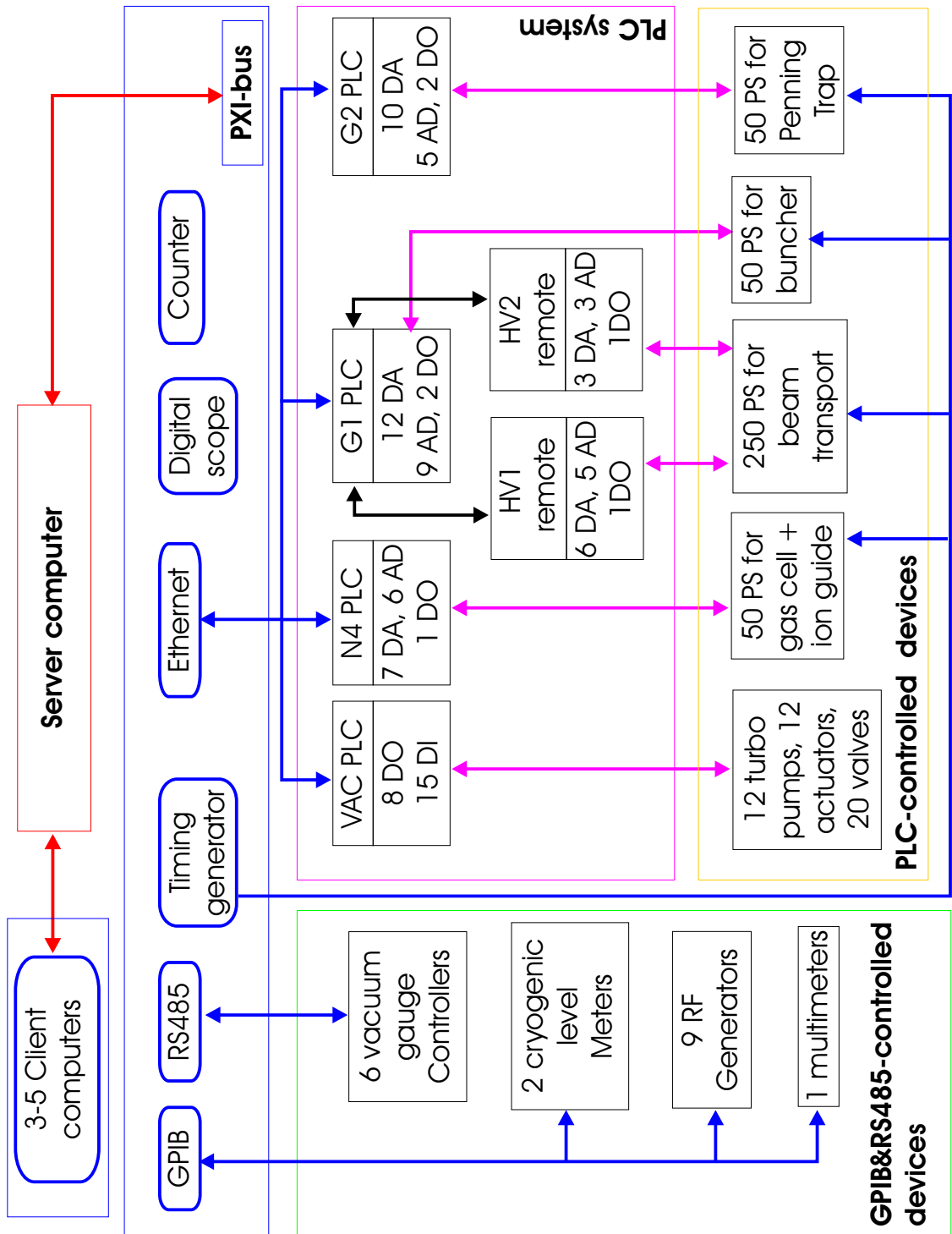


Figure 4.2: Structure of hardware system used in the LEBIT control and DAQ system. All components are grouped into five blocks. The first (red) block consists of the server computer and PXI-bus. The second (blue) block consists of all the PXI modules and client computers. The third (pink) block consists of all the PLC units of the PLC system. The fourth (yellow) block consists of all the PLC-controlled devices. The fifth (green) block consists of all the devices controlled by the PXI interface modules. Arrows indicate the connections between different equipments. PS: power supply, AD: analog/digital converter, DO: digital output, DI: digital input.

many manufacturers into a single system. It is physically separated from the server computer. In the case of a replacement of this computer, only the PXI module/PC interface needs to be mounted to the new computer. The PXI modules in LEBIT can be categorized into two groups. The first group provides standard interfaces to communicate with remote devices. An Ethernet/GPIB combo module² provides both an Ethernet port and a GPIB interface. The Ethernet port is used to connect to the PLC system. A GPIB module provides a fast GPIB connection for programmable instruments like multimeters, RF generators and the cryogenic level meter of the LEBIT magnet system. An RS485 module³ provides a robust serial connection to communicate with the vacuum gauge controllers. The second group includes three PXI instrumentation modules. The first is a timing generator⁴ that outputs timing patterns at a maximum rate of 10 MHz to trigger voltage outputs of the Bipolar power supplies to actuate RF-switches, beam gates and more. The other two are devices for data acquisition. A counter⁵ is used to record the beam intensity at the A1900 target monitor. A 100 MS/s digital oscilloscope⁶ is used mainly to measure the time-of-flight distribution of ions arriving at various detectors in LEBIT.

4.3.2 The PLC system

The PLC system is a distributed system that includes four dedicated PLC units. All the units are grouped and placed near the sections of the beam line that they need to control. Once programmed via the server computer, they can be operated independently from each other and from the server computer.

²NI PXI-8212 module

³NI PXI-8421/4 series module that is asynchronous RS485 interfaces

⁴MA202 16-channel digital word and timing generator from C&H Technologies, Inc.

⁵NI PXI-6602 timing and digital I/O module with eight 32-bit counter/timers and 32 lines of TTL/CMOS-compatible digital I/O

⁶NI PXI-5112 digitizer for high-speed applications

The PLC system for vacuum control

The vacuum control PLC unit (“VAC PLC”) is used to control turbo pumps, valves and actuators of the vacuum system with 8 DO modules⁷ and 15 DI modules⁸. Each of the vacuum devices is connected to one DO channel and two DI channels. A DO channel provides a 24 V signal to activate a device, for example a gate valve. At the same time, the vacuum device provides up to two 24 V digital signals that indicate its status, for example, gate valve open or gate valve close. The associated DI channels forward these digital signals to the server computer.

The PLC system for experiment control

The experiment control PLC system includes three independent PLC units, N4 PLC, G1 PLC and G2 PLC. They are used to control power supplies for the gas cell, the ion guides, the ion buncher and the Penning trap, as well as beam transport between these components. Each PLC unit connects to 10-20 DAC/ADC modules to provide programming voltages, and read monitor voltages. There are three types of DAC modules used in LEBIT: (1) 12 bit unipolar modules⁹ are used for the programming of the high-voltage ISEG power supplies; (2) 12 bit bipolar modules¹⁰ are used for bipolar power supplies; (3) 15 bit unipolar modules¹¹ are employed in cases where programming voltages with a higher precision are needed. Two types of ADC modules are employed to read voltages. 12 bit modules¹² are used to monitor power supply voltages. Thermocouple modules¹³ are used to read type-J thermocouples for temperature measurements, for example, the temperature in the LEBIT room or inside the ion buncher.

The N4 PLC controls the power supplies for the gas cell and ion guide sections.

⁷D4-16TD2

⁸D4-08TD1

⁹F4-16DA2

¹⁰F4-04DA2

¹¹F4-04DAS2

¹²F4-08AD

¹³F4-08THM

The G2 PLC controls those for the Penning trap section. The G1 PLC controls power supplies for the ion buncher section. There are two remote PLC units (“HV1”, “HV2”) connected to it via an Ethernet base controller with fiber optic connection¹⁴. These two remote units are used to control the power supplies for the beam transport sections operated on the high voltage platforms. The HV1 unit is responsible for the section between the N4 wall and the ion buncher, where all the devices before the ion buncher are operated at a base potential of -5 kV. The HV2 unit controls the section between the ion buncher and the Penning trap, where the devices between them are operated at a base potential of -2 kV.

4.3.3 Fast timing

The PXI-timing generator module MA202 is used to provide timing sequences for the experimental procedures. It can produce almost any conceivable asynchronous digital signal with 100 ns time-resolution for up to 16 individual outputs. The time base can be achieved with either an internal clock that is programmable with a period resolution of 50 ns, or an external signal. Fig. 4.3(a) shows an MA202 timing generator module in the PXI chassis. The 16 output channels are distributed into four groups in a patch panel. Each group can output four channels to a so-called “timing interface” via a standard RJ45 cable. Fig. 4.3 shows three of these interface boards plugged into the LEBIT backplane, with the right one in operation. Each of the 8 output channels in this operating board can be used to trigger a certain device that needs fast switches, e.g., the bipolar power supply discussed earlier.



(a)



(b)

Figure 4.3: Top: MA202 timing generator module mounted in the PXI chassis; Bottom: Timing interface board in operation.

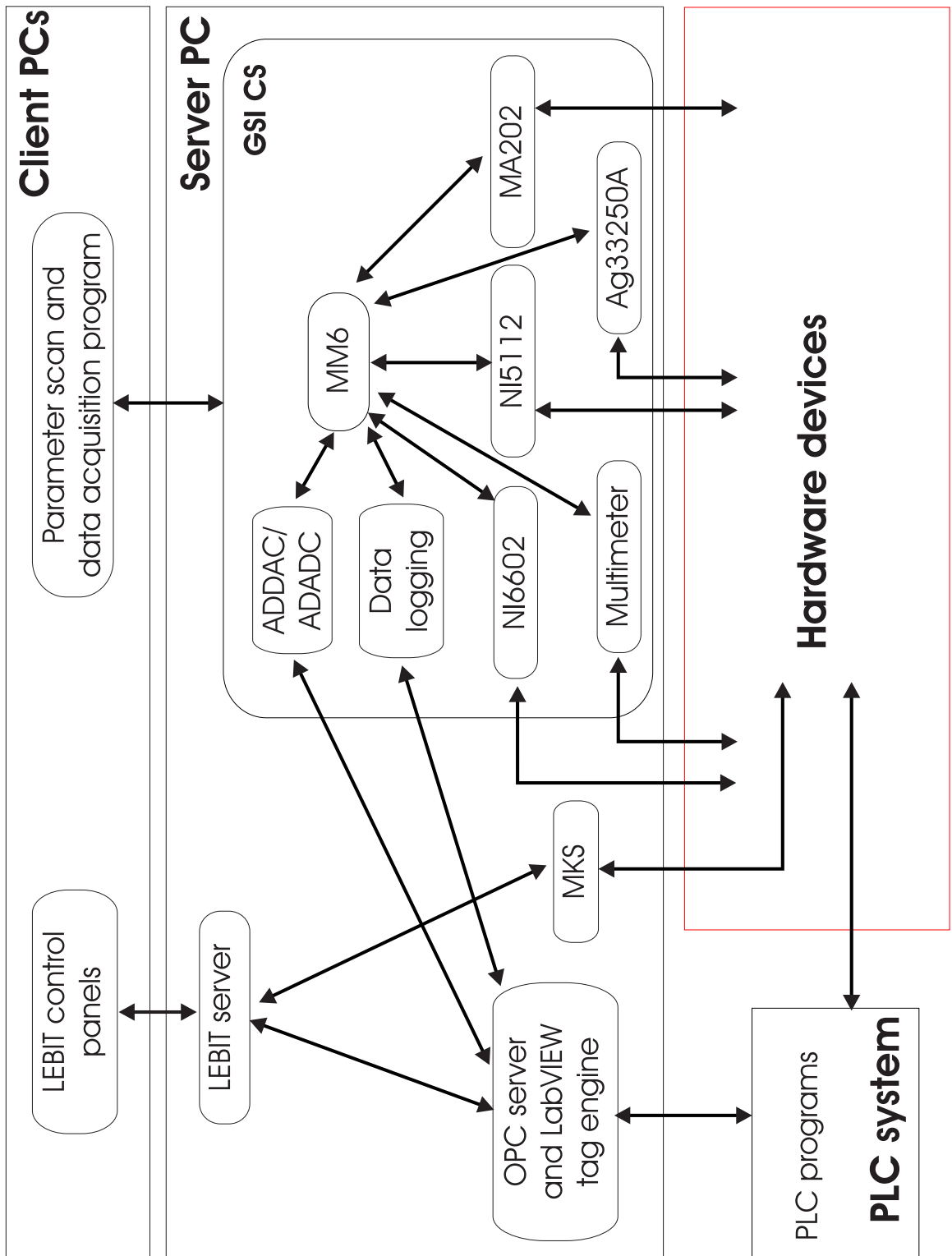


Figure 4.4: Structure of the software system used in the LEBIT control and DAQ system. Hardware devices to be controlled are presented in the red box.

4.4 Software of the LEBIT control and data acquisition system

A software package has been developed that works together with the hardware components for the LEBIT control and DAQ system. The complete diagram of its structure is shown in Fig. 4.4, with the controlled hardware represented by the red box. The control of the hardware components has been implemented with three levels of software packages, as illustrated in three blocks. The lowest-level block consists of PLC programs running on all the PLC units. Their function is to control all the PLC-controlled devices connected to the PLC system. The remaining devices are controlled with a set of software drivers, each specifically developed to control one type of device. These drivers belong to the second block, which contains two main server applications and the supporting programs running at the server computer. The LEBIT server is able to process manual controls of all the PLC-controlled devices. That is assisted by the package of an Object Linking and Embedding for Process Control (OPC) server and LabVIEW tag engine that organize the PLC addresses for the PLC programs, which will be discussed in detail in section 4.4.2. Another task of this server is to read the pressure from the vacuum gauge controller, which is achieved by calling the MKS driver. The other server program is the GSI Control System (CS), which controls different devices and processes experimental data via MM6, a central process developed for LEBIT. This process together with the GSI-CS server scans different parameters upon request from the parameter scanning and data acquisition program in the client computer. This is performed by calling the corresponding software drivers from MM6. The third block has two types of applications running on the client computers, corresponding to two server applications, respectively. One of them consists of a set of control panels. These panels are used to operate power supplies for experiment control and vacuum control by sending corresponding requests to the

¹⁴H4-EBC-F module

LEBIT server. The other type is a parameter scan and DAQ program. It is frequently used in beam tuning and mass measurements and communicates with the GSI-CS system.

4.4.1 PLC Software

Each PLC unit has a dedicated PLC program running on its CPU. A complete PLC program is able to periodically access all the programmable PLC modules with a constant cycle time. In LEBIT there are four independent PLC programs, each is running on an individual PLC CPU. Three of them control the experimental equipment of N4, HV1&HV2&G1, G2 and the fourth one is for vacuum system control. The last one has features of error-checking and emergency handling to ensure system safety. As an example, this PLC program checks to see if the pressure on each side of a gate valve is low enough for the valve to be opened safely. As another example, the program isolates a section by closing the gate valves on both ends of that section if its pressure raises above a maximum value. The DirectSOFT32 software package shipped with Automation Direct hardware is used for PLC programming. This software provides a Relay Ladder Logic(RLL) [51] programming method, a graphic representation that allows for boolean logic and general CPU register/accumulator manipulation. It uses contacts to represent inputs and coil symbols to represent outputs. A line of inputs and outputs with various numbers of instructions to handle logic between them is known as a rung. A set of rungs with different functionalities make a PLC program, defining the I/O operations for a PLC unit. A typical PLC ladder program consists of about 100 rungs and can update all available I/Os in each scanning cycle. The typical overall cycle time ranges from a few tens of milliseconds for a simple program to several seconds for a complex program.

Fig. 4.5 shows a portion of the ladder program controlling the LEBIT vacuum system. All four rungs are working together via different logic instructions to respond to a user's request of opening or closing of the gate valve between BOB3 and the

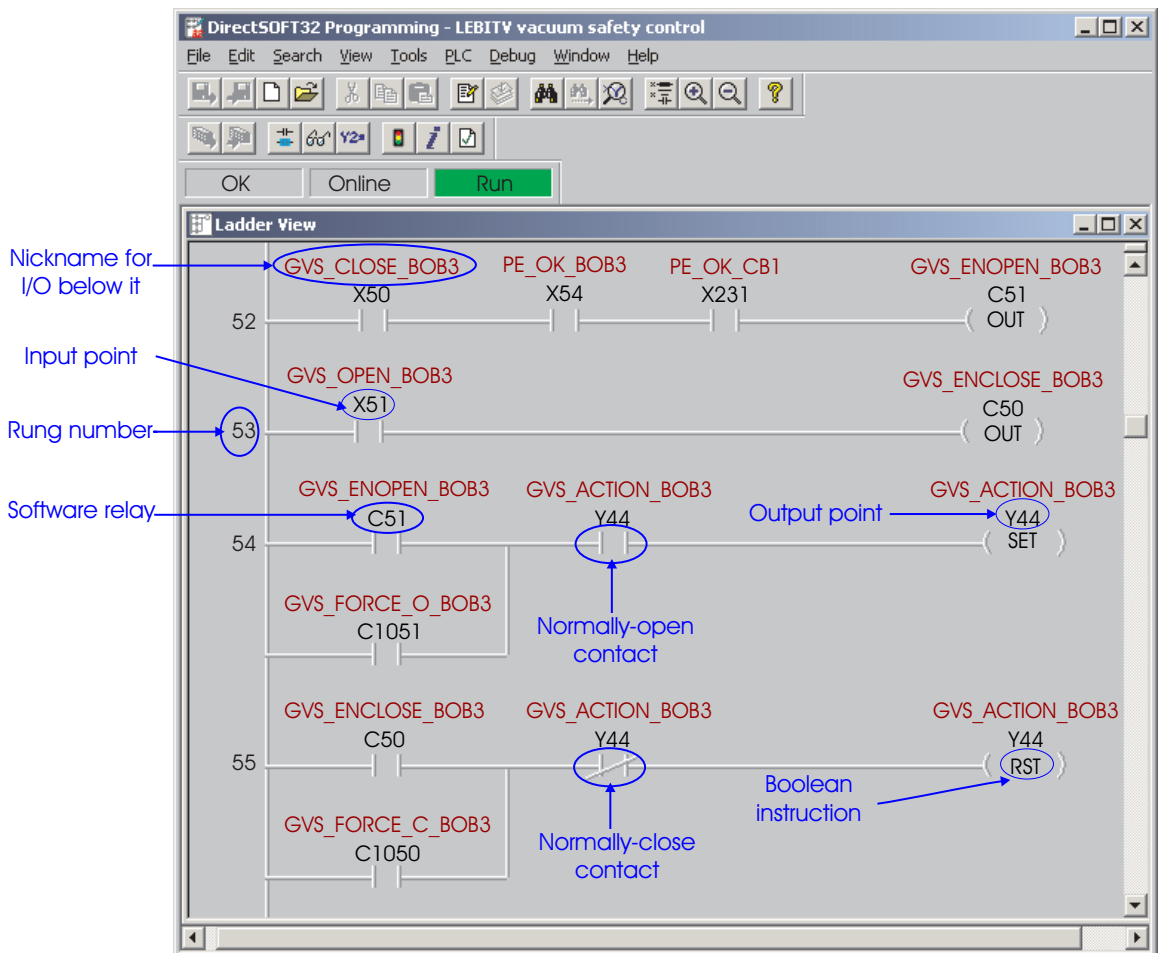


Figure 4.5: A ladder program segment of LEBIT’s vacuum control PLC. This segment controls the opening/closing action of a gate valve in a vacuum section (BOB3) of LEBIT.

ion buncher. The first two rungs with number 52 and 53 check a couple of necessary input points. Each of them corresponds to the status of one related device (vacuum, valve, pump or actuator), which can be used to determine if the valve can be opened or closed safely. Based on these conditions the last two rungs labeled with numbers 54 and 55 process the user's operation request of the valve by setting or resetting the output point of it. Then the corresponding PLC output module switches between 0 V and 24 V to open or close the gate valve.

The ladder programs to control the experimental equipment have more algorithmic instructions than that of the vacuum system. The output voltage of each power supply is linearly mapped from the corresponding programming voltage. Four parameters are used in this linear mapping, which includes scaling, offsetting and two other correction terms for calibration.

4.4.2 Server applications

The two main server applications, LEBIT server and GSI Control System (CS), reside on the server computer. Both of them are developed with LabVIEW under the Window 2000 operating system. They all implement the Datalogging and Supervisory Control (DSC) module and request-driven functionality. They communicate with the client applications via TCP/IP in the lab-wide local network.

OPC server and tag engine for PLC organization

An essential supporting component for PLC addressing is the combination of an OPC server and LabVIEW DSC tag engine. An OPC server can access one I/O point of a PLC module through the PLC-CPU, and return the voltage of that I/O to the client. Each I/O is then recognized by an item name and its actual value in the OPC server database. The LabVIEW DSC tag engine manages all the individual I/O points and addresses them through so-called "tags". When this tag engine is working as the OPC client, it can connect tags with OPC items and configure their parameters like alarm

levels and scaling. The PLC address used in the ladder program is usually chosen as the tag and item name for a PLC I/O. For convenience a nickname is assigned to each I/O and used instead of its address. The nickname reflects the function of the equipment connected to the I/O. A Microsoft Access database is used to organize all of the address-nickname entries. This database also contains information of the scaling factor, offset and calibration coefficients for the conversion between the programming voltage and the actual delivered voltage. Another LabVIEW program is used to retrieve the PLC address through the nickname. Then the LEBIT server applications can simply refer to the nickname to access the desired equipment.

LEBIT server

The LEBIT server responds to requests for manual-control operation of PLC-controlled devices, received from the LEBIT control panel applications via TCP/IP. This server also broadcasts the required device information to the clients. Requests from the clients are processed by a queue mechanism. The first request from each application is always to log on. Once processed, the server creates a unique link for that client and uses it for communication with that application until a log-off request from it is received. During that period the client can subscribe to a set of PLC addresses corresponding to a group of devices. Through them the connected client is able to send requests for the server to access those devices and perform desired operations. Once an operation is completed the server will broadcast the actual status of the controlled device to all the applications which have subscribed to its address. The server will also periodically broadcast an updated status for each subscribed device to all corresponding subscribers. Multiple clients can log on to the server which allows different experimenters to independently access and operate LEBIT equipment from different locations. The clients that control the same sections can share the updated information of the devices involved without interference with each other. The communications between the LEBIT server and the clients use plain-text ASCII instructions,

as listed in Table 4.2. That makes it possible to develop the client applications on almost any platform, which enhances the flexibility of the system.

Table 4.2: Plain-text ASCII instructions used for communication between the LEBIT server and the client applications.

Instruction	Brief description
login	process the log-on request to the server and add the generated link to the connection list
act	add the monitor signals ^a into the activated signal list for status broadcasting with required time interval
useSig	register the set signals ^b in the registration table for processing of the operational request
queryfilename	obtain the file name of the power supply settings for the controlled section from the database
setvalue	change the voltage of one power supply
setallvalue	change the voltages of a set of power supplies
setvac	perform a new operation on one vacuum system device
setinterval	change broadcasting time interval for one activated monitor signal
setallinterval	change broadcasting time intervals for a set of activated monitor signals
deact	delete the monitor signals from the activated signal list
setfilename	save the received file name of the poer supply settings for one controlled section to the database, and broadcast the file name to all the subscribers
Closeme/NoConn	delete the link of the corresponding client from the connection list, and remove all the related set signals from the registration table

^aassociated with the actual applied voltages of the power supplies or the actual status of the vacuum system devices

^bassociated with desired voltages of the power supplies or actions of the vacuum system devices

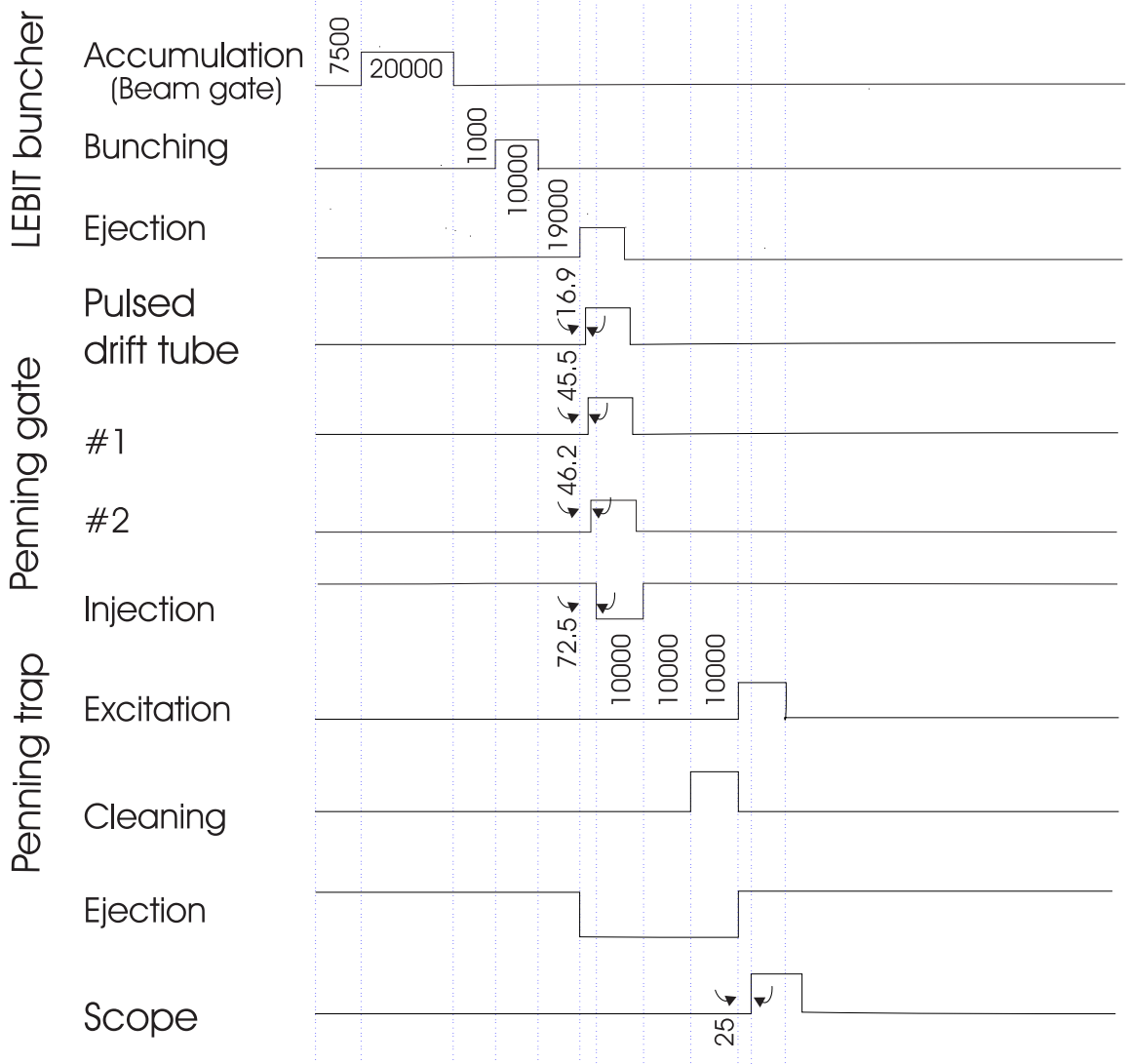
GSI control system

The GSI control program [52] was primarily developed at GSI for the dynamic control of a rather large number of experiment parameters. It is programmed in LabVIEW with an object-oriented approach. A class in this case is a collection of several LabVIEW files that allow a certain type of hardware device to be driven. More than one object for a class can be loaded in the memory at the same time. Once an object is

loaded as an instance, it can work as a software driver to control a device. The object communicates with the base process of the program with an event-driven mechanism so it can be replaced by another object. That makes it possible to implement the distributed control system by only taking the central object modules and adding specific add-ons depending on the experimental requirement.

The module “MM6” is the LEBIT-specific central process of the GSI CS. It is a class derived from the BaseProcess class of the GSI CS framework. It can control almost all the available hardware devices of LEBIT via the corresponding object. It also communicates with the parameter scan and DAQ program. That makes it possible to scan many parameters of LEBIT and to measure the corresponding system response with DAQ devices such as the digital oscilloscope, which is widely used for beam tuning and mass measurement.

Various objects can be dynamically loaded and configured to drive corresponding hardware devices upon being called from MM6. A typical scan starts with the initialization of all the involved devices. At this step each hardware device gets its initial value from its assigned object and is ready to be activated by the timing signals. The central process MM6 then activates the timing generator module MA202 to provide timing patterns as defined by the client. The next step is to set the scan-parameter to a new value within the scanning range. There are several types of parameters that can be scanned via different objects. A voltage can for example be adjusted via the ADDAC module, or a frequency/amplitude of the RF voltage can be changed via the Ag33240A module. After the scan-parameter is activated, the timing signal triggers the sequence of voltage changes on other power supplies, needed to provide the potentials for ion cooling, bunching, trapping, etc. In most cases, the response of the system to a change of the scan-parameter is recorded at the digital scope via the NI5112 module. The acquired signal is then transferred to the client program for display and data saving. At the end of a cycle additional information, like the A1900 beam intensity, can be logged via the Multimeter or the NI6602 module. This



- Note: 1. Unit is μs
 2. Numeric value denotes the time interval between two neighboring dash lines unless marked with arrows
 3. Time width for high state is $10000\mu\text{s}$ unless marked

Figure 4.6: Overview of a measurement cycle for a cyclotron resonance measurement of $^{86}\text{Kr}^+$. Not all steps require the same level of precision. For the most critical part, the injection of ions into the Penning trap, the timing sequence must be maintained to be better than $0.1\mu\text{s}$.

procedure is repeated periodically with the same set of scan values and a scan of the whole range of the scanned parameter typically consists of many such cycles. As an example, the cycle for a resonance measurement of $^{86}\text{Kr}^+$ is shown in Fig. 4.6. This cycle contains 15 steps and needs about 100 ms to complete. The first step of this sequence is to open the beam gate, which is triggered by a command from the parameter scan and data acquisition program running on the client computer. It is followed by the operation of the ion buncher, which includes beam accumulation, ion bunching, and ion ejection. After that the timing signal triggers the voltage switch for the pulsed drift tube and for the Penning gate. The next step is the operation of the Penning trap, which includes ion injection, RF excitation, removal of unwanted ions and ion ejection. At the end the timing signal triggers the digital scope for a signal acquisition. The GSI-CS server application shares data logging and PLC addressing with the LEBIT server. As a consequence, for example, the scanned power supply voltage values are updated simultaneously on the corresponding control panel interface.

4.4.3 Client applications

There are two types of LEBIT client applications running on the client computers under the Windows 2000/XP operating system. The first type consists of a set of LabVIEW based control panels to provide a GUI to access PLC-controlled devices through the LEBIT server. Due to differences in the PLC I/O types involved this can be further divided into experimental control and vacuum system control. The second type is a C++ based parameter scan and DAQ program. This program controls parameters and acquires data through the GSI-CS server application.

Control panels for experiment control

At present there are nine control panel applications for the LEBIT experiment. Their names and control tasks are listed in Table 4.3. Fig. 4.7 shows the main panel and two

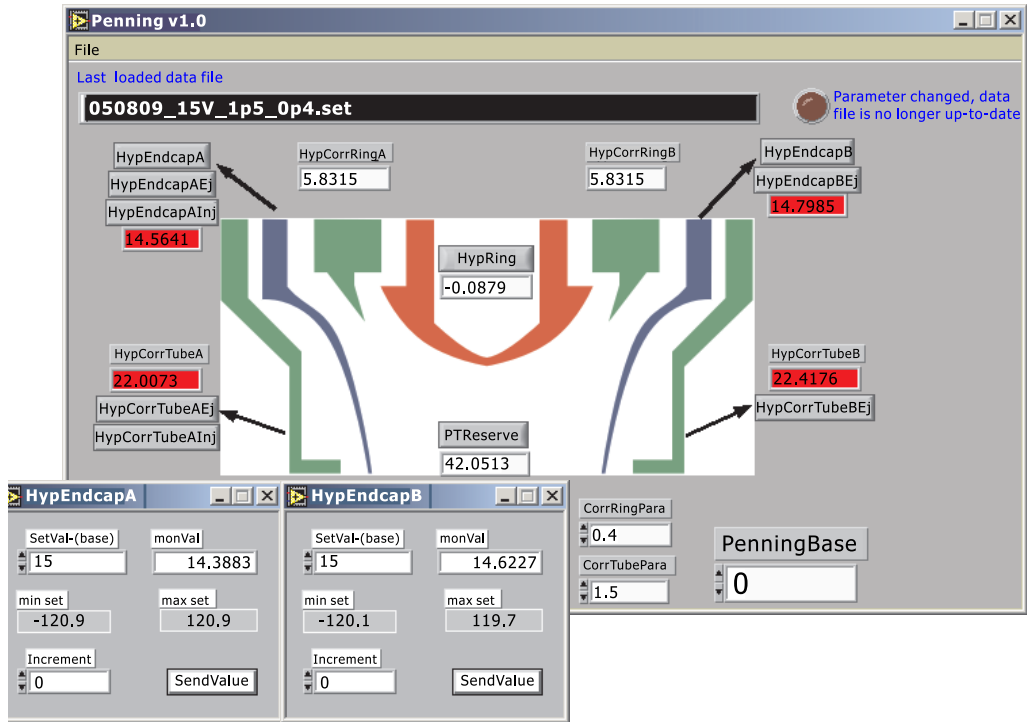


Figure 4.7: Control panel and popup dialog windows for the LEBIT Penning trap.

popup dialogue windows for the control of the Penning trap. The main panel displays the actual voltages for the electrodes in this group once it has logged onto the server. There is a unique nickname associated with each electrode, which corresponds to that in the server database. A small dialogue window will pop up if a nickname button is clicked. When that happens the main panel sends out a request to the LEBIT server to adjust the time interval for updating status of this electrode from the default value of 10 s to 1 s. That makes it feasible to read more frequently the feedback of the actual voltage applied to the electrode. The current set voltage for the electrode is displayed, as well as the allowed range and the monitored voltage. Another feature of this popup dialog window is to allow the setting of a new voltage for that electrode. Multiple popup dialogue windows for different electrodes can be opened at the same time, which makes it easier to control a number of parameters simultaneously. The main interface allows one to save the set of control parameters to a file and reload it at a later time, which makes it easy to switch between different settings. The file name of the currently applied setting file is displayed in the upper left corner. A

Table 4.3: LEBIT control panels for experiment control.

Name	Experiment section
gascell	Beam transport inside gas cell
ionguide	Beam transport and mass filtering in ion guide
n4tobob1	Beam transport from N4 wall to BOB1
bob1tobun	Beam transport from BOB1 to BOB3
testionsource	Beam transport inside the test ion source chamber
bun	Ion buncher: Ion cooling, bunching and extraction
buntopenning	Beam transport from the ion buncher to the Penning trap
penning	Penning trap: Ion capture, trapping and ejection
penningject	Beam transport from the Penning trap to the detector

warning light comes on if the settings have been changed but not saved to a file. The background color of the monitor signal is usually white. If there is more than 10% difference between the set and monitor value, that color changes to red to alert the user of a potential problem with this device.

Control panel application for vacuum control

There is one control panel for the vacuum system. To keep the interface compact, the vacuum control panel is split into seven logical units and arranged in a tab structure as illustrated in Fig. 4.8. The vacuum sections and their corresponding tab names are listed in Table 4.4. One tab page provides control of the vacuum equipment for that section, i.e., actuators, valves and turbo pumps. The control of each vacuum device is labeled with the nickname that is stored in the database of the server computer. Each device can be operated with a button located near its nickname. The status of the actuators, pumps and valves can be seen from the two status indicators labeled “in/out”, “run/fail” and “open/close” with a different color for visualization, respectively. Pressure readings from the vacuum gauge controllers are displayed in each section. The high voltages for MCP detectors and phosphor screens are displayed next to the corresponding actuator buttons. To prevent damage to the MCPs, the detector can only be moved when both the MCP and the phosphor screen voltage are

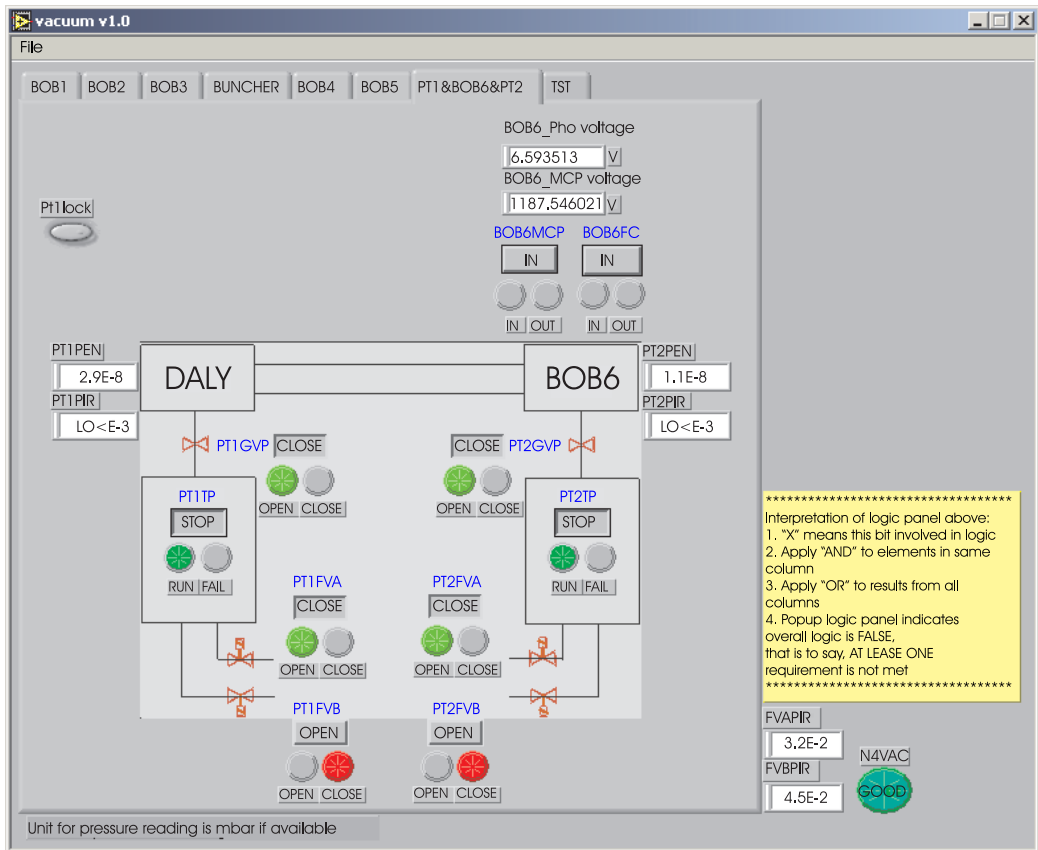


Figure 4.8: Control panel for the LEBIT vacuum system.

Table 4.4: Sections of the vacuum control application.

Tab name	Vacuum section
BOB1	BOB1 chamber
BOB2	BOB2 chamber
BOB3	BOB3 chamber
Buncher	Ion cooler and buncher
BOB4	BOB4 chamber
BOB5	BOB5 chamber
PT1&BOB6&PT2	Vacuum chamber including EL8, the Penning trap and BOB6
TST	Test ion source chamber

less than 100 V.

Parameter scan and data acquisition program

The main purpose of this application is to define a measurement cycle that the GSI-CS executes (See section 4.4.2) and to record the system's response to a change of up to parameters (1-dimension or 2-dimension). All control voltages in the PLC systems, all time steps in the setup of the timing generator (See Fig. 4.6), and the frequencies and amplitudes of all Artificial Function Generators (AFGs) may be used as scan parameters. The response of the system is read as a waveform (array of positive integer numbers), which in most cases can be interpreted as a time-of-flight (TOF) spectrum. To record a cyclotron resonance for a mass measurement (See Chapter 6) or a beam intensity change corresponding to a voltage scan, different DAQ devices are used. A digital scope attached to the MCP is used to measure the time-of-flight of the pulsed beam, and a pA-meter attached to the Faraday cup is used to measure the beam current. Both results can be cast into waveforms, which can be analyzed in the parameter scan and data acquisition program.

Fig. 4.9 shows the main panel of the parameter scan and DAQ program for a cyclotron frequency measurement of $^{39}\text{K}^+$. The small windows display different information: (1) the accumulated countrate as a function of the scanned value; (2) the

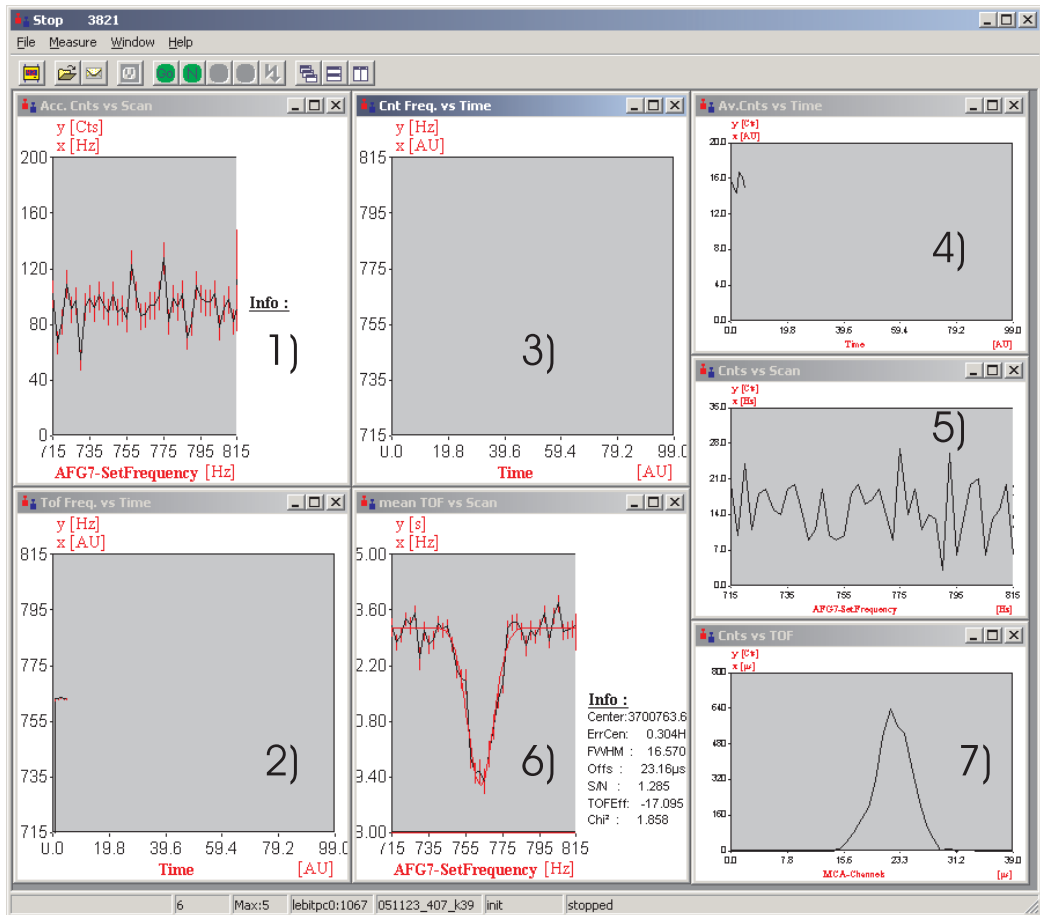


Figure 4.9: Main panel of the parameter scan and DAQ program for a cyclotron frequency measurement of $^{39}\text{K}^+$.

fitted center frequency as a function of the elapsed time; (3) the frequency of individual countrate as a function of the elapsed time; (4) the average countrate as a function of the elapsed time; (5) the countrate as a function of the scanned value; (6) the average time-of-flight as a function of the scanned value and (7) the accumulated countrate as a function of time-of-flight. Window #6 is most important for a mass measurement as it will display the cyclotron resonance curve.

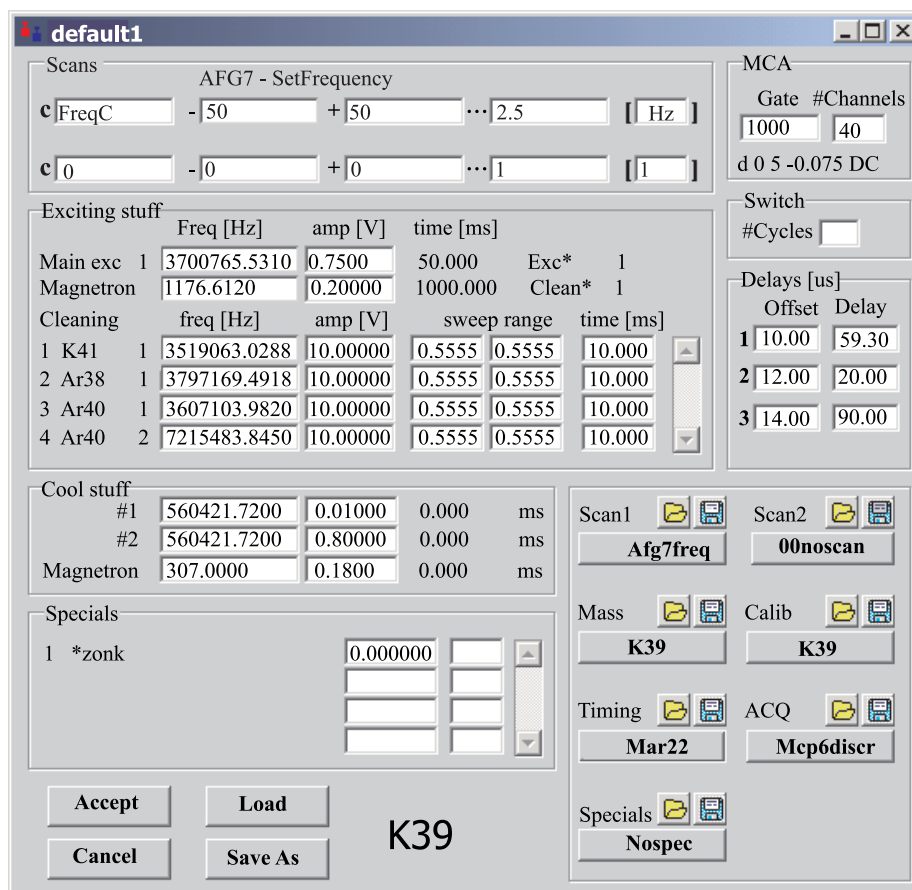


Figure 4.10: Configuration panel for a cyclotron frequency measurement of $^{39}\text{K}^+$.

This program saves the data obtained from the DAQ device together with configured data for the measurement cycle in one file. The data file uses a mixed text/binary format: The configured data is written as plain text and can thus be used with any text editor, the actual data is written as compressed binary data. A dedicated off-line evaluation program, EVA, is used to read the data file. The device setup allows one to select the server-side objects for the RF generators, timing generators and DAQ

devices. A recently added feature is data logging which allows one to periodically read counters or multimeters, and write their data to a separate log-file.

As an example, Fig. 4.10 shows the configuration panel setup for a cyclotron frequency measurement of $^{39}\text{K}^+$. A one-dimensional frequency scan with the frequency generator “AFG7” is selected. The center value, scan range and step value are displayed near the upper left corner. The optional second-dimensional scan is not used for this measurement. The “timing” configuration allows one to define the timing pattern for the measurement cycle. The selected DAQ device can be configured with the “ACQ” setup. The “Mass” configuration defines mass, charge and excitation scheme of the isotope/molecule that will be captured in the Penning trap. It also includes a list of charged particles that are to be removed from the Penning trap by dipole excitation. The “Calib” configuration stores the eigenfrequencies of the reference ion and proper excitation amplitudes which are used to calculate the excitation frequency and amplitudes of the ion under investigation.

4.5 System performance and future development

The LEBIT control and DAQ system has been running with full functionality for more than two years. It has proven essential when LEBIT was commissioned and would vary reliably in a number of beam times. All the timing signals and control voltages are set as precisely as expected. The response time of the system, i.e., the delay between the time a control voltage is requested to change to the time the changed voltage is applied, ranges from about 60 ms for the dedicated PLCs (N4, G2 and Buncher) to about 400 ms for the PLC unit where remote PLCs are attached. A couple of upgrades have been implemented, for example, the addition of a PID loop to stabilize the He pressure of the superconducting magnet. The safety programming of the vacuum PLC system has helped to defend a number of potentially harmful situations, such as power failure and failure of vacuum equipment. The control applications connected

to the LEBIT-server and the parameter scan and data acquisition program linked to the GSI-CS server provide reliable and intuitive control of the LEBIT experiment.

Chapter 5

Beam cooling, accumulation and bunching

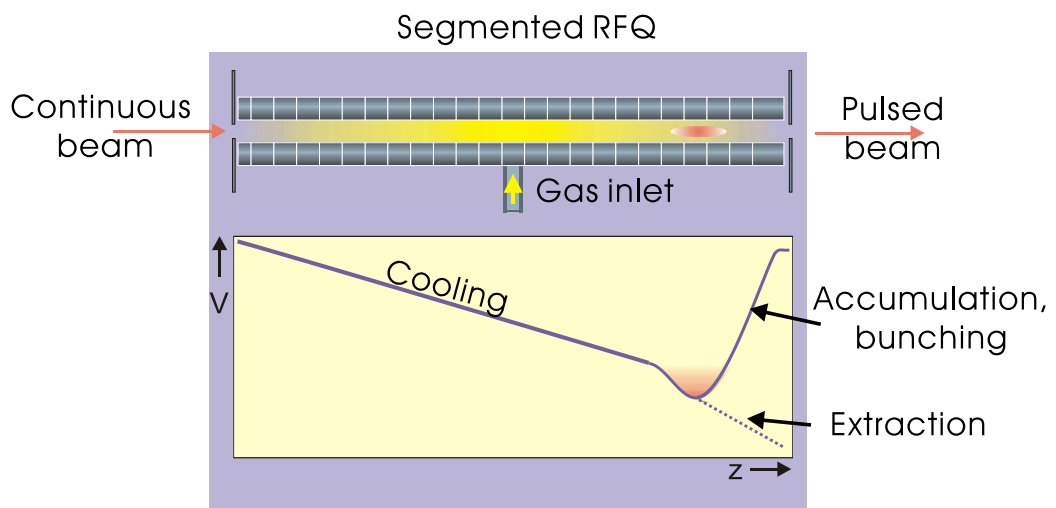


Figure 5.1: Top: Schematic presentation of a gas-filled RFQ ion cooler and buncher; Bottom: Sketch of DC potential in axial direction.

The ion beam from the gas stopping station needs to be cooled and bunched in order to be delivered to the Penning trap for a high-precision mass measurement. Cooling a continuous beam means to lower the transverse beam emittance and reduce the axial energy spread. Beam bunching is the conversion of a continuous beam into a pulsed beam, only ion pulses can efficiently be dynamically captured in the Penning trap. A cooled ion pulse not only features little transverse emittance but occupies a

small axial phase space area, i.e., it has little time and energy spread. A gas-filled RFQ ion cooler and buncher, a device derived from a linear Paul trap, can manipulate the beam to provide cooled ion pulses. A schematic representation of this device is shown in the top portion of Fig. 5.1. A continuous beam at an energy of a few electronvolts is injected into a gas-filled segmented RFQ structure. Proper RF voltages are applied to this structure so that the motion of the ions is confined in the transverse directions. The presence of the buffer gas, at a typical pressure of a few 10^{-2} mbar, rapidly reduces the beam energy and cools the transverse motion of the ions as the ions collide with the gas particles. The bottom portion of Fig. 5.1 shows a sketch of the DC potential along the axial direction. This potential decreases continuously to provide an electric field which drags the decelerated ions through the cooler so that the ions do not stop until they reach the end of the RFQ structure where they are trapped in a potential well. The trapped ions accumulate and cool inside the trap until thermal equilibrium with the buffer gas is established. Then the exit side of the potential well is lowered rapidly, as shown in the bottom portion of Fig. 5.1, to extract the ions as a cooled and pulsed beam.

5.1 The principle of the mass filter

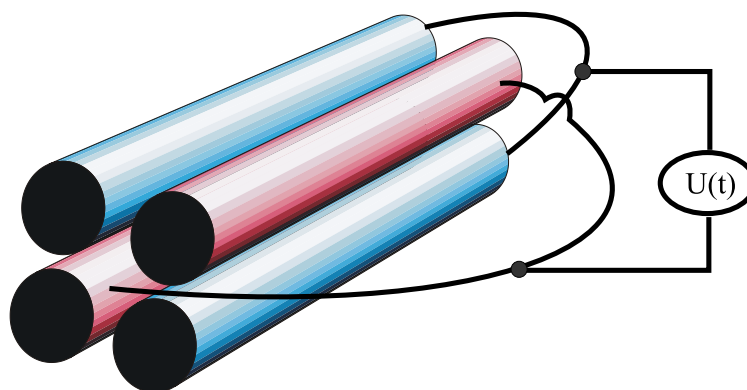


Figure 5.2: Sketch of a mass filter.

The ions in the RFQ ion cooler and buncher are confined in the transverse di-

reactions as in a conventional mass filter [53]. The radial confinement of ions can be obtained with any RF multipole electric field higher than the dipole configuration. The lowest-order multipole configuration is used in the quadrupole mass filter. A mass filter is a device consisting of four rod-shaped electrodes arranged as shown in Fig. 5.2. The RF quadrupole field is generated by applying an alternating RF voltage, $U(t)$, to the two pairs of diagonally opposite electrodes. In order to obtain a pure quadrupole field, the rods would need to have a hyperbolic shape. In practice, the rods are usually made of cylinders. In order to minimize higher-order multipole contributions, the radius of the cylindrical electrode, r_0 , and the distance from the axis to the surface of the cylindrical electrode, d_0 , have to satisfy $r_0/d_0 = 1.1468$ [54]. The RF voltage applied to the pairs of electrodes can be expressed as

$$U(t) = U_{\text{rf}} \cdot \cos(\omega_{\text{rf}} \cdot t + \phi) + U_{\text{DC}} \quad (5.1)$$

where U_{rf} , ω_{rf} and ϕ are the amplitude, frequency and phase, respectively, and U_{DC} is the DC component. The time-varying potential near the trap axis is

$$V = U(t) \frac{x^2 - y^2}{2d_0^2} \quad (5.2)$$

where d_0 is the half separation of two opposite rods. The time-averaged effective potential, the so-called pseudo potential, has a parabolic shape [55]. The equation of the ion motion in the radial direction then becomes

$$\ddot{\rho} = \frac{q}{m} \frac{\rho}{2d_0^2} \cdot U(t) \quad (5.3)$$

for an ion with mass m and charge q , where $\rho = \sqrt{x^2 + y^2}$ is the distance from the ion to the axis. This second order linear differential equation can be cast in the canonical

form of the so-called Mathieu equation [56]

$$\frac{d^2\rho}{d\xi^2} + (a_\rho - 2q_\rho \cos(2\xi))\rho = 0 \quad (5.4)$$

where ξ is a dimensionless phase parameter representing time, and the Mathieu parameters a_ρ and q_ρ are given by

$$\xi = \omega_{\text{rf}} t/2 \quad (5.5)$$

$$a_\rho = 8 \frac{qU_{\text{DC}}}{md_0^2\omega_{\text{rf}}^2} \quad (5.6)$$

$$q_\rho = 4 \frac{qU_{\text{rf}}}{md_0^2\omega_{\text{rf}}^2} \quad (5.7)$$

Due to the presence of the periodic coefficient $\cos(2\xi)$, there is no closed analytic solution to the Mathieu equation. The Floquet theorem [57] indicates that solutions of this equation are of the form

$$\rho(\xi) = Q(\xi)\Phi(\xi) \quad (5.8)$$

where $Q(\xi) = \exp(i\mu\xi)$ represents the slow motion (secular motion), and $\Phi(\xi)$ is a π -periodic function representing the micro-motion. The dimensionless quantity μ depends on the type of solution. For an unbound solution, the quantity μ is a complex number with a negative imaginary part that leads to an exponentially unstable motion. For a stable condition of $a_\rho, q_\rho \ll 1$ that results in a bound solution, the quantity q can be expressed as

$$\mu = \sqrt{a_\rho^2 + q_\rho^2/2}. \quad (5.9)$$

As can be seen from Eqn. 5.6, 5.7 both a_ρ and q_ρ depend on the mass-to-charge ratio m/q , so the linear quadrupole can be used as a mass filter when $U_{\text{DC}} \neq 0$ V. Fig. 5.3(a) shows the stability diagrams for transverse motions that lead to stable motion in x (yellow) and y (blue) directions. The superposition of these two individual

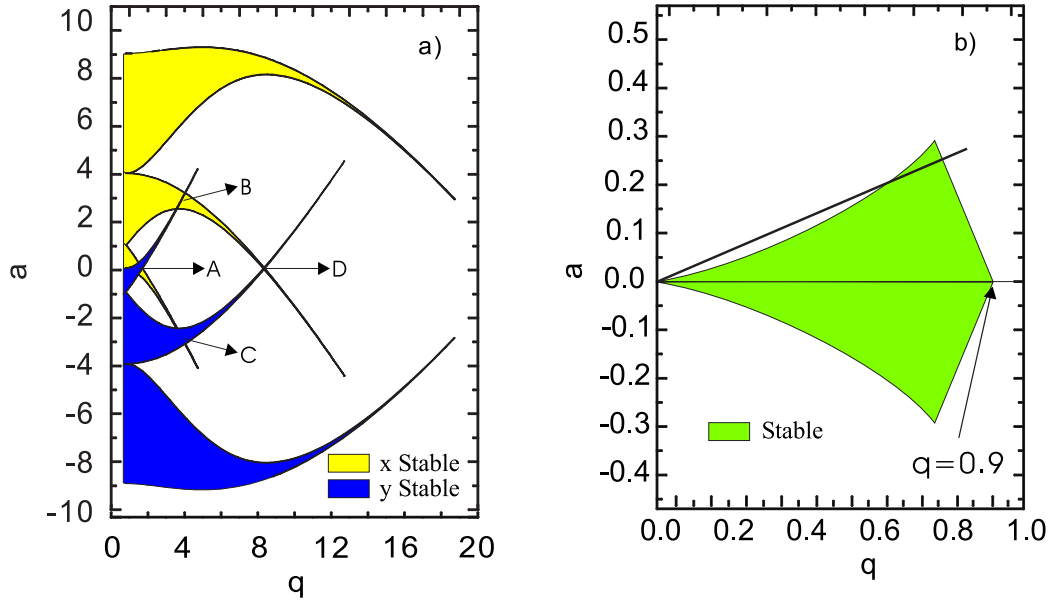


Figure 5.3: Stability diagrams for a mass filter. (a) superposition of the stable regions in both x (yellow) and y (blue) directions which are labelled as A, B, C, D; (b) expanded view of the stable region A.

stable regions leads to a set of radially stable regions which are labelled with the letters A, B, C and D, respectively. The most important stable region is that close to the origin (region A), which can be selected with small values of both U_{rf} and U_{DC} . A close-up view of this region is shown in Fig. 5.3(b). The narrow stable region near its tip can be used to mass-selectively confine ions. If U_{rf} and U_{DC} are kept at a constant ratio as illustrated in Fig. 5.3(b), then the mass filter will operate with a resolving power which is defined by the portion of the scan line that lies in the area of stability. A higher resolving power can be obtained by moving that line closer to the tip of the stable region. This technique has been used in the gas cell ion guide and buncher section of the LEBIT buncher system. The unstable region defined by $a=0$ and $q \in [0.9, 7]$ allows one to remove light contaminants from the beam. In order to provide the proper axial trapping potential, the linear Paul trap is usually made of a segmented mass filter structure, with the required DC voltages added to the RF voltages of the segments. The LEBIT cooler avoids the segmentation of the rods with a set of wedge-type cylindrical electrodes which will be discussed later.

5.2 Ion cooling with buffer gas

Ion cooling is the reduction the phase space volume occupied by an ensemble of ions. Several methods of ion cooling have been developed, such as electron cooling [58] and stochastic cooling [59] in storage rings, or laser cooling [60] in ion traps. The most widely used cooling technique for radioactive ions is buffer gas cooling in ion traps or ion guides. This method is a good choice for cooling of rare isotopes with short half-lives as it is fast and does not rely on the atomic properties of the ions.

The discussion of ion cooling in this section will focus on buffer gas cooling in a linear Paul trap. A balance is almost immediately reached between the damping force of the gas and the electric force when a low-energy ion is injected into the linear Paul trap. This can be described as

$$m \cdot \delta \cdot v_{\text{ion}} = q \cdot E \quad (5.10)$$

where v_{ion} is the resulting constant drift velocity of the ion with mass m and charge q , and E is the electric field strength. The quantity δ is the damping constant. It is related to a quantity called ion mobility K , which is defined as $K = v_{\text{ion}}/E$. The ion mobility scales with pressure p and temperature T . For this reason, the reduced ion mobility K_0 is introduced as

$$K_0 = K \frac{p}{1013 \text{ mbar}} \frac{273.16 \text{ K}}{T}. \quad (5.11)$$

Many experiments have been performed with drift chambers using a variety of combinations of ions and buffer gases to measure this quantity [61–64]. The reduced ion mobilities of Ar^+ and Kr^+ ions which are relevant for this thesis are listed in Table 5.1.

The corresponding damping time constant $1/\delta$ is expressed as

$$\delta = \frac{q}{m} \frac{1}{K_0} \frac{p}{1013 \text{ mbar}} \frac{273.16 \text{ K}}{T}. \quad (5.12)$$

Before the balance is established between the damping and electric force, the energy of the injected ions decreases exponentially as

$$E(t) = E_0 e^{-2\delta t} \quad (5.13)$$

where E_0 is the energy of the ions before cooling. Thus the time to reduce the energy by a factor of $1/e$ is

$$t_{\text{cooling}} = 1/(2\delta) = K_0 \frac{m}{2q} \frac{1013 \text{ mbar}}{p} \frac{T}{273.16 \text{ K}}. \quad (5.14)$$

As an example, the cooling time is $10 \mu\text{s}$ for the combination of Ar^+ ions with He gas at a pressure of $p=4 \times 10^{-2}$ mbar and a temperature of $T=300$ K. A good candidate of the buffer gas should have a high ionization potential to avoid charge exchange with the ions and a lower mass compared to the ions involved to avoid RF-heating [65]. Based on these two criteria, He and Ne are chosen as the cooling buffer gas for most of the ions investigated at LEBIT so far.

The position and momentum of the ions in the thermal equilibrium with the buffer gas are influenced by the effective potential and are assumed to have Gaussian distributions. Their standard deviations σ_s and σ_{v_s} are given as [66]

$$\sigma_s = \frac{1}{\beta\Omega} \sqrt{\frac{kT}{m}} \quad (5.15)$$

$$\sigma_{v_s} = \frac{2}{\Omega} \sqrt{\frac{kT}{m}} \quad (5.16)$$

where k is the Boltzmann constant, T is the gas temperature and Ω is the RF frequency. The secular parameter β can be calculated from the two Mathieu parameter a and q for $q \ll 1$ as

$$\beta = \sqrt{a + \frac{q^2}{2}}. \quad (5.17)$$

Eqn. 5.15 and 5.16 show that the beam emittance, which is proportional to $\sigma_s \cdot \sigma_{v_s}$,

Table 5.1: Reduced ion mobility K_0 for different ion and buffer gas combinations.

K_0^a , $10^{-4} \text{ m}^2/(\text{V} \cdot \text{s})$		Buffer gas			
		He	Ne	N_2	Ar
Ion	Ar^+	19.6	6.59		2.10
	Kr^+	17.3	7.69	1.96	2.17

^aValues are taken with the ratio of electric field strength to the neutral-gas number density E/N equal to $4 \times 10^{-21} \text{ V} \cdot \text{m}^2$.

depends on the temperature as

$$\varepsilon \propto T \quad (5.18)$$

which indicates the emittance can be reduced by lowering the temperature.

5.3 The LEBIT ion buncher system

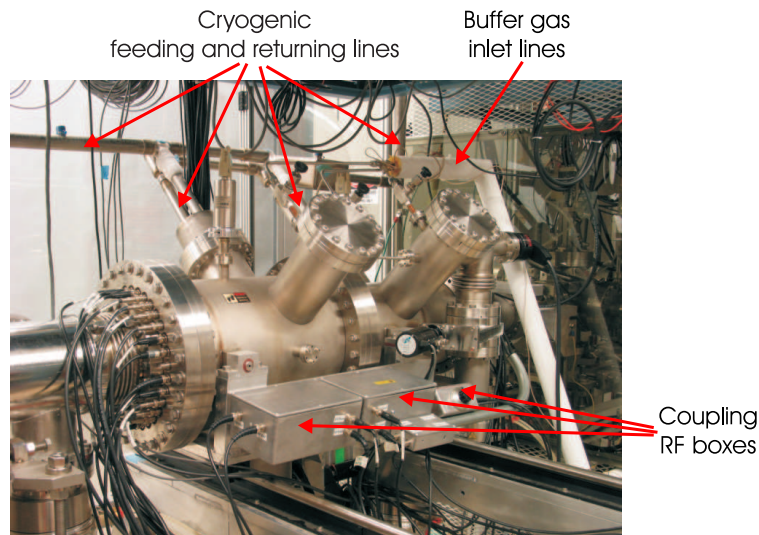


Figure 5.4: Front view of the fully assembled LEBIT ion buncher. The photograph shows the vacuum chamber that houses the electrode structure shown in Fig. 5.5. Near the top of the picture the liquid nitrogen and buffer gas supply lines can be seen.

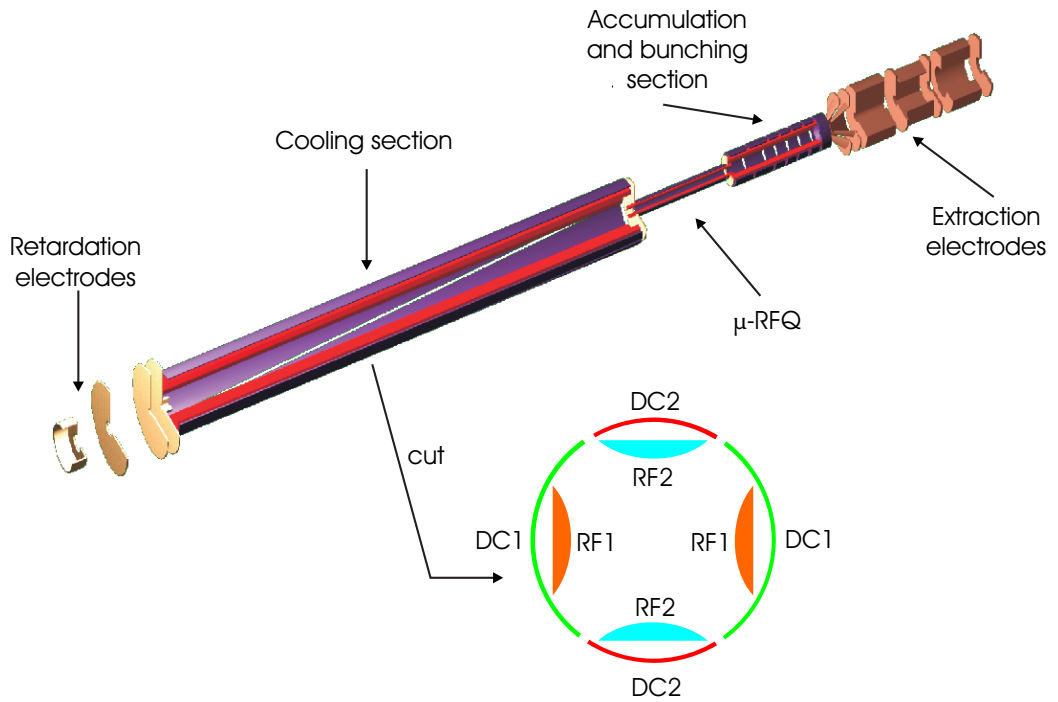
Fig. 5.4 shows a fully assembled LEBIT ion beam buncher. The vacuum chamber houses the electrode structure which can be seen in detail in Fig. 5.5. The voltages are supplied to the electrodes with the set of feed-throughs located at the two ends of the chamber. Two pairs of thermocouples are installed: One pair measures the tempera-

ture at two locations of the cooler section; the other pair is installed in the buncher section. Above the chamber the feeding and returning lines for liquid nitrogen can be seen which is used to cool the electrode structure to cryogenic temperature. A total of three buffer gas lines connect to the cooler and buncher sections to introduce buffer gas. In front of the vacuum chamber there are three aluminum boxes which contain the resonance circuits to supply RF voltages to the RFQ electrodes. The discussion of the ion buncher system will focus on four subsystems: the electrode configuration, the vacuum and gas inlet system, the electronic system for RF generation and the cryogenic cooling system.

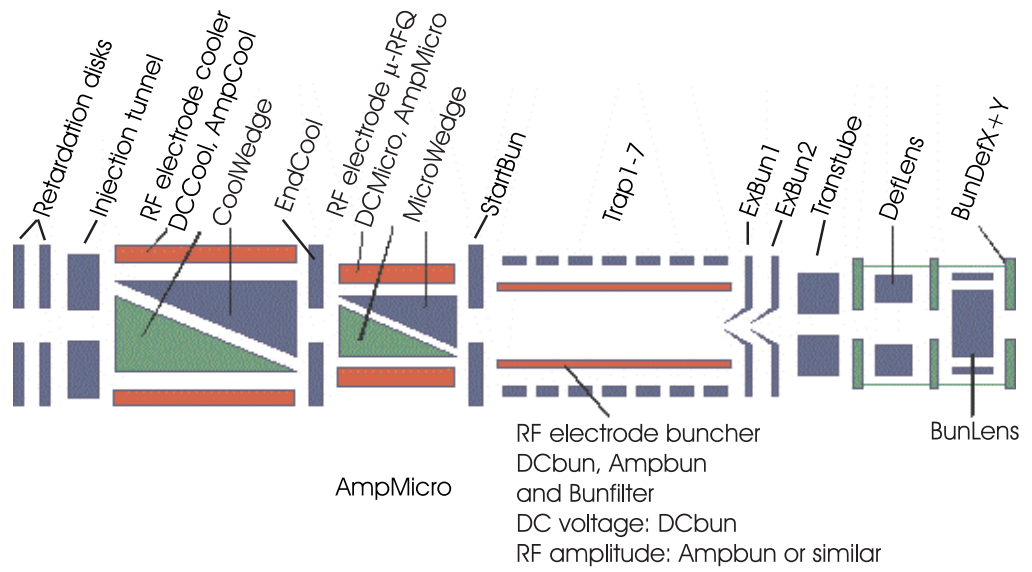
5.3.1 Electrode configuration

The configuration of the LEBIT ion buncher system is different from that of the conventional gas-filled RFQ trap sketched in Fig. 5.1. It consists of three RFQ sections: the ion cooler, a down-scaled version of the ion cooler (μ -RFQ) and the ion buncher. In operation, each section is filled with buffer gas at a different pressure. The typical pressure in the ion cooler, 4×10^{-2} mbar, is considerably higher than that in the ion buncher, which is typically at 8×10^{-4} mbar. The advantage of operating the buncher at low pressure is to avoid reheating of the ions during the ejection to the high vacuum environment. The conductance of the μ -RFQ is sufficiently small to provide enough differential pumping. When the buffer gas is present, the radial oscillation amplitude of the ions inside the cooler and buncher decreases very fast. This leads to a larger diameter of the cooler section than that of the buncher section.

Fig. 5.5(a) shows the schematic layout of the electrode configuration for this system. The leftmost components are a set of retardation electrodes for beam deceleration. The beam cooling section uses four wedge-type cylindrical electrodes encompassing four rods that create the RFQ trapping field. The cut view of this configuration is shown in the inserted figure. The two pairs of the wedge-shaped electrodes are marked DC1 and DC2, the two inner pairs of RF electrodes are labelled RF1 and



(a)



(b)

Figure 5.5: Electrode configuration of the LEBIT ion buncher system. (a) layout with a transverse cut through the cooler section; (b) schematic axial cut indicating electrodes with their nicknames as used in the control system.

RF2. The DC field penetration varies along the axis of this structure, and provides a linear drift potential with only two DC voltages. The pairs of RF electrodes create the RFQ electric field with two out-of-phase RF voltages. The μ -RFQ connects the cooler and buncher sections. The ion accumulation and bunching section is made of seven ring electrodes and four RFQ rods inside them. Both the cooler section and the trap section have been built with the option to operate at liquid-nitrogen temperature. Besides an increase of the acceptance of the system and a decrease in the time to establish thermal equilibrium, this will significantly reduce the emittance of the resulting pulses compared to an operation at room temperature. The last section is a set of extraction electrodes for reaccelerating the extracted ion pulses. Fig. 5.5(b) shows a schematic cut-view of all electrodes. The electrodes are labelled with their nicknames according to their functions as used in the control system. The RF electrodes are also marked with a three-word description for a better understanding.

When a continuous ion beam with an energy of 5 keV is injected into this system, it is first decelerated to an energy of a few electronvolts after the retardation electrodes. Most of the remaining energy is then quickly dissipated as the beam enters the cooler section and interacts with the buffer gas. The DC-drift field then drags the slowed ions to the bunching section through the μ -RFQ. The seven ring electrodes in the bunching section can be either operated to allow continuous transmission, or accumulate and trap the ion beam. For ion bunching, a series of voltages are applied to the trap electrodes to generate a trapping potential for ion confinement in the axial direction. The exit side of that potential is switched to a lower level quickly after the ions have thermalized at the trap center. The extracted pulsed beam is then accelerated with the extraction electrodes to about 2 keV and delivered to the Penning trap.

5.3.2 Vacuum and gas inlet system

The cooler section of the ion buncher is operated at a typical pressure of 4×10^{-2} mbar for fast cooling of ions. As mentioned previously, the pressure in the buncher section

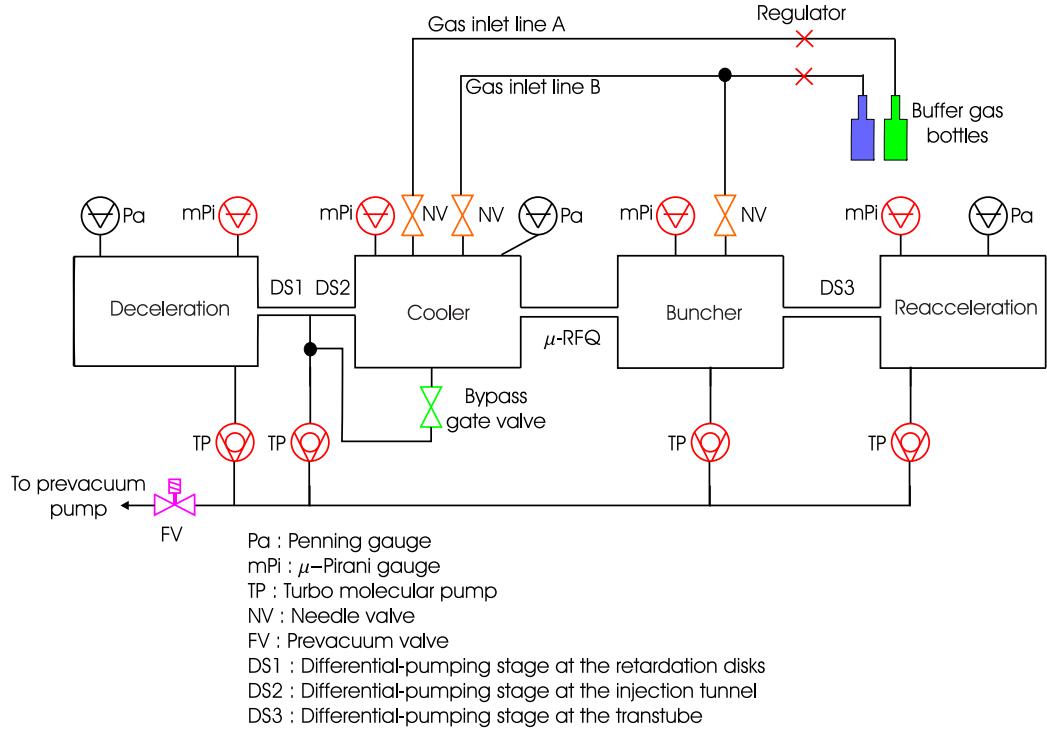


Figure 5.6: Vacuum and gas inlet system of the LEBIT ion buncher.

is kept at around 8×10^{-4} mbar to avoid collisions of ions with gas molecules during extraction. The μ -RFQ section connects the two sections and acts as a differential-pumping barrier. The deceleration and reacceleration regions before and after this system are operated in high vacuum. The transition from the high-vacuum sections to the rather high pressure in the cooler and buncher sections is obtained with three electrodes acting as differential-pumping stages. The electrodes are “Injection tunnel” and “Retardation disks” for the deceleration, and “Transtube” for the reacceleration, as shown in Fig. 5.5(b).

A schematic of the complete vacuum and gas inlet system is shown in Fig. 5.6. It consists of four vacuum sections separated by the differential pumping stages, which have typical pumping speeds ranging from 1.7 l/s to 5 l/s. A total of three Penning gauges are used to monitor the deceleration, cooler and reacceleration sections. When the ion buncher system is not operated with a buffer gas, the pressure in the UHV vacuum chamber is around 1×10^{-9} mbar. Each of the four sections has a μ -Pirani gauge attached. This gauge is based on a MKS Micro-Electro-Mechanical Systems

(MEMS) sensor with an extended pressure measurement range down to 10^{-5} mbar, two decades beyond a standard Pirani gauge. Each section is pumped with a dedicated turbo molecular pump¹. All turbo pumps connect to a dry scroll-pump through a common prevacuum valve. There is an additional bypass gate valve between the cooler section and its turbo pump. That valve is closed when the cooler is operated with buffer gas. In this gas, the buffer gas in the cooler section can only exit through the μ -RFQ and the “InjTunnel” electrode and a pressure of up to 10^{-1} mbar can be obtained without overloading buffer gas. The bypass gate valve is opened when the cooler is not operated with buffer gas. In this case the large pumping speed provided by the bypass allows for efficient pumping when the system is baked.

Buffer gas is introduced in the vacuum system through a set of needle valves. Two needle valves are used to fill either He, Ne or a mixture of them into the cooler section. One needle valve is used to fill He gas into the buncher section.

5.3.3 Electronic system for RF generation

Fig. 5.7 shows a diagram of the electronics circuit used to supply RF voltages to the RF electrodes in the ion cooler and ion buncher sections. Two passive components are used: (1) an impedance matching circuit consisting a transformer; (2) a resonance circuit formed by two inductors and the capacitance listed in Table 5.2 provided by the pairs of RF rods. The input RF voltage U_{RFi} is provided from an RF amplifier with 50Ω impedance. When the resonance frequency is hit the impedance between two checkpoints A and B is zero. The secondary coil of the transformer is split at the center, with the center taps connected to two DC voltages, U_{DC1} and U_{DC2} , respectively. The output voltages are $U_{RFo1} = A \cdot U_{RFi} + U_{DC1}$ and $U_{RFo2} = -A \cdot U_{RFi} + U_{DC2}$, where A is the amplification factor listed in Table 5.2. This circuit has been used to study the possibility of using the buncher section as a mass filter. A simpler version of this

¹TW300 and TW300H series from LEYBOLD. Pumping speeds for He are 230 l/s and 240 l/s respectively

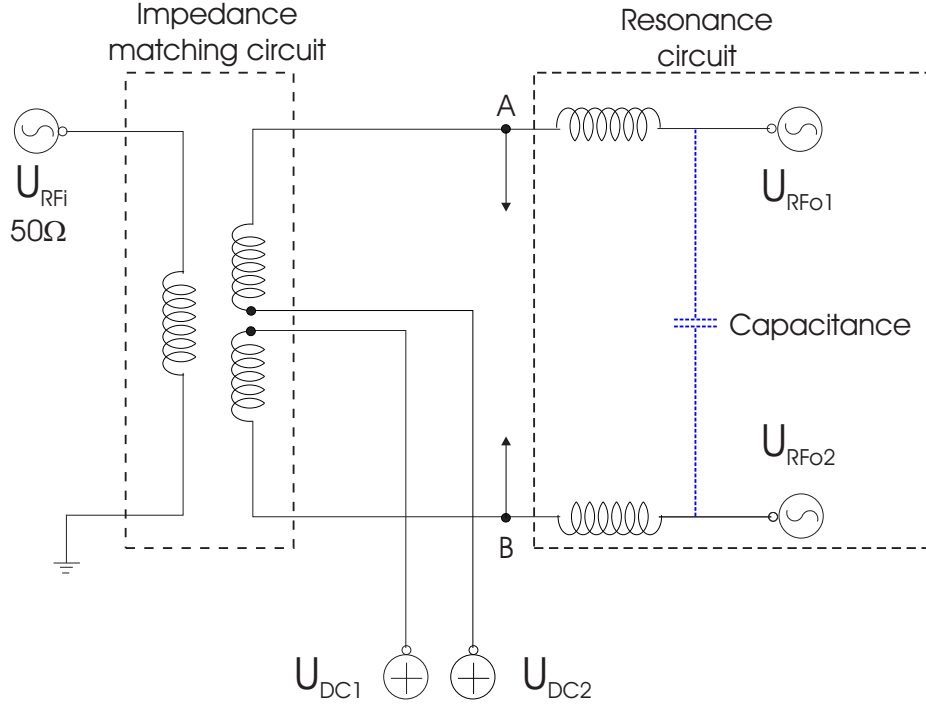


Figure 5.7: Sketch of the electronic circuit used to supply the RF voltage to the RFQ electrodes for the ion buncher system.

circuit is used to operate both the ion cooler and ion buncher sections in non-mass-filtering mode. In this case the center taps of two split coils are connected to each other. The common center tap connects to one DC input U_{DC} . The corresponding outputs then are $U_{RFo1} = A \cdot U_{RFi} + U_{DC}$ and $U_{RFo2} = -A \cdot U_{RFi} + U_{DC}$. The RF is supplied to the μ -RFQ without a resonance circuit, resulting to an amplification of $A=1$ (See Table 5.2). The circuits for all the three RF sections are operated at a frequency of 1.15 MHz. Each circuit is built differently, resulting in different phase shifts from from input to output. The RF generator provides the RF voltages of the μ -RFQ and the buncher with tunable RF phases to compensate for the shifts in the coupling circuits. The typical RF amplitudes (V_{pp}) for a mass of $A=39$ are about 800 V for the cooler, 50 V for μ -RFQ and 220 V for the buncher.

Table 5.2: Operating parameters for the RF generating circuit.

Section	Capacitance, μF	Power, W	Amplification, A
Cooler	19.2	31	10
μ -RFQ	45	30	1
Buncher	10.7	50	4

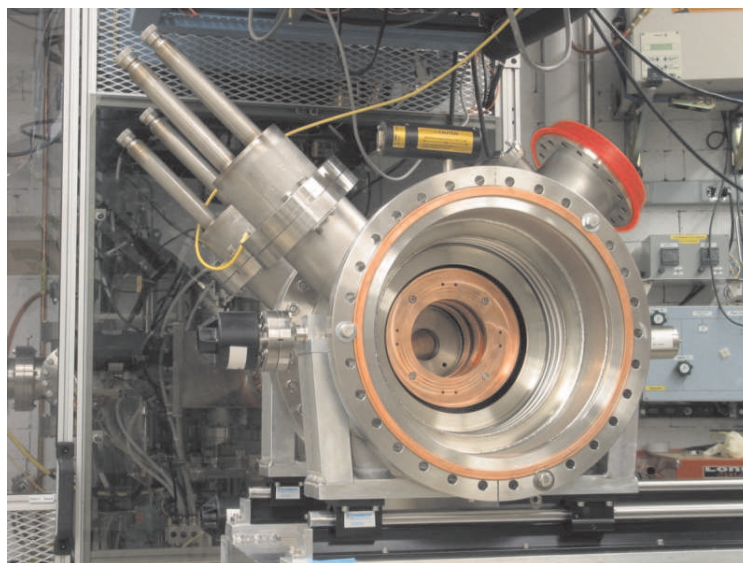


Figure 5.8: Photograph of the opened buncher vacuum with the electrode structure removed. The copper insert is the cooling baffle used to cryogenically cool the buncher section.

5.3.4 Cryogenic cooling system

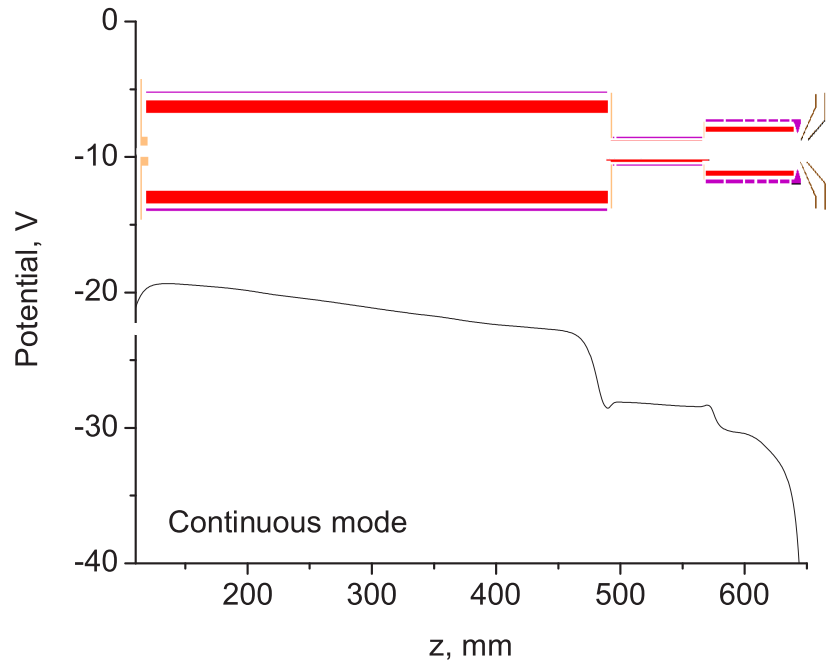
A cryogenic cooling system has been built to cool the ion buncher system with liquid nitrogen. Fig. 5.8 shows the cooling baffle installed in the vacuum chamber while the electrode structure of the buncher section is removed. The cooling baffle consists of several copper rings designed to provide efficient pumping of the buncher section while minimizing heating by radiation. The rings are thermally connected to the cryogenic feed-throughs for the liquid nitrogen. The extraction electrodes of the buncher section have “finger” contact with these plates. Two pairs of thermocouples are connected to selected points of the cooler and buncher electrode system. If the electrode structure had no thermal contact to the outside, one would be able to cool the system down to liquid nitrogen temperature. The lowest temperature measured in the cooler section so far is $T = -120$ °C. The lowest temperature obtained in the buncher section is $T = -30$ °C, most likely due to insufficient cooling of some electrodes near the extraction section.

5.4 Modes of operation

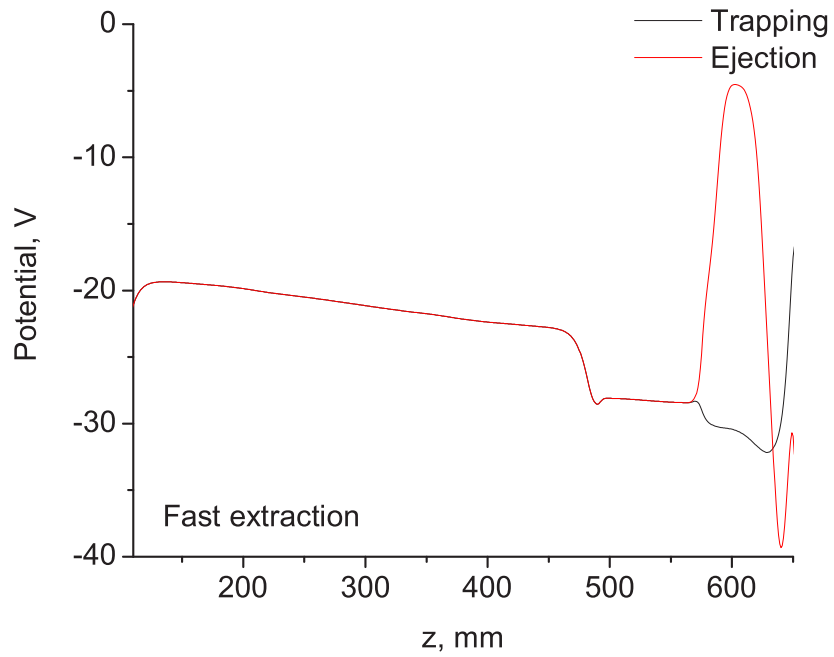
The LEBIT ion buncher system can be operated in either continuous or pulsed mode. In continuous mode, the injected beam leaves the system as a cooled continuous beam. In pulsed mode, the continuous beam is converted into cooled ion bunches.

5.4.1 Continuous mode

In this mode all three sections of the system work as a continuous beam cooler. The DC potential decreases along the axis of the system, as shown in Fig. 5.9(a). There are two steps along the axis, marking the entrance and exit of the μ -RFQ. This mode can be used to study the beam transmission through the ion cooler and buncher if a continuous beam is injected into the system. When that chopped beam is injected into the ion buncher operated in continuous mode, one can study the diffusion and



(a)



(b)

Figure 5.9: DC potential on the axis of the ion buncher operated in (a) continuous and (b) pulsed mode. A layout of the ion buncher is drawn on the top as the reference of the potential lines.

the time-of-flight of ions in the ion cooler under different operating conditions.

5.4.2 Pulsed mode

In this mode, two different sets of voltages are applied to the buncher section to first accumulate and cool ions and later release them as an ion bunch. The voltage on the axis are illustrated in Fig. 5.9(b). Slow ions exiting the ion cooler accumulate in the potential well of the trap and cool to the potential minimum. Then they are rapidly released as ion pulses by lowering the potential hill at the exit side. To change between accumulation and ejection, two sets of voltages are applied to the “Trap1-7” and “ExBun1” electrodes shown in Fig. 5.5(b). Two extraction scenarios have been developed:

Fast extraction

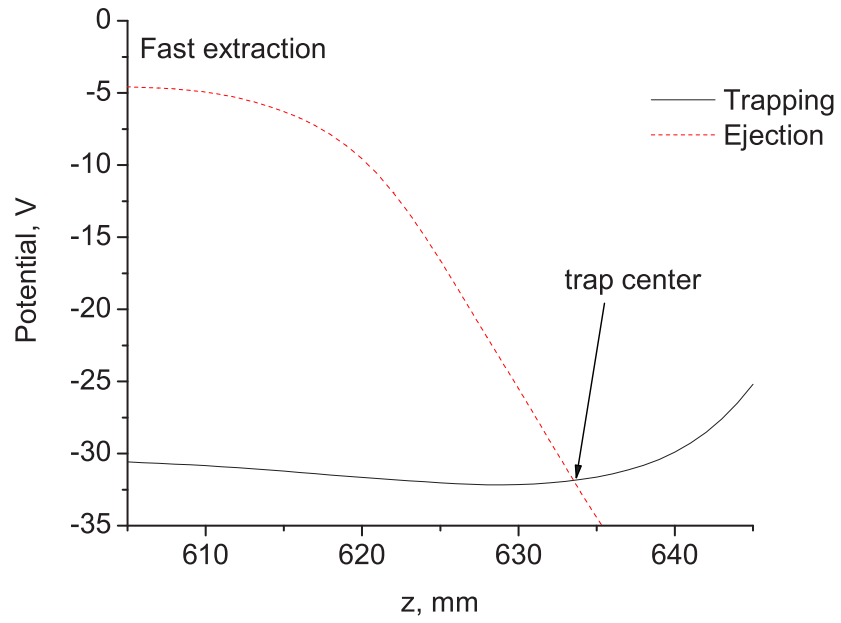
The ejection potential in this scenario has a steep slope as shown in Fig. 5.10(a). When the ejected pulse is recorded at the MCP detector downstream the buncher, it arrives early and features a narrow time-of-flight distribution. This scenario provides a mass resolving power which is typically around 50.

Slow extraction

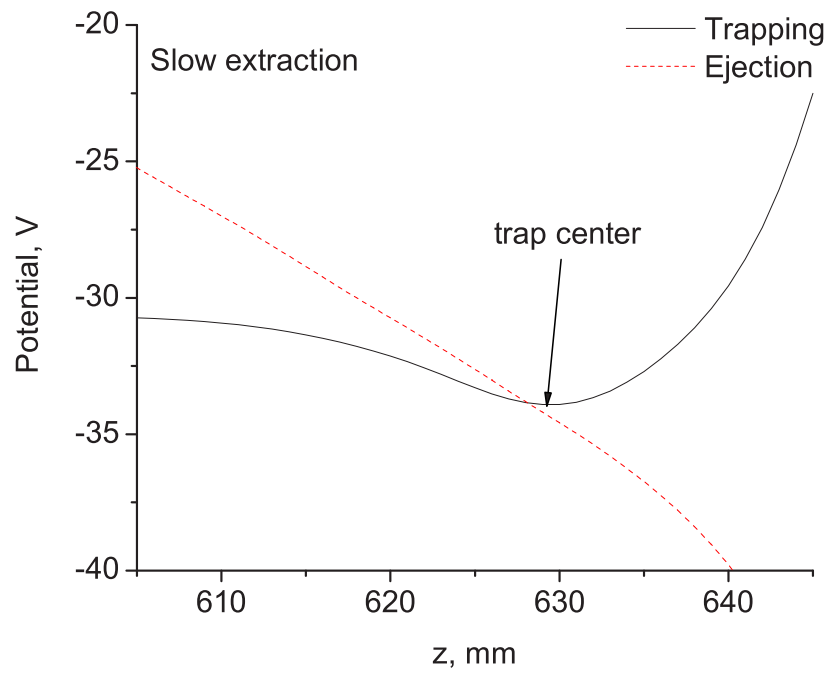
In this scenario the ejection potential has a shallow slope, which can be seen in Fig. 5.10(b). The ejected pulse arrives late at the detector and shows a wide time-of-flight distribution. This scenario has turned out to be the best one to properly inject ions into the Penning trap and is used for precision mass measurements.

5.4.3 Summary

Typical voltages used for the two buncher operation modes are listed in Table 5.3 and 5.4. The first table lists the common voltages for the cooler and μ -RFQ sections.



(a)



(b)

Figure 5.10: DC potential on the axis of the buncher section for the buncher operated in (a) fast extraction and (b) slow extraction scenario. A typical beam trajectory in the ion buncher is drawn on the top as the reference of the potential lines.

Table 5.3: Voltages applied to the electrodes in the cooler and μ -RFQ sections.

Name	RetDisk1	RetDisk2	InjTunnel	DCCool	CoolWedge1
Voltage, V	-760	-320	-50	-22.5	0
Name	CoolWedge2	EndCool	DCMicro	MicWedge1	MicWedge2
Voltage, V	-25	-35	-28.25	-26.7	-30
Name	StartBun	DCBun			
Voltage, V	-27.5	-30.9			

Table 5.4: Voltages applied to the electrodes in the buncher section for different operation modes. (Unit is V)

Electrode name	Continuous mode	Fast extraction scenario		Slow extraction scenario	
	Voltage	Trapping	Ejection	Trapping	Ejection
Trap1	-27	-27	30	-29	30
Trap2	-28	-28	110	-29.5	10
Trap3	-30	-30	110	-30	-10
Trap4	-35	-35	100	-35	-30
Trap5	-40	-40	0	-55	-50
Trap6	-50	-35	-120	-35	-70
Trap7	-60	-10	-15	0	-90
ExBun1	-70	-8	-35	0	0

The second table lists the voltages applied to the buncher section for the different extraction scenarios. The three sets of RF electrodes in the three sections require different RF amplitudes to obtain the same RF electric field due to their different dimensions. RF settings for two selected masses are listed in Table 5.5. These values result from amplitude scans that yielded optimum transmission.

Table 5.5: Optimum RF amplitudes for the three ion buncher sections. ($f=1.15$ MHz)

Mass	Cooler, V	μ -RFQ, V	Buncher, V
A \sim 39	708	54.4	224
A \sim 85	1060	114	272

5.5 Experimental systematic studies of the ion buncher

A series of measurements has been performed to systematically study the ion buncher system and assess its performance. Results of these measurements will be compared with corresponding simulations to check the predictions. The ion buncher system can be operated in two different modes as explained in section 5.4. For the continuous mode, ion transmission and cooling time have been studied for different buffer gas types, pressure and temperature. The time-of-flight of ions from the buncher exit to the detector have been measured, which is used to determine the temperature of the buffer gas in the cooler section achieved by cryogenic cooling. For the pulsed mode, ion transmission and output pulse shape have been measured for different buffer gas types, pressure, temperature and cooling time. Beam profiles have been measured at two different temperatures, and the beam emittance has been extracted from the results.

A test ion source has been used to generate stable ion beams for all the measurements discussed in this chapter. These ions ARE either noble gas ions such as Ar^+ and Kr^+ , or alkali ions such as K^+ and Rb^+ . An electrostatic deflector installed directly downstream the test ion source is used as a beam gate, to chop the continuous beam into a short pulse. A Faraday cup housed in BOB3 (See Fig. 3.3) between the beam gate and the ion buncher is used to measure the beam intensity. The opening time of the beam gate multiplied by the beam current determines the number of incoming ions. Together with beam current measured at another Faraday cup located at BOB4, BOB5 or BOB6 (See Fig. 3.3), the transmission efficiency at different locations can be obtained. An MCP detector housed in BOB5 (See Fig. 3.3) is used to measure the time of flight of ions travelling from the buncher exit to the detector. A phosphor screen attached to this MCP5 is used in conjunction with a CCD camera to record beam profiles. Data acquired from these detectors are then analyzed and compared to the results of the simulation.

5.5.1 Buncher operated in continuous mode

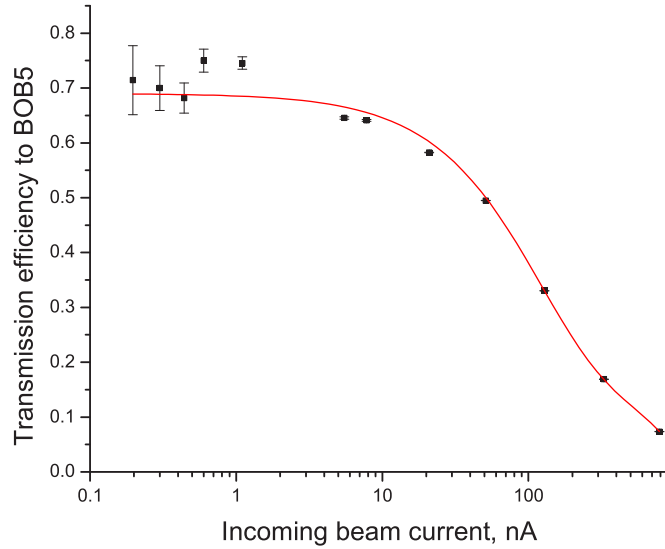


Figure 5.11: Transmission efficiency for a continuous beam as a function of incoming beam current. The solid curve is drawn to guide the eye.

The ion buncher operated in continuous mode acts as a beam cooler. This mode allows one to easily check the transmission efficiency of the cooler. The beam current is recorded at two Faraday cups located at BOB3 and BOB5. The transmission efficiency in this case is defined as the ratio of the beam current measured at BOB5 to that at BOB3. Fig. 5.11 shows the transmission efficiency measured as a function of the incoming beam current. The efficiency stays at about 70% until the current exceeds about 10 nA. Beyond that current the efficiency decreases and drops to about 10% at a current of 500 nA. That is in agreement to the simulation result using the particle in-cell calculation, which takes into account the space-charge effect in the μ -RFQ.

The continuous beam offers an insight to the beam transmission through the gas-filled ion cooler. However, a chopped beam as discussed before, is injected into the cooler and buncher operated in continuous mode to study the time-of-flight of ions and diffusion of ions due to the collisions with the buffer gas particles. The transmitted ion pulse features a larger time spread due to diffusion. Its time-of-flight from the

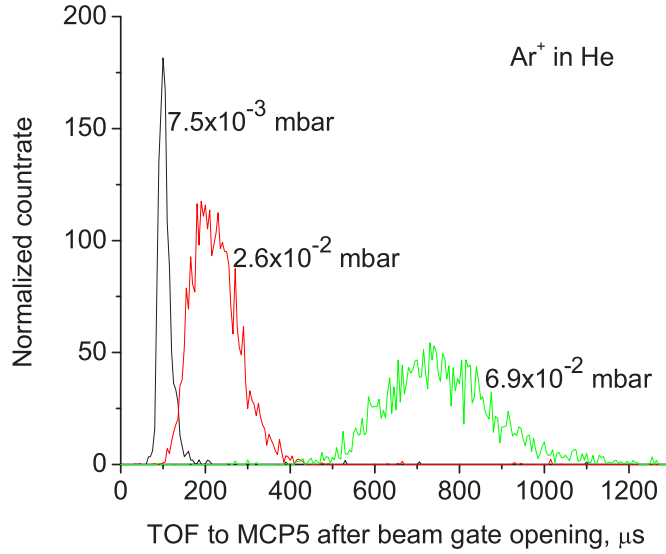


Figure 5.12: Time-of-flight distributions of ion pulses sent through the He filled ion buncher when operated in continuous mode for three values of pressure in the ion cooler.

beam gate to the MCP5 detector is recorded with the scope connected to the MCP5, which is triggered when the beam gate is opened. Fig. 5.12 shows three time-of-flight distributions of $^{40}\text{Ar}^+$ ion pulses sent through the cooler filled with Helium at three different pressures. The initial pulse width before entering the cooler is $3\ \mu\text{s}$ for all the investigated scenarios. The three curves have been normalized to the incoming beam current. As the distributions have approximately Gaussian shape, Gaussian functions have been fitted to the data to assess the pulse width and center. At a low pressure of 7.5×10^{-3} mbar, the pulse is centered at $100\ \mu\text{s}$ with a width of $30\ \mu\text{s}$. When the pressure is increased to 2.6×10^{-2} mbar, the pulse center shifts to $210\ \mu\text{s}$ and its width increases to $130\ \mu\text{s}$. At an even higher pressure of 6.9×10^{-2} mbar, the pulse center moves to $730\ \mu\text{s}$, and the pulse width doubles to $270\ \mu\text{s}$ compared to the 2.6×10^{-2} mbar case. Another observable quantity is the number of detected ions, which also increases with the increasing pressure. More measurements, which will be discussed later, have been performed with the system operated with different buffer gas types, pressures and temperatures.

Dependence of time-of-flight spectra on buffer gas type, pressure and temperature

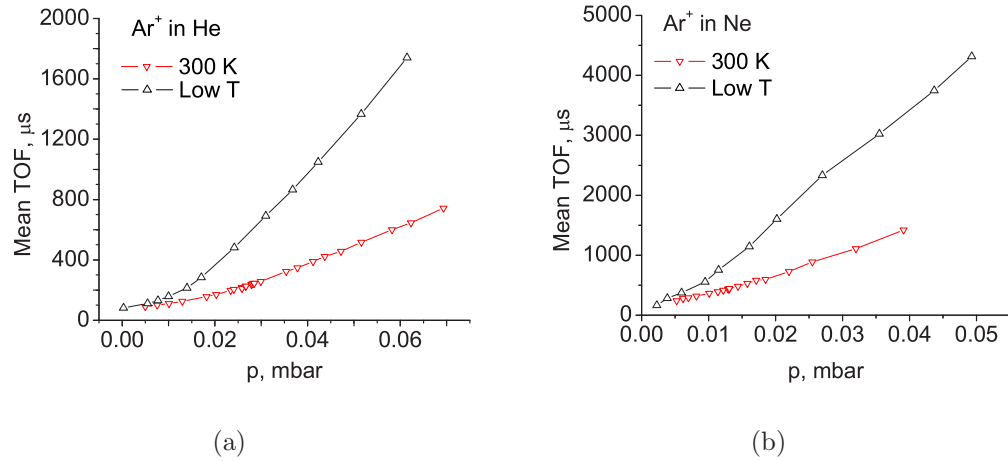


Figure 5.13: Time of flight of $^{40}\text{Ar}^+$ ion pulses from a beam gate at the ion source through the ion buncher system to MCP5 as a function of the buffer gas pressure when the ion buncher is operated in continuous mode. Buffer gas: (a) He; (b) Ne. Red curves: ion buncher operated at room temperature. Black curves: ion buncher cooled with liquid nitrogen.

The time-of-flight distributions of beam pulses sent through the ion buncher operated in continuous mode have been measured with a chopped $^{40}\text{Ar}^+$ beam from the test ion source. The time of flight of the beam from the beam gate to MCP5 has been measured, and the pulse width and height have been obtained as explained above. These two quantities have been studied to analyze their dependence on the operating parameters, including the buffer gas type, the buffer gas pressure and the temperature of the ion buncher. Helium and neon have been used as buffer gases in the cooler section at different pressures. Measurements have been performed with the ion buncher at room temperature ($T=300$ K) and a low temperature (via liquid nitrogen cooling). The lowest temperature in the cooling section obtained so far is around $T=200$ K due to technical reasons. The mean time of flight as a function of the buffer gas pressure is shown in Fig. 5.13(a) and (b), for the buffer gases He and Ne respectively. The mean time of flight almost linearly grows with the pressure in

both cases, except towards the low pressure where the slope is smaller. Another trend observed with both gas types is the larger mean time-of-flight at low temperature compared to room temperature. These measurements allow one to extract the ion mobility. With the assumption of a constant drift ion velocity v , the ion mobility can be expressed as

$$K=v/E \tag{5.19}$$

where E is the electric field that drags ions through the cooler section. The electric field can be obtained from the electrode configuration and the applied voltages. The drift velocity is simply given by the length of the cooler section divided by the mean time-of-flight of ions through this section. This time is calculated as the difference of the total measured time of flight minus the time of flight from the test ion source to the entrance of the cooler and the time of flight from the μ -RFQ to the detector. Outside the cooler section the effect of the residual buffer gas is neglected and the time-of-flight calculated from the mass and electric field. The ion mobility depends on the gas density which is proportional to the ratio of the pressure, p , and the temperature, T . This dependence is divided out to arrive at the reduced ion mobility K_0 as defined in Eqn. 5.11. A pressure correction has to be taken into account for the measurements at low temperature. The gas pressure is measured at a location where the gas is at room temperature. The true gas density inside the cooler thus needs to be scaled by a factor of $(300 \text{ K})/T$. It is useful to define an effective pressure p_{eff} as

$$p_{\text{eff}} = p_{\text{meas}} \frac{300 \text{ K}}{T} \tag{5.20}$$

with p_{meas} being the pressure reading from the vacuum gauge. In order to extract temperature from the experiment results of the time-of-flight, a new relation between ion mobility and the measured pressure is given based on Egn. 5.19, 5.11, 5.20 as

$$K_0/K = K_0 \frac{E}{v} \frac{p_{\text{meas}}}{1013 \text{ mbar}} \frac{273.16 \text{ K} \times 300 \text{ K}}{T^2} \tag{5.21}$$

The voltage difference between the two wedge-shaped electrodes in the cooler section that define the drag field (CoolWedge, see Fig. 5.5(b)) is 25 V in these measurements. An evaluation of the electric field of the cooler section with the Laplace-solve SIMION determines the axial field compound to $E=11.67$ V/m. Thus the ion velocity inside this section is calculated to be $v=474$ mm/(mean time-of-flight- $59.7 \mu\text{s}$). Fig. 5.13 can now be replotted as K_0/K with the K_0 values adopted from Table 5.1 as a function of the measured pressures of He and Ne, respectively. The temperature for cryogenic operation can then be extracted with Eqn. 5.21. The resulting curves are shown in Fig. 5.14. For cooling with He, one obtains two almost straight lines for the two different temperatures. Neither of the two lines exactly extrapolates to the origin, as suggested by Eqn. 5.21. This can be attributed to an offset in the pressure reading of the vacuum gauge (about 10^{-4} mbar). Two straight lines have been fitted to the data. The ratio of the slopes of the two fitted lines determines the temperature of the buffer gas in the case of cryogenic operation to be $T=181$ K. The same procedure has been applied in the case of Ne cooling, for which a temperature of $T=180.9$ K is obtained. These two numbers are in a good agreement with the thermocouple readings for the cooler section ($T=-100$ °C). An average temperature of $T=181$ K has been adopted for the analysis of the following measurements.

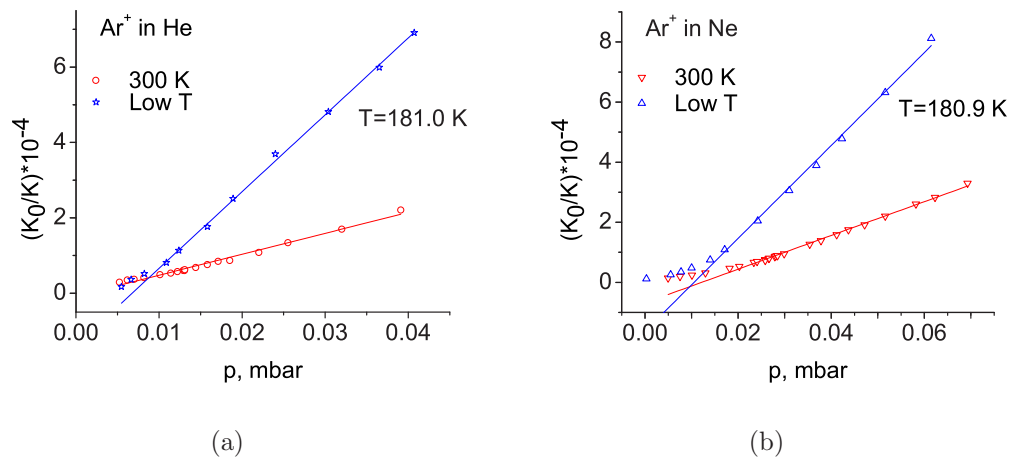


Figure 5.14: K_0/K as a function of the buffer gas pressure. (a) $^{40}\text{Ar}^+$ ions in He; (b) $^{40}\text{Ar}^+$ ions in Ne.

In order to normalize calibrated pressure readings for the different buffer-gas/temperature combinations, a modified effective pressure can be used. In this case a normalization term, $K_0(\text{He})/K_0$, is added to the previous definition as

$$P_{\text{effmod}} = P_{\text{meas}} \frac{300 \text{ K } K_0(\text{He})}{T K_0} \quad (5.22)$$

where $K_0(\text{He})$ and K_0 are ion mobilities for He and the gas used in the measurement, respectively.

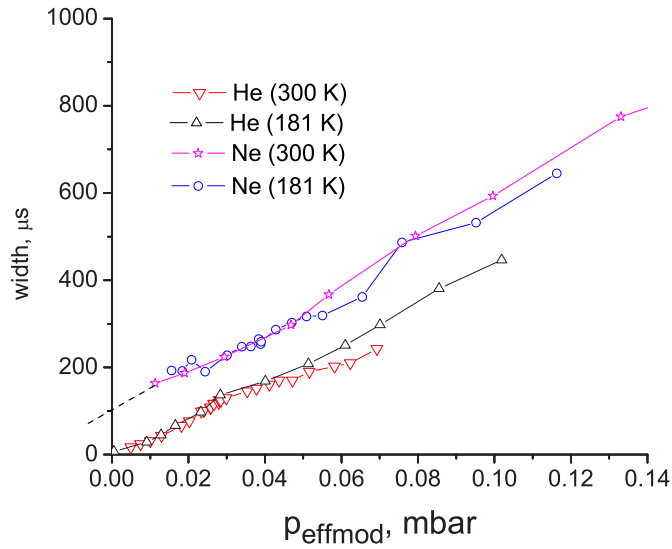


Figure 5.15: The width of time-of-flight distribution as a function of the modified effective pressure.

Fig. 5.15 shows the width of the time-of-flight distributions as a function of the modified effective pressure for the cooling of $^{40}\text{Ar}^+$ ions with He and Ne at two different temperatures. All four lines run almost parallel to each other. The data for cooling in He extrapolates to a near-zero pulse width, which is equal to the initial pulse width (beam gate opening time) of $t=3 \mu\text{s}$ and corresponds to a special scenario where no buffer gas is present in the cooler. A similar extrapolation is also observed in the data for Ne cooling, which corresponds to an initial pulse width of $t=100 \mu\text{s}$.

Dependence of transmission on the buffer gas type, pressure and temperature

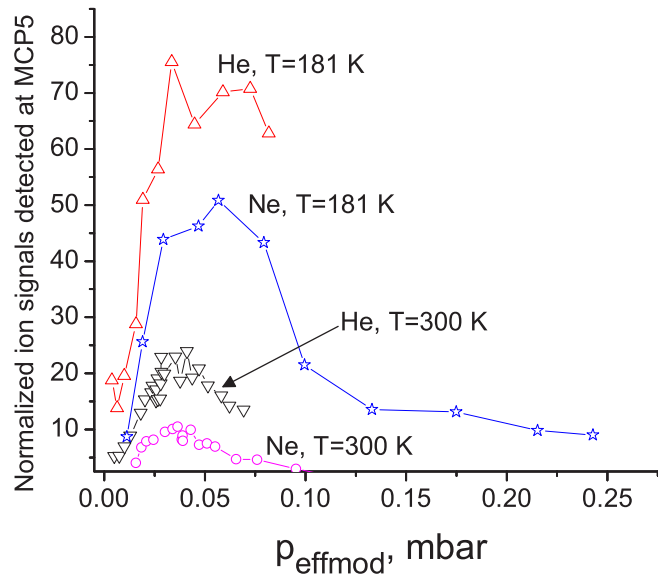


Figure 5.16: Normalized transmission of ion pulses sent through the cooler as a function of modified effective pressure when the ion buncher is operated in continuous mode.

In the measurement discussed above it was observed that the number of transmitted ions varied with the different operational conditions. Fig. 5.16 shows the normalized countrate at MCP5 as a function of the modified effective pressure. The four curves are the results for the four combinations of buffer-gas/cooler temperature. The maximum transmission for He cooling is about four times higher than that for Ne cooling. In both cases the transmission is higher at lower temperature. The transmission losses are due to the collisions between the ions and the buffer gas particles, in which case Ne and higher temperatures contribute more strongly. The modified effective pressure values at which the transmission reaches its maximum for a given temperature are the same for both He and Ne. This is not surprising since p_{effmod} is already scaled with the ion mobility. The pressure values for maximum transmission do not agree for different temperatures. This defies expectations because the modified

effective pressure is already normalized by the temperature effect.

5.5.2 Buncher operated in pulsed mode

The following measurements have been carried out to study the performance of the ion buncher when it is operated in pulsed mode: (1) dependence of ion transmission on the buffer gas type, pressure and temperature; (2) dependence of the ion transmission on the cooling time; (3) dependence of the time-of-flight distribution of ions from the buncher exit to the detector on the cooling time and (4) beam energy acceptance. The measurements use an ion beam from the test ion source. The “beam gate”, a voltage-pulsed deflector after the ion source, is used to produce an ion pulse containing a number of ions, defined by the ion current and the time the beam gate is opened (t_{beamgate}). This beam pulse is then delivered to the ion buncher, where it is cooled, accumulated and ejected as an ion pulse. The time of flight of the ejected ion pulse is recorded with a digital oscilloscope, connected to MCP5 which is installed downstream the buncher. The cooling time t_{cool} is counted from the time the beam gate is opened to the ejection of the pulse out of the buncher, where $t_{\text{beamgate}} \ll t_{\text{cool}}$. This cooling time is almost equal to the time period the ions spend in the buncher section, since their travelling time in the cooler section is very short (a few tens of μs). The ion transmission in pulsed mode is important as it determines how efficiently the beam can be delivered to the Penning trap mass spectrometer.

Fig. 5.17 shows typical time-of-flight distributions of $^{39}\text{K}^+$ pulses ejected out of the ion buncher. The distributions were obtained with the ion buncher operated at $T=200$ K both in fast and slow extraction scenarios, and $T=200$ K in fast extraction scenario (See section 5.4.2 for details on these extraction scenarios). A comparison between the two cases with the same (fast) extraction scenario shows a narrower width at low temperature ($\text{FWHM}(200\text{ K})=0.6\ \mu\text{s}$ and $\text{FWHM}(300\text{ K})=0.8\ \mu\text{s}$). That agrees to the dependence of axial distribution of ions on the temperature, i.e., $\sigma \propto \sqrt{kT/m}$ which is similar to those in the transverse directions represented in Eqn. 5.15 and

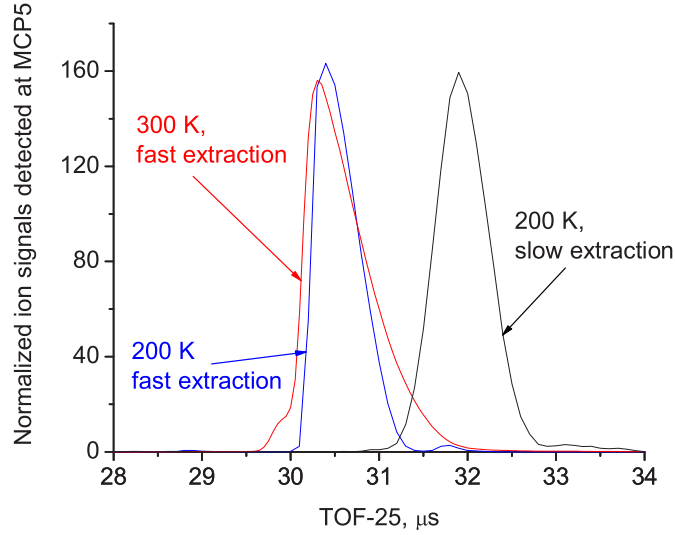


Figure 5.17: Time-of-flight distributions of extracted $^{39}\text{K}^+$ ion pulses recorded under different operating conditions (See text).

5.16. A comparison between the two extraction scenarios with the same temperature shows a $1.5 \mu\text{s}$ delay on the mean time-of-flight of the slow extraction scenario to that of the fast extraction scenario. This delay can be explained by the differing slopes of the ejection potential of the two extraction scenarios (See section 5.4.2 for details). The slow extraction scenario also yields a wider time spread ($\text{FWHM}(\text{slow})=0.7 \mu\text{s}$). Time-of-flight distributions have been recorded under a number of different operating conditions. The width, mean value and area of the time-of-flight distributions have been extracted, their dependence on the operating conditions will be discussed in the following sections.

Dependence of ion transmission on the buffer gas type, pressure and temperature

The measurements for this study was performed according to the following procedures. A pulsed beam of either Ar^+ , K^+ or Kr^+ ions from the test ion source is injected into the gas-filled ion cooler and buncher. The DC current of the beam is recorded at a Faraday cup installed in BOB3 as a reference of the transmission evaluation. The ions

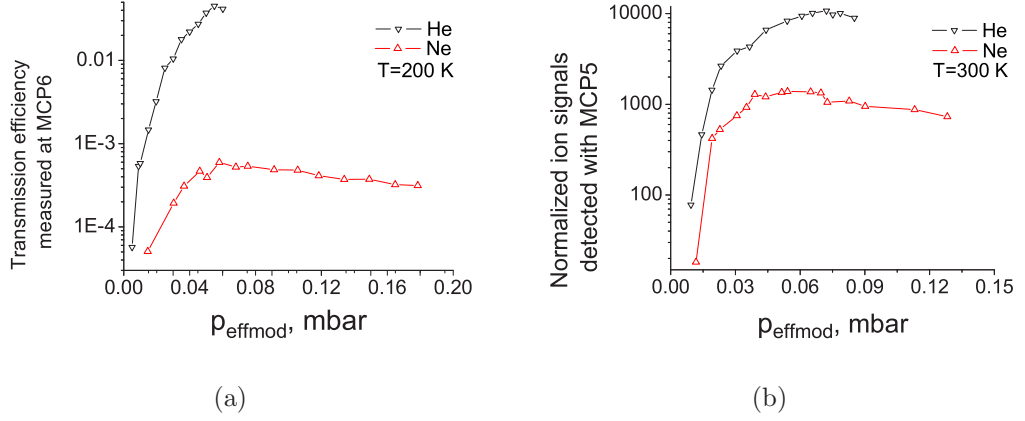


Figure 5.18: Transmission of accumulated and ejected $^{40}\text{Ar}^+$ ion through the ion buncher as a function of the modified effective pressure. (a) transmission efficiency from the test ion source to BOB6 with the cooler operated at a temperature of $T=200$ K; (b) transmission from the test ion source to BOB5 with the cooler and buncher operated at temperature, the transmission is normalized to the incoming current.

are accumulated for a certain cooling time in the buncher section and then ejected as a bunched ion pulse. The time of flight of the ejected ions are recorded at MCP installed in either BOB5 or BOB6 which is located downstream the Penning trap (See Fig. 3.3). Transmission is evaluated as the counted ions in the detector normalized to the incoming current. Operating conditions of buffer gas type, pressure and temperature are changed in each measurement to see their effect on the transmission. The transmission of ions critically depends only on the buffer gas pressure in the cooler section. A scan of the He-buffer gas pressure in the buncher section in the range from 1×10^{-4} mbar to 1×10^{-3} mbar shows little effect on ion transmission. This is not surprising, since a typical cooling time of $t_{\text{cool}} = 4 \times 10^{-2}$ mbar should allow ions to thermalize in the entire bunching pressure range investigated. A pressure of 8×10^{-4} mbar has been used for the buncher section, and the buffer gas pressure discussed from now will refer to that of the cooler section unless specified otherwise. The measurements have been performed at two temperatures. At low temperature ($T=200$ K) $^{40}\text{Ar}^+$ ion pulses have been sent to the MCP detector in BOB6. This detector and its readout electronics are calibrated for ion number counting. The overall transmission

efficiency from the test ion source to BOB6 has been measured for different buffer gas types and pressures. At room temperature ($T=300$ K) the same beam has been delivered to MCP5, where the beam transmission was measured for different operating conditions. Since MCP5 is not calibrated for ion counting, the transmission in this case is represented with the ion signal obtained with MCP5 normalized to the incoming beam current. Fig. 5.18 shows the transmission (a: to MCP6, b: to MCP5) as a function of the modified effective pressure in logarithmic plots. The two curves for He and Ne cooling at $T=200$ K follow the same trend, i.e., they increase with the increasing pressure, reach their maximum, and then decrease with the further increasing pressure. For both $T=200$ K and $T=300$ K, the maximum transmission is observed at the same modified effective pressure for the two buffer gases. All curves show the same trends as the results obtained for continuous mode operation, shown in Fig. 5.16. However, the significantly smaller efficiency obtained with Ne compared to He for $T=200$ K, shown in Fig. 5.18(a), is probably due to the partial pressure of Ne in the buncher section which leaks from the cooler section.

Dependence of ion transmission on the cooling time

This section deals with the effect of the cooling time on the ion transmission. The first part of the measurement aims at finding the smallest cooling time at which the transmission of ions reaches its maximum. For this purpose the cooling time has been scanned in a range of up to 25 ms. Fig. 5.19 shows the ion signal of $^{39}\text{K}^+$, detected with MCP5, as a function of the cooling time for a few combinations of buffer gas (He or Ne) and temperature ($T=300$ K or $T=200$ K). An exponential curve has been fitted to the data in each case. The time constants extracted from the four cooling scenarios are the same within their uncertainty of $\delta\tau \simeq 0.2$ ms. The average time constant of $\tau=1.65$ ms can be used to estimate the time for the count rate to reach $1/e$ of its maximum. The minimum cooling time shall be defined as the time when the count of the ion signal reaches 95% of its maximum, and is obtained at 7 ms.

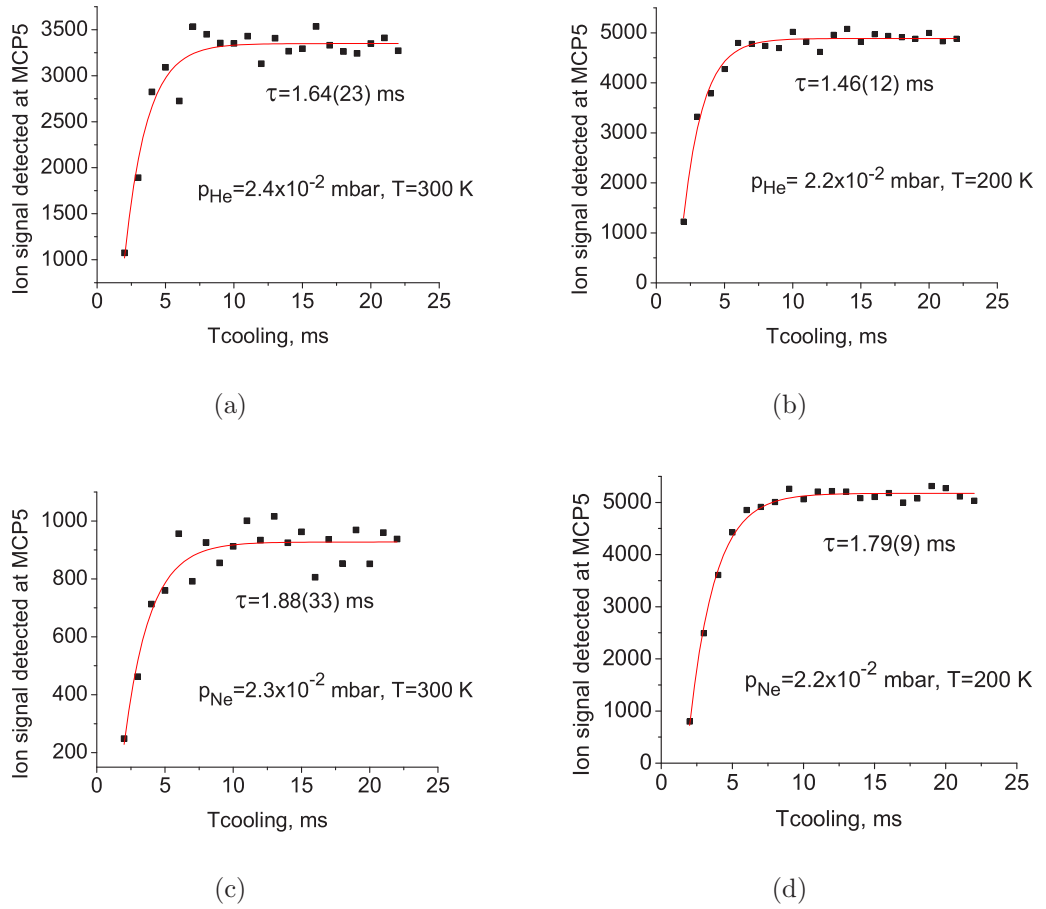
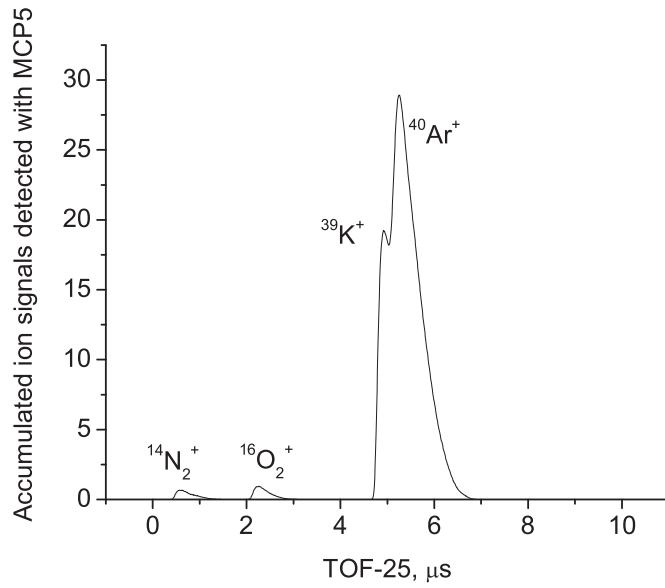


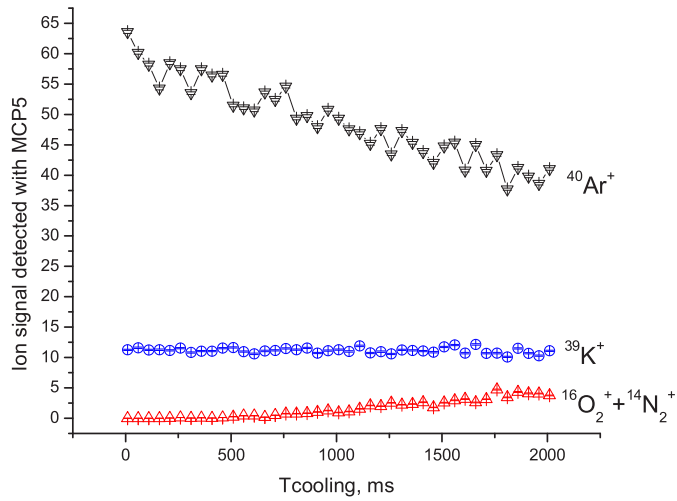
Figure 5.19: Transmission of $^{39}\text{K}^+$ ions, accumulated and bunched in the ion buncher operated in fast extraction scenario, as a function of cooling time. (a) He cooling at $T=300$ K; (b) He cooling at $T=200$ K; (c) Ne cooling at $T=300$ K; (d) Ne cooling at $T=200$ K. The red curve in each case represents an exponential fit to the resulting data, from which the time constant τ has been extracted.

Table 5.6: First level ionization potentials for some elements.

Element	K	N ₂	O ₂	Ar
Ionization potential, eV	4.34	15.58	12.07	15.76



(a)



(b)

Figure 5.20: Transmission of $^{40}\text{Ar}^+$ and $^{39}\text{K}^+$ ions having been cooled for a long time in the buncher. (a) accumulated time-of-flight spectrum over 50 cooling times scanned from 40 ms to 2000 ms; (b) ion signals of $^{40}\text{Ar}^+$, $^{39}\text{K}^+$ and combined $(^{16}\text{O})_2^+$ and $(^{14}\text{N})_2^+$ in the beam as a function of the cooling time. The curves have been obtained by gating on the time of flight of the contributing ions in the time-of-flight spectrum.

A second measurement was performed to check how long ion pulses can be stored in the buncher without significant losses. The measurement discussed above has been repeated with a longer cooling time. The injected beam in this case mainly contains noble gas ions, $^{40}\text{Ar}^+$, and some alkali ions, $^{39}\text{K}^+$, obtained from the test ion source. For each cooling time, one time-of-flight spectrum has been recorded with MCP5. Fig. 5.20(a) shows the accumulated time-of-flight spectrum obtained for cooling times scanned in 50 steps from 40 ms to 2000 ms. Two small peaks are observed in this spectrum together with the dominant ones of $^{40}\text{Ar}^+$ and $^{39}\text{K}^+$. The time of flight measured at MCP5 scales with the mass m as $\text{TOF} \propto \sqrt{m}$. Using the time of flight for $^{40}\text{Ar}^+$ (30.3 μs) as a reference, the ions with time of flight=25.6 μs and 27.3 μs are determined to be $(^{16}\text{O})_2^+$ and $(^{14}\text{N})_2^+$. These two contaminants are most likely ionized air molecules that enter the system through air leaks in the needle valves of the cooler and buncher sections. Ionization is likely to happen by charge-exchange with $^{40}\text{Ar}^+$ ions in the buncher. Fig. 5.20(b) shows the ion signal as a function of the cooling time for the different ion species. Each line is extracted by gating on the time of flight of the ions of interest. The small contributions from $(^{16}\text{O})_2^+$ and $(^{14}\text{N})_2^+$ have been added. The ion signal of $^{39}\text{K}^+$ stays almost constant up to a cooling time of two seconds. The ion signal of $^{40}\text{Ar}^+$ decreases with a time constant of $\tau=90$ ms, while the counts from the other two contaminants increase at a smaller rate, probably due to charge-exchanges occurred with other species with smaller abundances. The different behaviors between $^{40}\text{Ar}^+$ and $^{39}\text{K}^+$ can be explained by their ionization potentials. The ionization potentials [67] of these involved elements are listed in Table 5.6. The values of $(^{16}\text{O})_2$ and $(^{14}\text{N})_2$ are smaller than that of Ar, but significantly larger than that of K. That allows for charge exchange between $(^{16}\text{O})_2/(^{14}\text{N})_2$ and Ar^+ while not between them and K^+ . Even noble gases can be stored for 2 s without major losses. At a typical cooling time of 30 ms ion losses from charge-exchange can be neglected for all species.

Dependence of the time-of-flight distribution on the cooling time

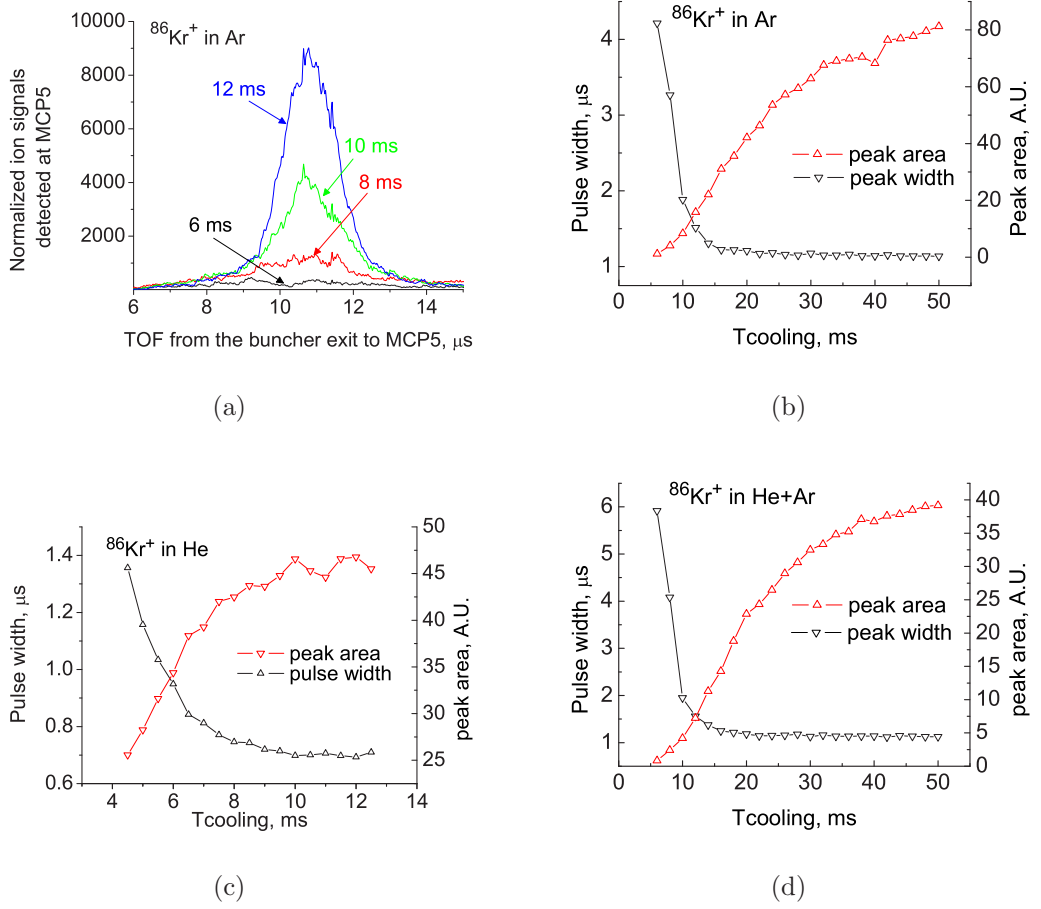


Figure 5.21: Effect of cooling time on the time-of-flight distribution of $^{86}\text{Kr}^+$ ions leaving the buncher operated in fast extraction scenario. (a) time-of-flight distributions of $^{86}\text{Kr}^+$ ions in Ar gas at a pressure of $p_{\text{Ar}} = 1.6 \times 10^{-2}$ mbar for different cooling time; (b) pulse width and peak area for the buffer gas Ar at $p_{\text{Ar}} = 1.6 \times 10^{-2}$ mbar; (c) pulse width and peak area for the buffer gas Ar at $p_{\text{He}} = 1.2 \times 10^{-2}$ mbar; (d) pulse width and peak area for a He+Ar mixture with partial pressures of $p_{\text{He}} = 1.2 \times 10^{-2}$ mbar and $p_{\text{Ar}} = 1.6 \times 10^{-2}$ mbar, respectively.

The shape of the time-of-flight distributions is largely influenced by the cooling time. A large width of the distribution is expected if ions are not cooled to thermal equilibrium. This provides an alternative approach to probe the minimum cooling time. A Kr^+ ion beam from the test ion source was cooled and bunched with the ion buncher operated in fast extraction scenario. Time-of-flight spectra have been

recorded at MCP5, with the cooler section filled with Ar gas at a pressure of 1.6×10^{-2} mbar. Some typical time-of-flight distributions with different cooling times are shown in Fig. 5.21(a). One observes that operation with a longer cooling time gives a smaller width and a larger integral of the distribution. Each time-of-flight distribution has been fitted with a Gaussian function. The extracted width and peak area from all distributions are plotted as a function of the cooling time as shown in Fig. 5.21(b). One can observe that the pulse width decreases exponentially with increasing cooling time, while the peak area increases. The width approaches a constant level at a cooling time of 15 ms, while the integral keeps increasing after that time. The measurement has been repeated for the cooler section filled with pure He gas at a pressure of 1.2×10^{-2} mbar and a mixture of He and Ar with partial pressures of 1.2×10^{-2} mbar and 1.6×10^{-2} mbar, respectively. The corresponding curves of the width and peak area as a function of the cooling time are shown in Fig. 5.21(c) and (d). Both cases yield a minimum cooling time of about 15 ms, similar to the case of Ar cooling and about twice as big as that discussed in section 5.5.2.

Measurement of the energy acceptance

The energy acceptance is the range of the energy of the injected beam at which one obtains good transmission through the ion buncher. For the test measurements reported here this energy is defined as the potential difference between the anode electrode of the test ion source and the entrance electrode (“InjTunnel”) of the ion buncher. The anode voltage was kept constant in order to maintain the same beam properties for this measurement. Instead the energy of the beam entering the cooler was varied by scanning the base voltage of the ion buncher. All DC voltages of the electrodes (from “InjTunnel” to “ExBun2”, see Fig. 5.5(b)) in the cooler and buncher sections can be changed by the same amount of the scanned base voltage. The transmission of an $^{40}\text{Ar}^+$ beam was measured for each base voltage in the scan. The voltages of almost all the electrodes in the buncher section are generated by bipolar power supplies with

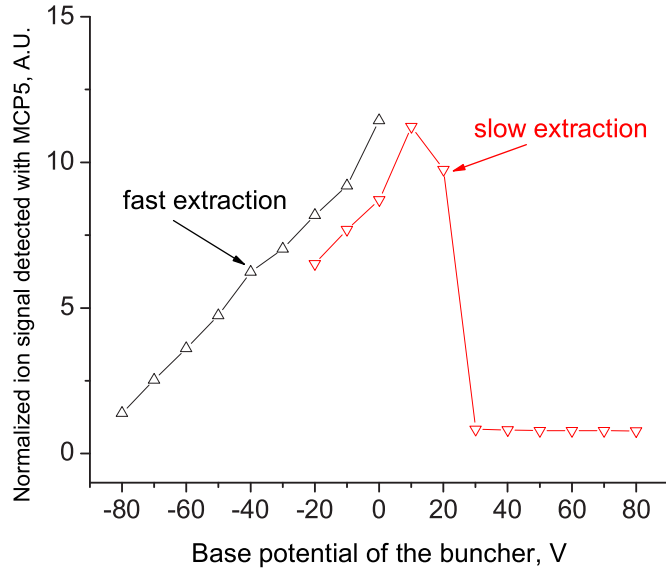


Figure 5.22: Energy acceptance of the ion buncher. The figure shows the ion signal detected with MCP5 as a function of the base potential of the ion buncher. The black curve is obtained with the buncher operated in fast extraction scenario, while the red curve is for slow extraction scenario.

an output range of ± 140 V. As some nominal operating voltages are close to the limits of the power supplies, it is impossible to obtain the complete energy acceptance when the buncher is operated in either one extraction scenario. Assuming that the axial energy is completely dissipated at the end of the cooler section, the energy acceptance should not be only sensitive to the scenario the ions are extracted from buncher. Thus the full range of this acceptance has been obtained with a combination of the fast and slow extraction scenarios. Fig. 5.22 shows the ion signal recorded with MCP5 as a function of the base voltage of the buncher. The data of ion signal are normalized to have the same maximum in two curves. The black curve is obtained when the buncher is operated in fast extraction scenario, whereas the red curve results from the slow extraction scenario. The beam transmission decreases to about 50% of its maximum at a base voltage of -50 V and begins to vanish at +50 V on the other side. Thus the beam acceptance of the LEBIT buncher can be stated as 100 eV.

5.5.3 Beam profiles and emittance measurements

According to Liouville's theorem, the beam emittance can not be reduced by electromagnetic manipulation. Ion cooling, however, allows one to reduce the phase space volume occupied by the beam. The ability of the LEBIT ion beam buncher to provide cooled ion pulses was investigated with a measurement of beam profiles and the inferred emittance. A beam of $^{40}\text{Ar}^+$ from the test ion source is sent to the LEBIT ion buncher system. Ions are extracted at an energy of 2 keV and detected at MCP5, where an image of the beam is generated with a phosphor screen and captured by a CCD camera. To reduce noise, the CCD camera is synchronized with the buncher ejection signal. The number of ions injected into the buncher has been kept at a low level to avoid saturation of the detector system. The ion cooler and buncher is filled with He buffer gas and operated in fast extraction scenario. Beam profiles have been recorded under a variety of operating conditions.

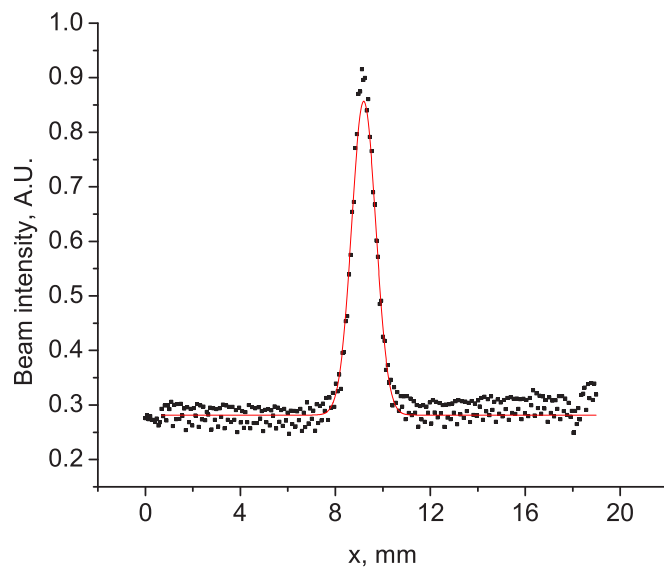


Figure 5.23: A beam profile extracted from a beam image. The solid curve is a Gaussian fit to the data points.

The beam image captured with the CCD camera is a 2-dimensional matrix of pixels. Each pixel represents the beam intensity of the position determined by its two

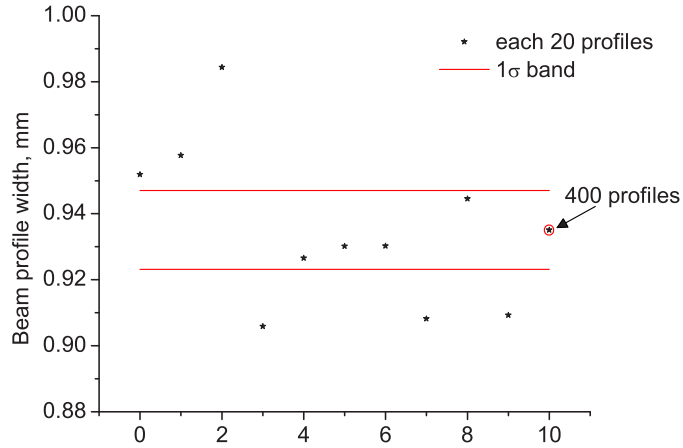


Figure 5.24: Scattering of the values obtained for the width of the beam profile. (See text)

mapped coordinates. A projection of that matrix to either direction (x or y) yields a 1-dimensional spatial distribution in that direction, which shall be called the beam profile. In order to be able to extract the emittance of the beam, an assumption has been made that the distribution in phase-space as Gaussian shape. The width σ and amplitude A of the projection can then be extracted from Gaussian fits. The width so obtained is used to represent the beam profile width in this discussion, and the amplitude is used to represent the beam profile height which relates to the ion density in the center of the beam spot. An example of a typical beam profile plotted together with the corresponding Gaussian fit curve is shown in Fig. 5.23. It is essential to set an idea of the uncertainties due to fluctuations of the widths and heights obtained. Beam profiles have been obtained by superimposing 20 or more individual profiles of the same beam. A collection of 200 beam images has been used to estimate the uncertainty level introduced. The collection of beam images has been rearranged to form 10 groups, each containing 20 randomly selected images. The 20 individual beam profiles obtained in each group are then superimposed to generate a new profile with a higher statistics. The resulting beam profile widths from the Gaussian fits of all the 10 profiles are plotted in Fig. 5.24. Their 1σ range (covering 68% of the confidence

interval) is calculated as $\sigma = \sqrt{\sum_{i=1}^n (s_i - \bar{s})^2/n}$, where n is the total number of groups and \bar{s} is the beam profile width averaged from all the individual one s_i . As a comparison the result obtained when all the 200 beam profiles are added. The figure shows that the average beam profile width of all the 10 individual groups is almost the same as the superimposing one from all the 200 profiles. The maximum deviation of the individual width away from the average width is observed to be about 6%.

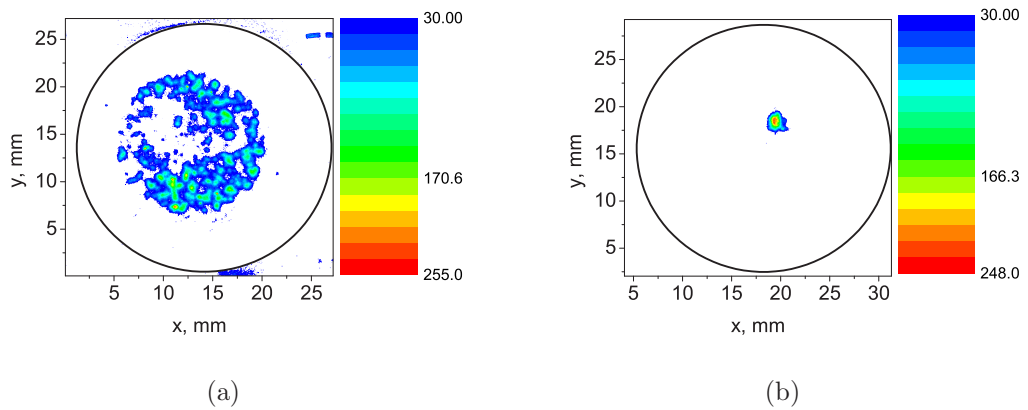


Figure 5.25: Beam images captured with a CCD camera.

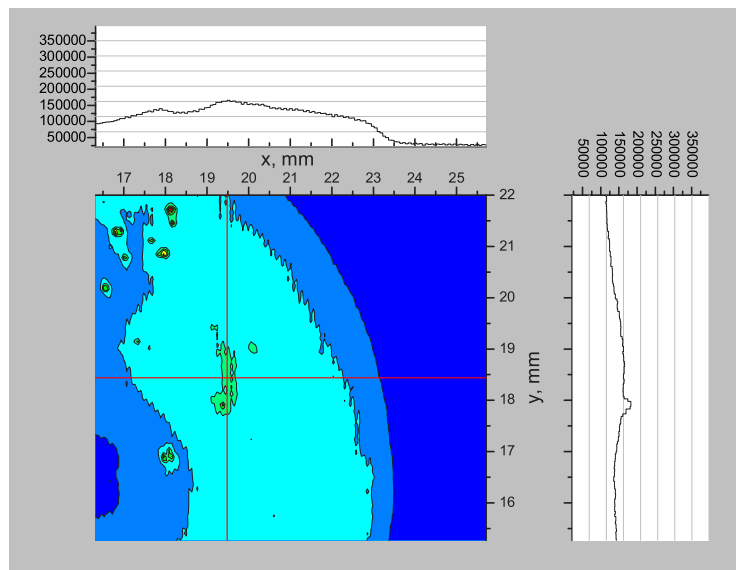


Figure 5.26: Structure of a defocused beam spot near the location of a focused beam spot, which is marked by the crossing of two straight lines.

As an example, Fig. 5.25 shows the beam images of a defocused (a) and a focused

(b) beam obtained with different voltages applied to Einzel lens EL7 between the ion buncher and MCP5. In order to test the homogeneity of the detector in the area where the focused beam spot is observed, a high-statistic measurement with a defocused beam was performed. Over 5000 beam images of that region have been accumulated. The superimposed high-resolution image of that region is shown in Fig. 5.26. The two crossing lines indicate the location of the focused beam. The vicinity of the focused beam spot shows rather uniform intensity within about ± 3 mm. The beam profile cuts of that area along two orthogonal directions are shown in the inserted figures on the top and right sides of the image. Each of them presents a smooth distribution with a variation of no more than 10% within about 1 mm corresponding to a rather flat gain of the detector.

Beam emittance measurement

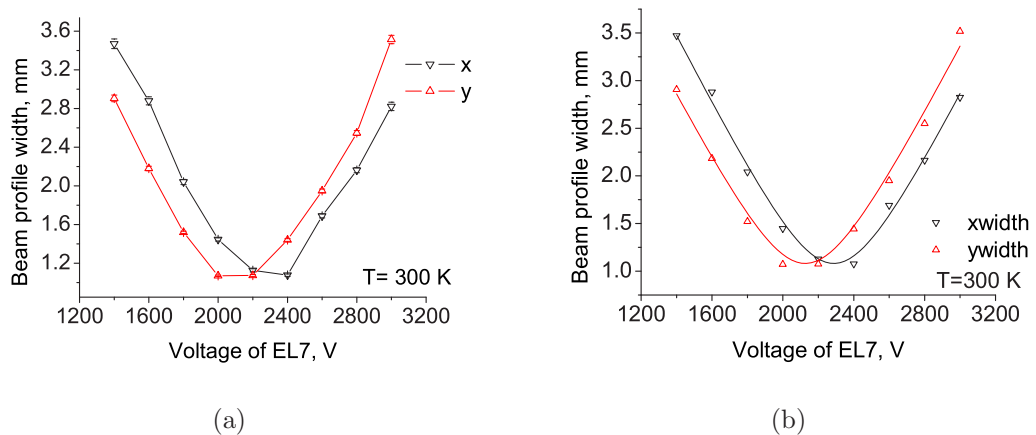


Figure 5.27: Results of the beam emittance measurements obtained with the ion buncher operated at $T=300$ K. (a) beam profile width in both x and y directions as a function of the EL7 voltage (b) Fitting of Eqn. 5.30 to the data of the horizontal beam profile width.

The goal of this measurement is to extract the emittance from the variation of the beam image as the beam is focused differently at the location of the detector. The beam focus is changed by adjusting the voltage of EL7, the Einzel lens between BOB4 and BOB5 (See Fig. 3.3). All the other operating parameters were kept at their

optimized values throughout the measurement. The measurement was performed at two different temperatures ($T=300$ K and $T=200$ K) with otherwise similar operating conditions. The result of the beam profile width as a function of the EL7 voltage at $T=300$ K is shown in Fig. 5.27(a). Two plots for the beam profile width in horizontal (x) and vertical (y) directions are obtained and resemble two near-quadratic curves. There is a 200 V shift of their centers which is likely due to an asymmetry of the beam. The data from the horizontal beam profile widths have been chosen for the beam emittance evaluation. The minimum value of the horizontal beam profile width, 1.0 mm, is reached when the voltage of EL7 is set to $U=2400$ V and a beam focus is obtained at the detector. That width can be used as the standard deviation σ_x of the spatial distribution in transverse phase space. If Gaussian distributions are assumed, then the standard deviation σ_{α_x} of the momentum² distribution can be obtained as follows. The distribution of the two components x and α_x in one transverse phase space is

$$f(x, \alpha_x) \propto \exp\left(-\frac{x^2}{2\sigma_x^2} - \frac{\alpha_x^2}{2\sigma_{\alpha_x}^2}\right) \quad (5.23)$$

The beam focus will move away from the axial location of the detector when the EL7 voltage strays from $U=2400$ V. The phase-space distribution of ions at the detector then moves away from the upright distribution of a focused beam. This movement in phase space can be expressed as a linear transformation

$$\begin{pmatrix} x \\ \alpha_x \end{pmatrix} = \begin{pmatrix} A & B \\ C & D \end{pmatrix} \begin{pmatrix} x' \\ \alpha'_x \end{pmatrix} \quad (5.24)$$

The variables x and α_x are the two phase space components of an ion at the position of the beam focus, while x' and α'_x are the corresponding components at a non-focus position. A, B, C and D are four matrix elements, that first order, linearly depend on the voltage of EL7. The spatial distribution of the defocused beam is obtained

²Here a convergent/divergent angle is used instead of the momentum as the second component in transverse phase space, which follows the convention used in the emittance calculations in Chapter 3

by inserting Eqn. 5.23 into Eqn. 5.24 and integrating the result over the momentum component:

$$\int_{-\infty}^{\infty} f(x, \alpha_x) d\alpha'_x \propto \int_{-\infty}^{\infty} \exp\left(-\frac{x^2}{2\sigma_x^2} - \frac{\alpha_x'^2}{2\sigma_{\alpha_x}^2}\right) d\alpha'_x \quad (5.25)$$

$$\propto \int_{-\infty}^{\infty} \exp\left(-\frac{(A x' + B \alpha'_x)^2}{2\sigma_x^2} - \frac{(C x' + D \alpha'_x)^2}{2\sigma_{\alpha_x}^2}\right) d\alpha'_x \quad (5.26)$$

$$\propto \exp\left(-\frac{(B C - A D)^2}{2(B^2\sigma_{\alpha_x}^2 + D^2\sigma_x^2)} x'^2\right) \quad (5.27)$$

The projection of the rotated distribution is again represented by a Gaussian distribution, with the standard deviation

$$\sigma^2 = \frac{B^2\sigma_{\alpha_x}^2 + D^2\sigma_x^2}{(B C - A D)^2} \quad (5.28)$$

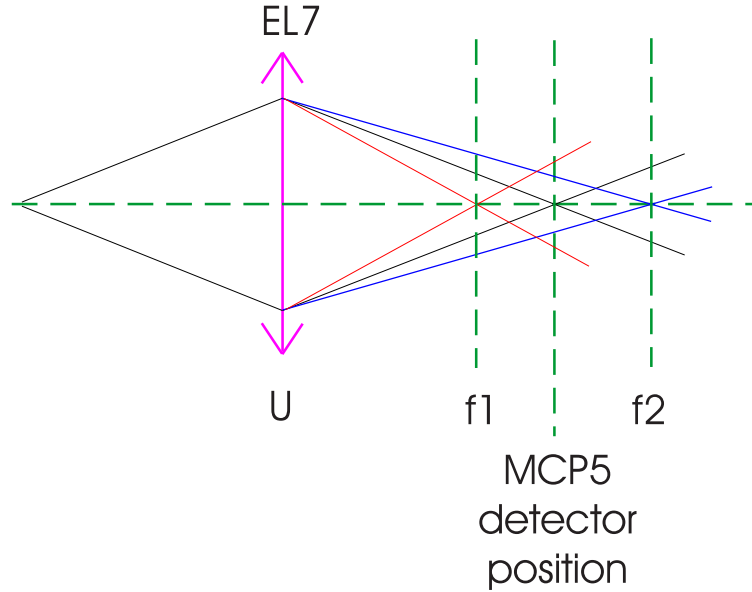


Figure 5.28: Sketch of the beam focusing manipulation that is implemented in the SIMION simulation to determine the linear transformation matrix.

A SIMION simulation has been used to find the four elements of the linear transformation matrix with the simplified scheme shown in Fig. 5.28. An ion beam of $^{40}\text{Ar}^+$ at an energy of 2 keV is sent through Einzel lens EL7 and focused at a location away from its origin. When the voltage of EL7 is set to $U=2400$ V the beam focus is at

the location of MCP5 detector. The beam focus will be at a closer position f1 when $U > 2400$ V or further away at f2 when $U < 2400$ V. Each beam transport simulation is performed with one of the EL7 voltages used in the measurement. A set of phase space distributions have been obtained at the location of the MCP5 detector. The phase-space coordinates of the same ions in different focusing scenarios then can be used to calculate the linear transformation that changes a deformed phase distribution into one at the focus. In order to solve the equation for the four variables (A, B, C and D) two ions have been chosen for each transported beam, which provide two parameter sets $(x_1, \alpha_{x1}, x_2, \alpha_{x2})$ and $(x'_1, \alpha'_{x1}, x'_2, \alpha'_{x2})$. Both of them have been plugged into Eqn. 5.23 to yield a linear relationship between each transformation matrix element and EL7 voltage. A correction of the EL7 voltage, ΔU , needs to be included to account for deviations of the calculated optics from the physical one. The resulting linear transformation matrix then becomes

$$\begin{pmatrix} x \\ \alpha_x \end{pmatrix} = \begin{pmatrix} -0.06451 + 0.00045 (U + \Delta U) & 0.5209 - 0.00022 (U + \Delta U) \\ -2.03258 + 0.00086 (U + \Delta U) & 2.00557 - 0.00042 (U + \Delta U) \end{pmatrix} \begin{pmatrix} x' \\ \alpha'_x \end{pmatrix} \quad (5.29)$$

where U is the measured voltage of EL7. The determinant of the matrices obtained equals to 1, which is expected from Liouville's theorem. Thus Eqn. 5.28 can be rewritten as

$$\sigma = \sqrt{B^2 \sigma_{\alpha_x}^2 + D^2 \sigma_x^2} \quad (5.30)$$

which can be used to fit the curve of the (horizontal) beam profile width. The fit for this case is shown in Fig. 5.27(b), and yields $\sigma_x = 1.08$ mm. Two other parameters σ_{α_x} and ΔU have also been determined from the fitting to be $\sigma_{\alpha_x} = 16.8$ mrad and $\Delta U = -116$ V, respectively. Thus the beam emittance is calculated to be $\varepsilon = 18.2\pi$ mm·mrad for 2σ , equivalent to 95% of the beam.

The measurement has been repeated for the system operated at $T = 200$ K, the results are shown Fig. 5.29. The voltage of EL7 corresponding to the minimum beam

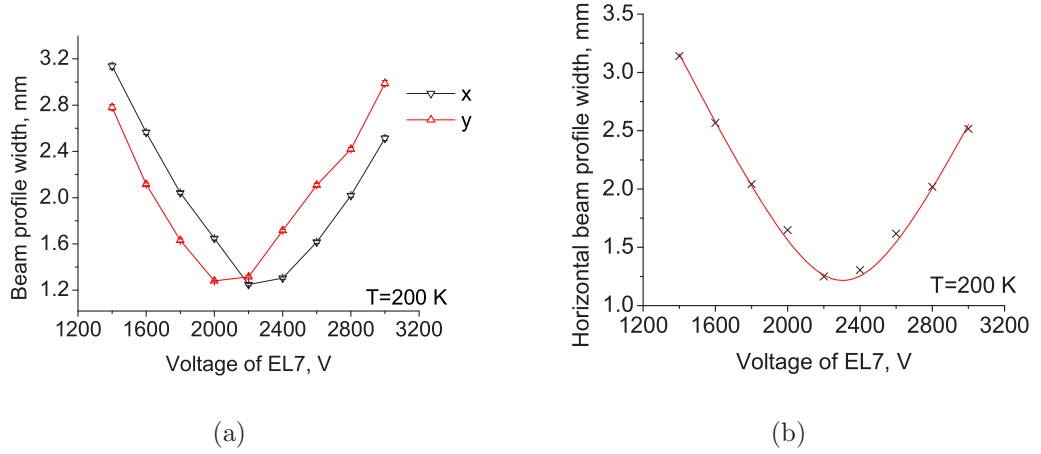


Figure 5.29: Results of the beam emittance measurements obtained with the ion buncher operated at $T=200$ K. (a) beam profile width in both x and y directions as a function of the EL7 voltage (b) Fitting of Eqn. 5.30 to the data of the horizontal beam profile width.

profile width in x direction is 2200 V in this case, which is also used in the corresponding SIMION simulation for the focused beam. The linear transformation matrix in this case is calculated with the same method as

$$\begin{pmatrix} x \\ \alpha_x \end{pmatrix} = \begin{pmatrix} 0.01655 + 0.00045 (U + \Delta U) & 0.48016 - 0.00022 (U + \Delta U) \\ -1.87548 + 0.00086 (U + \Delta U) & 1.92592 - 0.00043 (U + \Delta U) \end{pmatrix} \begin{pmatrix} x' \\ \alpha'_x \end{pmatrix} \quad (5.31)$$

By fitting Eqn. 5.28 to the data of the horizontal beam profile width, the standard deviations of the spatial and angle distribution and the offset voltage are determined to be $\sigma_x=1.22$ mm, $\sigma_{\alpha_x}=14.4$ mrad and $\Delta U=58$ V, respectively. The corresponding beam emittance for 95% of the beam is $\varepsilon = 17.6\pi$ mm · mrad, which is the same as that for $T=300$ K within the uncertainties. To illustrate the ability of the LEBIT cooler and buncher to deliver cold ion pulses, this emittance value shall be compared to that of a typical ISOL beam, $\varepsilon = 30\pi$ mm · mrad at an energy of 60 keV. The emittance of the LEBIT pulse at an energy of 60 keV is $\varepsilon_{\text{norm}} = 3.3\pi$ mm · mrad. Thus the LEBIT pulse is a factor 9 in emittance smaller than the ISOL beam.

Dependence of the beam profile on ion number, cooling time and RF amplitude

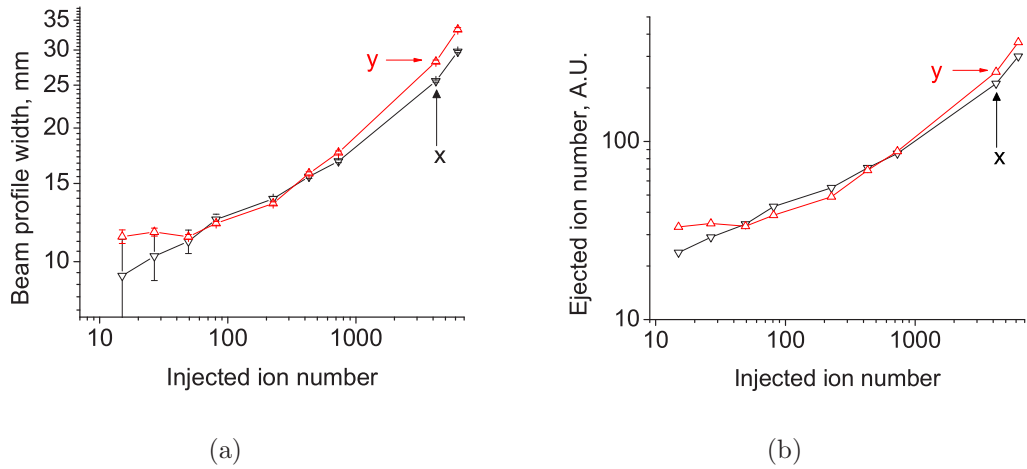


Figure 5.30: Effect of the number of injected ions on the beam profile at $T=200\text{K}$. (a) beam profile width (b) number of ions detected at MCP5.

In order to explore the effect of the number of injected ions, beam profiles were measured as a function of the opening time of the beam gate at $T=200\text{ K}$, while keeping the injected beam current constant. In order to focus on coordinate spread the voltage of EL7 is set to 2200 V so that the beam is focused onto the detector. The injected beam current has been measured with the Faraday cup at BOB3 and kept at an approximately constant level of 10 pA. The current multiplied by the beam gate opening time gives the injected ion number. The result of the measurement is shown in Fig. 5.30. The figure on the left shows the beam profile width as a function of injected ion number. The beam profile width increases steadily with increasing injected ion number. For small ion numbers, a larger uncertainty of the beam profile width is observed in y direction, most likely due to the residual noise in the ion signal. A similar trend has been observed for the detected ion number at MCP5. That number has been obtained with the beam profile height multiplied by the square of the beam profile width, which is proportional to the integration of the beam density over the whole beam spot area. As shown in the right figure the detected ion number also

decreases with the decreasing injected ion number except when a very small number of ions is injected. In that case the ejected ion number evaluated from the y-profile stays at an approximately flat level, while that from the x-profile keeps decreasing. The results of this measurement agree with the expectation within uncertainties in the y direction (the large error bar in the x-profile makes it difficult to conclude), which tells us that the beam profile width cannot be reduced further with the limited number of injected ions unless the system temperature is lowered.

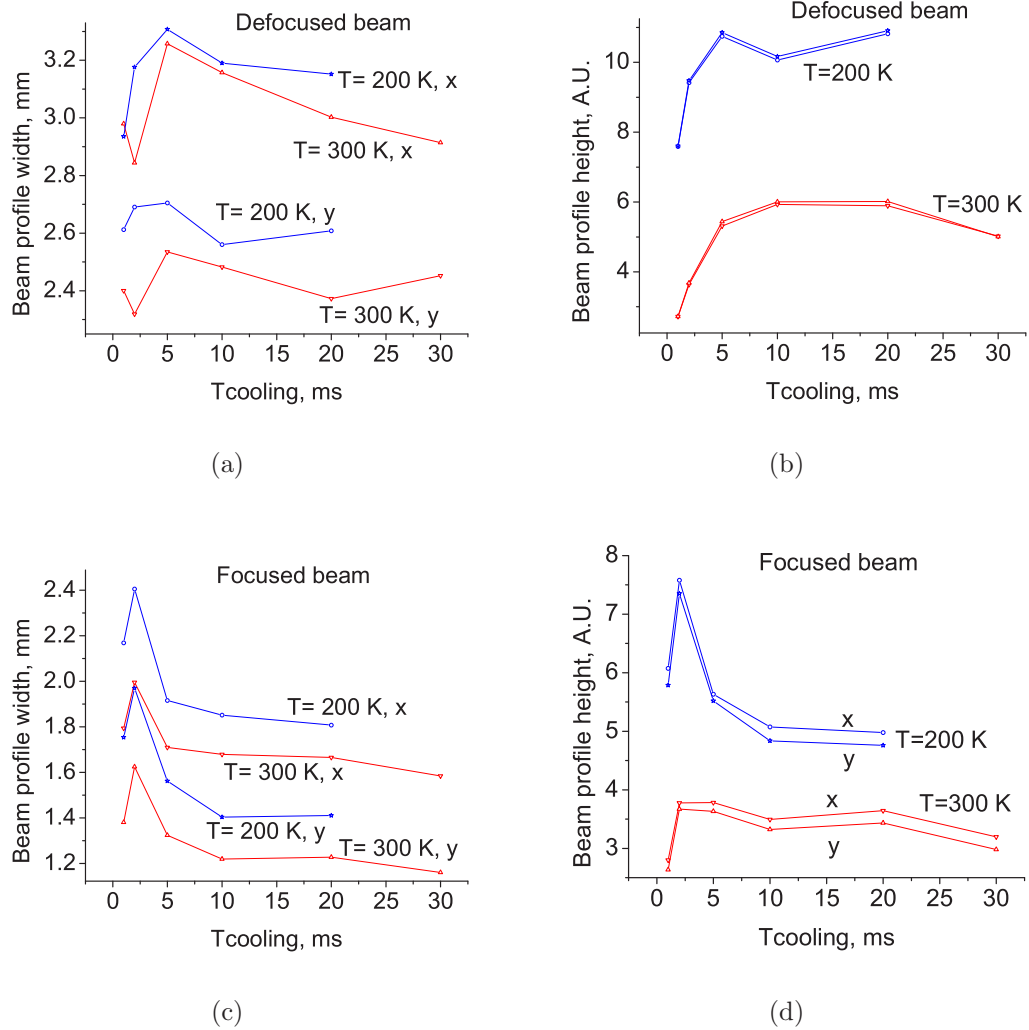
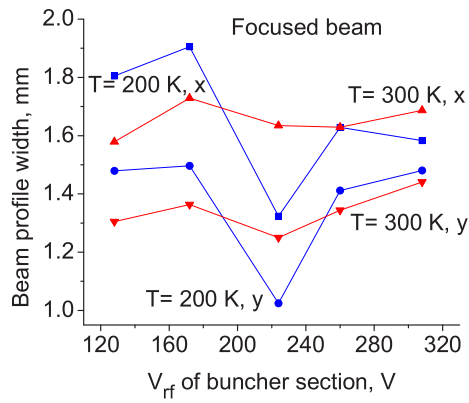


Figure 5.31: Effect of the cooling time on the beam profile. (a) beam profile width and height for a focused beam; (c)(d) beam profile width and height for a defocused beam.

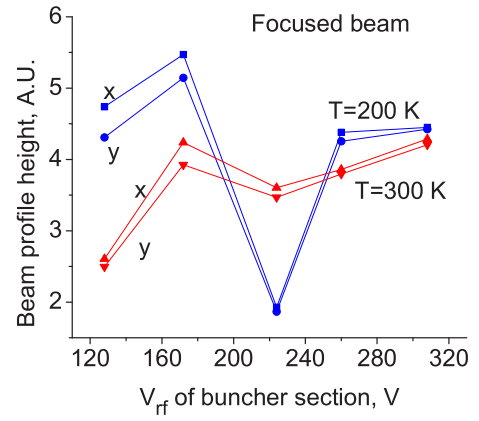
Another set of measurements was devoted to study the effect of the cooling time on

the beam profiles. These measurements have been performed with the cooler section operated at two temperatures of $T=300$ K and $T=200$ K. For each temperature beam profiles are obtained for both a focused and a defocused beam, corresponding to EL7 voltages of $U=2000$ V and $U=3000$ V, respectively. The widths and heights of the profile as a function of cooling time observed under these conditions are shown in Fig. 5.31. A striking feature is the observed difference between the beam profile widths in the two directions. For the defocused beam the width in y direction is much larger than that in the x direction at both temperatures, which implies that the beam profile height does not depend on the spatial symmetry of the beam. The inverse behavior is observed for the focused beam, where the beam profile width in the x direction is always larger. A similar behavior does not show up in the beam profile height. The curves of the beam profile height as a function of the cooling time are almost same in both directions. The height at low temperature $T=200$ K is much larger than that at the high temperature $T=300$ K for both focused and defocused beams. A dependence of the height on the cooling time similar to that of the width has also been observed. The difference in this case is the much slower change of the height at high temperature of $T=300$ K than that at the low temperature of $T=200$ K. The results of the measurement agree with expectations except when the cooling time is very small, where the experiment results give a small profile height instead of the maximum height. Both the width and height of beam profile should decrease with the increasing cooling time until a thermal equilibrium is reached.

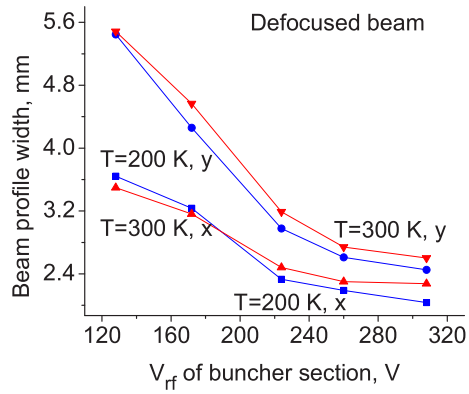
The last experiments with beam profile were to investigate the effect of RF amplitude. The measurements were again performed with both a defocused and a focused beam at two different temperatures of the cooler and buncher. The RF amplitude in the buncher section was scanned from $V_{rf}=130$ V to $V_{rf}=310$ V, which covers the range $q=0.24$ to $q=0.56$ for mass $A=40$. The width and height of the beam profiles as a function of this amplitude are shown in Fig. 5.32. The plots of the beam profile height present a rather smooth trend for both the focused and the defocused beam



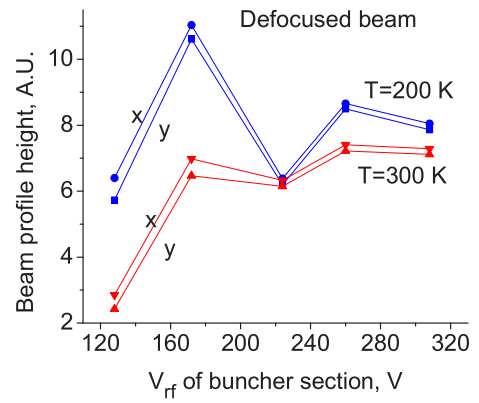
(a)



(b)



(c)



(d)

Figure 5.32: Effect of the RF amplitude used in the buncher section on the beam profile. (a) beam profile width and height for a focused beam; (c)(d) beam profile width and height for a defocused beam.

except for $V_{\text{rf}}=224$ V. The plots of the beam profile width, on the contrary, rather clearly exhibit a dependence of the beam profile on the RF amplitude. There is only little change of the width for the focused beam, while there is a clear decrease of the width of the defocused beam with increasing RF amplitude. This is contrary to expectation: The spatial distribution in transverse phase space should directly determine the beam profile of the focused beam. According to Eqn. 5.15, the width of the spatial distribution of trapped ions in thermal equilibrium is in first order inversely proportional to the RF amplitude. As the transverse spatial distribution at the detector should directly relate to the transverse distribution of trapped ions, one would expect a decrease of the beam profile width with increasing RF amplitude. The momentum distribution should contribute significantly to the beam profile width for the defocused beam. According to Eqn. 5.16, the momentum distribution of trapped ions does not depend on the RF amplitude, and with the same reasoning as for the focused beam one would expect hardly any dependence of the beam profile width on the RF amplitude. Significant discontinuities are observed for the beam profile height for both the focused and defocused beam, and width for the focused beam at $T=200$ K. The exact reasons of these observations will require further investigations.

5.5.4 Buncher section operated as a mass filter

Operating the buncher section as a mass filter would add another level of mass-selectivity in the LEBIT setup which would be an elegant way to exclude breakup products from CID in the cooler from being transported to the Penning trap. For this reason the ability of the buncher linear Paul trap to act as a mass filter has been investigated. Two DC voltages are used in this case to offset the RF voltages in the circuit discussed in section 5.3.3. These DC voltages are provided by two power supplies as $V_{\text{DC1}} = V_{\text{DCbun}} + V_{\text{Bunfilter}}$ and $V_{\text{DC2}} = V_{\text{DCbun}} - V_{\text{Bunfilter}}$. V_{DCbun} is the same voltage applied to the RF electrodes in the buncher section when operated in non-mass-filtering mode. $V_{\text{Bunfilter}}$ is an additional offset voltage for the Bunfilter sig-

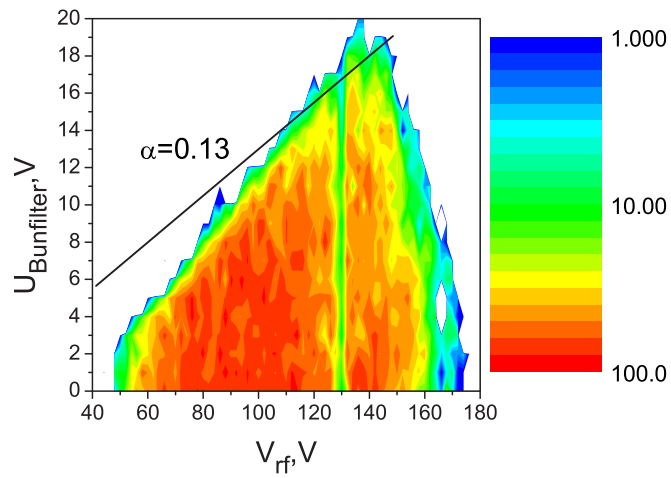


Figure 5.33: Transmission of $^{40}\text{Ar}^+$ ions as a function of RF amplitude V_{rf} and offset voltage $V_{\text{Bunfilter}}$. The straight line is for a mass scan with a ratio $\alpha=V_{\text{Bunfilter}}/V_{\text{rf}}=0.13$.

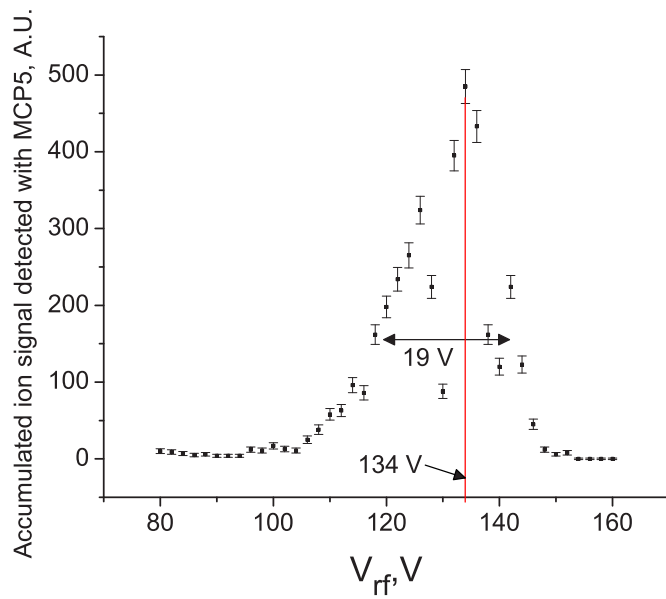


Figure 5.34: Transmission of $^{40}\text{Ar}^+$ ions as a function of RF amplitude V_{rf} and offset voltage $V_{\text{Bunfilter}}$ with $V_{\text{Bunfilter}}/V_{\text{rf}}=0.13$ (see Fig. 5.33) when the buncher section is operated as a mass filter. The vertical red line marks the center of the distribution at $V_{\text{rf}}=134$ V.

nal (See Fig. 5.5(b)) used only for mass-filtering operation. Again, a beam of $^{40}\text{Ar}^+$ ions from the test ion source was injected into the ion buncher. These ions are accumulated, mass-filtered, cooled once more and then ejected. The beam accumulation time is typically around 10 ms. The second beam cooling time after the mass filtering is typically around 20 ms. A reasonable mass-filtering time during which $V_{\text{Bunfilter}} \neq 0$ V has to be determined to ensure sufficient mass selectivity of the investigated ions as well as minimum ion loss of them. A time of 10 ms has been chosen based on these two criteria. A 2-dimensional scan of both the RF amplitude (V_{rf}) on the buncher section and $V_{\text{Bunfilter}}$ has been performed with this time. The resulting transmission as a function of V_{rf} and $V_{\text{Bunfilter}}$ when the buncher section is operated as a mass filter is shown in Fig. 5.33. The “valley” at $V_{\text{rf}}=134$ V indicates that ion loss occurs when the mass filter is operated in that region. This has also been observed elsewhere and can be associated with non-linear resonances due to higher order multipole terms in the trapping potential [68]. A series of measurements has been performed by scanning V_{rf} and $V_{\text{Bunfilter}}$ proportionally. The ratio α of $V_{\text{Bunfilter}}$ to V_{rf} has been continuously increased from $\alpha=0.08$ to $\alpha=0.14$ at which the tip of the transmission diagram is reached. The ratio of the width of the distribution to its center can be used to state a mass resolving power. For a constant V_{rf} , the beam transmission decreases with increasing α , while resolving power increases. The result for $\alpha=0.13$ is shown in Fig. 5.34, which gives a mass resolving power of 7 for mass 40. The corresponding transmission efficiency has been calculated to be 2% by comparing the accumulated ion signals detected at MCP5 with that of the non-mass-filtering operation. That is due to the following reasons: (1) non-linear resonance which results in ion loss for the mass-selected ions; (2) there is buffer gas filled in the buncher section which decreases the transmission of the mass-selected ions.

5.6 Buncher simulations

Three separate simulations have been performed to study the performance of the ion buncher. The first one simulates the ion transmission when the buncher is operated in continuous mode. The second one lets the ions accumulate in the buncher section when operated in pulsed mode. A third one simulates the ion ejection out of the buncher. SIMION is used in the simulation to calculate the relevant electric fields by solving the Laplace equation for the electrodes as designed and built. A separate code package is used to read in the field maps and calculate the trajectories of ions in the LEBIT ion buncher. This code implements damping with a microscopic treatment of collisions between the ions and the buffer gas atoms. The interaction between the ions and buffer gas atoms is discussed in detail in [69]. For the discussions in this thesis it can be expressed as a potential

$$V(r) = \frac{B}{r^N} - \frac{C_4}{r^4} - \frac{C_6}{r^6} \quad (5.32)$$

where B , N , C_4 and C_6 are four parameters and r is the separation between interactive ion and gas atom. The C_4/r^4 and C_6/r^6 terms describe the attractive potential parts, induced by dipole and quadrupole polarization, respectively. The B/r^N term stands for the repulsive potential part, where B and N can be empirically determined by fitting collision cross sections.

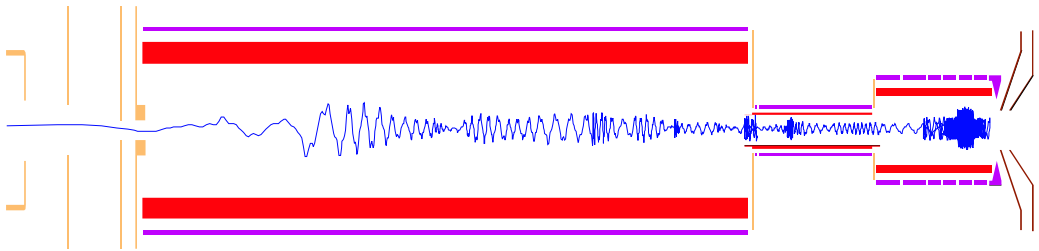


Figure 5.35: Simulated trajectory of an $^{40}\text{Ar}^+$ ion being cooled and captured in the ion buncher.

Four individual simulations will be discussed in the following. All of them assume

a singly charged ion beam with mass 40 as most of the measurements were performed with $^{40}\text{Ar}^+$ ions. A typical trajectory obtained from the simulation is shown in Fig. 5.35. The injected ion enters the ion cooler with an energy of a few electronvolts where it is slowed down by collisions with the buffer gas atoms. As it enters the buncher section, it picks up the energy of a few electronvolts due to the trapping potential (seen in Fig. 5.10). This energy is gradually dissipated as the ion thermalizes at the trap center. Each simulated trajectory is different from the other due to the statistical nature of the collisions. When a large number of ions are simulated, the collection of ions should act like the actual beam. This ion ensemble is cooled, accumulated in the ion buncher and ejected as pulsed beam. Each ejected ion has its own time-of-flight from the buncher exit to the detector, resulting a time-of-flight distribution which can be used to study the performance of the ion buncher.

The first simulation carried out studies the effect of buffer gas pressure and temperature on the time-of-flight of the ion pulses sending through the ion buncher is operated in continuous mode. The initial transverse phase space of the injected beam is estimated to have an emittance of $\varepsilon=100\pi$ mm mrad with an elliptical distribution. In total 1000 simulated ions are used to represent this phase space. These ions start in the last drift tube of the -5 kV beam transport section with an energy of 5010.4 eV, so that they enter the ion buncher with an energy of a few electronvolts. These ions are given an initial time spread of 3 μs which matches the beam gate opening time in the experiments. Different values of buffer gas pressure of He ranging from 5×10^{-3} mbar to 5×10^{-2} mbar were used in the simulations. All voltages needed for this simulation are the ones used in the experiments. The time-of-flight distributions of the transmitted ions are recorded at the location of MCP5. The simulated spectra for five buffer gas pressures at a temperature $T=300$ K are shown in Fig. 5.36. The corresponding results from the measurement as discussed in section 5.5.1 are displayed with square dots. The simulated and experimental results agree very well except for the highest pressures, where the simulated curve has a slightly larger width.

The simulation has been repeated for a gas temperature of $T=181$ K. In this case, the simulated buffer gas pressure is scaled as discussed in section 5.5.1 to reflect the pressure reading correction. Fig. 5.37 shows the results from the simulations and measurements for six different buffer gas pressures. Very good agreement is observed for low pressures. Again, a disagreement between simulations and experiments occurs for high pressures. That is probably due assumption of a uniform temperature made in the simulation, which is not the truth in the experiment.

A second simulation has been carried out to reproduce the time of flight of ions after the buncher. This simulation has been repeated for different extraction scenarios and temperatures. It starts with the same ion distribution for the injection of ions as discussed before, and again uses the same voltage settings as in the experiment. In this case the cooler section is assumed to be filled with He gas at a pressure of 2.4×10^{-2} mbar, and 8.0×10^{-4} mbar in the buncher section. A gas temperature of $T=250$ K in the buncher section is chosen to compare the result with that of the room temperature at $T=300$ K. This is based on the consideration of an inhomogeneous temperature distribution of the system under cryogenic cooling condition. The thermocouple located in the buncher section measures a temperature of $T=-20$ °C when the other one in the cooler section measures $T=-100$ °C. Four simulated time-of-flight spectra are shown in Fig. 5.38. Pulses for the same extraction scenario have the same center position, with the pulse widths at $T=300$ K being slightly wider than those at $T=250$ K. There is a $1.6 \mu\text{s}$ delay between the pulse centers of two extraction scenarios. The pulse width in slow extraction scenario is about 3 times wider than that of the fast extraction scenario. Each spectrum obtained from this simulation has a delay of $0.6 \mu\text{s}$ to its corresponding spectrum shown in Fig. 5.17. That is because the electrode configuration used in the simulation is based on the original design of the ion buncher, which is different from the current used configuration.

A third simulation was performed to study the effect of the cooling time on the time-of-flight distribution of ions extracted from the buncher operated in fast extrac-

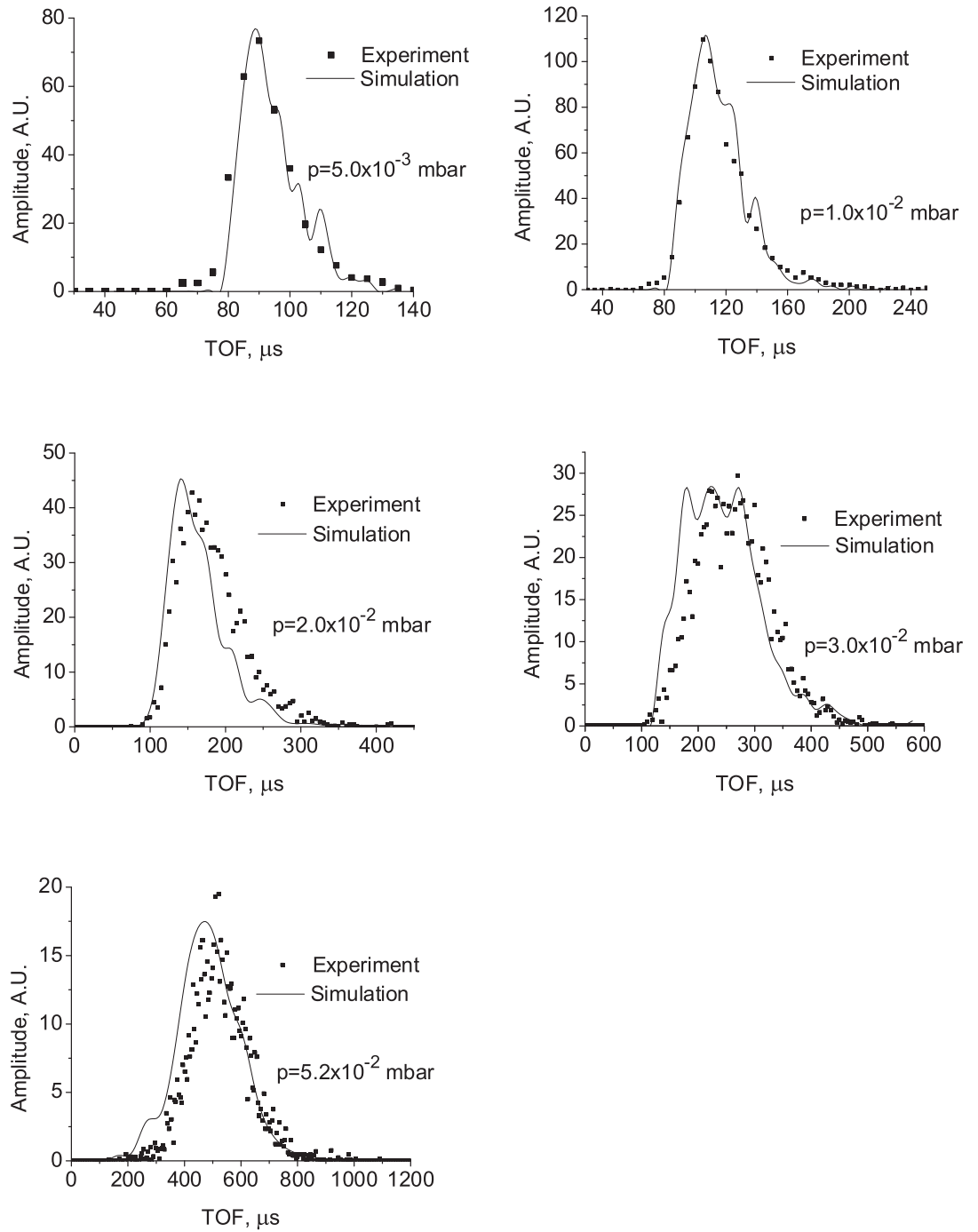


Figure 5.36: Simulated time-of-flight spectra of beam pulses sent through the ion buncher operated in continuous mode and detected at MCP5. The cooler section is filled with He gas at 5 different values of pressure at room temperature ($T=300$ K). The results from measurements (dots) are compared to the results from corresponding simulations (solid curves).

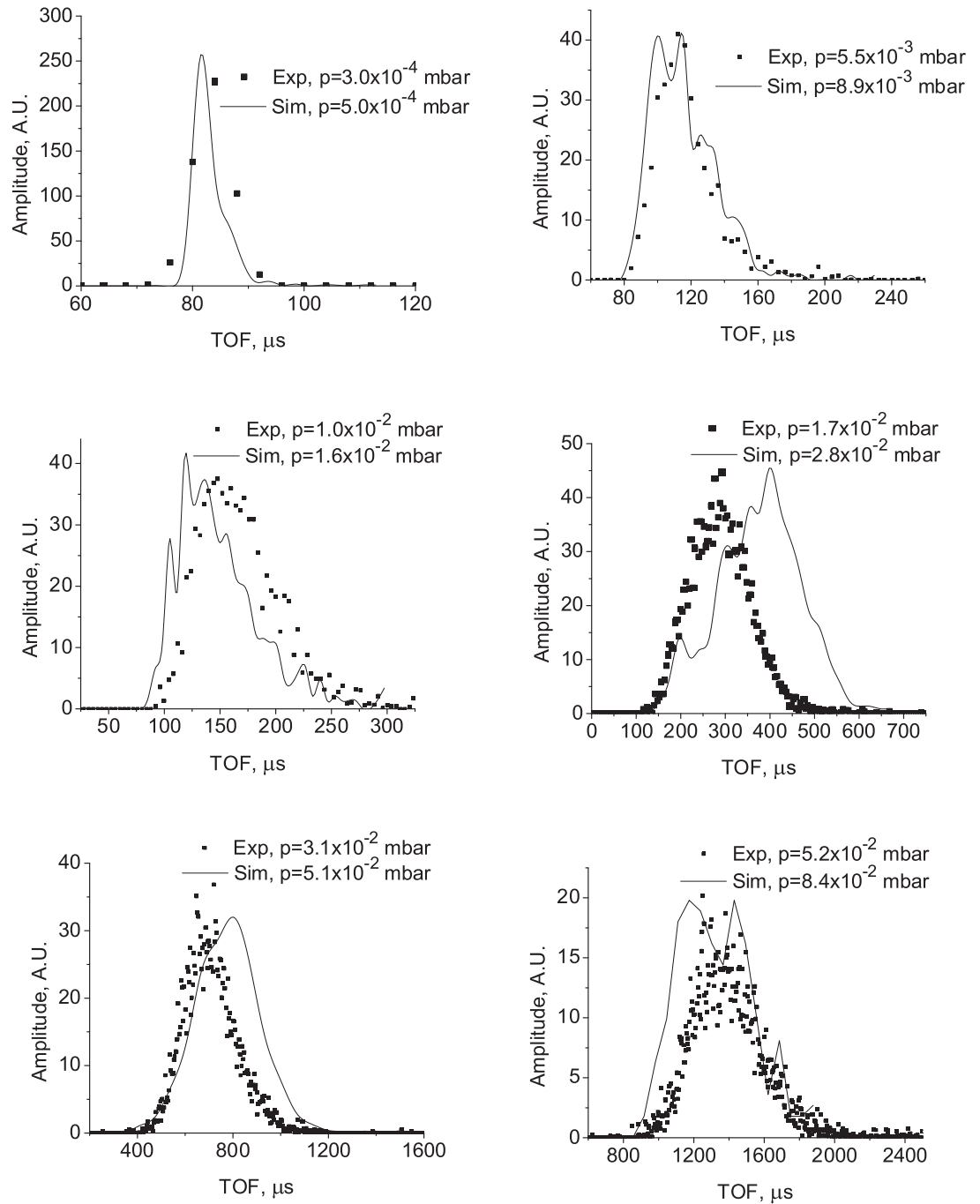


Figure 5.37: Simulated time-of-flight spectra of beam pulses sent through the ion buncher operated in continuous mode and detected at MCP5. The cooler section is filled with He gas at 6 different values of pressure at a low temperature ($T=181$ K). The results from measurements (dots) are compared to the results from corresponding simulations (solid curves). Pressure readings have been corrected as discussed in section 5.5.1.

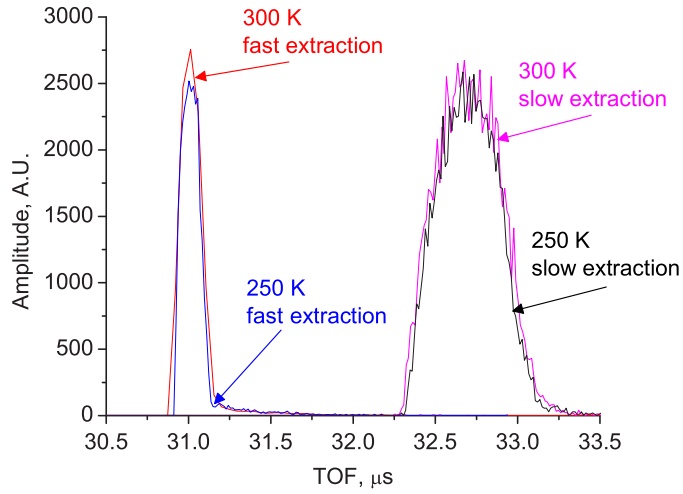


Figure 5.38: Results of the simulation for the time-of-flight spectra recorded at MCP5 when the ion buncher is operated in two extraction scenarios (slow and fast) and two temperatures ($T=250$ K and $T=300$ K).

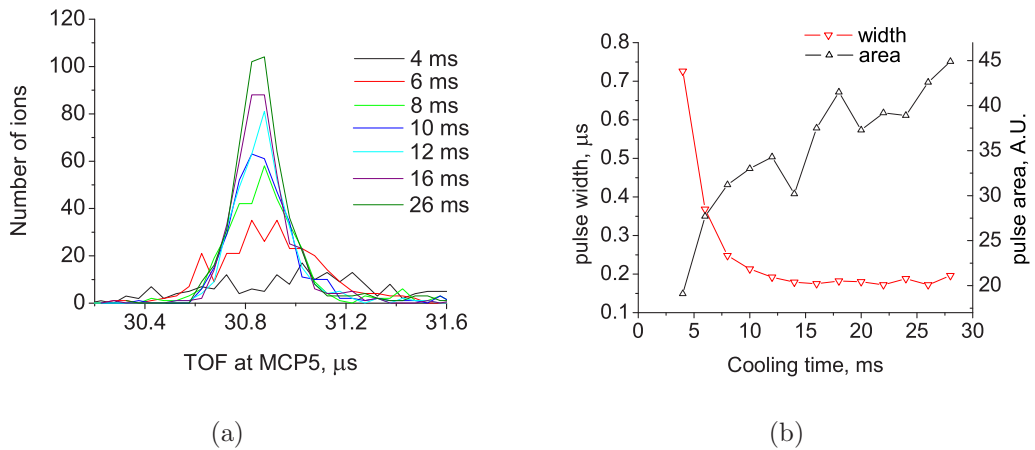


Figure 5.39: Simulated effect of the cooling time on the time-of-flight distribution of $^{40}\text{Ar}^+$ ion pulses extracted from the buncher. The buncher is operated in fast extraction scenario and at a temperature of $T=300$ K. (a) time-of-flight distributions (b) pulse width and area of the curves in (a) obtained from Gaussian fits to the spectra.

tion scenario. A series of 14 cooling times ranging from 2 ms to 28 ms were used in the simulation. Each simulation was carried out with one of these 14 cooling times for the injected ion beam with the beam profile discussed earlier. The beam ejection calculation for each cooling time starts at the moment the preceding beam injection calculation stops. That leads to the same phase between the radial oscillation of the ions and the RF voltage of the buncher section. The result of the simulation for a temperature of $T=300$ K is shown in Fig. 5.39. The figure on the left side displays the time of flight distributions of ions cooled with 7 selected cooling times. It is observed that the pulse width decreases with increasing cooling time, while the pulse height increases. That can also be seen from the extracted width and area obtained from Gaussian fits to the data, as shown in the right figure. The pulse width keeps decreasing with increasing cooling time until it leaves out at a cooling time of 12 ms. The pulse area however keeps increasing towards longer cooling times.

The axial energy of ions inside the ion buncher system ranges from 2 eV to 5 eV. This leads to a very high sensitivity of the beam transmission to the electric potential inside the system. Due to the low velocity and large damping, ions can easily stop or get temporarily trapped if there are even shallow potential wells along the ion guide. It is necessary to avoid such “parasitic” traps in the ion guide in order to keep the cooling time short.

The simulated number of ions recorded at the trap and the detector as a function of the cooling time are as shown in Fig. 5.40. The number of ions in the trap (red curve) increases with the cooling time. The overall trend for the ions at the detector (black curve) is the same as for the trapped ions.

The dependence of the ion numbers in the trap as a function of cooling time shall now be discussed more in detail. The axial distributions of the ions for three cooling times (14 ms, 20 ms and 28 ms) are shown in Fig. 5.41. The distribution for each cooling time features three groups. The axial positions of these groups correspond to the cooler exit, μ -RFQ exit and the trap center. The number of ions in each group

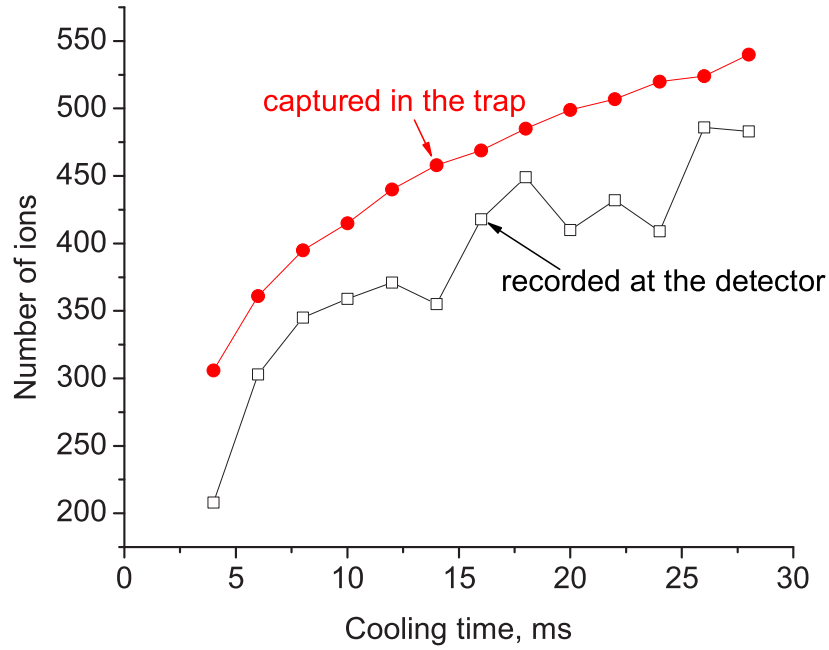


Figure 5.40: Simulated number of extracted $^{40}\text{Ar}^+$ ions as a function of the cooling time. The red curve the number of ions captured in the trap. The black curve shows the number of ions recorded at the detector.

is given next to the distribution. The numbers of ions stopped at the μ -RFQ exit decrease from 147 (14 ms cooling) to 121 (20 ms cooling), to 73 (28 ms cooling). Ions leaving the unwanted trap at the exit of the μ -RFQ gradually fill the trap in the buncher section. That leads to the different numbers of ions that reach the trap and is in a good agreement with the red curve in Fig. 5.40. The potential line shown in Fig. 5.9(b) indicates that the potentials at the cooler exit form a trap of 0.7 eV deep, and the potentials at the μ -RFQ exit forms another shallow trap of 0.1 eV deep.

A fourth calculation was performed to simulate the beam emittance and compare the results to the measurements discussed in section 5.5.3. For this simulation, an ion cloud of 10000 ions was generated. These ions start at the trap center of the buncher section, with a phase space distribution as defined in Eqn. 5.15 and 5.16. The simulation has been performed for two temperature conditions, at $T=300$ K and $T=250$ K, respectively. The phase space diagrams in the $x-\alpha_x$ plane for both cases are

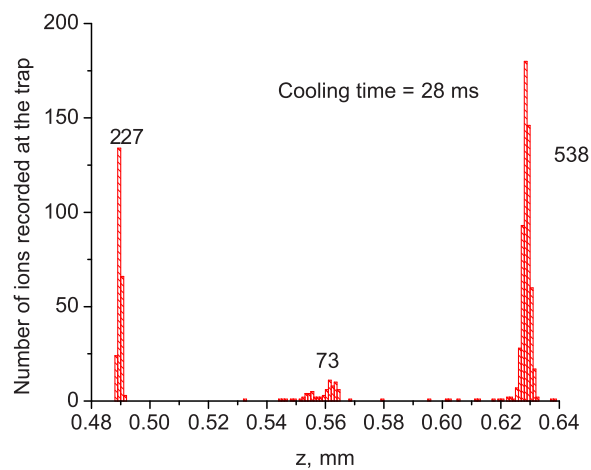
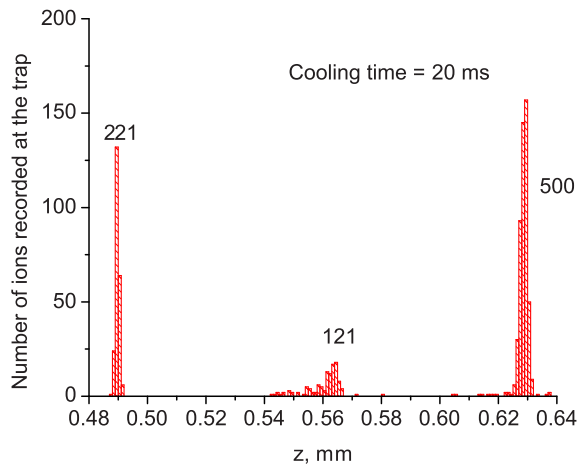
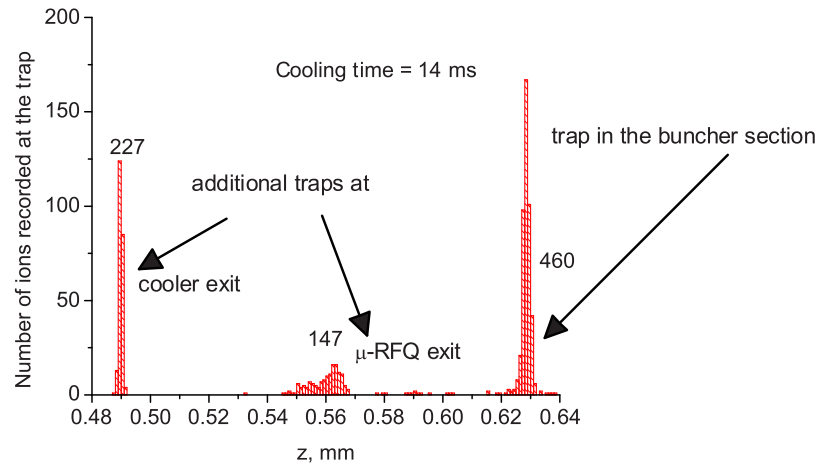


Figure 5.41: Simulated axial distributions of $^{40}\text{Ar}^+$ ions for 3 different cooling times. The positions the trap in the buncher section, and two additional “parasitic” traps at the cooler exit and μ -RFQ exit are indicated. The number of ions in each group is given next to the distribution.

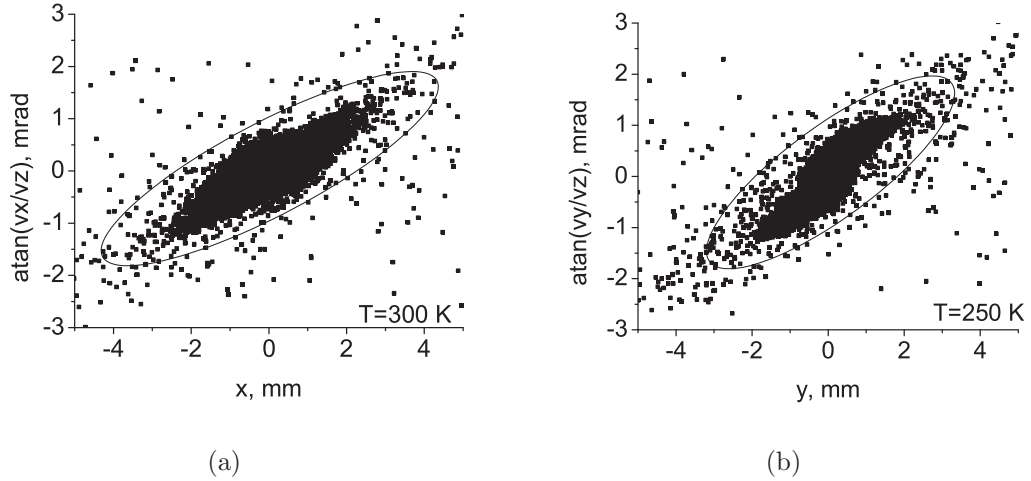


Figure 5.42: Simulated transverse emittance of $^{40}\text{Ar}^+$ ion pulses accumulated in the ion buncher and detected at the location of MCP5. (a) $T=300\text{ K}$; (b) $T=250\text{ K}$. The ellipse in each figure covers 95% of the ions.

shown in Fig. 5.42. The corresponding beam emittance in each case was evaluated with the area of the ellipse that covers 95% of ions, as discussed in Chapter 3. An emittance of mm mrad is obtained at $T=300\text{ K}$ and compared nicely within uncertainties to the experiment result of $\varepsilon=18.2\pi\text{ mm mrad}$ as obtained in section 5.5.3. For $T=250\text{ K}$, the calculated emittance is $\varepsilon=14.2\pi\text{ mm mrad}$, about 20% smaller than the measured value. That can probably be attributed to the effect of the RF phase, for which assumptions have been made in the simulation that are somewhat different from the actual condition in the experiment.

Chapter 6

First Penning trap mass measurement of rare isotopes

The initial experiments carried out at the LEBIT facility are mass measurements of exotic nuclei. For that purpose a 9.4 Tesla Penning trap mass spectrometer is used. The first high-precision mass measurements with LEBIT have been performed on the short-lived isotopes ^{37}Ca and ^{38}Ca . The ^{38}Ca isotope is a super-allowed β -emitter and can be used to test the CVC hypothesis [70]. The ^{37}Ca isotope is a potential test case for the Isobaric Multiplet Mass Equation. In this thesis the data for ^{37}Ca have been evaluated and the results have been applied to an improved determination of the energy of an excited state in ^{37}Ar .

6.1 Concept of the Penning trap

The ion confinement in a Penning trap is achieved by combining a homogeneous magnetic field $\vec{B} = B \cdot \hat{e}_z$ with an axial quadrupole electric field. The electric field is created by applying a DC voltage between hyperbolic trap electrodes as illustrated in Fig. 6.1. In these fields the stored ion performs three basic harmonic oscillations with different frequencies [71], as shown in Fig. 6.2. The axial motion parallel to the

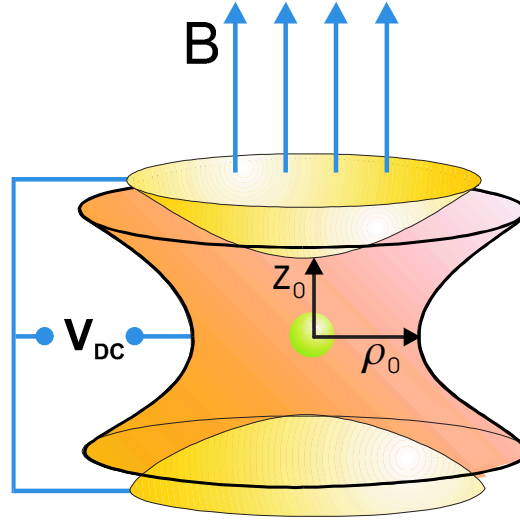


Figure 6.1: Basic electrode configuration of a Penning Trap.

magnetic field lines has an eigen frequency of

$$\omega_z = \sqrt{\frac{qV_{\text{DC}}}{md^2}} \quad (6.1)$$

where m/q is the mass-to-charge ratio of the ion, $d = \sqrt{\rho_0^2/4 + z_0^2/2}$ is the characteristic trap dimension, and V_{DC} is the voltage applied between the ring and endcap electrodes. Due to the existence of both the Lorentz force and the electric force in the plane perpendicular to the magnetic field, the radial motion is a superposition of two independent motions, which are called reduced cyclotron motion and magnetron motion. The oscillating frequencies of these two motions are

$$\omega_{\pm} = \omega_c/2 \pm \sqrt{\omega_c^2/4 - \omega_z^2/2} \quad (6.2)$$

with $\omega_c = qB/m$ being the cyclotron frequency of the ion in a pure magnetic field. Basic relations between the frequencies of these three eigen motions and the cyclotron frequency are

$$\omega_c = \omega_+ + \omega_- \quad (6.3)$$

$$\omega_c^2 = \omega_+^2 + \omega_-^2 + \omega_z^2 \quad (6.4)$$

and in the case of a strong magnetic field and a weak electrostatic field

$$\omega_+ \gg \omega_z \gg \omega_- \tag{6.5}$$

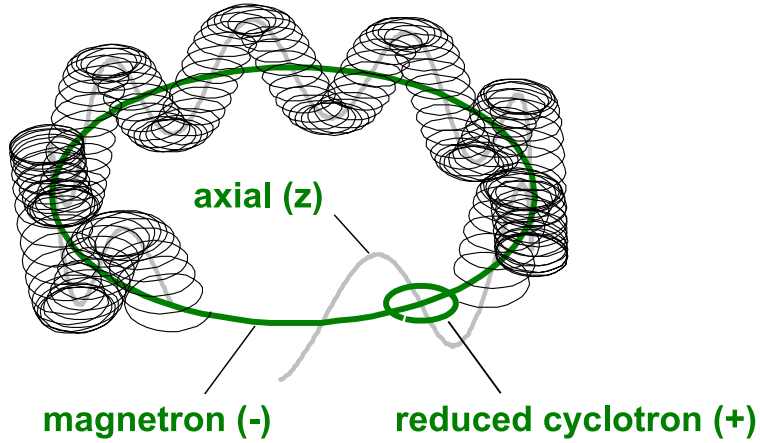


Figure 6.2: The three eigen motions of an ion stored inside a Penning trap.

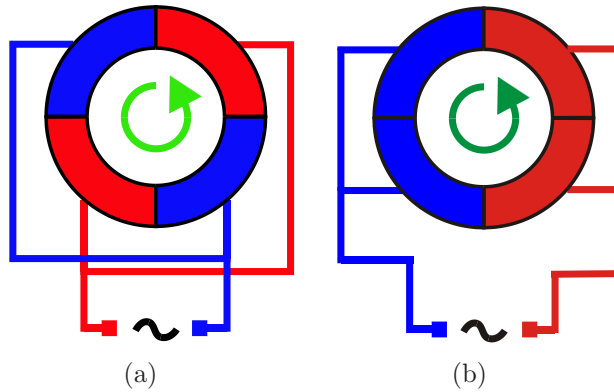


Figure 6.3: Electrode configurations to generate RF field for ion motion excitation. (a) quadrupole excitation; (b) dipole excitation.

For the mass determination of the stored ions or the removal of unwanted ions it is necessary to drive the ion motion with an external RF field. The most important excitation schemes are dipole and quadrupole excitations of the radial motion. The required electrode configurations are shown in Fig. 6.3. The ring electrode is separated into four symmetric segments in both cases. A pair of electrodes marked with the same color are connected to one of two RF voltages, which have same amplitude V_{rf} and frequency ω_{rf} but opposite polarities.

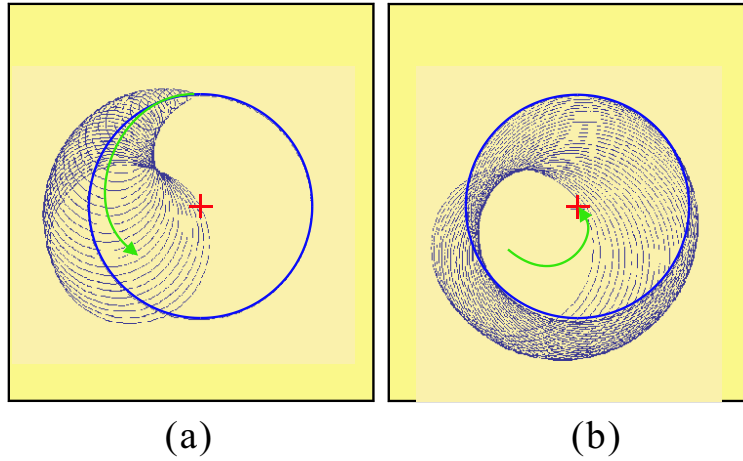


Figure 6.4: Conversion of an initial pure magnetron motion (a) into a pure reduced cyclotron motion (b) caused by a quadrupole excitation of the ion motion at the cyclotron frequency.

In the case of a quadrupole excitation, the RF voltages are applied between two pairs of opposing segments as shown in Fig. 6.3(a). If the RF frequency is set to be equal to the cyclotron frequency, a common mode excitation of the magnetron and reduced cyclotron motions is achieved. The simplest situation of this excitation starts from a pure magnetron motion as shown in Fig. 6.4(a). Under the influence of the quadrupole RF field, the oscillation amplitude of the magnetron motion decreases steadily, accompanied by an increase of the amplitude for the reduced cyclotron motion. Eventually the reduced cyclotron motion completely replaces the magnetron motion with an amplitude equal to that of the initial amplitude of the magnetron motion as shown in Fig. 6.4(b). As a result, the radial energy of the motion has significantly increased due to the difference between the two eigen frequencies, $\omega_+ \gg \omega_-$. The process shown in Fig. 6.4 reverses if the RF excitation of the ion motion continues. The period of this kind of harmonic beating between two eigen motions can be approximated by [71]

$$T_{\text{conv}} = \frac{4\pi\rho_0^2 B}{V_{\text{rf}}} \quad (6.6)$$

for $\omega_+ \gg \omega_-$. The RF amplitude $V_{+\rightarrow-}$ for a complete conversion from a pure magnetron motion into a pure reduced cyclotron motion or vice versa during an RF

excitation time T_{rf} is

$$V_{+\rightarrow-} = \frac{2\pi\rho_0^2 B}{T_{\text{rf}}}. \quad (6.7)$$

This conversion will not be complete if $\omega_{\text{rf}} \neq \omega_c$ or if the initial motion is not a pure magnetron motion, resulting in a smaller change of the radial energy.

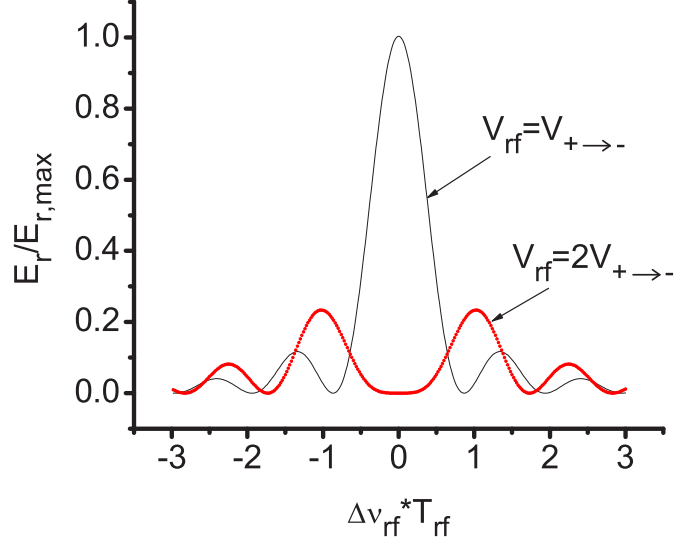


Figure 6.5: Normalized radial energy $E_r/E_{r,\text{max}}$ of the ion motion in the case of an azimuthal quadrupole excitation as a function of the detuning $\Delta\nu_{\text{rf}} \cdot T_{\text{rf}}$. The solid and dashed curves correspond to excitation amplitudes of $V_{\text{rf}}=V_{+\rightarrow-}$ and $V_{\text{rf}}=2V_{+\rightarrow-}$, respectively.

In order to determine the cyclotron frequency of the ion, an RF amplitude $V_{\text{rf}}=V_{+\rightarrow-}$ is chosen that leads to a full conversion of the magnetron into the reduced cyclotron motions. The RF frequency is scanned over a set of values close to the cyclotron frequency. The radial energy of the RF excitation of the ion motion depends on both the excitation time T_{rf} and the frequency difference of $\Delta\omega = \omega_{\text{rf}} - \omega_c$ as [71]

$$E_r \propto \frac{\sin^2(\omega_B T_{\text{rf}})}{\omega_B^2} \quad (6.8)$$

with

$$\omega_B = \frac{1}{2} \sqrt{(\Delta\omega)^2 + k_0^2} \quad (6.9)$$

and $k_0=2\pi/T_{\text{conv}}=V_{\text{rf}}/(2\rho_0^2B)$. Fig. 6.5 shows resonance profiles for two different RF amplitudes, which plot the radial energy E_r normalized by its maximum $E_{r,\text{max}}$ as a function of the detuning $\Delta\nu_{\text{rf}} \cdot T_{\text{rf}} = \Delta\omega/2\pi \cdot T_{\text{rf}}$. The solid curve is for the case of $V_{\text{rf}}=V_{+\rightarrow-}$, which corresponds to a complete conversion from a pure magnetron motion into a pure reduced cyclotron motion for $\omega_{\text{rf}} = \omega_c$. The dashed curve is for the case of $V_{\text{rf}}=2V_{+\rightarrow-}$, representing a full beating at the end of the excitation.

A time-of-flight resonance detection technique is used in LEBIT to determine the increase of radial energy. After capture and RF excitation the ions are ejected out of the Penning trap. Their time-of-flight to a detector located outside the strong magnetic field is measured. Each extracted ion will experience an accelerating force $\vec{F} = -\vec{\mu}(\partial B(z)/\partial z)$ where $\mu=E_r/B$ is its orbital magnetic moment and $\partial B(z)/\partial z$ is the gradient of the magnetic field. The orbital magnetic moment is proportional to the radial energy that the ion gained during the RF excitation. That leads to a larger acceleration and shorter time-of-flight of the ions, if the RF frequency ω_{rf} is equal to ω_c . The measured curve of the mean time-of-flight as a function of the applied RF frequency shows a resonance. The center of the resonance peak is equal to the cyclotron frequency, which can be used to determine the mass of the ions.

In the case of a dipole excitation, the RF voltages are applied between two pairs of neighboring segments of the ring electrode as shown in Fig. 6.3(b). The RF field can drive the radial motion with $\omega_{\text{rf}} = \omega_+$ or $\omega_{\text{rf}} = \omega_-$. The amplitude of the excited motion increases linearly with time. The excitation at ω_+ , which is strongly mass dependent, can be used to selectively remove ion species from the trap.

6.2 High precision mass measurement of ^{37}Ca with Penning trap mass spectrometer

The radioactive ^{37}Ca isotope was chosen as one of the first exotic nuclei for a high precision mass measurement with the LEBIT Penning trap mass spectrometer. It is

a short-lived nucleus with a half-life of only $T_{1/2}=181.1$ ms and located far away from the valley of stability on the nuclear chart. The rate of ^{37}Ca ions from the gas cell is low, which makes it a good candidate to test the performance of LEBIT with few statistics. Its published mass excess is $\text{ME}(^{37}\text{Ca})=-13162(22)$ keV [72] and has a rather large uncertainty. The ^{37}Ca isotope belongs to the isobaric quartet of $A=37$ and $T=3/2$. A precision mass measurement of it can in principle contribute to the further test of the Isobaric Multiplet Mass Equation (IMME), provided that the masses of all other isobaric analog states are well known.

In the ^{37}Ca experiment the following procedure was used. A primary beam of ^{40}Ca at an energy of 140 MeV/u is used to produce fragments in a thin Be target. Ions of $^{37}\text{Ca}^{17+}$ at an energy of 93 MeV/u are separated from other species by the A1900 fragment separator and transported towards the gas cell. Before entering the gas cell, this high energy beam is dispersed on a wedged solid degrader in order to minimize the final range distribution in the gas cell. After passing a Be window this beam enters the gas cell chamber, where the ions thermalize by collisions with the He gas at a pressure of 1 bar. During this process the ions reduce their charge state. The ^{37}Ca ions remain in the 2+ state due to their relatively lower ionization potential as compared to that of He in the 1+ state. The thermalized ions are guided to the supersonic nozzle at the end of the gas cell by an electric drifting field created inside the gas cell by means of an electrode system. After that the gas flow takes over and delivers ions to the RFQ ion guides. In the last section of ion guides the ions pass through a mass filter before they are accelerated for further transport. In the ^{37}Ca experiment, transported activity was observed at the end of the mass filter with a β - detector (See section 2.1) at mass-to-charge ratios $A/Q=27.5, 36.5, 45.5$ and 54.5 . These could be associated with doubly-charged molecular ions of $[^{37}\text{Ca}(\text{H}_2\text{O})_n]^{2+}$, where $n=1-4$. The attachment of water molecules is due to a relatively high partial water vapor pressure present in the gas cell during the time of the experiment. This was due to an earlier cleaning and reassembly of the gas cell. For ^{37}Ca mass measurement the mass filter

was set to select the lightest and most abundant of the molecules, $[^{37}\text{Ca}(\text{H}_2\text{O})]^{2+}$.

The mass separated beam was then transported to the ion buncher system as discussed in Chapter 5. After being trapped in the buncher section for enough time these ions are extracted and delivered to the Penning trap. In the calcium experiment, the cooler section was filled with Ne as the buffer gas, which was found to be very effective not only for ion cooling but also for dissociating the loosely-bound molecular ions via Collision Induced Dissociation (CID). That leads to the break-up of $[^{37}\text{Ca}(\text{H}_2\text{O})]^{2+}$ molecular ions into $^{37}\text{Ca}^{2+}$ atomic ions.

Prior to the actual mass measurement the composition of the ion cloud captured in the Penning trap was analyzed by searching for their cyclotron frequencies. The five main contaminants identified were Ne^+ , $[\text{N}(\text{H}_4)]^+$, $[\text{HO}]^+$, $[\text{C}(\text{H}_5)]^+$ and $[\text{H}_3\text{O}]^+$.

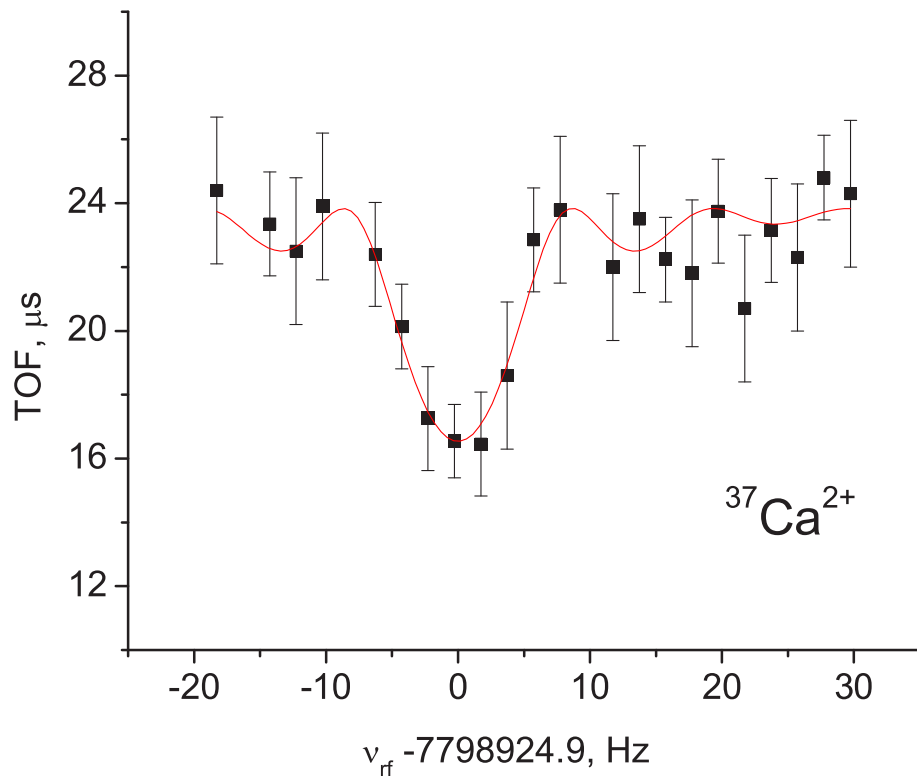


Figure 6.6: Cyclotron resonance for $^{37}\text{Ca}^{2+}$ ions obtained with a time-of-flight resonance detection technique. The solid line is a fit of the theoretical line shape to the data points.

The mass measurement of ^{37}Ca was performed according to the following sequence. Ions were ejected from the ion buncher and captured in the Penning trap. For all contaminating ion species listed above RF dipole excitations were applied with the corresponding reduced cyclotron frequencies ω_+ . This is important in order to avoid frequency shifts due to ion-ion interactions of unequal species [73]. After this cleaning process, which takes about 10 ms, an azimuthal RF excitation with a trial frequency close to $\omega_c(^{37}\text{Ca}^{2+})$ was applied to excite the remaining $^{37}\text{Ca}^{2+}$ ions. An RF excitation time of $T_{\text{rf}}=150$ ms was chosen, compatible with the half-life of the ions of 180 ms. The $^{37}\text{Ca}^{2+}$ ions ejected from the Penning trap were detected with the ion detector located outside the strong magnetic field (see Fig. 3.3). The time-of-flight of these ions, which depends on the radial energy the ions gained during the excitation process, is measured. The above procedure was repeated for different RF excitation frequencies. Fig. 6.6 shows one such resonance curve obtained for $^{37}\text{Ca}^{2+}$, which illustrates the mean time-of-flight of the ions from the trap to the ion detector as a function of the applied RF frequency. The resonance curve has been obtained by analyzing the time of flight of the ions in a minimum time window as narrow as possible without losing good ion events, in order to minimize the influence of possible background events for example due to detector dark pulses or the occasional presence of an unremoved contaminating ion. Since the ^{37}Ca countrate was very low (typically 0.5 ions/minute), this window was determined by analyzing the time-of-flight distributions of $[\text{H}_3\text{O}]^+$ ions, which have a very similar A/Q.

The measurement for the resonance shown in Fig. 6.6 took about 70 minutes and only 37 $^{37}\text{Ca}^{2+}$ ions were observed inside the chosen time-of-flight window. Due to the low total number of counts not all frequencies have a data point. The uncertainty of each time-of-flight point was evaluated with a maximum likelihood method. The solid line shows a fit of the theoretical resonance curve [71] to the data. The line width $\Delta\nu_{\text{FWHM}}=6.7$ Hz corresponds to a resolving power of $R=2\times 10^6$. Similar measurements were repeated nine times during a period of 18 hours. The $^{37}\text{Ca}^{2+}$ measurements were

alternated with a cyclotron frequency measurement of $[\text{H}_3\text{O}]^+$, serving as the reference ion for the magnetic field calibration. $[\text{H}_3\text{O}]^+$ was chosen as the reference for several reasons. It has a very small mass uncertainty of only $\delta m/m < 1 \times 10^{-9}$ and it was presented as a contaminant in the beam from the gas cell. With $A/Q=19$ it has a very similar mass-to-charge ratio as $^{37}\text{Ca}^{2+}$, which minimizes mass-dependent systematic effects. The reference measurements were performed about every two hours.

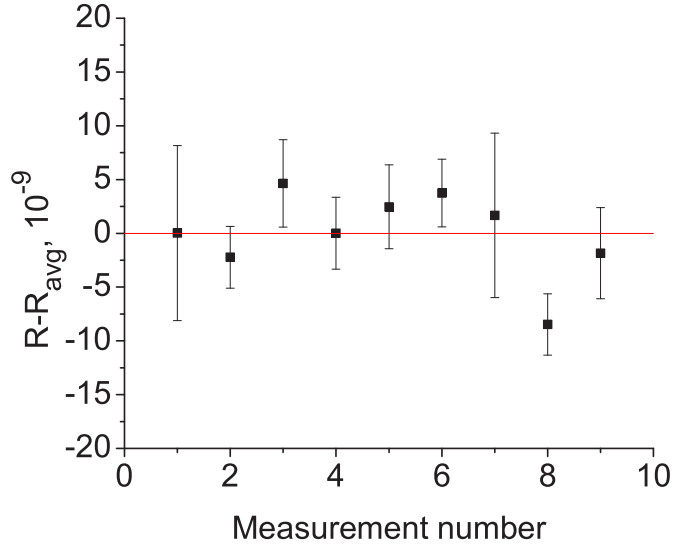


Figure 6.7: Measured cyclotron frequency ratios R between $(\text{H}_3\text{O})^+$ and $^{37}\text{Ca}^{2+}$ relative to the average value \bar{R} .

In the data evaluation the magnetic field was assumed to change linearly between each two consecutive reference measurements. The frequency ratio $R_i = \nu_c([\text{H}_3\text{O}]^+)/\nu_c(^{37}\text{Ca}^{2+})$ was determined by two reference measurements bracketing each $^{37}\text{Ca}^{2+}$ measurement. The individual results are summarized in Fig. 6.7, which shows the deviation of the single frequency ratios R_i from their weighted average $\bar{R} = 0.972371165(15)$. The statistical uncertainty of the weighted average of $\delta\bar{R} = 1.2 \times 10^{-8}$ (inner error) is in good agreement with the outer error of 1.5×10^{-8} calculated from the standard deviation for all individual results. This confirms that the scattering of the data is statistical, as already visible from Fig. 6.7.

There are a number of possible systematic errors that need to be analyzed. These

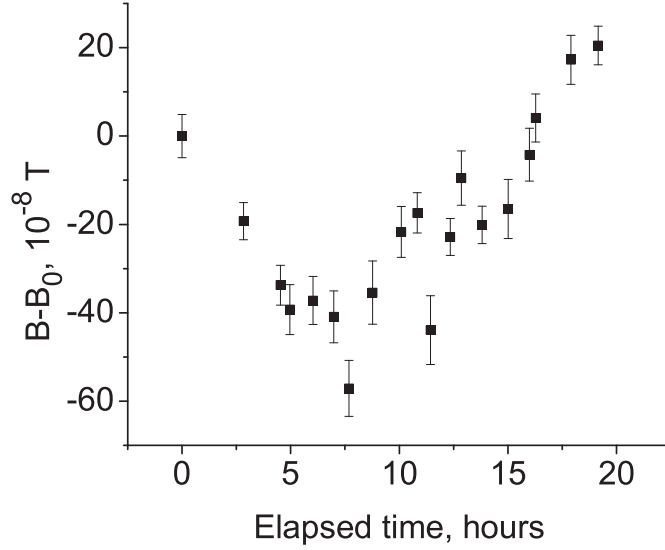


Figure 6.8: Magnetic field drift over an 18 hour time period of the $^{37}\text{Ca}^{2+}$ mass measurement.

errors have to be applied to \bar{R} before using it to determine the mass of ^{37}Ca . The first is from the magnetic field drift. The change of the magnetic field over 18 hours of measurement time is shown in Fig. 6.8. The magnetic field fluctuates due to the change of the pressure and temperature near the magnet. The effect of a non-linearity of magnetic field changes between reference measurements was analyzed and found to be less than 2×10^{-9} , which can be neglected. Based on earlier mass comparisons of ions with large mass differences and the very similar mass-to-charge-ratio of H_3O^+ and $^{37}\text{Ca}^{2+}$ mass-dependent systematic effects are estimated to similarly small. Another possible systematic error is due to the low statistics in the measurement and the possibility of background events detected in the time-of-flight window used to analyze the time of flight of the $^{37}\text{Ca}^{2+}$ ions. As will be discussed in more detail later, this error is $\delta R = 1.1 \times 10^{-8}$. It is used to obtain the final value for the frequency ratio of $\bar{R} = 0.972371174(19)$.

The atomic mass value for ^{37}Ca is obtained from \bar{R} via $m(^{37}\text{Ca}) = (2\bar{R})(m(\text{H}_3\text{O}) - m_e) + 2m_e$, where m_e is the electron mass. The binding energies of the missing electrons are neglected here because they are very small relative

Table 6.1: Input data and error budget for the determination of the mass of ^{37}Ca .

Input mass and mass excess values, keV	$\text{ME}(^1\text{H})$	= 7288.9705(1) [72]
	$\text{ME}(^{16}\text{O})$	= -4737.0014(1) [72]
	m_e	= 510.99906(15) [67]
	$\text{ME}(\text{H}_3\text{O})$	= 17129.9026(5)
Frequency ratio	$R_i = \nu_c([\text{H}_3\text{O}]^+)/\nu_c(^{37}\text{Ca}^{2+})$	= 0.972371174(19)
Statistical uncertainty	δR_{stat}	= 1.5×10^{-8}
Systematic uncertainty	δR_{sys}	= 1.1×10^{-8}
Total uncertainty	δR_{tot}	= 1.9×10^{-8}
^{37}Ca mass excess, keV	$\text{ME}(^{37}\text{Ca})$	= -13135.7(1.4)

to the measurement uncertainty. The mass excess of H_3O is $\text{ME}=17129.9026(5)$ keV. The resulting mass excess value for ^{37}Ca is $\text{ME}=-13135.7(1.4)$ keV. This value agrees well with the literature value $\text{ME}=-13162(22)$ keV presented in the Atomic Mass Evaluation (AME03) [72], but it is an order of magnitude more precise.

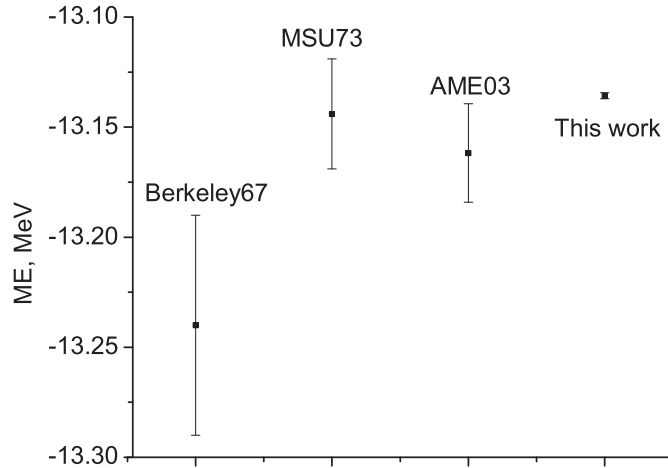


Figure 6.9: Comparison of the ^{37}Ca mass obtained in different experiments and the literature value (AME03).

As a comparison, the newly measured mass of ^{37}Ca is plotted together with the mass values of AME03 and two other experiments [17] [74] in Fig. 6.9. The AME03

Table 6.2: Comparison of the mass excess values for ^{37}Ca from different sources.

Source	ME(^{37}Ca), keV
Berkeley67 [74]	-13240(50)
MSU73 [17]	-13144(25)
AME03 [72]	-13162(22)
This work	-13135.7(1.4)

value is based on a combination of the two earlier experiment results. The Berkeley67 result is from an indirect mass measurement at the 88-inch cyclotron at Berkeley [74]. The mass of ^{37}Ca was determined via the $^{40}\text{Ca}(^3\text{He}, ^6\text{He})^{37}\text{Ca}$ reaction. The Q-value of the reaction was measured to be -24.27(5) MeV, resulting in a ^{37}Ca mass excess of -13.24(5) MeV. The other result (MSU73) is from a similar measurement [17] with a split pole spectrograph with a 70.7 MeV He beam from the Michigan State University cyclotron. The ^{37}Ca mass was determined by comparing the rigidity of ^6He particles from the $^{40}\text{Ca}(^3\text{He}, ^6\text{He})^{37}\text{Ca}$ reaction to the rigidity of ^6He particles in the previously measured $^{58}\text{Ni}(^3\text{He}, ^6\text{He})^{55}\text{Ni}$ and $^{24}\text{Mg}(^3\text{He}, ^6\text{He})^{21}\text{Mg}$ reactions. By doing that the mass excess of ^{37}Ca was measured to be -13.144(25) MeV. All of these results are listed in Table 6.2. The table and Fig. 6.9 show that the LEBIT result agrees very well with the earlier MSU result but has a much smaller uncertainty than any of the previous results.

6.3 Application of the ^{37}Ca mass measurement result together with the Isobaric Multiplet Mass Equation

Since the strong or hadronic interaction is nearly charge independent, the isospin formalism is one of the basic tools in nuclear as well as particle physics. Neutron and proton have isospin $T=1/2$ with $T_z(\text{neutron})=+1/2$ and $T_z(\text{proton})=-1/2$. Every state of

a nucleus has an isospin T and belongs to a $(2T+1)$ multiplet formed by analog levels in isobaric nuclei. The charge of each member is measured by its isospin projection $T_z=(N-Z)/2$. In light nuclei isobaric analog states (IAS) have nearly identical wave functions. The charge dependent energy difference of these states can be calculated in first-order perturbation theory under the assumption of only two-body coulomb forces. This leads to the simple equation,

$$M = a + bT_z + cT_z^2 \quad (6.10)$$

that gives the mass M of a member of an isospin multiplet as a function of T_z . This quadratic relation is called the isobaric multiplet mass equation (IMME). IMME was first introduced by Wigner [75] and its origin and deviation from the simple quadratic form were further discussed (see for example [76–78]). The coefficients a , b , c and, if a cubic form is considered, d are unique for each multiplet. Higher multiplets ($T \geq 3/2$) can be used to test if higher order terms, for example a cubic term dT_z^3 , is required to fit the masses of the isobaric analog states. A relatively recent compilation of completely measured multiplets and the corresponding evaluation of IMME coefficients can be found in [79]. Of all 32 known multiplets with $T \geq 3/2$ only the $A=9$, $T=3/2$ quartet and the $A=8$, $T=2$ quintet are significant exceptions where higher-order terms need to be included to reproduce the experimental data. Recent high-precision Penning trap mass measurements on $^{32,33}\text{Ar}$ have provided the so far most stringent test of IMME in the case of the $A = 32$, $T = 2$ quintet and the $A = 33$, $T = 3/2$ quartet [80]. Therefore, the quadratic form of IMME is considered a reliable tool to predict masses and excitation energies in multiplets with $T \geq 3/2$.

In this work the mass of ^{37}Ca has been measured. This isotope is a member of the $A = 37$, $T = 3/2$ quartet formed by the isobaric analog states in ^{37}Ca , ^{37}K , ^{37}Ar , and ^{37}Cl . The isospin projections are $T_z=-3/2$, $-1/2$, $1/2$ and $+3/2$, respectively. The first and fourth members are ground states, while the remaining two are excited states.

Table 6.3: Mass excess values of isobaric analog states (IAS) in the A=37 and T=3/2 quartet.

Nucleus	T_z	ME of GS (keV) ^a	E_x (keV) ^b	ME of IAS (keV)
³⁷ Cl	3/2	-31761.53(5)	0	-31761.53(5)
³⁷ Ar	1/2	-30947.66(21)	4993(6)	-25955(6)
³⁷ K	-1/2	-24800.20(9)	5049.7(8)	-19750.5(8)
³⁷ Ca	-3/2	-13135.7(1.4)	0	-13135.7(1.4)

^aData are from AME03 [72] except that of ³⁷Ca, which is taken from this work.

^bAvailable data are from reference [81].

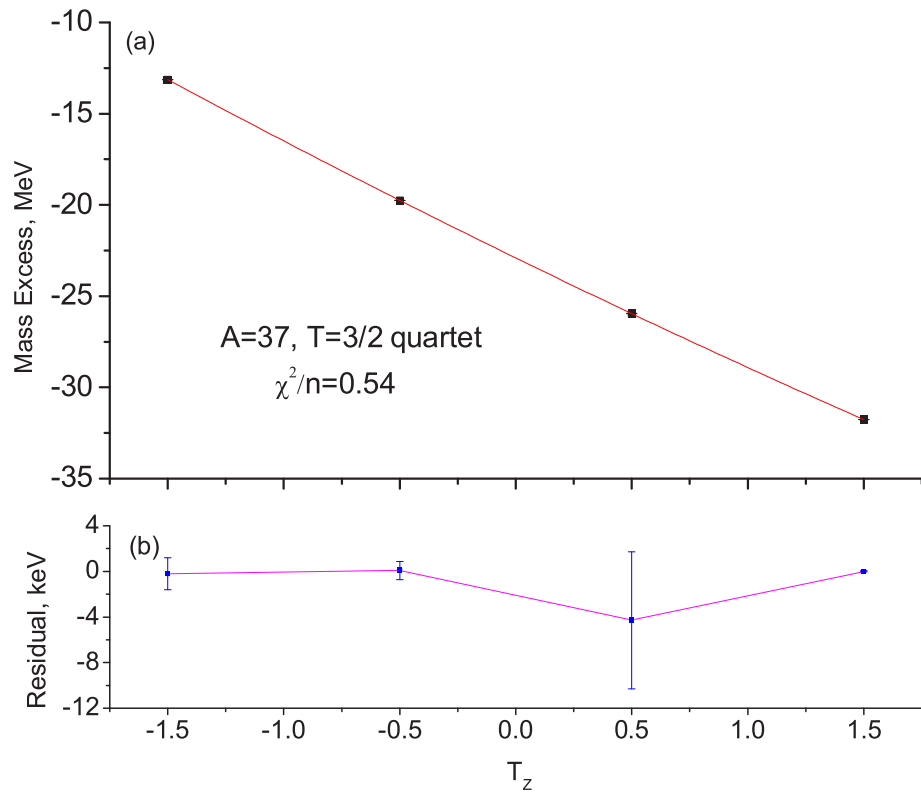


Figure 6.10: (a) Mass excess values of isobaric analog states in the A=37 and T=3/2 quartet. The solid line is from the quadratic fit of IMME to all data. (b) Residual.

Table 6.3 lists the available data for the $A=37$, $T=3/2$ quartet. The ground state mass values for ^{37}Cl , ^{37}Ar , and ^{37}K are taken from AME03 [72]. For ^{37}Ar the new mass excess value obtained with LEBIT is listed. Together with the known excitation energies [81] of the isobaric analog states in ^{37}Ar and ^{37}K this results in the mass values for the isobaric analog states given in the last column.

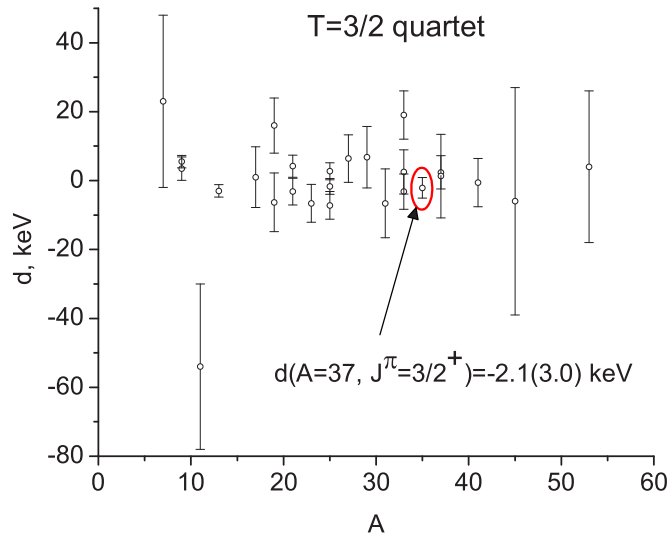


Figure 6.11: Values of the d coefficient of IMME for all the 25 $T=3/2$ quartets. The value of for the $A=37$, $J^\pi = 3/2^+$ quartet is from this work, all the rest data are taken from reference [79].

Fig. 6.10 shows the mass values of all isobaric analog states as listed in Table 6.3 together with a fit of IMME to these data and the corresponding residuals. The reduced χ^2 of this fit is 0.54. As an additional check, a higher term of dT_Z^3 is added to the quadratic form of IMME to investigate how adequate the first-order perturbation theory is to this quartet. All the four IMME coefficients with this new calculation are listed in Table 6.4. The fit results for the cubit coefficient, $d=-2.1(3.0)$ keV, indicates no need to include a cubit term in IMME. However, it should be noted that the uncertainty of d is still large compared to the most precise tests performed in some of the other quartets, as shown in Fig. 6.11. The mass of the ^{37}Ar IAS has a large uncertainty compared to all other members of the quartet, which does not allow for

Table 6.4: Extended coefficients of IMME for the $A = 37$, $T = 3/2$ and $J^\pi = 3/2^+$ quartet. All the masses of this quartet are used to calculate coefficients up to a cubic term.

IMME coefficients a,b,c,d, keV	
a	-22903.3(3.4)
b	-6204.0(6.8)
c	202.1(1.6)
d	-2.1(3.0)

a very high precision test of the quadratic form of IMME. In order to make such a test significant, the excitation energy of ^{37}Ar would need to be measured with an uncertainty lower than $\delta E_x(^{37}\text{Ar}) = 2.8$ keV, which is comparable to the maximum mass uncertainty of the other three members of this quartet.

Since three other members are now very well known due to the new LEBIT result, and assuming that the quadratic form of IMME is valid for this quartet, it is possible to predict the energy of the excited isobaric analog state in ^{37}Ar . Improved IMME coefficients are obtained by fitting the quadratic form of IMME to the three well known data. The resulting values are listed in Table 6.5. The table also lists the IMME coefficients given in [79], which were obtained with the earlier, less precise mass value for ^{37}Ca . As can be seen a drastic reduction of the uncertainty of the coefficients is obtained. Using IMME with the improved coefficients leads to a mass excess value of the excited ^{37}Ar state of $-25959.1(1.2)$ keV. Taking the ground state mass value into account results in an excited state energy of $E_x(^{37}\text{Ar})=4989(1)$ keV. This value agrees with the previous value of $4993(6)$ keV [81], but is a factor of six more precise.

6.4 Simulations of resonances under low statistics

The low statistics of $^{37}\text{Ca}^{2+}$ measurement could be a source of the systematic error for the mass determination in the case of background events that fall into the analysis

Table 6.5: Quadratic coefficients of IMME for the $A = 37$, $T = 3/2$ and $J^\pi = 3/2^+$ quartet. The previous data were calculated with old mass values of both ^{37}Ar and ^{37}Ca [79]. The coefficients from this work are calculated with the well-known masses of ^{37}Cl , ^{37}K and ^{37}Ca .

IMME coefficients a,b,c, keV		
	old [79]	this work
a	-22901(4)	-22905.57(97)
b	-6203(5)	-6208.60(45)
c	197(5)	203.08(61)

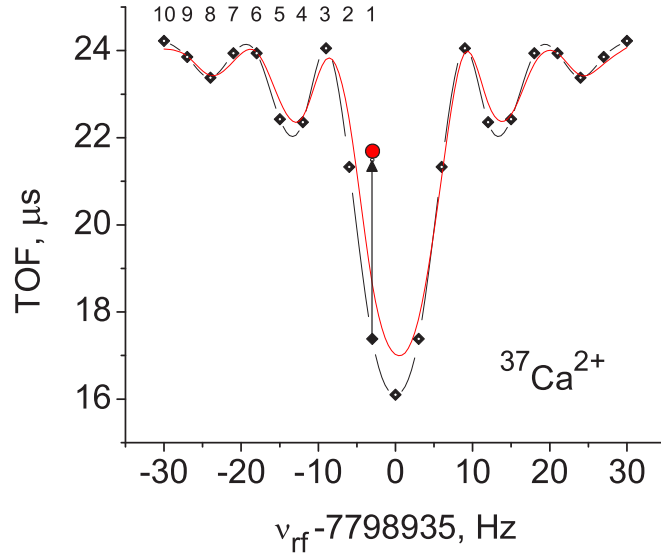


Figure 6.12: Examples of cyclotron resonance curves used to simulate the effect of background events in the case of low-statistics measurements. The black curve of connected dots represents the fit of the theoretical curve to undistorted time-of-flight data. The red solid curve shows a similar fit in the case of a background event shifting the mean time-of-flight of the off-center frequency point labelled **1**.

window for the time of flight of the ions for the cyclotron resonance determination. This events could be detector background or occasional unremoved contaminating ions. If present in the time-of-flight analysis window they can change the shape of the resulting resonance curve. That effect can be neglected when the mass measurement is performed with a high statistics but could be important at low statistics, depending on the ratio of good events to background events. The result can be a shift of the center frequency obtained via a fit of the theoretical curve to the data points as illustrated in Fig. 6.12. In order to be able to estimated a possible systematic error due to this effect a simulation under conditions close to that present during the ^{37}Ca experiment was performed.

The theoretical resonances shown in Fig. 6.12 curve consist of 21 frequency points as used in the experiment. It is assumed that only one ion is observed for one RF frequency. The time-of-flight of the ions is calculated as expected theoretically [71] for an RF excitation time of 150 ms. The result is an unperturbed set of data points as shown in the figure. An off-resonance frequency point is chosen (labelled 1-9). Its time-of-flight is changed in several steps between the unperturbed value and a value given by the upper baseline of the resonance. The theoretical resonance curve is fitted to each of these sets of perturbed data points. The procedure is repeated for all the labelled frequency points. An example of such a fit is the solid red curve shown in the figure. The observed frequency shifts $\Delta\nu/\nu_c = (\nu'_c - \nu_c)/\nu_c$ are shown in Fig. 6.13 for the different frequency points investigated. The maximum frequency shift is observed for the frequency point closest to the center of the unperturbed resonance curve. The simulations show a maximum effect of $\Delta\nu_{\text{max}}/\nu_c = 1.6 \times 10^{-8}$. This value is used in the further evaluation of the probability of such an event and in obtaining an estimate on the systematic error due to the background events in the case of low statistics measurements.

The next question is the probability for the maximum effect to occur. For this purpose a high statistics resonance of $[\text{H}_3\text{O}]^+$ was analyzed. Fig. 6.14 shows the band

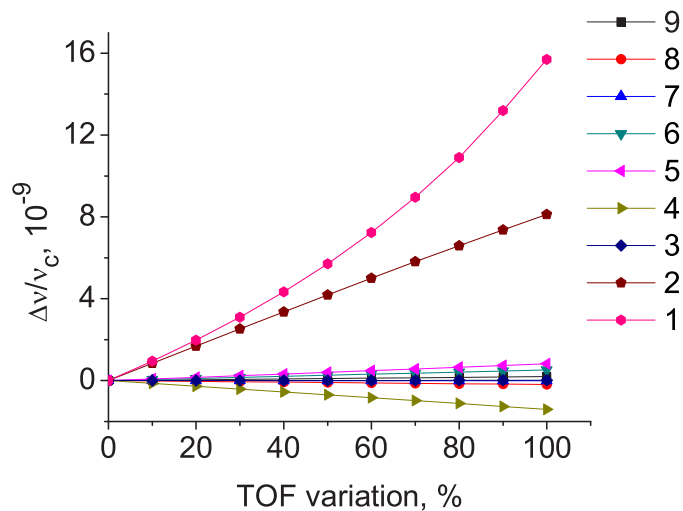


Figure 6.13: Simulated frequency shifts $\Delta\nu/\nu_c$ as a function of relative shift of the time-of-flight data for frequency points as labelled in Fig. 6.12.

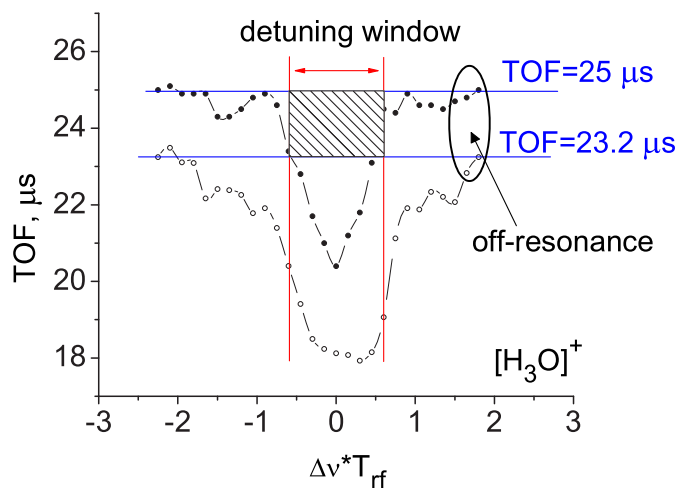


Figure 6.14: Cyclotron resonance curve of H_3O^+ . Shown is the band of minimum and maximum time-of-flight values for which ions were observed as a function of the detuning $\Delta\nu \cdot T_{\text{rf}}$. The band between $\text{TOF}=23.2 \mu\text{s}$ and $25 \mu\text{s}$ gives the range where ions are considered to be off-resonance (see text).

of minimum and maximum time-of-flight at which ions were observed at each frequency point. The horizontal lines between TOF=23.2 μs and 25 μs gives the time window in which ions can be considered to be off-resonance in first order. The vertical lines indicate the detuning range in which the data can be analyzed for the presence of background events or non-resonant ions. Events in the shaded area have to be considered as bad events.

After proper rescaling of the detuning window with respect to the different RF excitation time used in the H_3O^+ and $^{37}\text{Ca}^{2+}$ measurement, the shaded area was applied to a typical resonance curve of $^{37}\text{Ca}^{2+}$. Counting the events in this area and all events in the detuning range provides the information that about 20% of the events observed are to be considered bad. The possibility of the RF frequency to be the one that leads to a maximum frequency shift in either positive or negative direction is 1/10, corresponding to the inverse of the number of data points on each side of the center of the resonance. Taking these factors into account leads to a probability of only 2% to observe the maximum frequency shift of $\Delta\nu_{\text{max}}/\nu_c=1.6 \times 10^{-8}$ calculated earlier. For a confidence level of 68% this corresponds to a systematic uncertainty of $\delta R_{\text{sys}}=1.1 \times 10^{-8}$. This value together with the obtained statistical uncertainty has been used for the ^{37}Ca mass evaluation as discussed earlier.

Chapter 7

Summary

The Low Energy Beam and Ion Trap facility has been built and successfully commissioned at the Coupled Cyclotron Facility of the NSCL. LEBIT is the first system of its kind for low-energy atomic and nuclear physics experiments with thermalized rare isotope beams obtained by fast-beam fragmentation. It opens the door to high precision atomic mass measurements with Penning traps, laser spectroscopy for the study of charge radii and moments of rare isotopes, or the possibility of post-acceleration for nuclear astrophysics experiments. The first experiments performed with LEBIT are atomic mass measurements of short-lived isotopes. LEBIT consists of a gas stopping station in which fast-beam fragments are stopped, thermalized, and converted into a continuous low-energy beam of rare isotopes. A gas-filled radio frequency ion trap converts this beam into cooled ion bunches, which are then captured in a 9.4 Tesla Penning trap system for their mass determination. LEBIT was designed, built and brought into operation in a period of about 5 years. It is a complex system and many students and several postdocs have contributed to its realization. Within my PhD work I have been responsible for the ion optical design of the low-energy beam-line system and the development of a control system for LEBIT. I performed systematic studies of the performance of the ion beam cooler and buncher of LEBIT and analyzed the first mass measurements of a very short-lived rare isotope, ^{37}Ca .

The design of the electrostatic beam transport system for LEBIT has been based on detailed ion optical simulations. Relevant parameters were optimized to maintain the beam emittance throughout the system and to achieve a good transport efficiency. The realized system works very well, with operational parameters close to those simulated. No significant losses are observed in the beam line system.

The LEBIT control and data acquisition system has been developed with LabVIEW and C++. It has been operated for more than two years fulfilling all required features, which include system reliability, fast response, high precision, flexibility and safety.

A series of systematic measurements have been carried out to study the performance and properties of the LEBIT ion beam cooler and buncher. Ion mobility measurements have been used to characterize the cooling process and beam emittance and pulse width measurements have been carried out to characterize the properties of the extracted ion pulses. Results of the measurements are in a good agreement with corresponding simulations.

The first mass measurements of radioactive isotopes ^{37}Ca and ^{38}Ca were performed in July 2005. The ^{37}Ca measurement, evaluated in this thesis, provides a high-precision mass value of $M = -13135.7(14)$ keV which agrees very well with the literature values, but has a much lower uncertainty. The new mass value of ^{37}Ca has been applied to the Isobaric Multiplet Mass Equation for the $A=37$, $T=3/2$ quartet. The excitation energy of ^{37}Ar is now predicted with an uncertainty six times lower than the literature value, obtained from experimental data only.

Since the very first mass measurements of rare isotopes with LEBIT several other isotopes have been studied. At the time of completing this thesis they are $^{66}, ^{67}\text{As}$, ^{65}Ge and $^{81}, ^{81m}\text{Se}$. This is a very successful start of a mass measurement program that can be expected to significantly contribute to the better understanding of nuclear structure, the synthesis of elements in nuclear astrophysical processes, and the test of fundamental interactions and symmetries.

Appendix A

Details of ion optical simulation of the beam transport

In this chapter I will present details of the ion optical simulation for the LEBIT beam transport system. The transverse phase space diagrams for the continuous and pulsed beam with the corresponding emittance values will be presented for all sections except for the beam transport from the switchyard to the Penning trap, where the radial energy pickup is more important and will be discussed instead. The optimum parameters of all the involved elements will be presented.

A.1 Notation used in the simulation

For the convenience of the discussion I will adopt the following notations throughout this chapter, unless otherwise specified.

1. Voltage of a single-electrode element: Single numeric value relative to the base potential V_{base} of the investigated section.
2. Voltage of an Einzel lens: Single numeric values that represents the voltage of the end electrode relative to its V_{base} . The voltages of the external electrodes are the same as the base potential V_{base} .

Table A.1: Parameters used in the ion optical simulation of the beam transport from the gas cell to the N4-shielding wall.

Parameter	Description
Urf1	RF Amplitude of the second last ion guide segment
Urf2	RF Amplitude of the last ion guide segment
Uoff1	DC offset of the second last ion guide segment
Uoff2	DC offset of the last ion guide segment
Udc1	DC voltage of the second last ion guide segment
Udc2	DC voltage of the last ion guide segment
Freq	RF frequency for both ion guide segments
Uaccel1	DC voltage of the first acceleration electrode
Uaccel2	DC voltage of the second acceleration electrode
Uaccel3	DC voltage of the third acceleration electrode
Uaccel4	DC voltage of the fourth acceleration electrode
Uel0	DC voltage of Einzel lens 0
U10def	DC voltage of the 10 degree deflector
Paccel1(l)	Position of the first acceleration electrode
Paccel2(l)	Position of the second acceleration electrode
Paccel3(l)	Position of the third acceleration electrode
Paccel4(l)	Position of the fourth acceleration electrode
Pel0(l)	Position and dimension of Einzel lens 0
P10def(c)	Position of the 10 degree deflector

3. Position of a single-electrode element: Single numeric value of distance between its center (marked as **(c)**) or left edge (marked as **(l)**) and the origin of the considered section.
4. Position and dimension of an Einzel lens: A series of numeric values in the format of **a | b | c | d**, where **a** follows the rule #3, **b** is the thickness of the external electrode, **c** is the gap thickness between the neighboring electrodes and **d** is the thickness of the center electrode.

A.2 From the gas cell to the N4-shielding wall

In the beam transport simulations for this section, the parameters listed in Table A.1 have been optimized. The table also gives a brief description of each parameter.

Table A.2: Optimum parameters of the elements of the beam transport system from the gas cell ion guide to the N4-shielding wall.

Parameter	Voltage relative to V_{base} , V	V_{base} , V
Uoff1	-10	0
Uoff2	-20	
Udc1	45	
Udc2	0	
Uaccel1	-20	
Uaccel2	-2600	
Uaccel3	-1100	
Uaccel4	-5000	
Uel0	-2070	-5000
U10def	± 355	
	Position and dimension, mm	
Paccel1(1)	35	
Paccel2(1)	50	
Paccel3(1)	65	
Paccel4(1)	80	
Pel0(1)	271 40 8 300	
P10def(c)	1311	

A SIMION user program was used to generate both RF and DC voltages applied to the last segments of the ion guide after the gas cell. Ions started in these fields and their transport through the remaining system up to the beam observation box (BOB1) was optimized with SIMION to achieve a beam focus at BOB1. The optimum parameters determined by this simulation are given in Table A.2. The calculated beam profile at the center of BOB1 has already been shown in Fig. 3.11.

A.3 From the N4-shielding wall to the ion buncher

A.3.1 Straight line transport from the N4-shielding wall to the ion buncher

The parameters listed in Table A.3 have been optimized for the beam transport in this section. Since we want to transport the beam directly to the ion buncher, the

Table A.3: Parameters used in the ion optical simulation for the straight line beam transport from the N4-shielding wall to the ion buncher.

Parameter	Description
Uwlens	DC voltage of the wall lens
Uel2	DC voltage of Einzel lens 2
Uel3	DC voltage of Einzel lens 3
Pwlens(c)	Position of the wall lens
Pel2(c)	Position of Einzel lens 2
Pel3(c)	Position of Einzel lens 3
Pquad(c)	Position of the quadrupole deflector

Table A.4: Optimum parameters of the elements for the straight line beam transport from the N4-shielding wall to the ion buncher.

Parameter	Voltage relative to $V_{\text{base}}=-5$ kV, V
Uwlens	2870
Uel2	-5500
Uel3	-5550
	Position and dimension, mm
Pwlens(c)	1200 80 5 1210
Pel2(c)	2700 30 5 30
Pel3(c)	3200 30 5 30
Pquad(c)	2960

voltages on the electrodes of the quadrupole deflector are all set to zero.

The optimal settings of all the involved elements are listed in Table A.4. The corresponding transverse phase space diagrams of the beam after transport with that are shown in Fig. A.1.

A.3.2 From the test ion source to the ion buncher

For this section only the parameters for the two vertical lenses and the quadrupole deflector, as listed in Table A.5, needed to be optimized. The voltage of for the lens after the deflector is kept the same as that for the straight line transport from the N4-shielding wall to ion buncher.

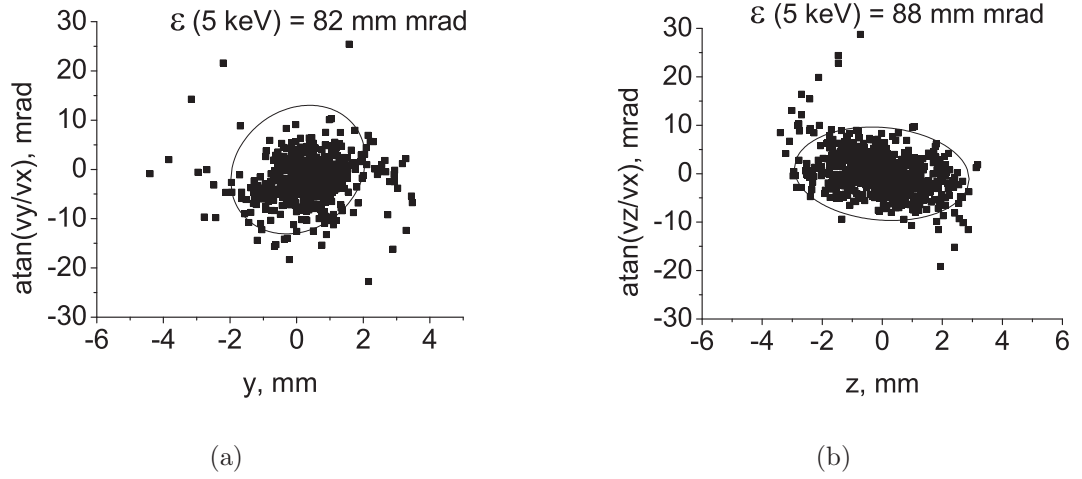


Figure A.1: Transverse phase space diagrams along the (a) horizontal and (b) vertical direction at BOB3, for the straight line beam transport from the N4-shielding wall (BOB1) to the ion buncher.

Table A.5: Parameters used in the ion optical simulation of the beam transport from the test ion source to the ion buncher.

Parameter	Description
Uquadm	DC voltage on the main electrodes of the quadrupole deflector
Uquadc	DC voltage on the correction electrodes of the quadrupole deflector
Upel	DC voltage on the vertical planar Einzel lens
Ucel	DC voltage on the vertical cylindrical Einzel lens
Ppel(c)	Position of the vertical planar Einzel lens
Pcel(c)	Position of the vertical cylindrical Einzel lens

Table A.6: Optimum parameters of the elements for the beam transport from the test ion source to the ion buncher.

Parameter	Voltage relative to $V_{\text{base}} = -5 \text{ kV}$, V
Uquadm	± 4325
Uquadc	± 2422
Upel	-6000
Ucel	-6530
Position and dimension, mm	
Ppel(c)	95 14 3 14
Pcel(c)	195 30 5 30

With the optimum parameters listed in Table A.6, the beam transport gives the transverse phase space diagrams shown in Fig. A.3, indicating negligible emittance increase when compared to those before the transport (Fig. A.2).

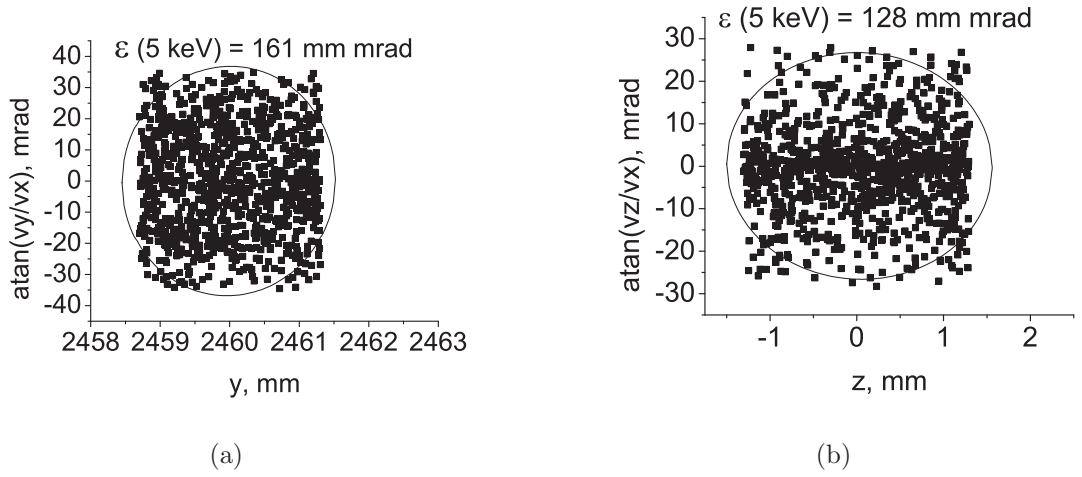


Figure A.2: Transverse phase space diagrams along the (a) horizontal and (b) vertical direction at the position of the test ion source.

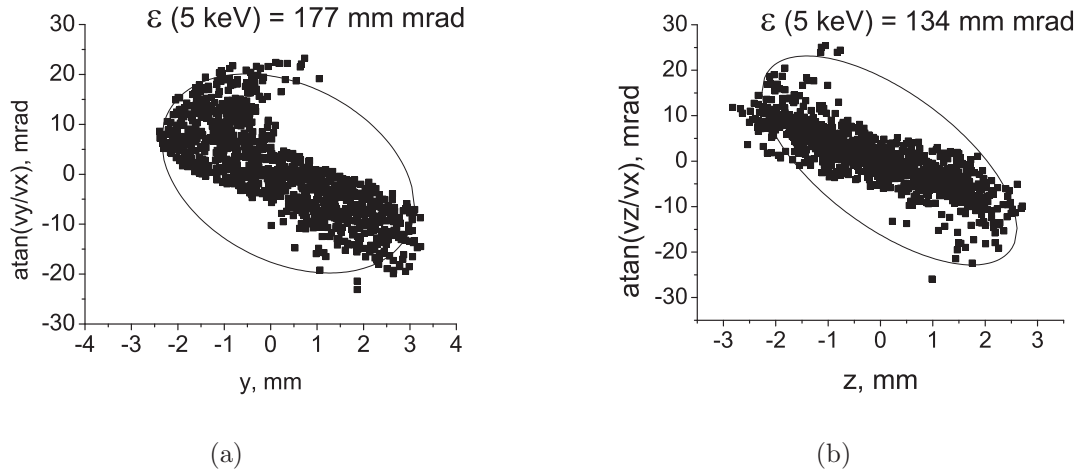


Figure A.3: Transverse phase space diagrams along (a) horizontal and (b) vertical direction of the beam transported from the test ion source, recorded at BOB3.

A.4 From the ion buncher to the Penning trap and other experimental areas

A.4.1 Straight line beam transport from the ion buncher to the Penning trap

From the ion buncher to BOB4

The parameters used in this simulation are listed in Table A.7.

The transverse phase space diagrams for three different masses at the beginning of this section are shown in Fig. A.4. The switching time of the potential of the pulsed drift tube was determined for each mass. For the minimum tube length of 600mm, Fig. A.5 gives the axial spatial distribution of the ions inside the pulsed drift tube.

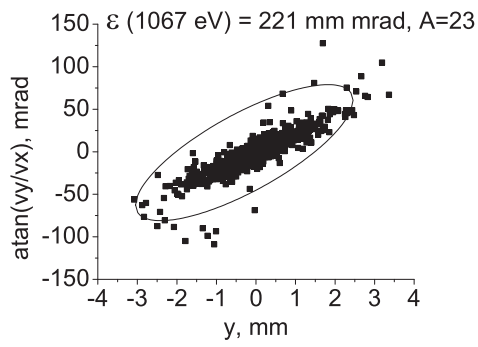
The optimal settings found in the simulation are listed in Table A.8. Resulting transverse phase space diagrams for different masses are shown in Fig. A.6 and A.7 for the final beam energy of 2 kV and 60 keV, respectively.

Table A.7: Parameters used in the ion optical simulation of the beam transport from the ion buncher to BOB4.

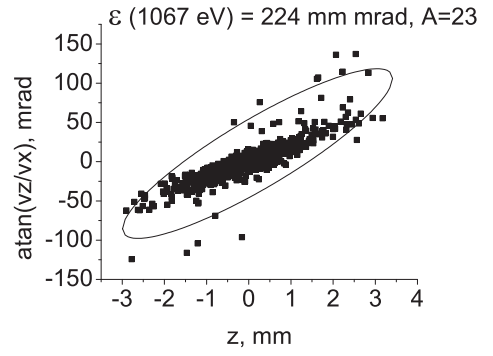
Parameter	Description
Utrantube	DC voltage on the transfer tube (differential pumping tube)
Uens	DC voltage on the U shape dummy lens
Udeflens	DC voltage on the deflector lens
Udtinj2k	DC voltage on the pulsed drift tube before potential switching for 2 keV acceleration
Udtinj60k	DC voltage on the pulsed drift tube before potential switching for 60 keV acceleration
Udtej2k	DC voltage on the pulsed drift tube after potential switching for 2 keV acceleration
Udtej60k	DC voltage on the pulsed drift tube after potential switching for 60 keV acceleration
Plens2k	DC voltage on the lens after the tube for 2keV acceleration
Plens60k	DC voltage on the lens after the tube for 60 keV acceleration
Ptrantube(1)	Position of the transfer tube
Plens(1)	Position of the U shaped dummy lens
Pdeflens(1)	Position of the deflector lens
Pdt(1)	Position of the pulsed drift tube
Plens2(c)	Position of the lens after the pulsed drift tube

Table A.8: Optimum parameters of the elements for the beam transport from the ion buncher to BOB4.

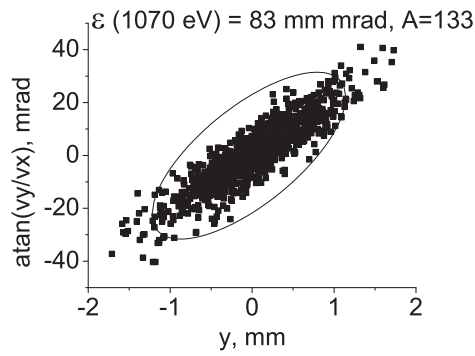
Parameter	Voltage relative to V_{base}, V	V_{base}, V
Utrantube	-1100	0
Uens	-2000	
Udeflens	-3600	
Udtinj2k	-2000	
Udtinj60k	-2000	
Udtej2k	0	-2000
Udtej60k	58000	
Uens2k	0	
Uplens60k	48200	
	Position and dimension, mm	
Ptrantube(1)	0	
Plens(1)	38	
Pdeflens(1)	123	
Pdt(1)	180	
Plens2(c)	820	



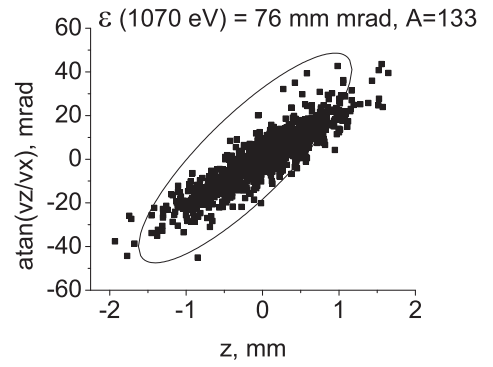
(a)



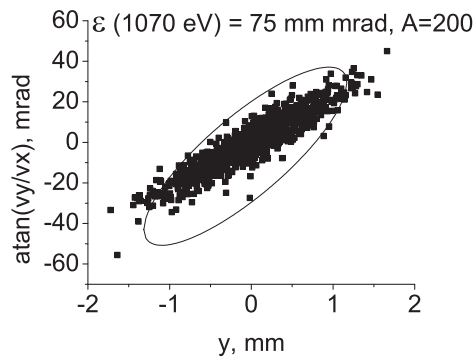
(b)



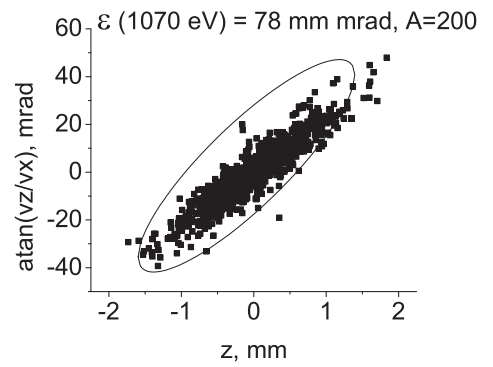
(c)



(d)

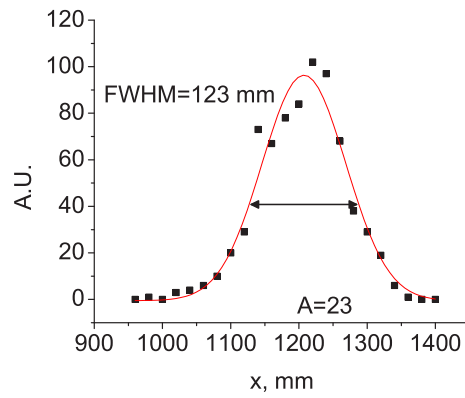


(e)

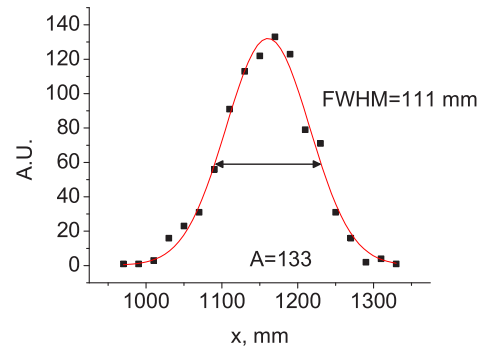


(f)

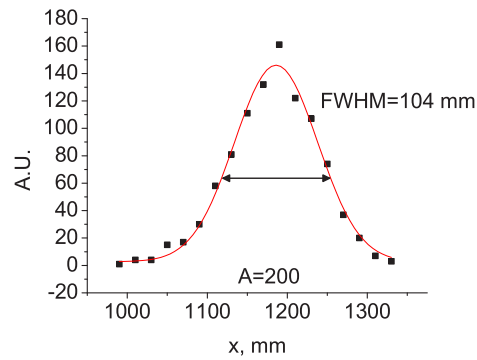
Figure A.4: Transverse phase space diagrams along the (a) horizontal and (b) vertical direction for three different masses ($A=23$, 133 and 200) at the exit of the transfer tube.



(a)

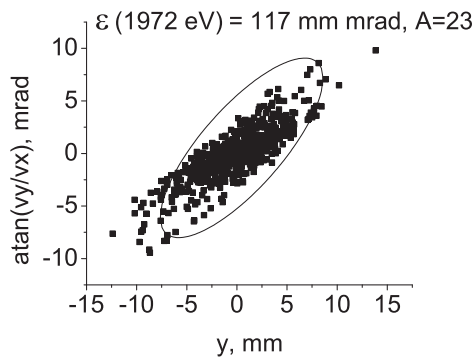


(b)

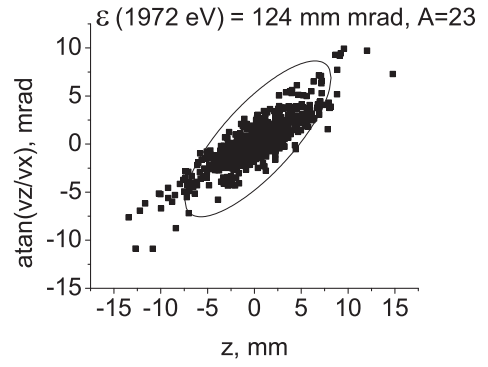


(c)

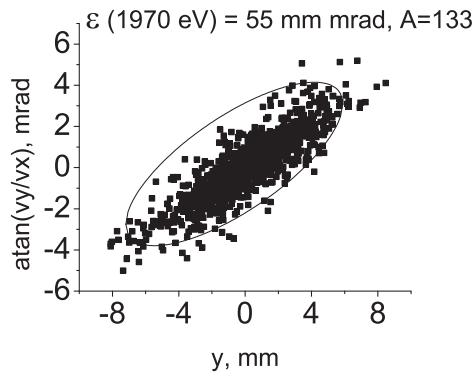
Figure A.5: Axial spatial distribution of ions inside the pulsed drift tube with the optimum potential switching time. (a) $A=23$ with $t=8.5 \mu\text{s}$ (b) $A=133$ with $t=19.5 \mu\text{s}$ (c) $A=200$ with $t=24.5 \mu\text{s}$.



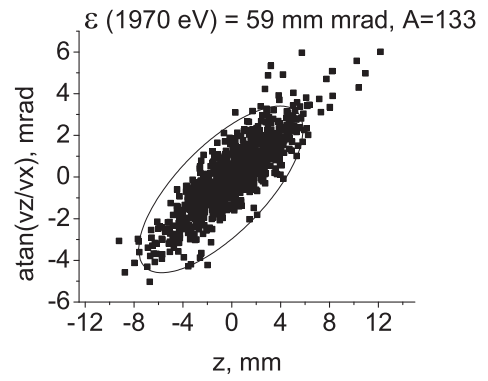
(a)



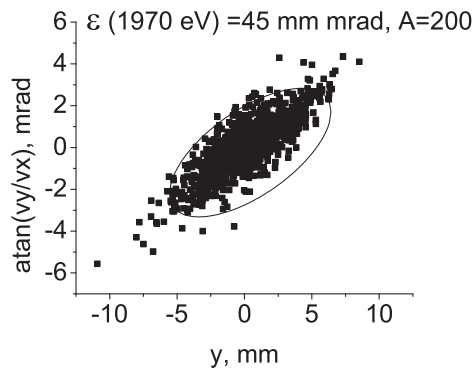
(b)



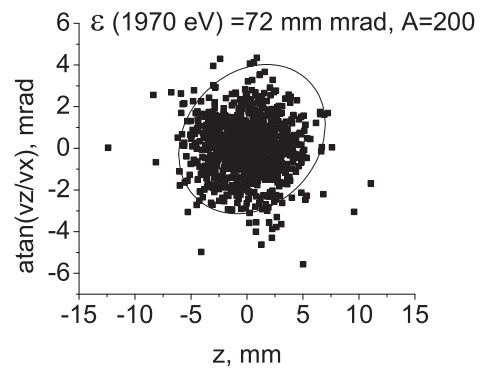
(c)



(d)

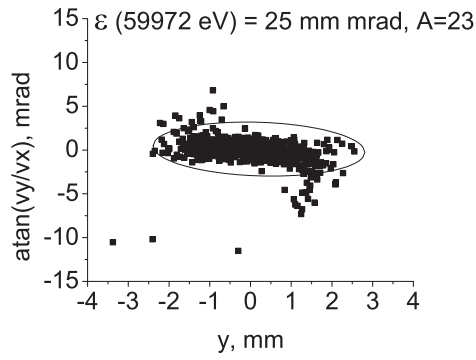


(e)

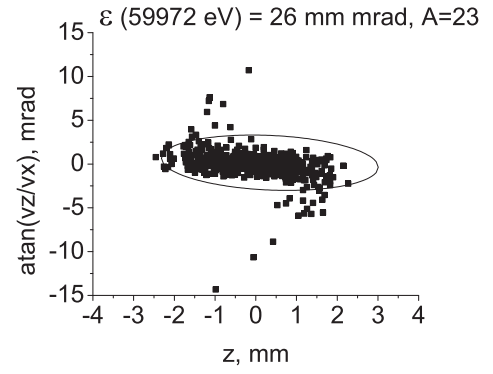


(f)

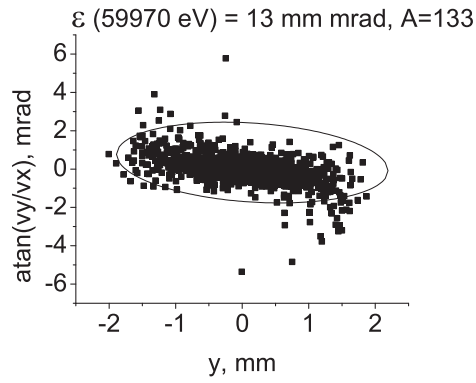
Figure A.6: Transverse phase space diagrams along the (a) horizontal and (b) vertical direction for three different masses ($A=23$, 133 and 200) which are transported from the ion buncher to BOB4 with an final energy of about 2 keV.



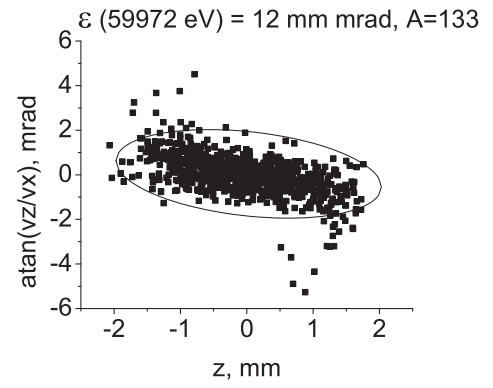
(a)



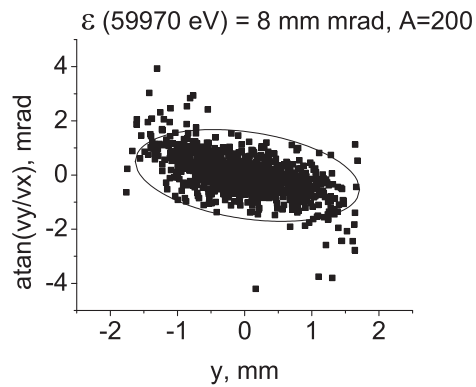
(b)



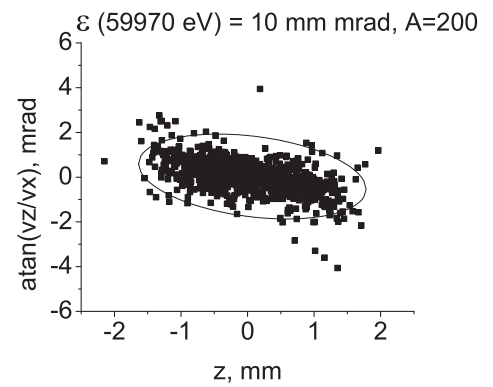
(c)



(d)



(e)



(f)

Figure A.7: Transverse phase space diagrams along the (a) horizontal and (b) vertical direction for three different masses ($A=23$, 133 and 200) which are transported from the ion buncher to BOB4 with an final energy of about 60 keV.

Table A.9: Parameters to be optimized in the ion optical simulation of the beam transport from BOB4 to the Penning trap.

Parameter	Description
Uens1	DC voltage on the first Einzel lens
Uens2	DC voltage on the second Einzel lens
Plens1	Position and dimension of the first Einzel lens
Plens2	Position and dimension of the second Einzel lens

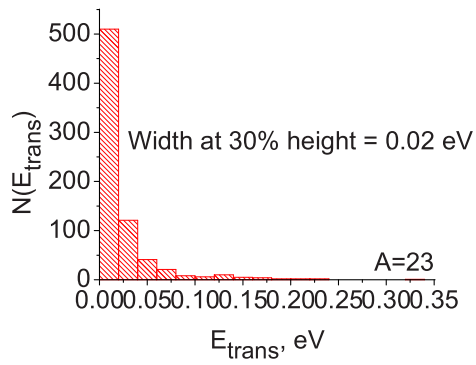
Table A.10: Optimum parameters used for the elements of the beam transport from BOB4 to the Penning trap.

Parameter	Voltage relative to $V_{\text{base}} = -2$ kV, V
Uens1	-3600
Uens2	-5900
	Position and dimension, mm
Plens1	100 60 10 60
Plens2	1170 100 20 100

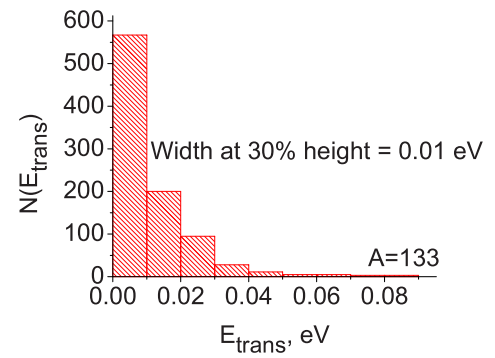
From BOB4 to the Penning trap

The main task of this simulation was to minimize the radial energy pickup of the ions when injected into the magnetic field of the Penning trap. Two Einzel lenses are used with their corresponding parameters listed in Table A.9.

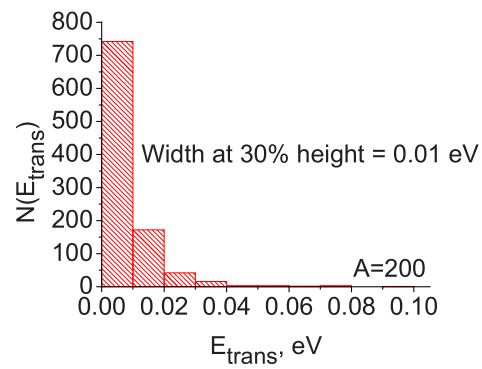
Starting with 2 keV beams with properties as calculated in the simulations discussed in section A.4.1, the initial transverse energy distributions of ions with three different masses are shown in Fig. A.8. There is nearly no transverse energy at the beginning. From the simulations optimal parameters listed in Table A.10 were obtained. The transverse energy distribution for the three different masses are shown in Fig. A.9. In the case of the lightest ions, the radial energy increases about 5 eV for these optimized parameters. However, this is still small compared to the radial energy of 190 eV this ion would have if it performs a cyclotron motion of 1 mm radius.



(a)

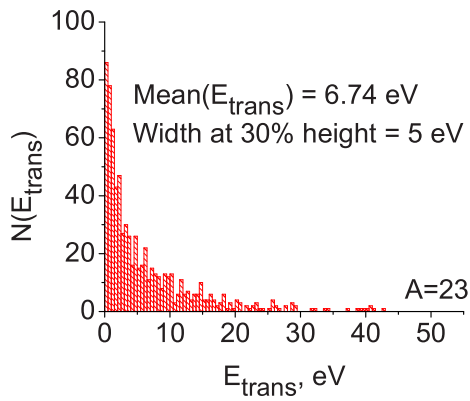


(b)

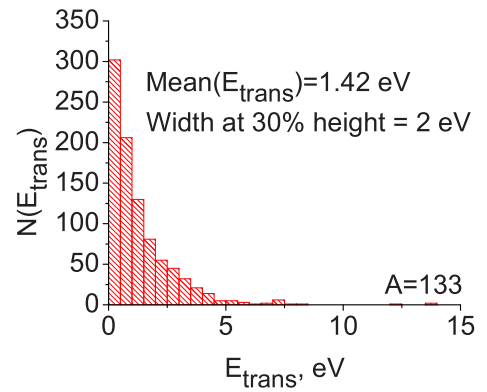


(c)

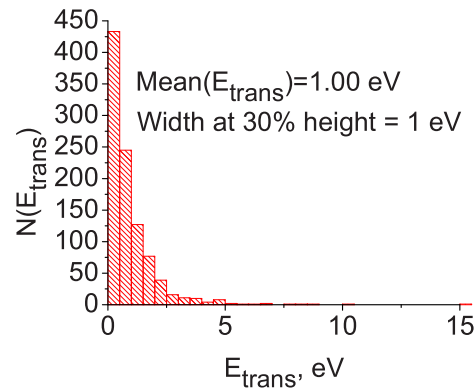
Figure A.8: Transverse energy distribution for three different masses ((a) $A=23$ (b) $A=133$ (c) $A=200$) before entering the magnetic field.



(a)



(b)



(c)

Figure A.9: Transverse energy distribution for three different masses ((a) $A=23$ (b) $A=133$ (c) $A=200$) before the center of the magnetic field.

A.4.2 Optional beam transport through a switchyard

In this section we follow the notations marked in Fig 3.16 and Fig 3.17 to discuss optimization of the parameters of the two electrostatic beam bending and delivering systems. Table A.11 lists all the available parameters used in the simulation.

Table A.11: Parameters used in the ion optical simulation for the beam transport from BOB4 through a switchyard.

Parameter	Description
Uqpa1	DC voltage of the first segment of the quadrupole triplet for the 60 ⁰ beam line
Uqpa2	DC voltage of the second segment of the quadrupole triplet for the 60 ⁰ beam line
Uqpa3	DC voltage of the third segment of the quadrupole triplet for the 60 ⁰ beam line
Uqpb1	DC voltage of the first segment of the quadrupole triplet for the 90 ⁰ beam line
Uqpb2	DC voltage of the second segment of the quadrupole triplet for the 90 ⁰ beam line
Uqpb3	DC voltage of the third segment of the quadrupole triplet for the 90 ⁰ beam line
Rkicker	Radius of the beam steerer in both cases
Rbender	Radius of the beam bender in both cases
HWkicker	Half of the gap width of the beam steerer in both cases
HWbender	Half of the gap width of the beam bender in both cases
DL1h	Distance between the beam origin and the center of the beam steerer for the 60 ⁰ beam line
DL2h	Distance between the center of the beam steerer and the beginning of the beam bender for the 60 ⁰ beam line
DL3h	Distance between the end of the beam bender and the beginning of the first segment of the quadrupole triplet for the 60 ⁰ beam line
L1h	Length of each segment of the quadrupole triplet for the 60 ⁰ beam line
DL4h	Distance between two consecutive segments of the quadrupole triplet for the 60 ⁰ beam line
DL5h	Distance between the end of the quadrupole triplet and the beam detector for the 60 ⁰ beam line
DL1v	Distance between the beam origin and the center of the beam steerer for the 90 ⁰ beam line
Continued on next page	

Table A.11 – (Continued) Parameters used in the ion optical simulation for the beam transport from BOB4 through a switchyard.

Parameter	Description
DL2v	Distance between the center of the beam steerer and the beginning of the beam bender for the 90 ⁰ beam line
DL3v	Distance between the end of the beam bender and the beginning of the first segment of the quadrupole triplet for the 90 ⁰ beam line
L1v	Length of each segment of the quadrupole triplet for the 90 ⁰ beam line
DL4v	Distance between two consecutive segments of the quadrupole triplet for the 90 ⁰ beam line
DL5v	Distance between the end of the quadrupole triplet and the beam detector for the 90 ⁰ beam line
Aperh	Aperture of the quadrupole triplet for the 60 ⁰ beam line
Aperv	Aperture of the quadrupole triplet for the 90 ⁰ beam line

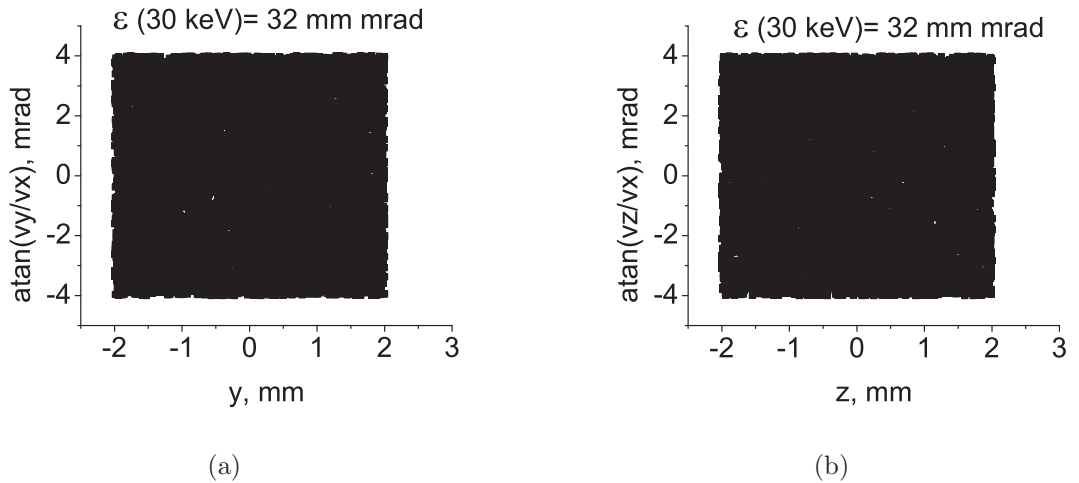


Figure A.10: Initial transverse phase space diagrams along the (a) horizontal and (b) vertical direction for the beam transport from BOB4 through a switchyard.

The initial beam is assumed to have a rectangular distribution in phase space, as shown in Fig. A.10. The optimum parameters found for both the 60⁰ and the 90⁰ beam transport are listed in Table A.12. Transverse phase space diagrams at the end of the 60⁰ beam line are given in Fig. A.11.

Table A.12: Optimum parameters of the elements for the beam transport from BOB4 through a switchyard.

Parameter	Voltage, V
Uqpa1	1496.1
Uqpa2	-1724
Uqpa3	1560.2
Uqpb1	1229.3
Uqpb2	-1574.7
Uqpb3	1281.6
	Position and dimension, mm
Rkicker	287
Rbender	300
HWkicker	17.5
HWbender	17.5
DL1h	100
DL2h	250
DL3h	197.6
L1h	120
DL4h	60
DL5h	300
DL1v	180
DL2v	250
DL3v	262.8
L1v	160
DL4v	80
DL5v	40
Aperh	28
Aperv	37

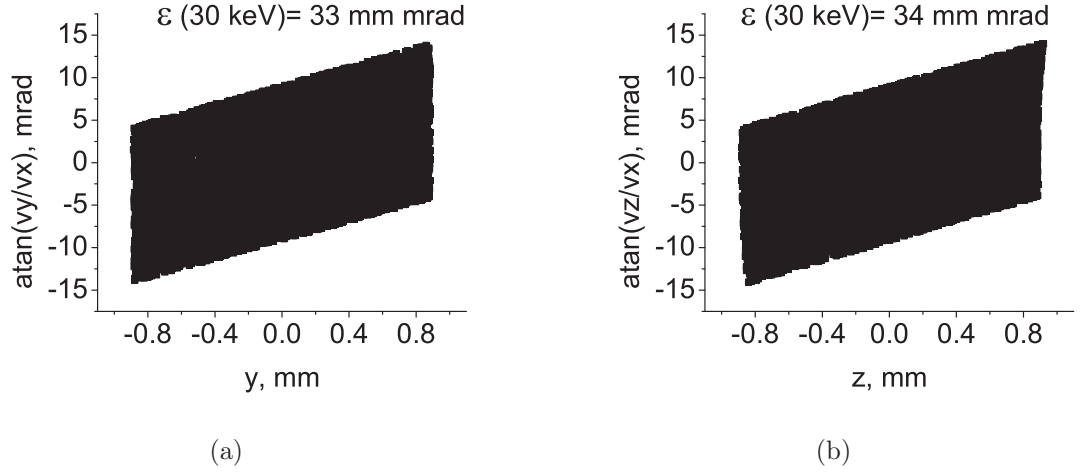


Figure A.11: Transverse phase space diagrams along (a) horizontal and (b) vertical direction of the beam being bent by 60° .

Table A.13: Effect of the energy spread on the increase of the transverse emittance.

bending angle	$(\epsilon_f/\epsilon_i)_{x\alpha}$		$(\epsilon_f/\epsilon_i)_{y\beta}$	
	$\delta = 0$	$\delta = 0.000167$	$\delta = 0$	$\delta = 0.000167$
60°	1.0584	1.0634	1.0261	1.0249
90°	1.0508	1.0662	1.0238	1.0231

Another test of this system is to introduce an axial energy spread in the beam

$$\delta = \frac{E - E_0}{E_0} = 0.000167 \tag{A.1}$$

which is about 5 eV for $E_0 = 30$ keV. The corresponding emittance comparison is listed in Table A.13, which shows a small increase in the case that includes the energy spread.

Bibliography

- [1] F.-K.Thielemann *et al.* *Phys. Rep.*, **227**:269, 1993.
- [2] H.Schatz *et al.* *Phys. Rep.*, **294**:167, 1998.
- [3] D.Lunney, J.M.Pearson, and C.Thibault. *Rev. Mod. Phys.*, **75**:1021, 2003.
- [4] C.Thibault *et al.* *Phys. Rev. C*, **12**:644, 1975.
- [5] N.A.Orr *et al.* *Phys. Lett. B*, **258**:29, 1991.
- [6] E.K.Warburton *et al.* *Phys. Rev. C*, **41**:1147, 1990.
- [7] M.Beiner *et al.* *Nucl. Phys. A*, **238**:29, 1975.
- [8] R.Smolańczuk and J.Dobaczewski. *Phys. Rev. C*, **48**:R2166, 1993.
- [9] J.Dobaczewski, W.Nazarewicz, and T.R.Werner. *Phys. Scr.*, **T56**:15, 1995.
- [10] W.Satula *et al.* *Phys. Lett. B*, **407(2)**:103, 2000.
- [11] P.G.Hansen, A.S.Jensen, and B.Jonson. *Annu. Rev. Nucl. Part. Sci.*, **45**:591, 1995.
- [12] P.G.Hensen and B.Jonson. *Europhys. Lett.*, **4**:409, 1987.
- [13] I.Tanihata. *J. Phys. G*, **22**:157, 1996.
- [14] K.Riisager *et al.* *Europhys. Lett.*, **49(5)**:547, 2000.
- [15] R.P.Feynman and M.Gell-Mann. *Phys. Rev.*, **109**:193, 1958.
- [16] J.C.Hardy and I.S.Towner. *Phys. Rev. C*, **71**:055501, 2005.
- [17] W.Benenson *et al.* *Phys. Rev. C*, **8(1)**:210, 1973.
- [18] R.C.Barber and K.S.Sharma. *Nucl. Instr. and Meth. B*, **204**:460, 2003.
- [19] L.G.Smith. *Proceedings of the International Conference on Nuclidic Masses*, edited by H. Duckworth. University of Toronto Press, Toronto, Canada, 1960.
- [20] L.G.Smith. *Proceedings of the 3rd International Conference on Atomic Masses*, edited by R. Barber. University of Manitoba Press, Manitoba, Canada, 1967.

- [21] M.P.Bradley *et al.* *Phys. Rev. Lett.*, **83A**:4510, 1999.
- [22] S.Rainville *et al.* *Hyperfine Int*, **132**:177, 2001.
- [23] M.Epherre, G.Audi, C.Thibault, R.Klapisch, G.Huber, F.Touchard, and H.Wollnik. *Phys. Rev. C*, **19**:1979, 1979.
- [24] K.S.Sharma *et al.* *Nucl. Instr. and Meth. B*, **26**:1987, 1987.
- [25] G.D.Alkhazov *et al.* *Z. Phys.*, **310**:247, 1983.
- [26] G.D.Alkhazov *et al.* *Z. Phys.*, **344**:425, 1993.
- [27] H.Savajols *et al.* *Hyperfine Int*, **132**:245, 2001.
- [28] R.Béraud *et al.* *Nucl. Instr. and Meth. A*, **346**:196, 1994.
- [29] G.Auger *et al.* *Nucl. Instr. and Meth. A*, **350**:235, 1994.
- [30] M.Chartier *et al.* *Phys. Rev. Lett.*, **77**:2400, 1996.
- [31] M.Stadlmann *et al.* *Phys. Lett. B*, **586**:27, 2004.
- [32] H.Geissel *et al.* *Nucl. Phys. A*, **585**:115c, 2001.
- [33] Yu.A.Litvinov *et al.* *Nucl. Phys. A*, **756**:3, 2005.
- [34] D.Lunney *et al.* *Phys. Rev. C*, **64**:054311, 2001.
- [35] C.Bachelet *et al.* *Eur. Phys. J. A*, **25**:s1.31, 2005.
- [36] D.Rodriguez *et al.* *Phys. Rev. Lett.*, **93**:161104, 2004.
- [37] M.Mukherjee *et al.* *Phys. Rev. Lett.*, **93**:150801, 2004.
- [38] A.Kellerbauer *et al.* *Phys. Rev. Lett.*, **93**:072502, 2004.
- [39] F.Herfurth *et al.* *Eur. Phys. J. A*, **15**:17, 2002.
- [40] F.Herfurth *et al.* *Phys. Rev. Lett.*, **87**:142501, 2001.
- [41] F.Herfurth *et al.* *Eur. Phys. J. A*, **25**.s01:17, 2005.
- [42] G.Savard *et al.* *Hyperfine Int*, **132**:223, 2001.
- [43] M.Block *et al.* *Eur. Phys. J. A*, **25**.s01:49, 2005.
- [44] A.Jokinen *et al.* *Eur. Phys. J. A*, **25**.s01:27, 2005.
- [45] V.L.Ryjkov *et al.* *Eur. Phys. J. A*, **25**.s01:53, 2005.
- [46] G.Bollen *et al.* *Nucl. Instr. and Meth. A*, **532**:203, 2004.
- [47] L.Weissman, P.A.Lofy, D.A.Davies, and D.J. Morrissey. *Nucl. Instr. and Meth. A*, **531**:416, 2004.

- [48] SIMION, 2006. <http://www.simion.com/>.
- [49] M.Berz, J.Hoefkens, and K.Makino. *COSY INFINITY Version 8.1 Programming Manual*. MSUHEP-20703, Department of Physics and Astronomy, Michigan State University, 2002.
- [50] Hermann Wollnik. *Optics of Charged Particles*. Academic Press Inc., San Diego, California 92101, 1987.
- [51] C.T.Jones. *Programmable Logic Controllers: The Complete Guide to the Technology*. Patrich-Turner Publishing Co., Atlanta, Ga, 1998.
- [52] D.Beck, K.Blaum, H.Brand, F.Herfurth, and S.Schwarz. *Nucl. Instr. and Meth. A*, **527**:567–579, 2004.
- [53] W.Paul, H.P.Reinhard, and U.von Zahn. *Z. Phys.*, **152**:143, 1958.
- [54] P.H.Dawson. *Quadrupole Mass Spectrometry and its Application*. Elsevier, Amsterdam, 1976.
- [55] H.G.Dehmelt. *Adv. At. Mol. Phys.*, **3**:53, 1967.
- [56] N.W.MaLachlan. *Theory and Applications of Mathieu Functions*. Charendon Press, Oxford, 1947.
- [57] Carmen Chicone. *Ordinary Differential Equations with Applications*. Springer-Verlag, New York, 1999.
- [58] V.V.Parkhomchuk and A.N.Skrinsky. *Rep. Prog. Phys.*, **54 No.7**:919–947, 1991.
- [59] B.Appasamy J.Eschner and P.E. Toschek. *Phys. Rev. Lett.*, **74, Number13**:2435, 1995.
- [60] R.Calabrese *et al.* *Optics Communications*, **123**:530, 1996.
- [61] H.W.Ellis *et al.* *At. Data and Nucl. Data Tables*, **17**:177, 1976.
- [62] H.W.Ellis *et al.* *At. Data and Nucl. Data Tables*, **22**:179, 1978.
- [63] H.W.Ellis *et al.* *At. Data and Nucl. Data Tables*, **31**:113, 1984.
- [64] L.A.Viehland and E.A.Mason. *At. Data and Nucl. Data Tables*, **60**:37, 1995.
- [65] R.Blümel *et al.* *Phys. Rev. A*, **40**:808, 1989.
- [66] Stefan Schwarz. *Manipulation of Radioactive Ion Beams using a Paul Trap and Direct Mass Measurements of Neutron-Deficient Mercury Isotopes at the ISOLTRAP-Experiment*. PhD thesis, der Johannes Gutenberg-Universität in Mainz, 1998.
- [67] Editor-in-Chief David R.Lide. *Handbook of Chemistry and Physics*. 83rd Edition, 2002.

- [68] R.Alheit *et al.* *Int. J. Mass Spec. Ion Process*, **154**:155, 1996.
- [69] E.W.McDaniel and E.A.Mason. *The Mobility and Diffusion of Ions in Gases*. New York, Wiley, 1973.
- [70] G.Bollen *et al.* To be published in *Phys. Rev. Lett.*, *Experiments with Thermalized Rare Isotope Beams from Projectile Fragmentation - A Precision Mass Measurement of the Super-Allowed β -Emitter ^{38}Ca* .
- [71] M.König *et al.* *Int. J. Mass Spec. Ion Process*, **142**:95–116, 1995.
- [72] G.Audi, O.Bersillon, J.Blachot, and A.H.Wapstra. *Nucl. Phys. A*, **729**:3–128, 2003.
- [73] G.Bollen *et al.* *Phys. Rev. C*, **46**:R2140, 1992.
- [74] Gilbert W.Butler *et al.* *Phys. Rev.*, **166**:1096, 1968.
- [75] E.P.Wigner. *Proceedings of the Robert A. Welch Foundation Conderence on Chemical Reserach*. anything, Houston, 1958.
- [76] J.Jänecke. *Phys. Rev.*, **147**:735, 1966.
- [77] G.T.Garvey. *Nuclear Isospin*. Academic Press, New York, 1969.
- [78] G.T.Garvey. *Annual Review of Nuclear Science*. Annual Reviews, Palo Alto, 1969.
- [79] J.Britz, A.Pape, and M.S.Antony. *At. Data and Nucl. Data Tables*, **69**:125, 1998.
- [80] K.Blaum *et al.* *Phys. Rev. Lett.*, **91**:260801, 2003.
- [81] P.M.Endt and R.B.Firestone. *Nucl. Phys. A*, **633**:1–220, 1998.